# Single And Double Perovskite Multiferroic Nanostructures With Their Diverse Applications

*Thesis submitted for the degree of*

**Doctor of Philosophy**

*in*

**Physics (Experimental)**

*By*

**Mahebub Alam**

Department of Physics

University of Calcutta

August, 2019

*Dedicated to my beloved parents…*

# Acknowledgement

These four and half years I have spent at S N Bose National Centre for Basic Science, Kolkata, is the source of most valued experiences of my life. I sincerely acknowledge the direct and indirect support of so many people throughout this demanding period of my pursuit of research. First of all I owe my heartfelt gratitude to my supervisor Prof. Kalyan Mandal, for giving me the opportunity to work in his laboratory. It was a countless desire to work under his direction. He always encouraged and motivated me to think and accomplish my research work independently in challenging areas. Without his constructive suggestion, and constant support, any of my research work would not come to fruition.

I am grateful to S. N. Bose National Centre for Basic Sciences (SNBNCBS), Kolkata, for offering a pleasant and green campus, advanced instrumental facilities, working research environment. I am also grateful to Department of Science and Technology (DST), India, for financial supports.

A large part of this thesis work would not have been possible without the active involvement of Dr. Gobinda Gopal Khan (informally, Gogo da). The initation of our collaboration was undecided. We were casually discussing about some problem while preparing the samples, and gradually the informal discussion consolidated into something comprehensive and tangible. Working with him was always a pleasure. He always encourages me a lot about my research work. Our sharing of some common hobbies like photography and travel naturally enhances the intimacy.

I had the pleasure to work with my seniors and labmates: Dr. Madhuri Mandal, Dr. Arka Chaudhuri, Dr. Rajasree Das, Dr. Debasish Sarkar, Dr. Ashutosh Kumar Singh, Dr. Monalisa Pal, Dr. Arup Ghosh, Dr. Rupali Rakshit, Keshab Karmakar, Souvanik Talukdar, Indranil Chakraborty, Dipika Mandal, Subrata Ghosh, Dipanjan Maity, Anupam Gorai,

Swarnali Hait, Priyanka Saha, Saheli Samanta, Esma Khatun, Kaushik Baishya, Priya Maity, Shashank Gupta, Deblina Majumdar, and Suchandra Mukherjee, for providing me a homely and cheerful environment in lab. I must thank especially to Arka Da, Monalisa Di, Arup Da, and Rupali Di for constantly providing technical assistance. For any kind of assistance whatsoever, Arka da always took pains to make himself available. Arup Da admired

# Contents

## Chapter 2: Experimental Details [34-70]

**Chapter 3:  Synthesis of $CoFe_2O_4$/ $BiFeO_3$ Bilayered Nano Hollow Spheres & Study Their Multiferroic Properties** **[71-95]**

# List of Publications:

1. **\*M. Alam**, K. Mandal, G. G. Khan

   "Double perovskite $Y_2NiMnO_6$ nanowires: high temperature ferromagnetic–ferroelectric multiferroic"

   **RSC Advances,** 6 (2016) 62545-62549.

2. **\*M. Alam**, K. Karmakar, M. Pal, and K. Mandal

   **"**Electrochemical Supercapacitors Based on Double Perovskite $Y_2NiMnO_6$ Nanowires**"**

   **RSC Advances,** 6 (2016) 114722-114726**.**

3. **\*M. Alam**, S. Talukdar, K. Mandal

   **"**Multiferroic properties of bilayered $BiFeO_3/CoFe_2O_4$ nano-hollowspheres**"**

   **Materials Letters,** 210 (2018) 80–83.

4. **\*M. Alam**, I. Chakraborty, K. Mandal

   **"**Microwave synthesis of surface functionalized $ErFeO_3$ nanoparticles for photoluminescence and excellent photocatalytic activity**"**

   **Journal of Luminescence,** 196 (2018) 387–391.

5. D. Mandal, **M. Alam** and K. Mandal

   **"**$NiFe_2O_4$ Nano-hollow spheres with improved Magnetic and Dielectric Properties**"**

   **Physica B: Condensed Matter,** 554 (2019) 51-56.

6. P. Saha, R. Rakshit, **M. Alam,** and K. Mandal

   **"**Strain driven magnetic and electronic properties of Zn doped $Fe_3O_4$ nano-hollow spheres**"**

   **Physical Review Applied,** 11 (2019) 024059-024070.

7. **\*<u>M. Alam</u>**, K. Mandal, G. G. Khan

"Room Temperature Ferromagnetism and Ferroelectricity in double perovskite $Y_2NiMnO_6$ Nanostructured Thin Films"

**Journal of Applied Physics (Submitted).**

8. **\*<u>M. Alam</u>** and K. Mandal

"Room temperature magnetoelectric coupling in multiferroic $ErFeO_3$ nanoparticles"

**Physica B: Condensed Matter (Submitted).**

9. **<u>M. Alam,</u>** D. Majumdar and K. Mandal

" magnetic and magnetoelectric in Er-doped $BiFeO_3$ ceramics with excellent gas-sensing property"

**(Ready for submission).**

**\*** <u>These publications are included in this thesis.</u>

# Chapter 1 | Introduction

In this chapter we discussed about the multiferroic properties and its importance. The detailed literature review of various works that motivate to work in this specific field, a brief outline of entire work has been also discussed.

## 1.1. Introduction

Multiferroics are one of the most fascinating kinds of multifunctional materials that coexist in several ferroic orders such as ferroelectricity [1, 2, 3], ferromagnetism [4, 5, 6], ferroelasticity [7, 8, 9], ferrotoroidicity [10], etc. These ordered parameters simultaneously bring out novel physical phenomena that can be used to develop possibilities for new devices, including sensors [11, 12], data storage [13, 14, 15], novel spintronics devices [16, 17, 18], integrated circuits [19, 20], random access memory [21, 22, 23], filters [24, 25], and photovoltaic devices [26, 27, 28, 29]. Materials with more than one ferroic order parameters present in a single-phase are called multiferroic materials. However, there are few multiferroic materials showing the coexistence of ferromagnetic (FM) and ferroelectric (FE) properties in the same phase i.e. the material possesses spontaneous polarization (P) and switching of the ferroelectric domain in the material can be controlled by using an externally applied magnetic field. Similarly, spontaneous magnetization (M) and spin ordering in the material can be controlled by using an externally applied electric field. Therefore, the search for novel multiferroics, where these two phenomena are mutually coupled, is of significant scientific and technological interest [21, 30, 31]. The coupling between electric and magnetic ordering is called the magnetoelectric (ME) effect and is defined as the induction of magnetization by an electric field or the induction of polarization by a magnetic field, providing a possibility to develop new devices based on this phenomena.

## 1.2. Brief Historical Background

In 19$^{th}$ century electricity and magnetism are intrinsically combined into one common system and their coupling was given by Maxwell equations. In 1894 Pierre Curie proposed the existence of the probability of electricity and magnetism in some insulators, according to crystal symmetry. The real beginning of this field started in 1959 with a short remark by Landau and Lifshitz in a volume of their Course of Theoretical Physics [32]. Nothing significant happened afterwards until 1960, when

Astrov experimentally asserted the coexistence of two types of ordering in the first real magnetoelectric material $Cr_2O_3$ [33], following Dzyaloshinskii's prediction one year earlier [34]. But $Cr_2O_3$ was not conductive for practical purpose because of antiferromagnetism and paraelectricity coupled with each other. In $20^{th}$ century, the progress on magnetoelectric was quite slow because of the unavailability of magnetoelectric material and poor performances. In the 1990s a new twist occurred in magnetoelectric physics. In 1994, Schmid [35] introduced a new terminology: multiferroics, which may show two types of ordering – ferroelectricity (the spontaneous ordering of electric dipole moment) and ferromagnetism (the spontaneous ordering of orbital and spin magnetic moment) in a single phase material. Later in 2000, Nicola Spaldin clarified the existing of magnetism and ferroelectricity in single-phase perovskite oxide materials [36]. Boracite may be the first known multiferroic material. Very soon several other multiferroic materials such as $PbFe_{0.5}Nb_{0.5}O_3$, $Ti_2O_3$ are found naturally or synthesized artificially [37]. But the main breakthrough occurred in 2003, when Ramesh's group successfully synthesized $BiFeO_3$ thin film [38]. $BiFeO_3$ was the first magnetoelectric material which gives excellent multiferroic property along with room temperature application. Again second experimental success was the discovery of a new class of multiferroic $TbMnO_3$ [39], in which ferroelectricity and magnetism coupled with each other. $TbMnO_3$ shows strong magnetoelectric coupling with 100% ferroelectric domain flip in presence of several tesla magnetic fields. In the very next year, two other similar multiferroic materials were discovered. One was orthorhombic $TbMn_2O_5$ [23] and another was hexagonal $HoMnO_3$ [40]. Like $TbMnO_3$, $TbMn_2O_5$ also shows strong magnetoelectric coupling property and gives switchable polarization in the presence of an external magnetic field. But $HoMnO_3$ was beginning to draw attention because of its high ferroelectric curie temperature (875 K), although its antiferromagnetic Neel temperature is very low (75 K). In the beginning, a material exhibits ferroelectricity and ferromagnetism defines as a multiferroic material, as shown in Fig. 1.1. But nowadays multiferroic is a well-established concept. A material exhibits one anti-ferroic order plus one ferroic order is called multiferroic, as illustrated in Fig.

1.2. The multiferroicity/multiferroic region has been significantly expanded. In fact, most of the type-II multiferroics show antiferromagnetic and ferroelectric order.
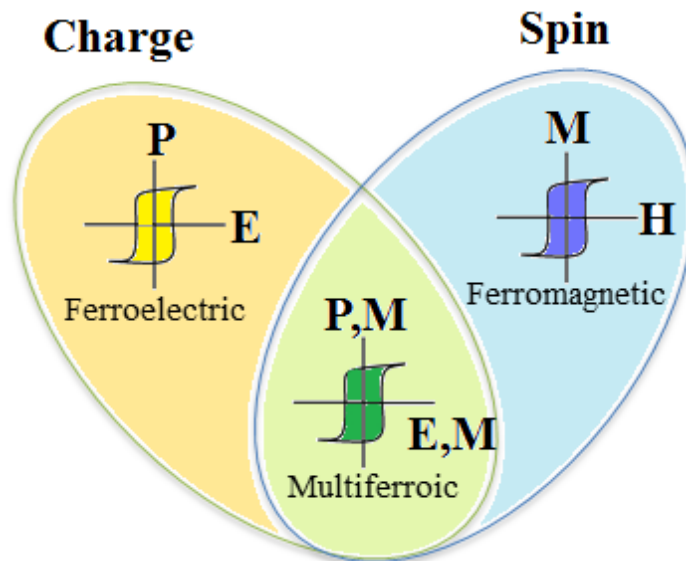


**Fig. 1.1:** Multiferroics combine the properties of ferroelectrics and ferromagnets. In the ideal case, the magnetization of a ferromagnet in a magnetic field displays the usual hysteresis (blue), and ferroelectrics have a similar response to an electric field (yellow). If we manage to create multiferroics that are simultaneously ferromagnetic and ferroelectric (green), then there is a magnetic response to an electric field, or, vice versa, the modification of polarization by magnetic field. And, in principle we have here the basis for making a 4-state logic state: (P+M+), $(P + M +), (+ −), (− +), (−)$ [1].



**Magnetically polarizable**
**Electrically polarizable**
**Multiferroic**
**Magnetoelectric**
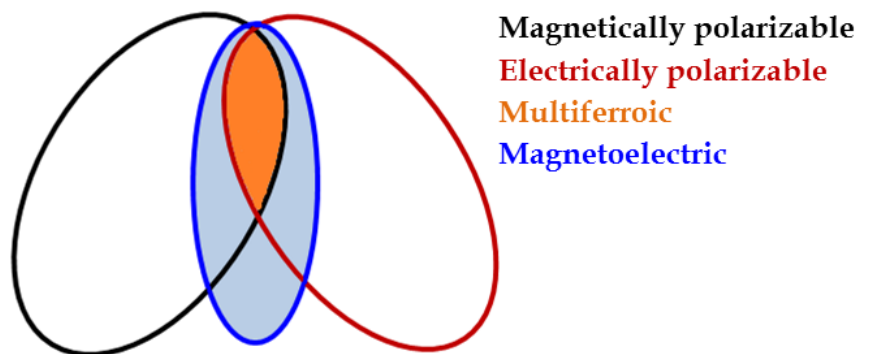
**Fig. 1.2:** An updated version, where the multiferroic zoo contains more members, not limited to the ferromagnetic + ferroelectric materials. For example, if a material is antiferromagnetic and ferroelectric, it can be certainly considered as a multiferroic. Magnetoelectric materials, which show magnetoelectric response/coupling, cover an even broader spectrum beyond ferroic materials.

## 1.3. Magnetoelectric Coupling in Multiferroic Materials

By definition, multiferroic is the property of a material which exhibits both ferroelectric and ferromagnetic property in a single phase. But the question arises how these two ferroic (FE, FM) properties coupled with each other. FE and FM are the intrinsic property of a material and their coupling is called magnetoelectric coupling gives a new property of the material. In this coupling, polarization can be generated by an applied magnetic field and magnetization can be induced by an applied electric field [30, 41]. The ME effect in a single crystal is conventionally stated in Landau theory [42] by expressing the free energy (F) of the system as:

$$F(E,H) = F_0 - P_i^s E_i - M_i^s H_i - \frac{1}{2}\varepsilon_0\varepsilon_{ij}E_iE_j - \frac{1}{2}\mu_0\mu_{ij}H_iH_j - \alpha_{ij}E_iE_j - \frac{1}{2}\beta_{ijk}E_iH_jH_k \qquad (1.1)$$

$$- \frac{1}{2}\gamma_{ijk}H_iE_jE_k - \frac{1}{4}\delta_{ijkl}H_iH_jE_kE_l - \cdots$$

Where $F_0$ is the ground state free energy and $P_i^s$, $M_i^s$ are the components of spontaneous polarization and spontaneous magnetization respectively. $E_i$ and $H_i$ are the component of electric (E) and magnetic field (H). i, j, k, l are the subscript for those four components in spatial coordinates. The permittivity of vacuum is denoted by $\varepsilon_0$ and the relative permittivity $\varepsilon_{ij}$(T) is independent of applied electric field. Similarly $\mu_0$ and $\mu_{ij}$ are the free space and relative magnetic permeability respectively. $\alpha_{ij}$ is the linear ME coupling term. $\beta_{ijk}$ and $\gamma_{ijk}$ are the quadratic coupling terms in third order and $\delta_{ijkl}$ represents biquadratic coupling term. After minimizing the free energy, we can obtain the polarization and magnetization.

$$P_i(E,H) = \frac{-\partial F}{\partial E_i} = P_i^s + \varepsilon_0\varepsilon_{ij}E_j + \alpha_{ij}H_j + \frac{1}{2}\beta_{ijk}H_jH_k + \gamma_{ijk}H_iE_j + \frac{1}{4}\delta_{ijkl}H_kH_jE_l \qquad (1.2)$$

$$M_i(E,H) = \frac{-\partial F}{\partial H_i} = M_i^s + \mu_0\mu_{ij}H_j + \alpha_{ij}E_j + \beta_{ijk}H_jE_i + \frac{1}{2}\gamma_{ijk}E_jE_k + \frac{1}{4}\delta_{ijkl}H_jE_kE_l \qquad (1.3)$$

The linear magnetoelectric coupling coefficient $\alpha_{ij}$ is limited by the relation [43]

$$\alpha_{ij}^2 < \varepsilon_{ii}\mu_{jj} \qquad (1.4)$$

We can get a phenomenological idea about the coupling property from the Ginzburg-Landau approach. The free energy can be formulated as the Taylor expansion of two order parameters and describes the linear coupling between M and P. Here only even

power of M and P appears because the free energy is invariant under time reversal. For example, if the time sequence is reversed, F will change with the presence of a term like M which is physically impossible. But the mixed terms also holds with same time-reversal and space inversion.

Now the expansion for the spatially uniform system can be written as

$$F(\vec{P},\vec{M}) = F_0 + \alpha\vec{P}^2 + \frac{\beta}{2}\vec{P}^4 + \alpha\vec{M}^2 + \frac{\beta}{2}\vec{M}^4 + \gamma\vec{P}^2\vec{M}^2 - \vec{P}\vec{E} - \vec{M}\vec{H} \qquad (1.5)$$

Where, $F_0$ is the original free energy in absence of electric and magnetic field. $\alpha_{ij}$ and $\alpha_{ij}$ are the Landau coefficients. Last two terms describe the effect of the conjugate field on order parameter. $\gamma\vec{P}^2\vec{M}^2$ describes the lowest order coupling. Different multiferroic coupling properties are shown in Fig. 1.3.
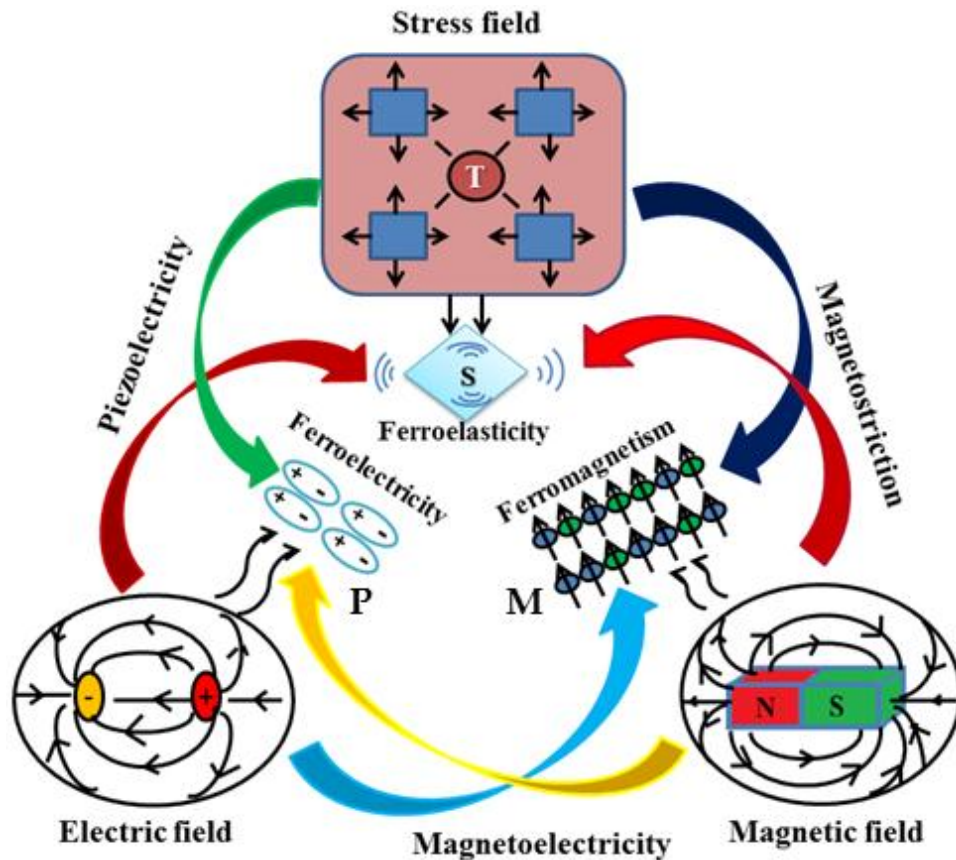


**Fig. 1.3:** Schematic illustrating magnetic-elastic-electric couplings in multiferroic materials. Here, M is magnetization, S is mechanical strain, and P is dielectric polarization [44].

# 1.4. Microscopic Origin of Ferroelectricity and Magnetism

The microscopic origin of magnetism is the presence of localized electron. In case of a transition metal or rare-earth ions, the partially filled d or f electrons are responsible for this. But the origin of ferroelectricity is quite different. According to the type of multiferroic, there are many microscopic origins of ferroelectricity and ferromagnetism. Generally multiferroic is two type – type-I multiferroic and type-II multiferroic.

## *1.4.1. Type-I multiferroic*

In case of type-I multiferroic the origin of ferroelectricity and ferromagnetism are different and they are largely independent with each other. Since the origin is different, the coupling between electricity and magnetism is weak in case of type-I multiferroic. These multiferroic materials are called old multiferroic materials. In these multiferroics, the ferroelectric Curie temperature is quite high and larger than the magnetic transition temperature. The spontaneous polarization is also high $\sim$ 10-100 $\mu C/cm^2$. These multiferroics are also good ferroelectric materials. Type-I multiferroic has several subclasses according to their mechanism of ferroelectricity.

### 1.4.1.1. Multiferroic perovskite

Multiferroic perovskite is a well-known class of ferroelectrics. Among perovskite [45], there are many magnetic and also many ferroelectric materials [46]. Out of these, there seems to be a mutual exclusion of magnetism and ferroelectricity in perovskite materials. For magnetism, one required partially filled d orbital of transition metal ions. The ferroelectricity is caused by the off-center motion of transition metal ions from its original position. This off-center ion makes a covalent bond with oxygen using their empty d shell. Somehow, the presence of real d electron of the transition metal depresses the process and obstructing the ferroelectricity in perovskite. This is called $d^0$ vs $d^n$ problem. This problem can be overcome simultaneously by preparing perovskite like $ABO_3$, where B is the magnetic transition metal ions with d electron and are partially replaced by ferroelectric TM ions with empty d electrons to make the

configuration stable. In $PbFe_{1/2}Ta_{1/2}O_3$ and $Pb(Fe^{+3}_{1/2}Nb^{+5}_{1/2})O_3$ multiferroic Nb$^{+5}$, Ta$^{+5}$ ions are ferroelectric cations and Fe$^{+3}$ ions are magnetic.

**1.4.1.2. Multiferroic in which ferroelectricity is induced by lone pair electrons**

A lone pair refers to a pair of electrons that are not shared with any other atom present in the compound. These electrons are not participating in any chemical bonding and are called dangling or lone pair [47, 48, 49,]. These electrons are found in the outer most shell of an atom. In the case of BiFeO₃ (Fig. 1.4), BiMnO₃ and PbVO₃, Bi⁺³, Pb⁺³ have 6s electrons and plays a crucial role in the origin of ferroelectricity. More microscopically in these compounds the lone pair electrons are separated in one direction and make the dipole moment.
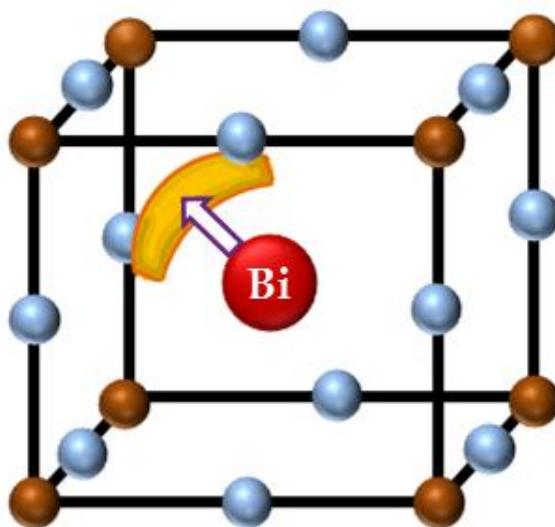


**Fig. 1.4:** The sketch of ordering of lone pairs electrons (yellow lobes) in BiFeO₃. Dark orange points are Fe ions and light blue points are oxygens [50].

**1.4.1.3. Multiferroic in which ferroelectricity originates from charge ordering**

One more mechanism for the origin of ferroelectricity is the charge ordering of electrons. This type of ferroelectricity observed in transition metal compounds, especially those compounds in which different valance states are present. Due to charge ordering both sides of the bond turnout to be inequivalent and leads to ferroelectricity. LuFe₂O₄ is the first proposed charged ordering multiferroic material, where the Fe⁺³

and $Fe^{+2}$ arrangements create the charge ordering. This mechanism can work in many systems like $Pr_{1/2}Ca_{1/2}MnO_3$ [51], $RNiO_3$ [17], $TbMn_2O_5$ [23] and $Ca_3CoMnO_6$ [52].

### 1.4.1.4. Multiferroic with geometric ferroelectricity

Geometric ferroelectricity occurs due to rotational distortion of transition metal oxides. Here the A side cation is smaller in size, so the oxygen octahedra collapse around it. For example in the case of $YMnO_3$ (Fig. 1.5) [53], the rigid $MnO_5$ tilts for closer packing, so that the oxygen ion moves closer to the smaller Y ion.
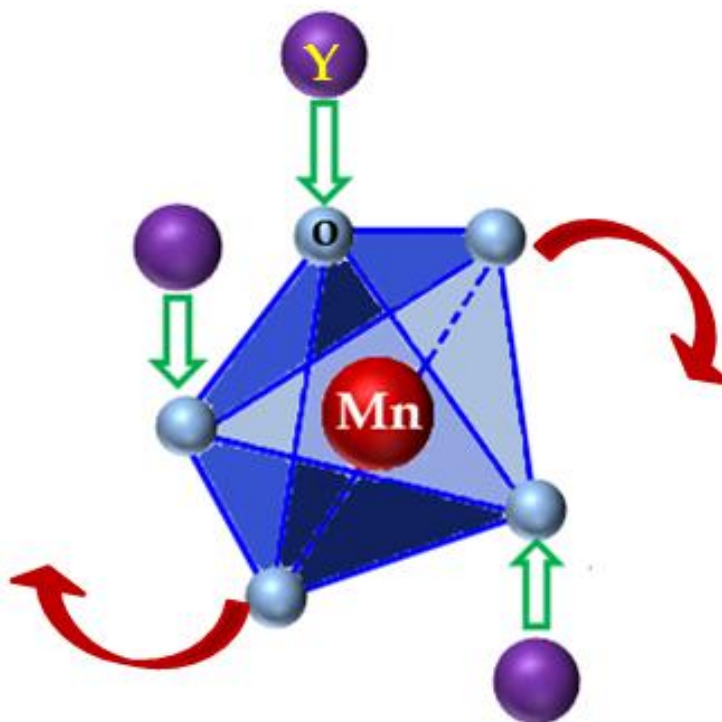
**Fig. 1.5:** Schematic picture of appearance of geometric ferroelectricity in $YMnO_3$ due to tilting of rigid $MnO_5$ octahedra [50].

## *1.4.2. Type-II multiferroic*

In case of type-II multiferroic materials significant coupling between FE and FM occurs, as the origin of ferroelectricity is caused by an exotic magnetic ordering. These multiferroic materials are comparatively new and best candidate for multiferroic applications [23, 39]. According to their mechanisms, type-II multiferroic can be divided into two groups. First one, in which the ferroelectricity is caused by a spiral type

magnetic ordering and the second one, in which the ferroelectricity seems even collinear magnetic ordering.

### 1.4.2.1. Spiral magnetic ordering type-II multiferroics

The nonlinear cycloidal spiral spin structure is the reason of ferroelectric polarization, and magnetic frustration is the source of this spin structure. Basically rare-earth manganites $RMnO_3$ (R = Y, Yb, Dy, Gd, etc.) and $Ni_3V_2O_6$ are showing this type of behavior [54, 55, 56]. In multiferroic manganites (Pbnm space group) the inversion symmetry is broken by some complex spiral magnetic ordering. These manganites are called pseudo- proper polarization because the polarization is created by a magnetization [17, 57]. To understand about the spiral spin magnetic ordering we consider $TbMnO_3$ [39]. At antiferromagnetic transition temperature, $T_{N1}$= 41 K, the magnetic spin structure has a form of the sinusoidal spin-wave. All the spins are directed in the same direction; however, the value of native moment varies periodically in space. Below $T_{N2}$ =28 K the Mn spin structure changes in such a way that spin sweep out in a cycloid. Here above $T_{N2}$ =28 K the magnetic order is collinear and paraelectric antiferromagnetic phase but below $T_{N2}$ =28 K, it shows the ferroelectric phase with cycloidal spiral magnetic structure. The inverse Dzyaloshinskii-Moriya (DM) interaction can be described by this mechanism. Due to the nonlinear magnetic ordering Mn-O-Mn bonds creates an off-centrosymmetric displacement of the oxygen ions and ferroelectric polarization develops. An applied external magnetic field can easily flip the direction of ferroelectric polarization [39, 58]. The polarization is given by a relation [59],

$$P \sim r_{ij} \times [S_i \times S_j] \sim [Q \times e] \tag{1.6}$$

where $r_{ij}$ is the vector connecting two neighboring spins $S_i$ and $S_j$. Q is the wave vector describing the spiral and e ~ [Q x e] is the spin rotation axis. The microscopic mechanism of this polarization is related to the spin- orbit interaction. The $Ni_3V_2O_6$, $DyMnO_3$, and $Ba_{0.5}Sr_{1.5}Zn_2Fe_{12}O_{22}$ are also showing same type of ferroelectric polarization [54, 55, 56]. But the ferroelectric polarization developed in such away are much smaller ($10^{-3}$ - $10^{-4}$) than the traditional ferroelectricity (type-I multiferroics).

**1.4.2.2. Collinear magnetic structures type-II multiferroics**

The magnetically driven ferroelectricity is created by the collinear magnetic ordering without any involvement of spin-orbit interaction. Here the magnetic moments are associated along a specific axis. Ferroelectric polarization appears in these materials due to the symmetric super-exchange interaction plus the charge ordering [60]. In this case, the magnetic moment is formed by ↑↑↓↓ spin structure. Here the magnetic order is competing for nearest neighbor ferromagnetic interaction ($J_{FM}$) and next-nearest neighbor antiferromagnetic interaction ($J_{AFM}$). If the magnetic spins are aligned along a chain with ↑↑↓↓ structure then the symmetric super-exchange interaction decreases the bond angle between two parallel spins and increases the bond angle between the antiparallel spins. This arrangement breaks the inversion symmetry of the system and ferroelectric polarization is developed along a particular direction (along chain direction). The simplest example of this type of material is $Ca_3CoMnO_6$ [52]. It consists of a one-dimensional chain with alternate $Co^{+2}$ and $Mn^{+4}$ arrangements. Many other perovskite materials such as $RMn_2O_5$ (R = Dy, Tb, Er, Y) belong to this group [17]. $TbMn_2O_5$ is one of them, where $Mn^{+3}$ (S=2) is surrounded by oxygen pyramids and $Mn^{+4}$ (S=3/2) is surrounded by oxygen octahedral. It consists of several complex magnetic phase transition and ferroelectric transition accompanied by electric polarization along the b- axis [23].

## 1.5. Single perovskite Materials (ABO₃)

In the case of single perovskite multiferroic oxides, the general chemical formula is $ABO_3$. Here A and B are two different cations having A cation is larger than B cation, and X is an anion that bonds to both. For an ideal cubic structure B cation is 6-fold coordination, surrounded by an octahedral of anions and the A cation is 12 fold co-ordination, as shown in Fig. 1.6. According to chemical formula or origin of ferroic property single phase multiferroics can be divided into some sub groups. We will discuss some of them.
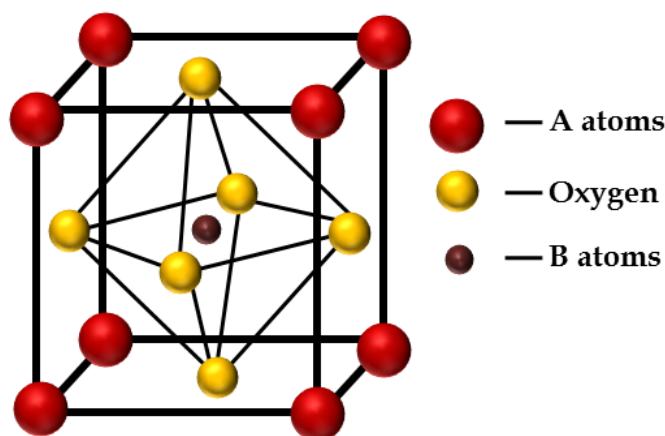
**Fig. 1.6:** General single perovskite structure [59].

## 1.5.1. Multiferroic BiFeO₃

### 1.5.1.1 Crystal structure

The crystal structure of $BiFeO_3$ is rhombohedrally distorted perovskite structure, which belongs to the 3Rc space group [62]. The reported lattice parameter of $BiFeO_3$ unit cell is found to be $a_{rhombohedral} = 3.96$Å and angle $\alpha = 89.3^0 - 89.4^0$ [63, 64]. Here the oxygen octahedral also rotates along the polar [111] axis [65]. This rhombohedral structure can be described interms of the hexagonal unit cell and denoted by [001]hexagonal ‖ [111]pseudocubic. Here the lattice parameters is found to be $a_{hexagonal} = 5.58$Å and $c_{hexagonal} = 13.89$Å [63, 66]. In pure cubic structure the oxygen octahedra rotation angle should be zero, but in the case of $BiFeO_3$ the rotation angle around the [111]pseudocubic axis is $11^0$-$14^0$ [62, 64]. This change in rotation angle in $BiFeO_3$ distorts the oxygen octahedra and changes Fe-O-Fe bond angle [64, 67]. This Fe-O-Fe bond angle is important since it controls the magnetic exchange and orbital overlap between Fe and O in $BiFeO_3$. It also controls the conductivity and magnetic ordering temperature [68]. The ferroelectric polarization arises in $BiFeO_3$ duo to the large displacement of Bi lone pair relative to $FeO_6$ octahedra. Out of eight possible directions, the ferroelectric polarization lies in [111] polar pseudocubic plane [69]. Basically at room temperature $BiFeO_3$ is G-type antiferromagnetic, in which Fe spins are ferromagnetically ordered within [111] plane and antiferromagnetically aligned adjacent [111] plane [70]. In case of

bulk $BiFeO_3$ the spin structure is cycloid type [71]. But the favorable alignment is the antiferromagnetic spin order along [111] plane [72]. So the $BiFeO_3$ have shown a large ferroelectric polarization as well as a small net magnetization [73].

### 1.5.1.2 Magnetism

In $BiFeO_3$, both short-range and long-range magnetic orderings are present simultaneously. But the short-range magnetic ordering in $BiFeO_3$ is G-type antiferromagnetic [74]. Here the spin of each $Fe^{+3}$ ion is surrounded by six antiparallel spins of nearest neighbor $Fe^{+3}$ ions. Due to magnetoelectric coupling, the spins are not perfectly antiparallel to each other; they make an angle to generate weak canting moment [68]. However, in the case of long-range antiferromagnetic ordering, the spin structure is not homogeneous. It consists of an incommensurate cycloid spin structure with a fixed distance of 62 - 64 nm as shown in Fig. 1.7 along [110] direction [71]. In 1982 Sosnowska first proposed this type of magnetic spin structure [74]. Subsequently verified by various experiments [74, 75, 76, 77]. In 2000 and 2003 Zalesskii and his teammates proposed that at low temperature the cycloid spin structure is distorted due to spin reorientation [78, 79]. But they did not have any idea about the phase transition temperature. Different research groups independently found different spin reorientation transition temperature and are 140 K and 200 K [80, 81]. At 140 K the magnon anomalies are observed and at 200 K the phonon-magnon coupling occurs [82]. The Fe ion substitution by Nb, Sc, Mn, Zr, Ti, and Co ions also increases the magnetization [83, 84, 85, 86, 87]. In this case, changing the Fe – O – Fe bond angle and varying the Fe valance state due to charge compensation increase the spin.
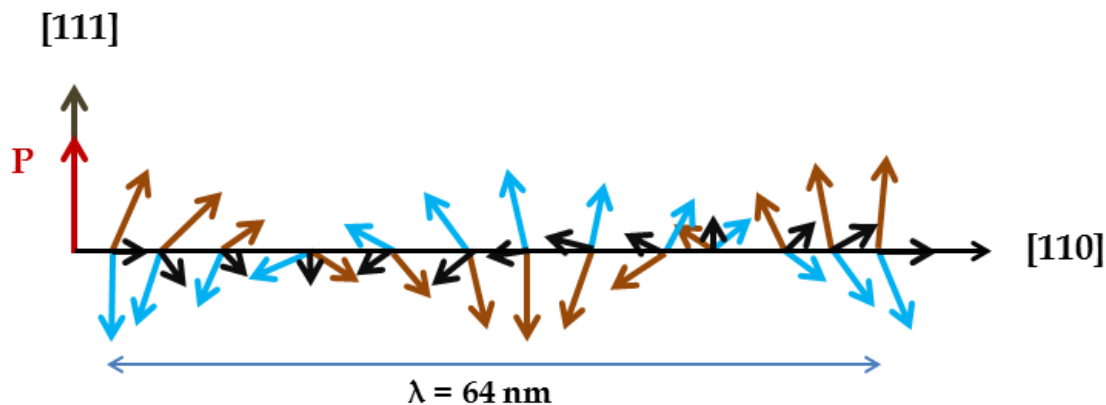
**Fig. 1.7:** Schematic representation of the spin cycloid. The canted antiferromagnetic spins (deep orange and light blue arrows) give rise to a net magnetic moment (black arrows) that is specially averaged out to zero due to the cycloidal rotation. The spins are contained within the plane defined by the polarization vector (dark red) and the cycloidal propagation vector (black) [74].

### 1.5.1.3 Ferroelectricity

Magnetoelectric material $BiFeO_3$ has a high critical temperature ($T_C$=1103 K) for ferroelectric polarization [38]. Generally ferroelectric perovskite contains transition metal (TM) ions with empty d-orbital for ferroelectric polarization. But in case of $BiFeO_3$ the development of large ferroelectric polarization is the arrangement of $Bi^{+3}$ lone pair $6s^2$ electrons, just like $d^0$ configuration. These $6s^2$ lone pair electrons break the local inversion symmetry to form the coordinate bond along [111] direction (Fig. 1.4). In bulk $BiFeO_3$ the FE polarization is directed along [001]$_{hexagonal}$/[111]$_{pseudocubic}$ direction. It was reported earlier that the spontaneous FE polarization is 3.5 $\mu C/cm^2$ and 6.1 $\mu C/cm^2$ along [100] and [111] directions, respectively [88]. However after about 30 years of measurements on high quality single crystal [89], thin-film [38], and ceramics [90], those claims have mostly been dismissed. Ramesh's group reported that a high quality $BiFeO_3$ thin film shows remnant polarization as high as $P_r \sim 55$ $\mu C/cm^2$ along the [001] direction [38]. Later, the obtained outcome was confirmed by using ab initio simulation package [91]. Studies exposed that high density of defect and nonstoichiometry of species are the main reason for low FE polarization in $BiFeO_3$ [92, 93]. These problems can be abridged by quick liquid phase heating [94] and produce stoichiometric and defect-free samples.

### *1.5.2. Orthoferrites*

In addition orthorhombic and hexagonal manganites, orthorhombic $RFeO_3$ (orthoferrites) family is worthy of investigation for significant multiferroicity. Several orthoferrites are truly multiferroics. It is already reported that single-crystal $DyFeO_3$ shows high magnetoelectric coupling property below its (Dy) antiferromagnetic ordering temperature (~ 3.5 K) [95]. Here an applied magnetic field along c-axis induces a ferroelectric ($\geq 0.2\,\mu C/cm^2$) as well as weak ferromagnetic moment ($\geq 0.5\ \mu_B$/formula unit) along c-axis [95]. The ferroelectric polarization is created by the striction through the exchange interaction between the $Dy^{+3}$ and $Fe^{+3}$ spins. Next year the same group observed that in $GdFeO_3$ the spontaneous polarization is $0.12\,\mu C/cm^2$ below its antiferromagnetic ordering temperature (~ 2.5 K) [95]. Another research report is that like magnetic field induce polarization an externally applied electric field can induce magnetic moment in $RFeO_3$ (R=$Dy_{0.75}Tb_{0.25}$ or $Dy_{0.75}Gd_{0.25}$). The electric field control of magnetization is a developing topic for next generation of spintronic devices [16, 17, 18]. It is observed that most of the orthoferrites show magnetoelectric effects at extremely low temperature at which the ordering of rare-earth 4f spins occurs, barring a few exceptions. In $SmFeO_3$ the ferroelectric polarization exists at room temperature along b axis [96]. Here the canted antiferromagnetic magnetic ordering and their nonequivalent spin pairs of Fe ions are responsible for this ferroelectric polarization [96]. Also the ferroelectric Curie temperature is quite high ~ 670 K. Similar $LuFeO_3$ shows high-temperature multiferroicity, where $Lu^{+3}$ is nonmagnetic [97].

## 1.6. Double perovskite Materials ($A_2BB'O_6$)

In the case of single-phase multiferroic perovskite oxides, the general chemical formula is $ABO_3$. Here the transition metal (TM) ions formed an octahedral with six fold co-ordination and the A cation is 12 fold co-ordination. Basically, at RT several materials are showed multiferroic property because of their different requirements. Hence, it is very argent to discover new RT multiferroic materials. From this perspective view of

material design, peoples are choice double perovskite families of multiferroic material with chemical formula $A_2BB'O_6$. Here B and B' are two different cations having formed $BO_6$ and $B'O_6$ octahedra separately. Here many important properties depend on the arrangement of B and B' cations. Depending on the arrangement of B and B', complex double perovskites are formed three different patterns like layered, columnar, and rocksalt as shown in Fig. 1.8. But most of the synthesized double perovskites are randomly disordered or rocksalt type of arrangement of B and B' cations. Very few of double perovskite multiferroics show layered ordering of B and B' cations [98]. Layered ordering is favorable if B and B' cations have different valance electrons (at least two). Again if $BO_6$ and $B'O_6$ octahedra have different geometry like one of them is John-Teller distorted ($BO_6$) and another one is undistorted ($B'O_6$), then layered ordering is more stable compared to rocksalt ordering. Using this concept Anderson et al. successfully synthesized layered $La_2CuSnO_6$ compound [98]. Later many other layered double perovskite $R_2CuSnO_6$ (R = Y, Nd, Pr, Sm, etc.) are successfully synthesized [99]. It is not necessary for all John-Teller distorted B or B' ions to form layered ordering. Many of them (such as $La_2CuTiO_6$) show random arrangement [100]. Recently various double perovskites ($La_2CuIrO_6$, $La_2CuMnO_6$, $Y_2NiMnO_6$, $Tb_2NiMnO_6$, $Sr_2CoWO_6$, $Ca_2CoWO_6$, $Sr_2CoTeO_6$, $Ca_2CoTeO_6$, $Bi_2NiMnO_6$, $Bi_2CoMnO_6$, $Bi_2FeCrO_6$ and $La_2NiMnO_6$) have been investigated [101, 102, 103, 104, 105]. The origin of ferroelectricity and ferromagnetism are different in different double perovskites multiferroic. Out of these, in some double perovskite multiferroics, ferroelectric polarization is induced by exotic magnetic ordering, like as ↑↑↓↓ spin structure induced type–II multiferroics [106]. This type of multiferroic shows ferromagnetism because of super-exchange interaction between $B^{+2}$ and $B'^{+4}$ ions [107, 108, 109]. Single-phase $La_2NiMnO_6$ (LCMO) shows coupling between electronic, magnetic and dielectric properties using magnetocapacitance and magnetoresistance effect [110]. At around 280 K the dielectric and resistive properties are enormously altered by applying the magnetic field. The Curie temperature borders on RT (~ 280 K) [105]. Like LCMO many other multiferroics double perovskites have

high magnetic and electric transition temperature. $Bi_2FeCrO_6/Nd_{0.1}Bi_{0.9}FeO_3$, the bilayered thin film shows a transition temperature around 440 K [111]. Similarly, $Bi_2FeCrO_6$, the thin film deposited on $LaAlO_3$ substrate shows high temperature ferroelectric (900 K) as well as ferromagnetic (between 600 and 800 K) transition temperature. This high temperature ferroelectric and ferromagnetic transition temperature makes the double perovskite materials more interesting in device applications.
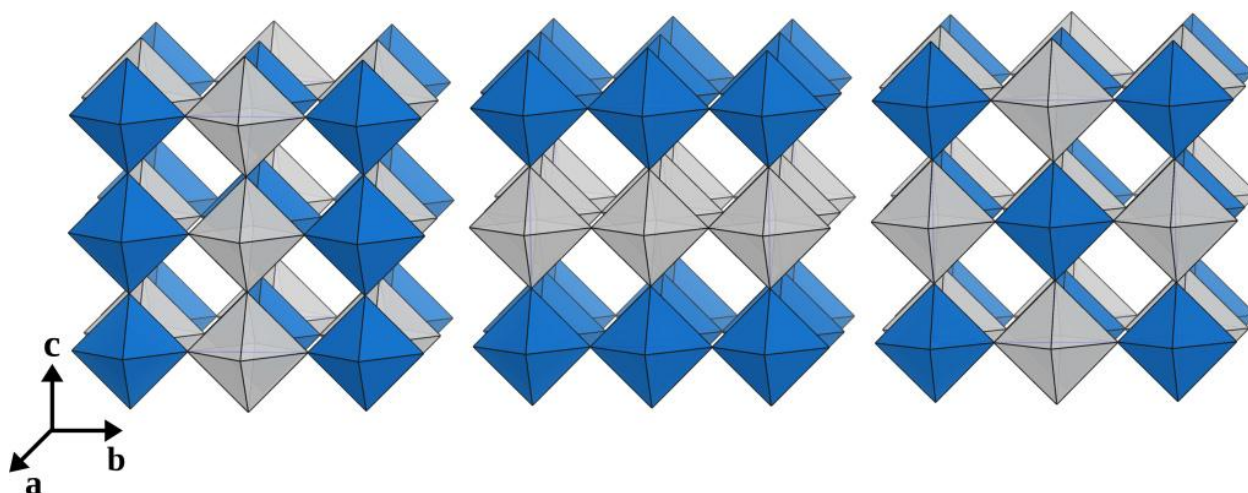


**Fig. 1.8:** Schematic representation of three different ordering of $BO_6$ and $B'O_6$ octahedra, possible in a double perovskite structure. The $BO_6$ and $B'O_6$ octahedra are marked with two different colors. From left to right, the figure shows the columnar, layered, and rocksalt ordering [112].

## 1.7. Multiferroic Composite System

Naturally single-phase material with multiferroic properties (ferroelectric and ferromagnetic) are rarely present and either their magnetoelectric coupling property at room temperature (RT) is weak or it is applicable at very low temperature [23, 106, 113, 114, 115]. So RT multiferroic material is still a debatable object. In contrast, to overcome these problems, multiferroic composite materials are the best way in which ferroelectric and Ferri-/ferromagnetic - both phases are present [116, 117, 118, 119]. Since both the FE and FM properties are present in a single material, so they are suitable for technological application for their large magnetoelectric coupling property. Because of

RT unavailability of multiferroic materials, people have tried to prepare composite multiferroic theoretically and experimentally [120, 121, 122, 123]. In 1972 Suchtelen first proposed two-phase composite type materials and then $BaTiO_3 - CoFe_2O_4$, the composite was successfully synthesized in Philips Laboratory [124, 125, 126]. They used quinary Fe – Co – Ti – Ba – O system for the preparation of composite material using the unidirectional solidification method. The obtained composite material showed much more magnetoelectric (ME) coupling property compared to the single-phase multiferroic material. But the sample preparation in this way is very complicated. After 20 years Newnham group and some Russian scientists had prepared a composite material in a very easy cost-effective way [127, 128, 129]. Newnham [130] introduced the concept of two-phase connectivity in composite material in three different schemes: (i) 0-3 type particulate composites of piezoelectric and magnetic oxide grains; (ii) 2-3 type laminate composites of $BaTiO_3$ based FE ceramics and ferrites, PZT and ferrites, $(SrBa)Nb_2O_5$ and ferrites; [128, 129, 131] (iii) 1-3 type fibre composites with fibre/rod of one phase embedded in the matrix of another phase, as shown in Fig. 1.9. Recently various ME multiferroic composites are investigated. In the early 1990s some particulate composite ceramics like PZT or $BaTiO_3$ are prepared by conventional sintering process, but the ME coupling coefficient is very low [127, 128, 129, 132]. This problem has been solved by careful control of synthesis process [133]. Ryu et al. have already studied the sintered behavior and ME properties in a particular composite of PZT and Ni-based ferrite [134, 135]. Later high ME coefficient was found in many other composite materials [133]. Recently people are focused on multiferroic nano-composites thin film, in which FE (like as $BaTiO_3$, $BiFeO_3$, PZT) and FM oxides (like as $CoFe_2O_4$, $NiFe_2O_4$,) are deposited by a different technique like Pulsed Laser Deposition and Polymer-Assisted [16, 116, 136, 137, 138]. In this way, the nano-structure thin film provides more degrees of freedom and increase lattice strain or interlayer interaction, which also enhances the ME effect. Again a mechanical constraint also grows in between thin film and the

substrate. This mechanical constraint and two phase's nano structured thin films enormously affect the ME coupling interaction [116, 139, 140].
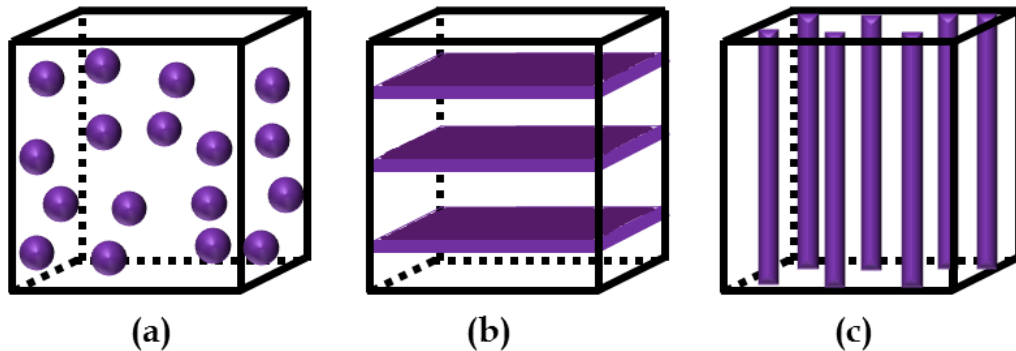


**Fig. 1.9:** Schematic illustration of three bulk composites with the three common connectivity schemes: (a) 0-3 particulate composite, (b) 2-2 laminate composite and (c) 1-3 fibre/rod composite.

## 1.8. Device Application

### *1.8.1. Data storage*

In multiferroic materials, more than one ferroic properties exist in a phase and their coupling properties are widely used in device elements. The binary info is coded in FeRAM (ferroelectric random access memory) and MRAM (magnetic random access memory) by using ferroelectric polarization and ferromagnetic magnetization. The presences of FE and FM property allow four-state logics in a single device [141]. In more complexes, it additionally permits eight logic states [142]. Magnetoelectric coupling property furthermore applies in magnetoelectric random access memory (MERAM). In MERAM an applied voltage can switch the magnetization of the ferromagnetic layer using their interfacial exchange coupling between multiferroic and a ferromagnet as shown in Fig. 1.10. So ultimately the presence of ferroelectric polarization can switch the magnetization by using their ME coupling property [143].
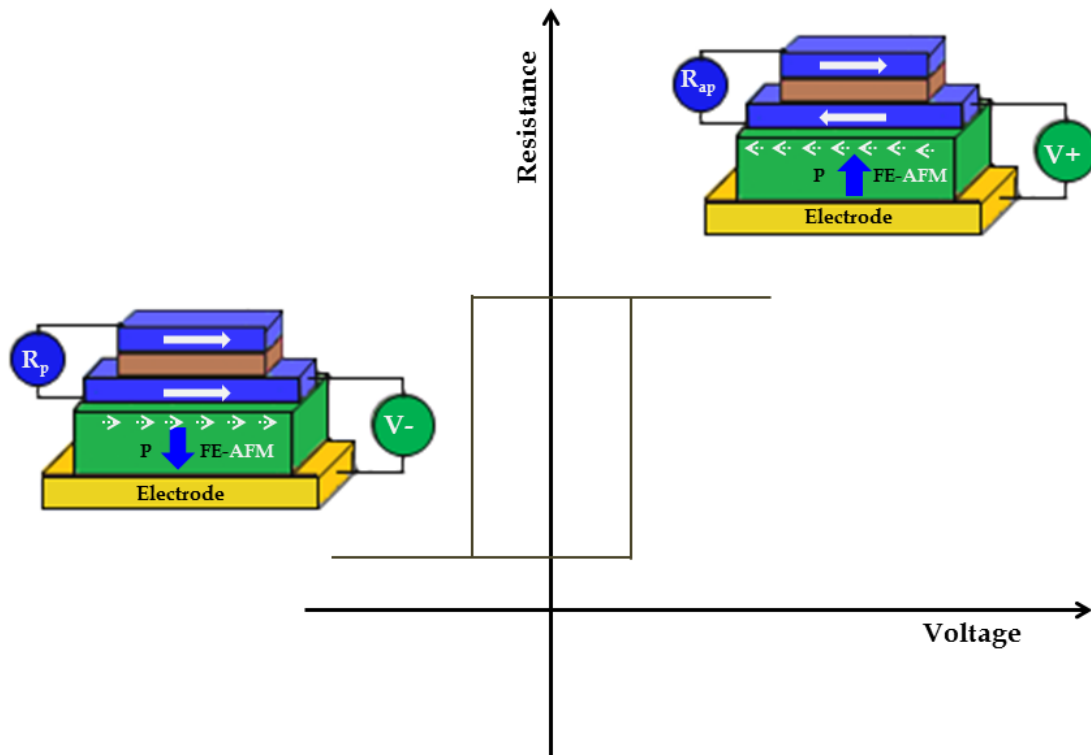
**Fig. 1.10:** MERAMs based on exchange-bias coupling between a multiferroic that is ferroelectric and antiferromagnetic (FE-AFM, green layer), and a thin ferromagnetic electrode (blue layer). A tunneling barrier layer between the two top ferromagnetic layers provides the two resistive states [143].

## *1.8.2. Optoelectronic devices*

Broadly speaking, the multiferroic materials are broadly speaking employed in optical and electronic device application [144]. A suitable band gap (BiFeO$_3$ ~ 2.8 eV) and conductivity of multiferroic material enhances the photo-ferroelectric properties [145, 146, 147]. It is previously reported that BiFeO$_3$ displays a significant photo-response in visible range [146]. In bulk multiferroic BiFeO$_3$ the electric conduction is extremely nonlinear and unidirectional [144].  In presence of an external electrical voltage, the electrical dipole is flipped i.e. a photovoltaic (PV) impact is detected in multiferroic. Multiferroic ferroelectrics are generally high insulating materials [1]. Any leakage current is taken into account as a serious problem; however it usually happens because of crystallographic defects. In presence of high energy illumination, a bulk photo current is induced even in insulator and it is called photovoltaic (PV) effect [148,

149, 150]. This PV effect in multiferroic materials is totally different from p-n junction semiconductors [151, 152]. Here a linear polarizer is placed in between light source and BiFeO$_3$ for light polarization on the PV effect. The in plane component of FE polarization and electric field vector makes an angle θ and varies from zero to 360$^0$. At zero bias the photocurrent as shown in Fig. 1.11 with blue circle follows a sinusoidal form with periodicity 180$^0$. The maximum photocurrent is found when light is in plane with FE polarization and minimum when they are perpendicular to each other. Now the polarizer is rotated by an angle 90$^0$ and adjusted at optimum photocurrent (green circle) and the similar measurement is taken. This demonstrates that the reproducible angular dependence is not due to any artifact of the optical setup. This observation of switchable diode and PV effect should advance studies of BiFeO$_3$ based multifunctional devices [144].
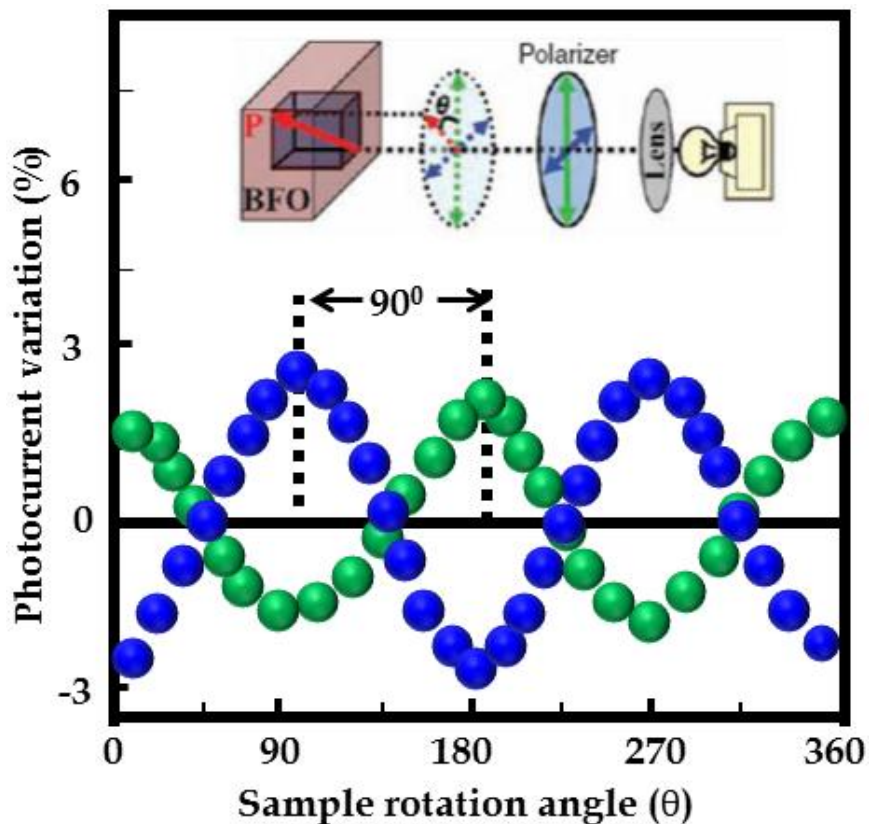


**Fig. 1.11:** Variation of photocurrent with sample rotation under illumination with a linearly polarized light. The experimental sketch is shown in the inset. The PV effect becomes maximum when the polarized-light electric field is parallel to the in-plane component of the ferroelectric polarization and minimum when the field is perpendicular to the in-plane component [144].

## 1.9. Motivation of the Thesis

Usage of magnetoelectric properties of single and double perovskite multiferroic materials above RT for technical purposes is very difficult. Large electric polarization and magnetization are needed for the operation. In magnetoelectric RAM, the ultrafast electrical WRITE operation is combined with the nondestructive magnetic READ operation. This is the best combination of FRAM and MRAM. But for an effective READ/WRITE operation we need larger value of polarization as well as magnetization.

In the case of type-I multiferroic, the origin of ferroelectric polarization as well as magnetization are different and the magnetoelectric coupling is very weak. But the value of electric polarization is large. Single perovskite $BiFeO_3$ shows RT ME coupling property, but it is very weak for practical purposes. Our motivation is to enhance the magnetoelectric coupling property of $BiFeO_3$. $BiFeO_3$ have cycloidal spiral magnetic ordering with wavelength ~ 62 nm. So the magnetic moment in the macroscopic case is weaker. It is, therefore, important to modify the spin cycloidal structure or consider as a composite component with a magnetic material (such as $CoFe_2O_4$). $BiFeO_3/CoFe_2O_4$ composite material not only increases the magnetization but also increases the magnetoelectric coupling properties using their magnetoelastic coupling property. So we have synthesized $BiFeO_3/CoFe_2O_4$ composite nano-hollow spheres and studied their multiferroic properties. Since the coupling is very weak in single perovskite type-I multiferroic materials, we consider an alternate way to choose single and double perovskite type-II multiferroics for better coupling property. Very few of them show RT magnetoelectric coupling. We consider single perovskite $ErFeO_3$ and double perovskite $Y_2NiMnO_6$ type-II multiferroics for better ME coupling. In the case of $ErFeO_3$, the $Fe^{3+}$-O-$Fe^{3+}$ super-exchange interaction contributes an AFM ordering with a weak FM component. An antisymmetric Dzyaloshinskii-Moriya (DM) exchange interaction ($D_i . S_i$ x $S_j$) (where $D_i$ is the exchange interaction intensity, $S_i$ and $S_j$ are two nearest spins) is attributed to the weak FM component between adjacent spins and introduced spin-orbit interaction. As a result an electric polarization P ~ $e_{ij}$ x ($S_i$ x $S_j$) is produced due to local crystal anisotropy. So we have synthesized $ErFeO_3$ nanoparticles

and studied their multiferroic properties. Double perovskite $Y_2NiMnO_6$ shows E-type antiferromagnetic ordering in absence of an applied magnetic field. However, the transition temperature is very low (~ 90 K). So the synthesis of nanostructures can be a solution to this problem since the thin-film or nanowires have a large concentration of surface spin and surface polarization of the electrons. So we have synthesized $Y_2NiMnO_6$ nanostructures (thin film and nanowires) and studied their multiferroic properties.

Therefore, long term research has been focused on the synthesis of single and double perovskite type-II nano-structures for advanced multiferroic properties and technological applications. Multiferroic NPs, NWs, thin film and bilayered nano-hollow spheres (NHSs) gain enormous attention due to their long range applications from data storage [13, 14, 15], energy sector, sensors [11, 12], novel spintronics devices [16, 17, 18], integrated circuits [19, 20], random access memory [21, 22, 23], filters [24, 25], and photovoltaic devices[26, 27, 28, 29].

## 1.10. Thesis Organization

The entire thesis has been divided into six different chapters. A brief outline of the chapters is given below.

**Chapter 1** gives a brief introduction about the single and double perovskite multiferroic structures with their crystal structure, magnetic, electrical, magnetoelectric properties**.** Here we have also discussed about the origin of ferroelectric, magnetic and magnetoelectric properties of different multiferroic materials. Moreover, the motivation of thesis work and the outline of work done are also included.

**Chapter 2** focuses on synthesis procedures, various techniques for characterization and measurements.

**Chapter 3** describes the synthesis of different sizes of $CoFe_2O_4$ nano-hollow spheres by solvothermal method and deposited a ferroelectric layer of $BiFeO_3$ with different amount on the outer surface of $CoFe_2O_4$ nano-hollow spheres by wet chemical method.

It discusses the detailed description of electric, magnetic and magnetoelectric properties.

**Chapter 4** presents the synthesis of $ErFeO_3$ nanoparticles by cost-effective and much lesser time-consuming microwave method. Detailed description of electric, magnetic and magnetoelectric properties also discussed. To study the effect of ligand on the properties of $ErFeO_3$, we solubilized the as-prepared $ErFeO_3$ NPs into water by functionalization with disodium tartrate ligand. Multicolor photoluminescence and photocatalytic properties are also studied in details.

**Chapter 5** describes the synthesis of $Y_2NiMnO_6$ nanowires by template free solvothermal method and studies their electric, magnetic, magnetoelectric and supercapacitive properties. Detailed study reveals that at room temperature $Y_2NiMnO_6$ nanowires show weak ferromagnetism as well as ferroelectricity. We demonstrate that the surface spin and the surface charge polarization are responsible for the unusually high temperature multiferroic property of the NWs.

**Chapter 6** presents the multiferroic properties of $Y_2NiMnO_6$ thin films deposited on gold sputtered Si(100) substrate by pulse laser deposition (PLD) technique. Detailed studies show that both room temperature ferromagnetism and the spontaneous room temperature ferroelectricity are mutually coupled with each other and they have a similar origin.

**Chapter 7** draws the conclusions and gives an idea about the scope for future work.

## 1.11. Bibliography

[1]     M. Dawber, K. M. Rabe, and J. F. Scott, *Rev. Mod. Phys*. **77**, 1083 (2005).

[2]     S. H. Wemple, *Phys. Rev. B* **2**, 2679 (1970).

[3]     G. Gerra, A. K. Tagantsev, N, Setter, and K. parlinski, *Phys. Rev. lett.* **96**, 107603 (2006).

[4]     P. G. Radaelli, G. Iannone, M. Marezio, H. Y. Hwang, S-W. Cheong , J. D. Jorgensen and D. N. Argyriou, *Phys. Rev. B* **56**, 82658276 (1997).

[5]     Y. Tomioka, A. Asamitsu, Y. Moritomo, H. Kuwahara and Y. Tokura, *Phys. Rev. Lett.* **74**, 5108 (1995).

[6]     B. Keimer, N. Belk, R. J. Birgeneau, A. Cassanho, C. Y. Chen, M. Greven, M. A. Kastner, A. Aharony, Y. Endoh, R. W. Erwin and G. Shirane, *Phys. Rev. B* **46**, 1403414053 (1992).

[7]     N. Balke, S. Choudhury, S. Jesse, M. Huijben, Y. H. Chu, A. P. Baddorf, L. Q. Chen, R. Ramesh & S. V. Kalinin, *Nature Nanotechnology* **4**, 868 (2009)

[8]     S. H. Baek, H. W. Jang, C. M. Folkman, Y. L. Li, B. Winchester, J. X. Zhang, Q. He, Y. H. Chu, C. T. Nelson, M. S. Rzchowski, X. Q. Pan, R. Ramesh, L. Q. Chen & C. B. Eom, *Nature Materials,* **9**, 309 (2010).

[9]     W. Li, Z. Zhang, E. G. Bithell, A. S. Batsanov, P. T. Barton, P. J. Saines, P. Jain, C. J. Howard, M. A. Carpenter, A. K. Cheetham, *Acta Materialia*, **61**, 4928 (2013).

[10]    P. Tolédano, M. Ackermann, L. Bohatý, P. Becker, T. Lorenz, N. Leo, and M. Fiebig, *Phys. Rev. B* **92**, 094431( 2015).

[11]    P. Filippov, P. Yu, G. G. Ihas and V. V. Vainberg, *Rev. Sci. Instrum.* 80, 094902 (2009).

[12]    M. Vazquez and A. Hernando, *J. Phys. D: Applied Physics* **29**, 939 (1996).

[13]    J. F. Scott, *Nat. Mater.* **6**, 256 (2007).

[14]    G. Reiss and A. Hutten, *Nat. Mater.* **4**, 725 (2005).

[15]    J. P. Wang, *Nat. Mater.* **4**, 191 (2005).

[16]    R. Ramesh and N. A. Spaldin, *Nat. Mater.* **6**, 21 (2007).

[17]    S. W. Cheong and M. Mostovoy, *Nat. Mater.* **6**, 13 (2007).

[18]     H Bea, M Gajek, M Bibes and A Barthelemy, *J. Phys.: Condens. Matter* **20**, 434221 (2008).

[19]     X. Li, K. terabe, H. Hatano, H. Zeng and K. Kitamura, *J. Appl. Phys.* **100**, 106103 (2006).

[20]     Y. H. Xie, Y.Y. Lin and T. A. Tang, *Integrated Ferroelectrics* **67**, 255 (2004).

[21]     M. Fiebig, T. Lottermoser, D. Frohlich, A.V. Goltsev, R.V. Pisarev, *Nature* **419**, 818 (2002).

[22]     C. A. F. Vaz, J. Hoffman, C.H. Ahn, R. Ramesh, *Adv. Mater.* **22,** 2900 (2010).

[23]     N. Hur, S. Park, P.A. Sharma, J.S. Ahn, S. Guha, S.W. Cheong, *Nature* **429**, 392 (2004).

[24]     S. Ju, T-Y. Cai, G-Y. Guo, and Z-Y. Li, *Phys. Rev. B* 75, 064419 (2007).

[25]     X. Yang , Y. Gao , J. Wu , S. Beguhn , T. Nan , Z. Zhou , M. Liu , and N. X. Sun, *IEEE Tranactions Magnetics* **49**, 5485, (2013).

[26]     M. Alexe, D. Hesse, *Nature Communication* **2**, 256 (2011),

[27]     R. Nechache, C. Harnagea, S. Li, L. Cardenas, W. Huang, J. Chakrabartty and F. Rosei, *Nature Photonics* **9**, 61 (2015).

[28]     W. Ji, K. Yao and Y. C. Liang, *Advanced Materials* **22**, 1763 (2010).

[29]     G. G. Khan, R. Das, N. Mukherjee, and K. Mandal, *Phys. Status Solidi RRL* **6**, 7 (2012).

[30]     W. Eerenstein, N. D. Mathur and J. F. Scott, *Nature* **442,** 759 (2006).

[31]     R. Das, G. G. Khan and K. Mandal, *Journal of Applied Physics* **111**, 104115 (2012).

[32]     L. D. Landau and E. M. Lifshitz, *Electrodynamics of continuous media (Fizmatgiz, Moscow*, (1959).

[33]     D. N. Astrov, *Sov. Phys. JETP* **11,** 708 (1960).

[34]     I. E. Dzyaloshinskii, *Sov. Phys. JETP* **10**, 628 (1959).

[35]     H. Schmid, *Ferroelectrics* **162**, 317 (1994).

[36]     N. A. Hill, *J. Phys. Chem. B* **104**, 6694 (2000).

[37]     G. T. Rado, *Phys. Rev. Lett.* **13**, 335 (1964).

[38]   J. Wang, J. B. Neaton, H. Zheng, V. Nagarajan, S. B. Ogale, B. Liu, D. Viehland, V. Vaithyanathan, D. G. Schlom, U. V. Waghmare, N. A. Spaldin, K. M. Rabe, M. Wuttig, and R. Ramesh, *Science* **299**, 1719 (2003).

[39]   T. Kimura, T. Goto, H. Shintani, K. Ishizaka, T. Arima, and Y. Tokura, *Nature (London)* **426**, 55 (2003).

[40]   T. Lottermoser, T. Lonkai, U. Amann, D. Hohlwein, J. Ihringer, and M. Fiebig, *Nature (London)* **430**, 541 (2004).

[41]   H. Schmid, *Proceedings of MEIPIC* **2**, (1993).

[42]   M. J. Fiebig, *J. Phys. D: Appl. Phys.* **38**, 123, (2005).

[43]   W. F. Brown, R. M. Hornreigh, and S. Shtrikman, *Phys. Rev.* **168**, 574, (1968).

[44]   H. Palneedi, V. Annapureddy, S. Priya and J. Ryu, *Actuators* **5**, 9 (2016).

[45]   J. B. Goodenough and J. M. Longo, *New Series Vol. III. 4 Springer, Berlin*, (1970).

[46]   T. Mitsui, *New Series Vol. 16 (1) Springer, Berlin,* (1981).

[47]   N. A. Hill, A. Filippetti, *J. Magn. Magn. Mater.* **976**, 242 (2002).

[48]   N. A. Hill, P. Battig and C. Daul, *J. Phys. Chem B* **106**, 3383, (2002).

[49]   N. A. Hill, K. M. Rabe, *Phys. Rev. B* **59**, 8759, (1999).

[50]   D. Khomskii, *Physics* **2**, 20 (2009).

[51]   D. V. Efremov, J. van den Brink, and D. I. Khomskii, *Nature Mater.* **3**, 853 (2004).

[52]   Y. J. Choi, H. T. Yi, S. Lee, Q. Huang, V. Kiryukhin, and S.-W. Cheong, *Phys. Rev. Lett.* **100**, 047601 (2008).

[53]   B. B.van Aken, T. T. M. Palstra, A. Filippetti, and N. A. Spaldin, *Nature Mater.* **3**, 164 (2004).

[54]   J. Strempfer, B. Bohnenbuck, M. Mostovoy, N. Aliouane, D. N. Argyriou, F. Schrettle, J. Hemberger, A. Krimmel, and M. v. Zimmermann, *Phys. Rev. B* **75**, 212402 (2007).

[55]   G. Lawes, A. B. Harris, T. Kimura, N. Rogado, R. J. Cava, A. Aharony, O. Entin-Wohlman, T. Yildirim, M. Kenzelmann, C. Broholm, and A. P. Ramirez, *Phys. Rev. Lett.* **95**, 087205 (2005).

[56]   T. Kimura, G. Lawes, and A. P. Ramirez, *Phys. Rev. Lett.* **94**, 137201 (2005).

[57]    P. Toledano, *Phys. Rev. B* **79**, 094416 (2009)].

[58]    T. Kimura, G. Lawes, T. Goto, Y. Tokura, and A. B. Ramirez, *Phys. Rev. B* **71**, 224425 (2005).

[59]    H. Katsura, N. Nagaosa, AV. Balatsky, Phys. Rev. Lett. 95, 057205 (2005),, M. Mostovoy, *Phys. Rev. Lett.* **96**, 067601 (2006).

[60]    M. E. Fisher and W. Selke, *Phys. Rev. Lett.* **44**, 1502 (1980).

[61]    U. Krishnan, M. Kaur, M. Kumar, and A. Kumar, *Journal of Photonics for Energy* **9**, 021001 (2019).

[62]    J. M. Moreau, C. Michel, R. Gerson, W. J. James, *J. Phys. Chem. Solids* **32**, 1315 (1971).

[63]    V. S Filip'ev, I. P Smol'yaninov, E. G Fesenko, I. I Belyaev, *Crystallogr.* **5**, 913 (1960). [64] F. Kubel, H. Schmid, *Acta Cryst. B* **46**, 698 (1990).

[65]    A. M. Glazer, *Acta Cryst. B* **28**, 3384 (1972).

[66]    J. D. Bucci, B. K. Robertson, W. J. James, *J. Appl. Cryst.* **5**, 187 (1972).

[67]    A. Palewicz, R. Przenioslo, I. Sosnowska, A. W. Hewat, *Acta Cryst. B* **63**, 537 (2007).

[68]    G. Catalan, and J. F. Scott, *Advanced Materials* **21**, 2463 (2009).

[69]    F. Zavaliche, R. R. Das, D. M. Kim, C. B. Eom, S. Y. Yang, P. Shafer, and R. Ramesh, *Appl. Phys. Lett.* **87**, 182912 (2005).

[70]    Y.-H. Chu, L. W. Martin, M. B. Holcomb, and R. Ramesh, *Materials today* **10,** 16 (2007).

[71]    D. Lebeugle, D. Colson, A. Forget, M. Viret. A. M. Bataille, and A. Gukasov, *Appl. Phys. Lett.* **100**, 227602 (2008).

[72]    C. Ederer, and N. A. Spaldin, *Phys. Rev. B* **71**, 060401 (2005).

[73]    B. Feiming, W. Junling, M. Wuttig, L. Jiefang, W. Naigang, A. P. Pyatakov, A. K. Zvezdin, L. E. Cross, D. Viehland, *Appl. Phys. Lett*, **86**, 032511 (2005).

[74]    I. Sosnowska, T. P. Neumaier, and E. Steichele, *J. Phys. C* **15**, 4835 (1982).

[75]    J. F. Scott, M. K. Singh, R. S. Katiyar, *J. Phys.: Condens. Matter* **20**, 322203 (2008).

[76]  A. Palewicz, T. Szumiata, R. Przenioslo, I. Sosnowska, I. Margiolaki, *Solid State Commun.* **140**, 359 (2006).

[77]  R. Przenioslo, A. Palewicz, M. Regulski, I. Sosnowska, R. M. Ibberson, K. S. Knight, *J. Phys.: Condens. Matter* **18**, 2069 (2006).

[78]  A. V. Zalesskii, A. K. Zvezdin, A. A. Frolov, A. A. Bush, *JETP Lett.* **71**, 465 (2000).

[79]  A. A. Bush, A. A. Gippius, A. V. Zalesskii, E. N. Morozova, *JETP Lett.* **78**, 389 (2003).

[80]  M. Cazayous, Y. Gallais, A. Sacuto, R. de Sousa, D. Lebeugle, D. Colson, *Phys. Rev. Lett.* **101**, 037601 (2008).

[81]  M. K. Singh, W. Prelier, M. P. Singh, R. S. Katiyar, J. F. Scott, *Phys. Rev. B* **77**,144403 (2008).

[82]  J. F. Scott, *J. Magn. Magn. Mater.* **321**, 1689, (2009).

[83]  W. Jie, R. Haumont, R. Jarrier, P. Berhtet, and B. Dkhil, *Appl. Phys. Lett.* **96,** 102509, (2010).

[84]  X. Qingyu, Z. Haifa, W. Wu, T. Qiu, and M. X. Xu, *Appl. Phys. Lett.* **95,** 112510, (2009).

[85]  W. Yao, Q. Jiang, H. He, and C. W. Nan, *Appl. Phys. Lett.* **88**, 142503 (2006).

[86]  M. Kumar, and K. L. Yadav, *Appl. Phys. Lett.* **91**, 112911, (2007).

[87]  S. R. Shannigrahi, A. Huang, N. Chandrasekhar, D. Tripathy, and A. O. Adeyeye, *Appl. Phys. Lett.* **90**, 022901 (2007).

[88]  J. R. Teague, R. Gerson, W. J. James, *Solid State Commun.* **8**, 1073 (1970).

[89]  D. Lebeugle D. Colson, A. Forget, M. Viret, P. Bonville, J. F. Marucco, S. Fusil, *Appl. Phys. Lett.* **91**, 022907 (2007).

[90]  V. V. Shvartsman, W. Kleemann, R. Haumont, J. Kreisel, *Appl. Phys. Lett.* **90**, 172115 (2007).

[91]  C. Ederer, N. A. Spaldin, *Phys. Rev. Lett.* **95**, 257601 (2005).

[92]  X. Qi, J. Dho, R. Tomov, M. G. Blamire, and J. L. MacManus-Driscoll, *Appl. Phys. Lett.* **86**, 062903 (2005).

[93]  S. K. Singh, H. Ishiwara and K. Maruyama, *J. Appl. Phys.* **100**, 064102 (2006).

[94]   Y. Wang, L. Zhou, M.F. Zhang, X.Y. Chen, J.M. Liu, and Z.G. Liu, *Appl. Phys. Lett.* **84,** 1731 (2004).

[95]   Y. Tokunaga, S. Iguchi, T. Arima, and Y. Tokura, *Phys. Rev. Lett.* **101**, 097205 (2008).

[96]   J. H. Lee, Y.K. Jeong, J.H. Park, M.A. Oak, H.M. Jang, J.Y. Son, and J.F. Scott, *Phys. Rev. Lett.* **107**, 117201(2011).

[97]   U. Chowdhury, S. Goswami, D. Bhattacharya, J. Ghosh, S. Basu, and S. Neogi, *Appl. Phys. Lett.* **105**, 052911 (2014).

[98]   M. T. Anderson, K. B. Greenwood, G. A. Taylor, and K. R. Poeppelmeier, *Prog. Solid State Chem.* **22**, 197 (1993).

[99]   M. Azuma, S. Kaimori, and M. Takano, *Chem. Mater.* **10**, 3124 (1998).

[100]  N. Ramadass, J. Gopalakrishnan, and M. V. C. J. Sastri, *Inorg. Nucl. Chem.* **40**, 1453 (1978).

[101]  G. J. Blasse, *Inorg. Nucl. Chem.* **27**, 993 (1965).

[102]  J. Su, Z. Z. Yang, X. M. Lu, J. T. Zhang, L. Gu, C. J. Lu, Q. C. Li, J. –M. Liu, and J. S. Zhu, *ACS Appl. Mater. Interfaces,* **7**, 13260 (2015).

[103]  H. S. Nair, D. Swain, N. Hariharan, S. Adiga, C. Narayana, and S. Elzabeth, *J. Appl. Phys.* **110**, 123919 (2011).

[104]  A. P. Ayala, I. Guedes, and E. N. Silva, M. S. Augsburger, M. del C. Viola, and J. C. Pedregosa, *J. Appl. Phys.* **101**, 123511 (2007).

[105]  H. J. Zhao and X. M. Chen, *AIP Advances* **2**, 042143 (2012).

[106]  M. Alam, K. Mandal, and G. G. Khan, *RSC Advances* **6**, 62545 (2016).

[107]  N. S. Rogado, J. Li, A. W. Sleight, and M. A. Subramanian, *Adv. Mater.* **17**, 2225 (2005).

[108]  J. B. Goodenough, *Phys. Rev.* **100**, 564 (1955).

[109]  R. I. Dass, J. Q. Yan, and J. B. Goodenough, *Phys. Rev. B* **68**, 064415 (2003).

[110]  S. Zhao, L. Shi, S. Zhou, J. Zhao, H. Yang, and Y. Guo, *J. Appl. Phys.* **106**, 123901, (2009).

[111] S. Kamba, D. Nuzhnyy, R. Nechache, K. Zaveta, D. Niznansky, E. antava, C. Harnagea, and A. Pignolet, *Phys. Rev. B* **77**, 104111 (2008).

[112] K. Samanta, and T. S. Dasgupta, *Phys. Rev. B* **95,** 235102 (2017).

[113] R. Tackett, G. Lawes, B. C. Melot, M. Grossman, E. S. Toberer, and R. Seshadri, *Phys. Rev. B* **76**, 024409 (2007).

[114] Y. Yamasaki, S. Miyasaka, Y. Kaneko, J.-P. He, T. Arima, and Y. Tokura, *Phys. Rev. Lett.* **96**, 207204 (2006).

[115] R. Das, T. Sarkar and K. Mandal, *J. Phys. D: Appl. Phys.* **45,** 455002 (2012).

[116] X.-M. Liu, S.-Y. Fu, C.-J. Huang, *Materials Science and Engineering B* **121,** 255 (2005).

[117] X.-H. Liu, Z. Xu, S.-B. Qu, X.-Y. Wei, J.-L. Chen, *Ceramics International* **34,** 797 (2008).

[118] Y. H. Tang, X. M. Chen, Y.J. Li, X.H. Zheng, *Materials Science and Engineering B* **116,** 150 (2005).

[119] A. Chaudhuri, K. Mandal, *J. Magn. Magn. Mater*. **377,** 441 (2015).

[120] G. Srinivasan, E.T. Rasmussen, J. Gallegos, R. Srinivasan, Y.I. Bokhan, V.M. Laletin, *Phys. Rev. B* **64,** 214408 (2001).

[121] N. Cai, J. Zhai, C.W. Nan, Y.H. Lin, Z. Shi, *Phys. Rev. B* **68,** 224103 (2003).

[122] N. Cai, C.W. Nan, J.Y. Zhai, Y.H. Lin, *Appl. Phys. Lett.* **84** 3516 (2004).

[123] J. G. Wan, X.W. Wang, Y.J. Wu, M. zeng, Y. Wang, H. Jiang, W.Q. Zhou, G.H. Wang, J.M. Liu, *Appl. Phys. Lett.* **86,** 122501 (2005).

[124] J. van Suchtelen, *Philips Res. Rep.* **27**, 28 (1972).

[125] J. Boomgard, D. R. Terrell, R. A. J. Born, and H. F. J. I. Giller, *J. Mater. Sci.* **9**, 1705 (1974).

[126] J. Boomgard, A. M. J. G. Run, and J. Suchtelen, *Ferroelectrics* **10**, 295 (1976).

[127] G. Harshe, J. P. Dougherty, and R. E. Newnham, *Int. J. Appl. Electromagn. Mater*. **4**, 145 (1993).

[128] S. Lopatin, I. Lopatin, and I. Lisnevskaya, Ferroelectrics 162, 63 (1994).

[129] M. I. Bichurin, I. A. Kornev, V. M. Petrov, and I. Lisnevskaya, *Ferroelectrics* **204**, 289 (1997).

[130] R. E. Newnham, D. P. Skinner, and L. E. Cross, *Mater. Res. Bull.* **13**, 525 (1978).

[131] X. M. Chen, Y. H. Tang, and I. W. Chen, *J. Appl. Phys.* **96**, 6520 (2004).

[132] T. G. Lupeiko, I.V. Lisnevskaya, M.D. Chkheidze, B.I. Zvyagintsev, *Inorg. Mater.* **31** 1245 (1995).

[133] J. Ryu, A.V. Carazo, K. Uchino, H.E. Kim, *J. Electroceram.* **7**, 17 (2001).

[134] J. Ryu, S. Priya, A.V. Carazo, K. Uchino, H.E. Kim, *J. Am. Chem. Soc.* **84,** 2905 (2001).

[135] J. Ryu, A.V. Carazo, K. Uchino, H.E. Kim, Jpn. *J. Appl. Phys.* **40,** 4948 (2001).

[136] N. Dix, V. Skumryev, V. Laukhin, L. F`abrega, F. S´anchez, J. Fontcuberta a *Materials Science and Engineering B* **144** 127 (2007).

[137] H. Luo, H. Yang, S. A. Baily, O. Ugurlu, M. Jain, M. E. Hawley, T. M. McCleskey, A. K. Burrell, E. Bauer, L. Civale, T. G. Holesinger, and Q. Jia, *J. AM. CHEM. SOC.* 129, 14132 (2007).

[138] H. Zheng, J. Wang, S. E. Lo?and, Z. Ma, L. Mohaddes-Ardabili, T. Zhao, L. Salamanca-Riba, S. R. Shinde, S. B. Ogale, F. Bai, D. Viehland, Y. Jia, D. G. Schlom, M. Wuttig, A. Roytburd, and R. Ramesh, *Science* **303**, 661 (2004).

[139] D. H. Kim, N. M. Aimon, X. Y. Sun, L. Kornblum, F. J. Walker, C. H. Ahn, and C. A. Ross, *Adv. Funct. Mater.* **24**, 5889 (2014).

[140] M. Vopsaroiu, M Stewart, T Hegarty, A Muniz-Piniella, N McCartney, M Cain and G Srinivasan, G. V. Duong, R. S. Turtelli, R. Groessinger, *J. Magn. Magn. Mater.* **322,** 1581 (2010).

[141] M. Gajek, M. Bibes, S. Fusil, K. Bouzehouane, J. Fontcuberta, A. Barthelemy, and A. Fert, *Nature Mater.* **6**, 296 (2007).

[142] F. Yang, M. H. Tang, Z. Ye, Y. C. Zhou, X. J. Zheng, J. X. Tang, J. J. Zhang, and J. He, *J. Appl. Phys.* **102**, 044504, (2007).

[143] M. Bibes, and A, Barthélémy, *Nature Materials* **7**, 425 (2008).

[144] T. Choi, S. Lee, Y. J. Choi, V. Kiryukhin, S.-W. Cheong, *Science* **324,** 63, (2009).

[145] S. J. Clark, J. Robertson, *Appl. Phys. Lett.* **90**, 16868 (2007).

[146]  S. R. Basu, L. W. Martin, Y. H. Chu, M. Gajek, R. Ramesh, R. C. Rai, X. Xu, J. L. Musfeldt, *Appl. Phys. Lett.* **92**, 091905, (2008).

[147]  R. Das, G. G. Khan, S. Varma, G. D. Mukherjee, and K. Mandal, *J. Phys. Chem. C* 117, 20209 (2013).

[148]  V. M. Fridkin, B. N. Popov, *Sov. Phys. Usp.* **21**, 981 (1978).

[149]  A. M. Glass, D. Von der Linde, T. J. Negran, *Appl. Phys. Lett.* **25**, 233 (1974).

[150]  G. Dalba, Y. Soldo, F. Rocca, V. M. Fridkin, Ph. Sainctavit, *Phys. Rev. Lett.* **74**, 988 (1995).

[151]  P. Poosanaas, A. Dogan, S. Thakoor, K. Uchino, *J. Appl. Phys.* **84**, 1508 (1998).

[152]  L. Pintilie, I. Vrejoiu, G. L. Rhun, M. Alexe, *J. Appl. Phys.* **101**, 064109 (2007).

# Chapter 2 | Experimental Details

The chapter describes different synthesis techniques of single and double perovskite multiferroic nanostructures. Various techniques to characterize their physical, electronic, optical, electrical and magnetic properties are also presented herein.

## 2.1. Experimental Details

In this chapter we will briefly describe various experimental techniques to synthesize unique nanostructures of various materials. Also we will discuss characterization processes employed to investigate different properties of these nanostructured materials.

## 2.2. Fabrication Techniques of Different Nanostructures

### 2.2.1. Wet Chemical Method

Generally, wet chemical method is used for the production of nano- or ultra- dispersed inorganic materials in an aqueous or non- aqueous solutions. The synthesis process has been done in liquid phase and most importantly it can produce much smaller, monodispersed grains usually at lower temperature and have shorter duration of phase formation compared to conventional solid state procedure. It is mainly a "bottom-up" method to synthesize nanostructures. Here nanostructures are synthesized by chemical reduction of metal salts, electrochemical trails or through controlled decomposition of different metastable organometallic compounds. Here we have synthesized $BiFeO_3$ nano layer on the surface of $CoFe_2O_4$ nano hollow spheres by facile wet chemical method.

### 2.2.2. Solvothermal Method

Hydrothermal synthesis is a well-known and effective technique for crystallizing materials directly from aqueous solution by controlling the thermodynamic (temperature, pressure, capping agent, chemical composition and reaction time) and non-thermodynamic (stirring, sonication etc.) variables. In this process different polar solvent like water, ethanol and non-polar solvent like benzene, ethylene glycol, ethylene di-amine are used under high pressure and temperature (basically above boiling point of the solvent). It helps to develop an autogeneous pressure [1, 2]. If the water solvents are used as a reaction medium then the process is called hydrothermal method; whereas, in case of non-aqueous solvents it is called solvothermal method. In this

process the reactants are placed into a closed atmosphere i.e. in an autoclave under high pressure and temperature condition. The autoclave is placed in an oven at a constant temperature. With increase in temperature the vapour pressure increases and at constant temperature the vapour pressure is much more the normal vapour pressure of the solvent. Here the vapour pressure inside the reaction container (here autoclave) not only increases with temperature but also depends on some experimental factor such as the percentage fill of the vessel, any salt dissolved into the reaction medium and capping agent. With increase in vapour pressure the boiling point of the solvent increases. So the reaction takes place in a higher temperature. Hence the reaction goes in a faster rate. At this stage hydroxides converts into respective oxides and subsequent fusion of these oxides form the required compound. In our cases the desired compound are $CoFe_2O_4$ nano hollow spheres, $Y_2NiMnO_6$ nanowires. We do not have any further annealed the compounds for crystallization. Here the vapour pressure is the main reaction parameter which controls the nanostructures size and phase formation. If we use different reaction solvent rather than water, then the vapour pressure will be different. This will turn affect the formation of nanostructures size, shape with same compound.

The viscosity of the solvent also plays a crucial role on the morphology of the nanostructures. Diffusion also controls the formation of final product. The diffusion coefficient is related with hydrodynamic diameter (d) of the nanostructures by according to Einstein- Stokes theorem, $D = K_BT/3\pi\eta d$. Where $K_B$ is the Boltzmann constant, T is the temperature and $\eta$ is the viscosity of the medium. For a low viscous solvent the rate of diffusion is high and it prevent nucleation occurring to form larger aggregates. At higher temperatures water plays an essential role in the precursor material transformation because the vapor pressure is much higher. For example, the viscosity of water decreases with increasing temperature, such as at 500 °C and 10 bar, the viscosity of water is only 10% of its magnitude under ambient conditions [3]  At higher temperature the physical properties (like solubility and reactivity) of the reactants changes which leads to form high quality nanostructure. In hydrothermal

process the particles are formed by dissolution and crystallization mechanism. The schematic diagram of an autoclave is shown in Fig. 2.1.
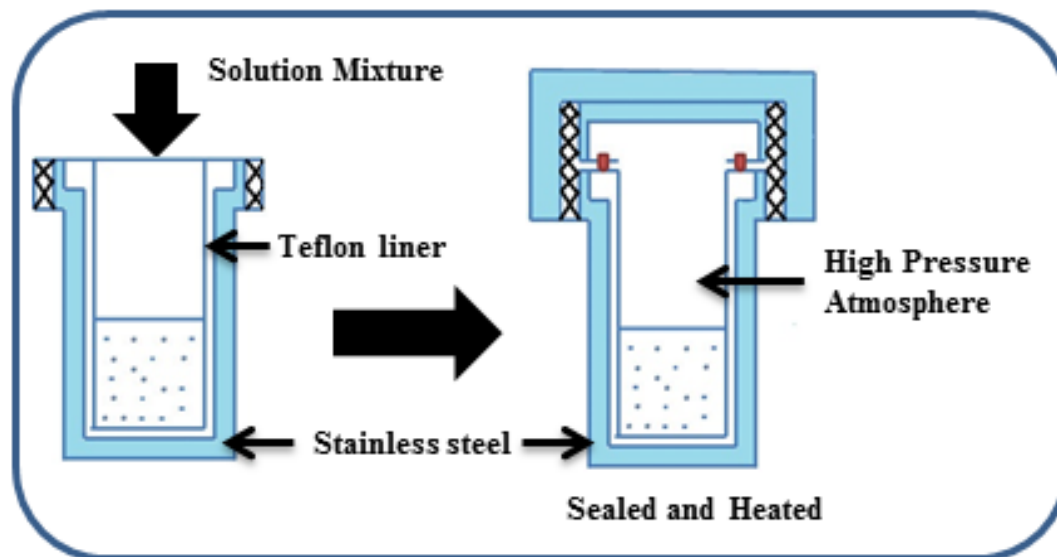


**Fig. 2.1:** Schematic diagram of an autoclave and a Teflon chamber used in solvothermal synthesis.

It is a Teflon chamber which enclosed by stainless steel autoclave. The solution mixture is transformed into a Teflon liner up to its 70% of total volume. Then the autoclave is tightly sealed and put into an oven at constant temperature. The autoclave creates two temperature zones and a convection motion of the water will start immediately. During heating the water below gets heated and ascent and the cold water from the top descend. This motion will not stop until the temperature of the entire solution remains same everywhere. With decrease in temperature the solution becomes supersaturated in the upper part and crystallization sets in. Nanostructures prepared according to this process usually have high crystallinity, different shapes and moderate size distribution [4, 5].

## 2.2.3. *Microwave-assisted synthesis*

Microwave-assisted synthesis process is faster synthesis process compared to any other conventional synthesis method. In conventional heating process at least one or more heating steps for long time period is required. But the microwave heating is a faster

chemical reaction, rapid material production and short time (usually in minute) taking process. It is a low cost, energy saving and high efficient material production process. In case of conventional heating usually used electric furnace or oil bath, this heats first the wall of the reactor and then the reactants by conduction or convection process. So it takes more time to transfer the heat energy from source to solvent. But in case of microwave heating the heat energy directly heated the target materials without any time delay.

Microwave irradiation is electromagnetic irradiation (in the frequency range 0.3 to 300 GHz) and the energy is not sufficient to break any chemical bond. For example the energy of a commercially used microwave with frequency 2.45 GHz is only $1.0 \times 10^{-5}$ eV. This energy is very low to break any chemical bond, even lower than the Brownian motion. This energy is only capable to create the molecular rotation.
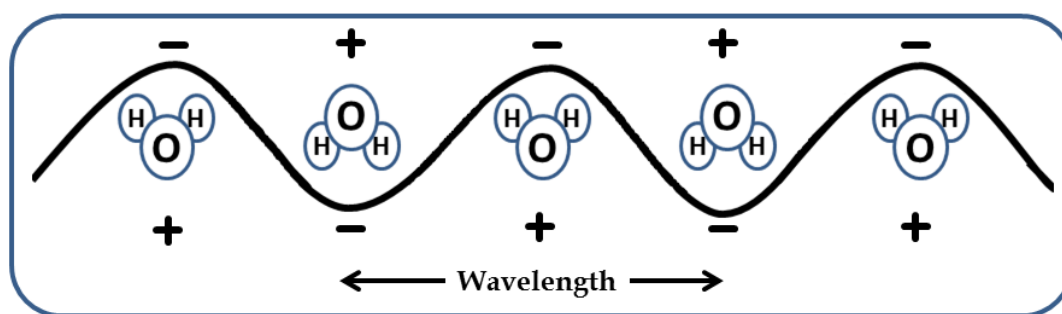


**Fig. 2.2:** Water molecules in an alternating electric field under microwave irradiation.

Dipolar polarization and ionic conduction are the two main microwave heating mechanism for materials synthesis process. Microwave generally heat any dipolar or ionic materials. During heating dipolar molecules (negative and positively charged parts) oscillates according to the microwave oscillating field. This oscillation creates rotation and ultimately heat energy is generated. The schematic diagram of water molecules in an alternating electric field under microwave irradiation is shown in Fig. 2.2. In case of ions, any ion present in the solution will move according to the orientation of the electric field. Because of the ever changing electric field, the ions changed their direction in the solution and give rise the solution temperature due to

friction and collision. In our case the reaction take place much faster and convert the hydroxides to the respective oxides and subsequent fusion of the oxides to form the desired compound ($ErFeO_3$).

## *2.2.4. Pulsed Laser Deposition (PLD) Technique: Thin Films*

PLD is a very well-known technique to synthesis high quality thin film samples with the designs required for the application purposes [4]. Here a high power laser beam is focused in a vacuum chamber to strike a target material which is to be deposited as a thin film. The material is vaporized in a form of plasma plume and deposits on a substrate. This process is done in presence of a background gas or ultra-high vacuum.
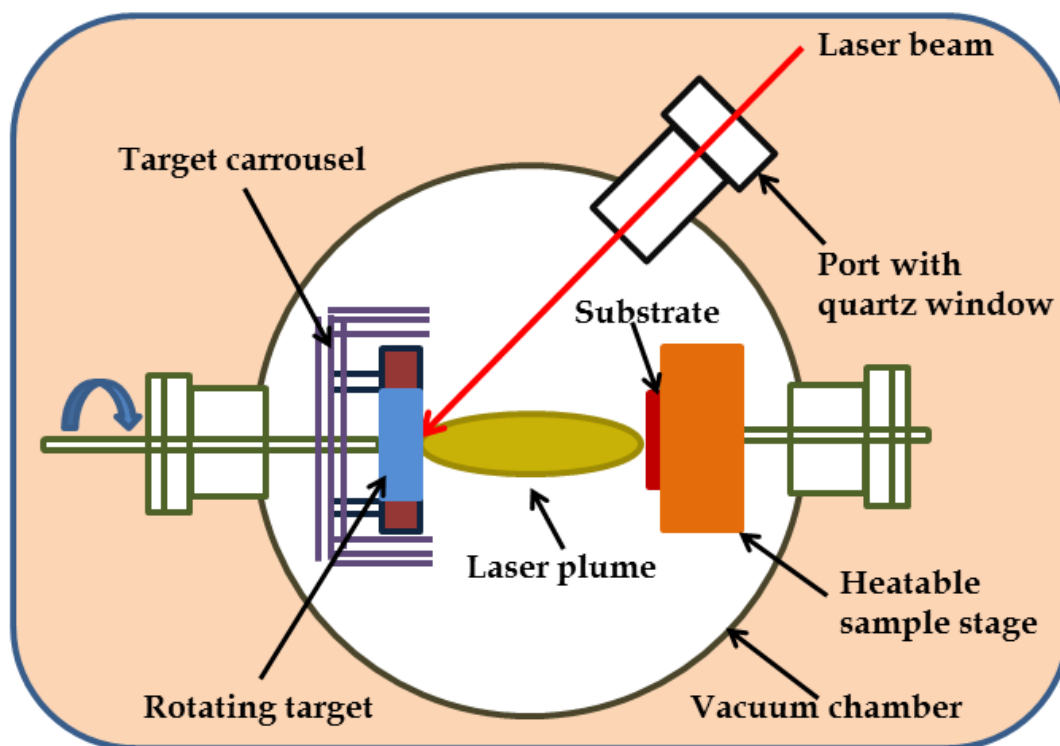


**Fig. 2.3:** Schematic diagram of PLD set up.

The detail mechanism of a PLD is very complex and divided into four stages:

**2.2.4.1. Laser ablation of the target material and creation of plasma**

In this case a laser beam is incident on the surface of the bulk material and penetrates into the surface within the penetration depth. A strong electric field, generated by the laser beam, is sufficient to remove an electron from the bulk material of the penetrated

volume. This process happens in a very short period of time (~ps). These electrons oscillate within the penetrated volume and collide with the atoms of the bulk material. During collision electrons transfer energy to the lattice of the target material within the surface region. This energy heated up the surface and the material is vaporized.

### 2.2.4.2. Dynamic of the plasma

In this stage the vaporized plasma plume is directed parallel to the normal vector of the target surface towards the substrate due to columbic repulsion. The distribution of the plasma plume is depending on the background pressure of the chamber and described by a $\cos^n(x)$ law with a shape similar with Gaussian curve.

### 2.2.4.3. Deposition of the ablation material on the substrate

Third stage generally determines the quality of the film. In this case the high energetic plasma plumes are bombarding the substrate surface and sputtering of atoms from the surface. The sputtered atoms and the plasma particles from the target material form a collision region and serves as a condensation of particles. In a high condensation rate, thermal energy is reached quickly and the film grows at a constant rate on the surface of the substrate.

### 2.2.4.4. Nucleation and growth of the film on the substrate surface

The nucleation and growth kinetics of the film depends on several parameters such as:

**Laser parameter:** Laser intensity (Joule/cm$^2$), laser energy and ionization degree of the ablated material will affect the film quality, the stoichiometry and the deposition flux.

**Surface temperature:** The nucleation density largely depends on surface temperature. Generally with increasing temperature the nucleation density decreases.

**Substrate surface:** The roughness of the substrate surface and lattice mismatch of the target material and substrate also affect the nucleation and growth of the film.

**Background pressure:** The background pressure plays a crucial role for the stoichiometric transfer from target to substrate. For example, at low oxygen background

pressure off stoichiometric film will grow which will affect the nucleation density and film quality. The schematic diagram of a PLD setup is shown in Fig. 2.3. We have used PLD technique to deposit $Y_2NiMnO_6$ thin films on Si(100) substrates. Here we have used oxygen and argon as background gas for the film deposition.

## 2.3. Sample Characterization

### *2.3.1. Structural and Surface Morphology Characterization Techniques*

#### 2.3.1.1. X-Ray Diffractometer (XRD)

X-ray crystallography relies on the twin wave/particle nature of x-rays to determine information about the crystallographic structure, chemical composition and physical properties of materials. It is a common method for the study of micro and nano-structure, thin films, and bulk samples in a non-destructive way. The generation of monochromatic X-rays and the X-rays diffracted by crystalline powders are very complex. Basically, X-rays are generated by a cathode ray tube, filtered to produce monochromatic radiation, collimated to concentrate, and directed toward the target [5]. X-rays is considered as a waves of electromagnetic radiation with wavelength about 1 Å ($10^{-10}$ m), which is comparable with the size of an atom. When an incident monochromatic x-ray beam interacts with target material elastically is scattering of those X-rays from atoms within the target material. The scattered X-ray produces constructive and destructive interference (with a diffraction ray) when it satisfy the Bragg's law

$$2dsin\theta = n\lambda \tag{2.1}$$

here, $d$ is the spacing between two atomic planes, $\theta$ is the incident angle, $n$ is any integer, and $\lambda$ is the wavelength of the x-ray beam. The Bragg's law is illustrated in Fig. 2.4.
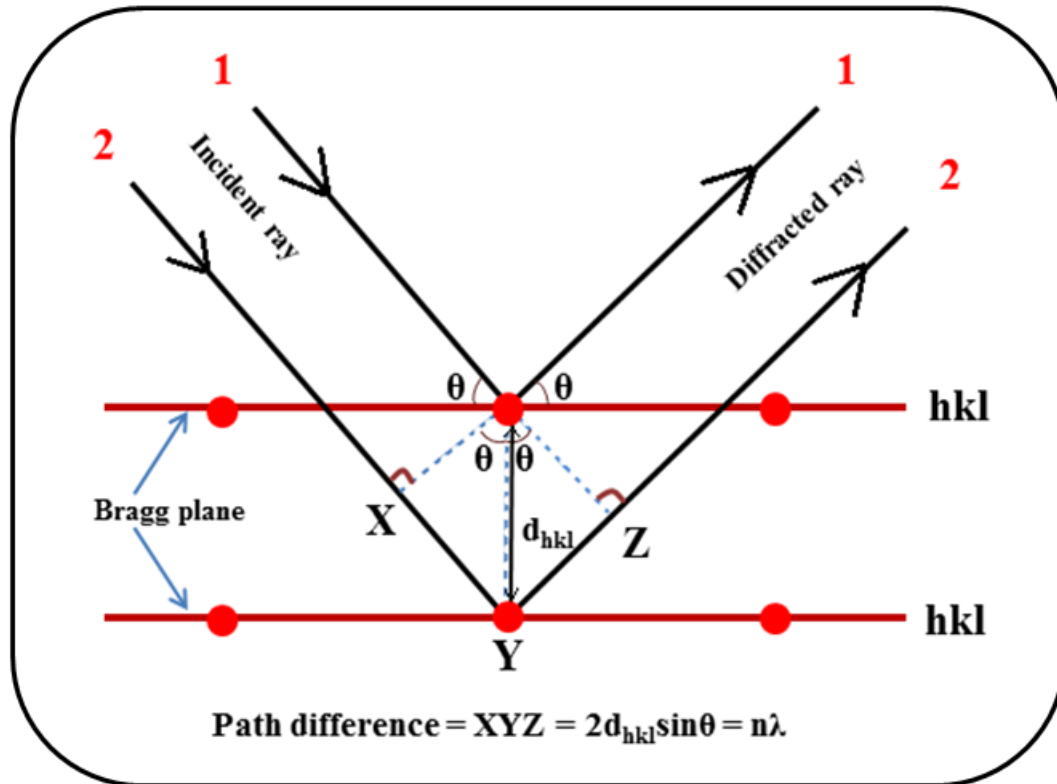
**Fig. 2.4:** Schematic diagram of diffraction of X-rays by a crystal.

In order to determine the phase and the crystal orientation of a particular sample (ceramics, Nanoparticles, thin films and nanowires), experimental diffraction patterns can be compared to those in the JCPDS (Joint Committee on Powder Diffraction Standard) database or may be some other standard data base. Each crystallographic plane has three indices h, k, l. Hence with the help of the data base each plane can be indexed with different hkl.
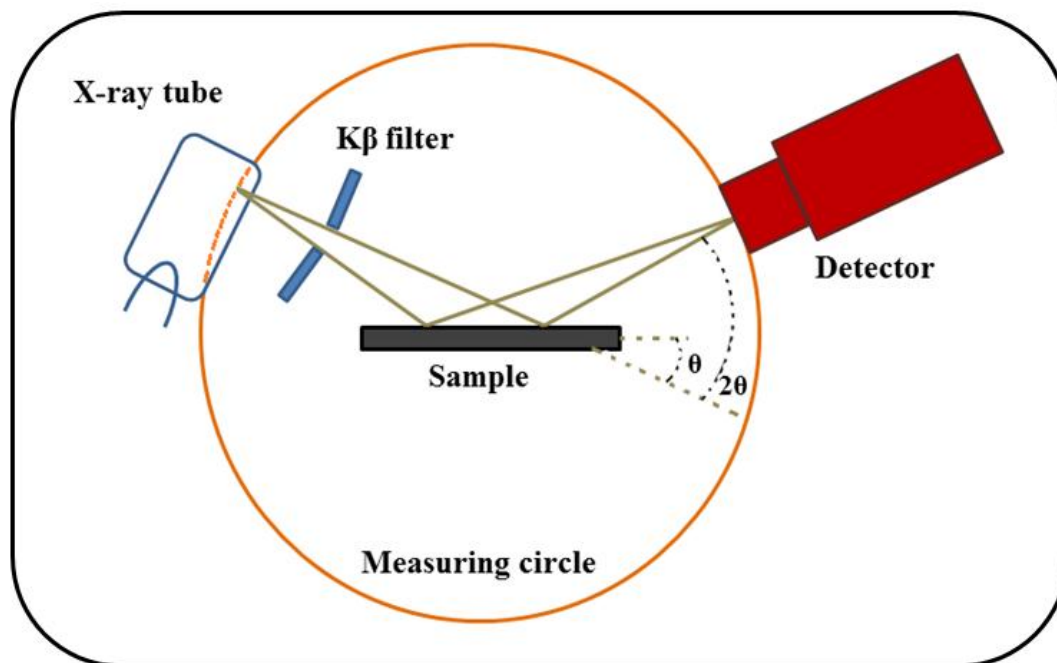
**Fig. 2.5:** Schematic diagram of X-ray diffraction.

For phase and structure of all samples, we have used Panalytical (*X'part Pro*) X-ray diffractometer using $CuK_\alpha$ radiation ($\lambda$ = 1.5418 Å). Basically in this typical system ($\theta$ - $2\theta$ system) X-ray tube is kept fixed and specimen moves at a half rate of the detector to maintain the $\theta$ - $2\theta$ geometry as shown in the Fig. 2.5.

### 2.3.1.2. X-ray photoelectron spectroscopy (XPS)

X-ray photoelectron spectroscopy is a quantitative technique to analyze the structure of atoms and obtain the information about the electronic structure as well as ionization energies. It works by brightening a sample with an x-ray beam and then measured the kinetic energy and the number of electrons expelled from the material. With this technique we are capable to get chemical composition of many materials. It gives which chemical elements exist on the surface of the material, such as Fe, O etc. XPS is totally based on the mechanism of photoelectric effect, which was described by Einstein in 1905. The schematic diagram of XPS mechanism is shown in Fig. 2.6. XPS was developed by Kai Siegbahn and his research group in the mid-1960s at the University of Uppsala, Sweden. Using this technique one can determine the composition of materials, electronic state.
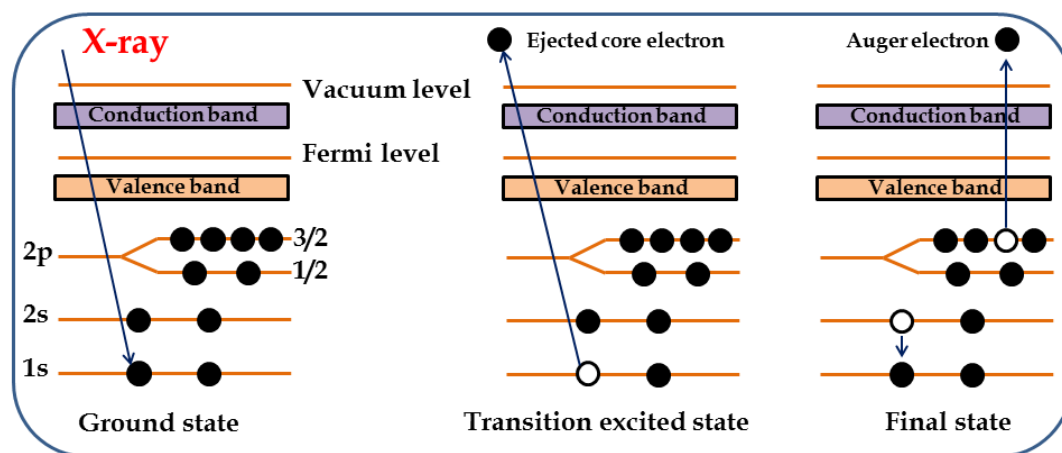
**Fig. 2.6:** Schematic diagram of XPS mechanism.

XPS is a method to determine the energy spectrum of photoelectron ejected from the sample. If the energy of the incident x-ray is hν, then the kinetic energy of the ejected electron is given by

$$E_K = h\nu - E_B - \phi \qquad (2.2)$$

where $E_K$ is the kinetic energy of the ejected electron, $E_B$ the binding energy of the atomic orbital and $\phi$ is the spectroscopic work function. The kinetic energy of the photoelectron gives the information about the elements present in the sample and the intensity gives the idea about the concentration of the elements in the sample. The work function $\phi$ is a correction factor for instrumental adjustment.

For each and every element, there is a characteristic set of peaks for each core atomic orbital in the photoelectron spectrum. The kinetic energy of the photoelectron spectrum is determined by the photon energy and the respective binding energies [6]. The chemical composition of our sample has studied by X-ray photoelectron spectroscopy (XPS) using XPS, PHI 5000 Versa Probe II Scanning at Indian Institute of Technology (IIT) Kharagpur.

## 2.3.2. Electron Microscopes

### 2.3.2.1. Scanning Electron Microscope (SEM)

A scanning electron microscope (SEM) is a widely used electron microscope that produces topographical features (such as grain size, distribution of the particles etc.) of a sample by scanning the surface with a focused beam of electrons. The focused beam of electrons interacts with the atoms in the sample and producing various signals that contain information about the surface topography and composition of the sample. In electron microscope the electron beam is highly energetic and examines objects at sub-micrometer length scale [7].
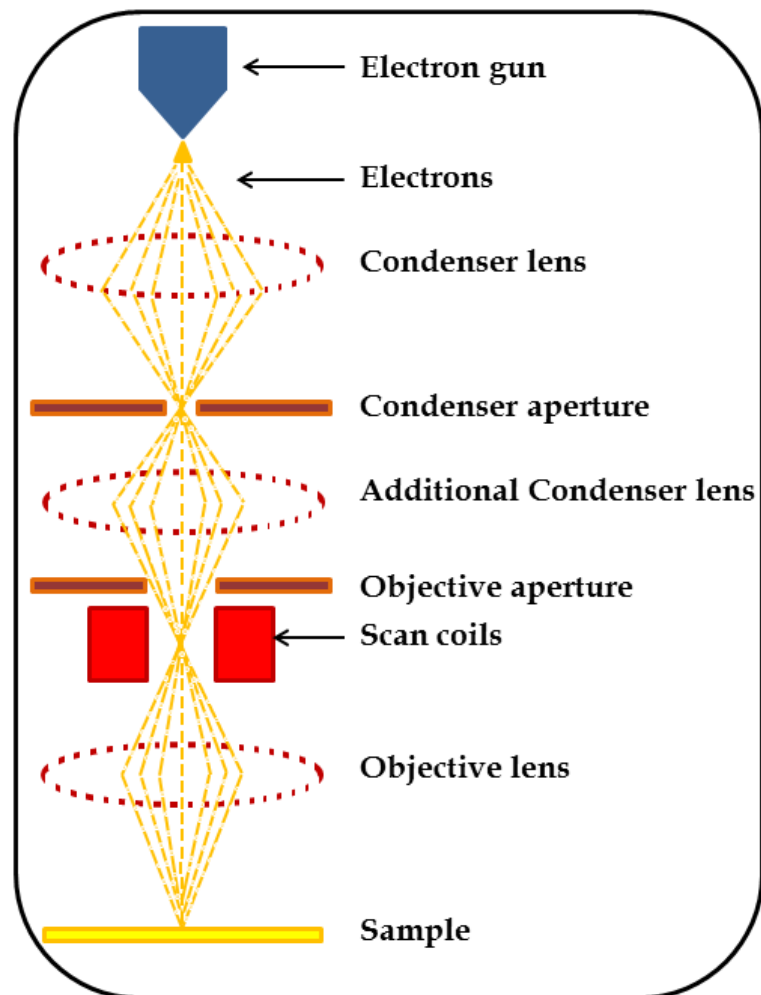


**Fig. 2.7:** Schematic diagram of a SEM unit.

The basic working steps of a scanning electron microscope involved are the following: here the electron beam is generated either thermodynamically or field emitted from an electron gun in high vacuum and confined a fine narrow probe that rastered over the surface of the specimen [8]. The electron beam is accelerated towards the specimen (with a positive electrical potential) and is confined, focused. Then the beam is directed in a particular direction using various metallic aperture and magnetic lenses resulting in a monochromatic beam. The schematic diagram of a SEM unit is shown in Fig. 2.7. SEM works on a voltage between 2 to 50 kV and its scanning beam diameter is about is 5 nm - 2 µm. A field-emission cathode in the electron gun of a SEM (FESEM) provides narrower probing beams at low as well as high electron energy. When the primary electron beam incident on the specimen sample, it interacts with the atoms at various depths within the sample and affecting the electron beam. When, the electron beam interacts with the sample, the energy exchange between the electron beam and the sample results deceleration of incident electrons through the energy dissipation and various types of signals are produced including secondary electrons (SE), reflected or back-scattered electrons (BSE), characteristic X-rays, specimen current (absorbed current) visible light (cathod-luminescence) (CL), and transmitted electrons. All the signals (especially secondary electrons and back-scattered electrons) are separated according to their energies [9]. In case of secondary electron imaging the electrons are emitted from very close to the sample surface. Consequently, back-scattered electrons are produced very high intense images, less than 1 nm in size and reflected from the sample elastically but the electrons immerge from deeper within the sample and make the image resolution less. For image formation, the electrons are collected by a suitably placed detector in the microscope in proper positions. In case of non-conducting sample, like; $BiFeO_3$, a thin gold is coated on the sample to avoid the static charge accumulation during SEM imaging. When an electron beam is incident on the sample surface, electrons are ejected from the atoms including sample's surface. Then an electron from higher shell fills the electron vacancy and an X-ray known as characteristic X-ray is emitted to balance the energy difference between the two

electrons. The spectrum of X-rays is used for elemental analysis. The process is called Energy dispersive analysis of X-ray (EDAX). Because of high energetic and narrower beam, field emission SEM (FESEM) results in both improved spatial resolution and minimized sample charging and damage.

**2.3.2.2. Transmission Electron Microscope (TEM)**

Transmission electron microscopy (TEM) is a microscopy technique in which a beam of electrons is transmitted through a specimen to form an image. Basically, here two types of electrons interact with the specimen sample for image formation, one is unscattered electrons (transmitted beam) and another one is scattered electrons (diffracted beam). It is a versatile instrument to capable of characterizing the internal structure of the specimen with wide range of imaging in analytical method. The schematic diagram of a TEM unit is shown in Fig. 2.8. Here the monochromatic electrons stream is generated by an electron gun at the top. Then the electron stream is focused into a narrow coherent beam after crossing the condenser lens. Here the first lens determine the spot size and the second lens control the brightness knob of the spot on the sample and makes it widespread spot to pin point beam. Then the beam is constrained by the condenser aperture and banging out high angle electrons. The electron strikes the specimen and parts of it are transmitted.

A part of electron beam gets scattered (diffracted beam) elastically or inelastically with the sample specimen. Elastically (no loss of energy) scattered electron beam is getting diffraction according to Bragg's law while passing through the crystalline sample specimen. Same energy electron beam is entering the sample surface normally. The electrons make same scattering angle when scattered from same atomic spacing. Magnetic lenses collated the scattered electrons into a spot, each spot corresponding to a specific atomic spacing (or crystalline plane). This pattern gives information about the orientation, atomic arrangements and phases present in the area of the sample being examined.

But the unscattered electrons beam (transmitted electron beam) produce the two dimensional image of the sample. These unscattered electrons beam are inversely proportional to the thickness of the sample. These transmitted electrons beam is focused by the objective lens into an image. In thicker portion of the sample, less number of unscattered electrons beam are transmitted and so will appear darker, consequently thinner portion will permit much number of electrons and will appear brighter. This mode of operation to create contrast in image is known as bright field imaging mode. In order to take microscopic images of ferromagnetic nanowires (NWs), nanoparticles (NPs) and nano-hollow spheres (NHSs).
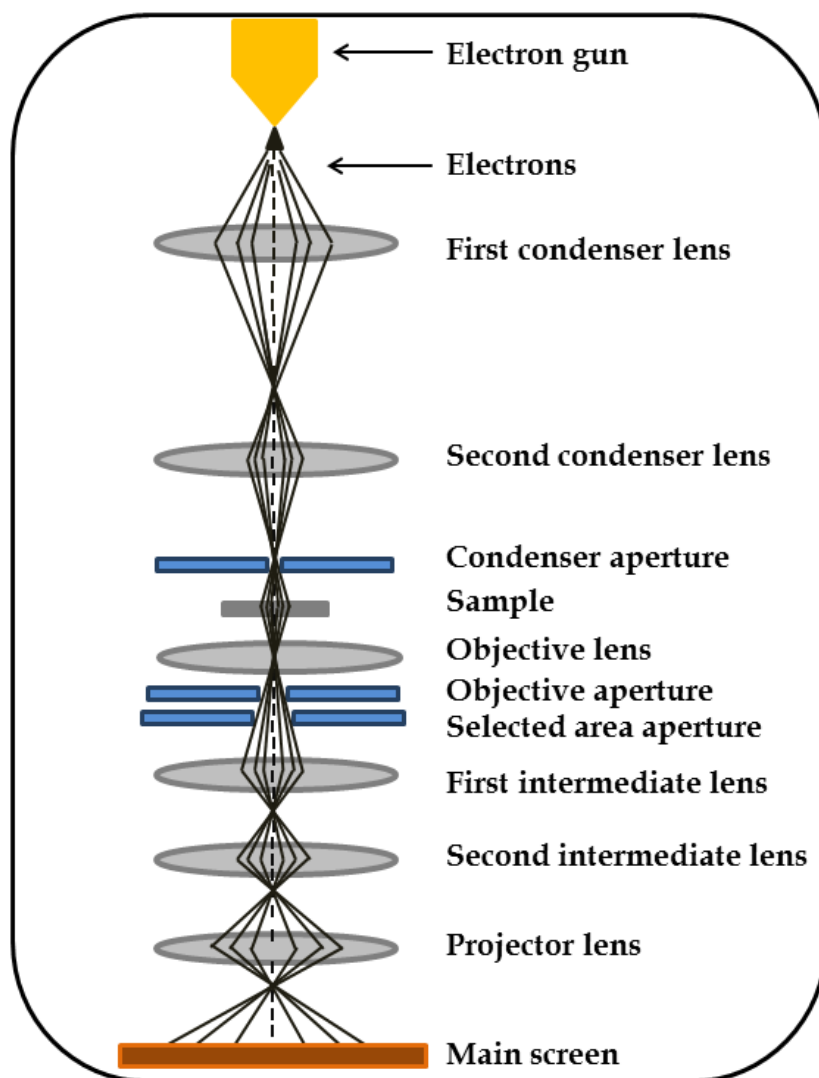


**Fig. 2.8:** Schematic diagram of a TEM unit.

For transmission electron microscopy (TEM) study samples were prepared by drop casting as prepared samples dispersed in EtOH, on a 300 mesh carbon coated copper grid and dried overnight in vacuum. Particle size was calculated from TEM micrographs and elemental analysis is carried out from EDAX spectrum recorded by a FEI Tecnai TF-20 field-emission high resolution TEM operating at 200 keV.

## 2.3.3. Scanning Probe Microscopy (SPM)

An SPM (Scanning Probe Microscope) is a widely used microscope for the study of surface morphology of a specimen in nano scale level. It can scan the sample specimen from 100 μm to 10 pm [10]. SPM is an essential instrument to observe the point defects and structural defects of the specimen surface with the atomic resolution. So it is a much needed technology in the field of nano-science and nanotechnology. We have used several SPM techniques in this thesis such as AFM, MFM and PFM for the characterization of the thin films. A Vecco-3100 scanning probe microscope set up was used for the characterization of the sample.

### 2.3.3.1. Atomic force microscopy (AFM)

AFM is a very high quality resolution (in the order of Å) probe microscope which measure the topography of a sample surface in nano scale range. Here the sample surface and the mechanical probe give the information about the sample topography. The probe is chosen very thin and sharp at the end of the cantilever. The tip radius is about 5 to 20 nm. A single crystal cantilever with very good spring constant about 0.1 to 1 N/m is used and made of silicon dioxide ($SiO_2$), or silicon nitride ($Si_3N_4$). The schematic diagram of an AFM system is shown in Fig. 2.9.

The basic working principle of an AFM is that a laser beam is incident on the cantilever and the cantilever moves up and down according to specimen surface. The deflection of the beam reflected from the cantilever is collected by a well-placed diode. Depending on the specimen sample, the interaction between sample surface and the cantilever probe works in two different ways. One, contact mode in which the probe is connected with the sample surface and it follows the Van der Waal's law of interaction. The other

mode is the taping mode or non-contact mode. In this typical mode, a signal is driven to a piezoelectric crystal with frequency range 10 kHz to 1 MHz. The piezoelectric crystal mechanically oscillates the cantilever probe near its resonance frequency on the sample surface. The oscillation frequency changes due to the interaction between the probe and the sample surface with respect to driven signal.
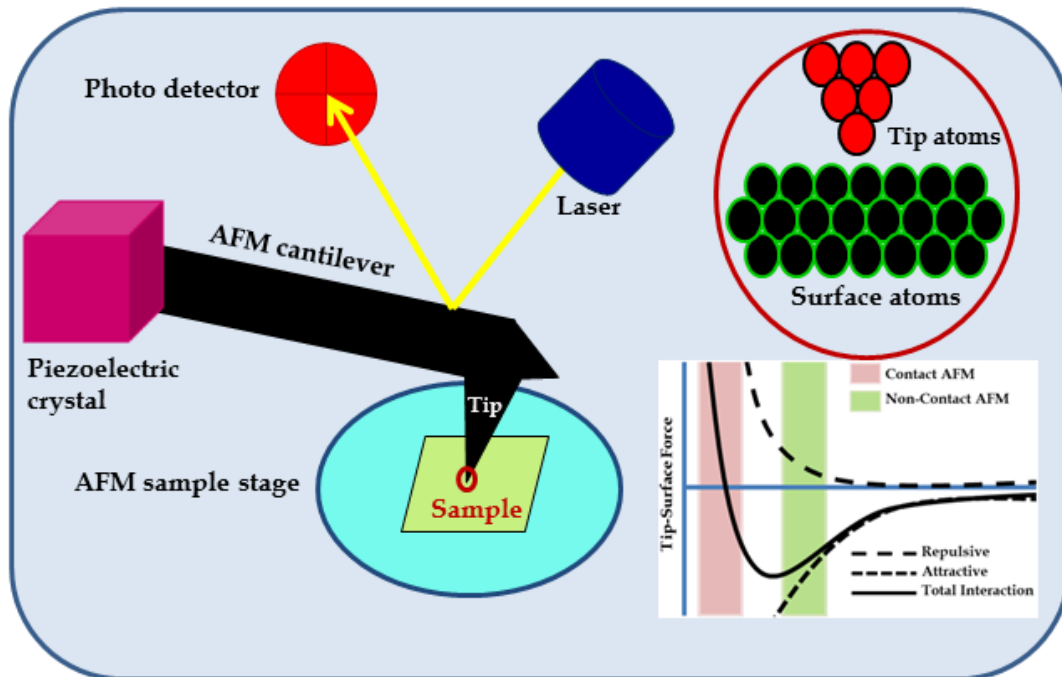


**Fig. 2.9:** Schematic diagram of Atomic Force Microscopy (AFM) system.

## 2.3.3.2. Magnetic force microscopy (MFM)

Magnetic force microscope is an essential tool to know the magnetic structure of the specimen sample. A sharp magnetic tip is used to scan the sample surface. The magnetic interaction between tip and sample surface are detected and used to know the magnetic structure of the specimen surface. The schematic diagram of a MFM system is shown in Fig. 2.10.

In case of MFM, the AFM tip is coated with a small coercive magnetic material (such as Ni or Co). Here the coercivity of the tip is taken very low, because tip's magnetic state (or magnetization) does not change during the imaging. The magnetic tip interacts with only the out-of-plane component of the stray field originating from a

domain wall of a magnetic material. Here each line scanning of the cantilever is recorded twice. Firstly the topographical information of the material is recorded by it in AFM tapping mode and this information is used during the second scan in order to keep the cantilever always at a certain probe sample distance. This sample to probe distance is called Lift Height. During second recording the tip is only affected by the stray field of the material. Therefore these two combinations give the accurate magnetic state of the material. Typical resolution can be achieved when Lift Height is about 30 nm [11], although resolutions as low as 10 to 20 nm are attainable [12]. During scanning the magnetic tip deflected according to the direction of stray field of the material and we get the bright and dark spots.
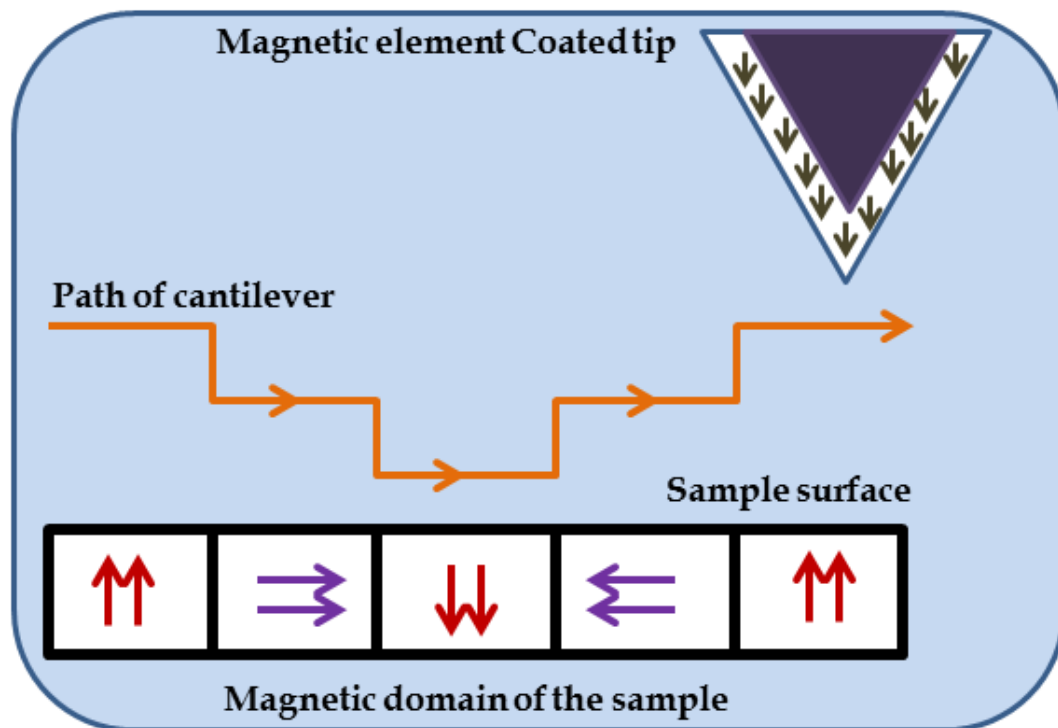


**Fig. 2.10:** Schematic diagram of Magnetic Force Microscopy (MFM) system.

### 2.3.3.3. Piezoresponse force microscopy (PFM)

Piezoresponse force microscope (PFM) is an essential tool to know the topography and ferroelectric domains structure simultaneously with high resolution in nano scale range. Here the AFM tip is coated with a conducting material such as platinum, gold, tungsten

and even conductive diamond. The schematic diagram of a PFM system is as shown in Fig. 2.11.

The basic working principle of PFM is as follow: when the conducting PFM probe is connected with the sample surface, an alternating current is applied to the probe. Hence, PFM is a contact-mode AFM in which an electrically biased conductive AFM tip is used as a probe of local electromechanical coupling via the converse piezoelectric effect. Due to CPE the cantilever is deflected and the deflection is recorded through standard photodiode detector.
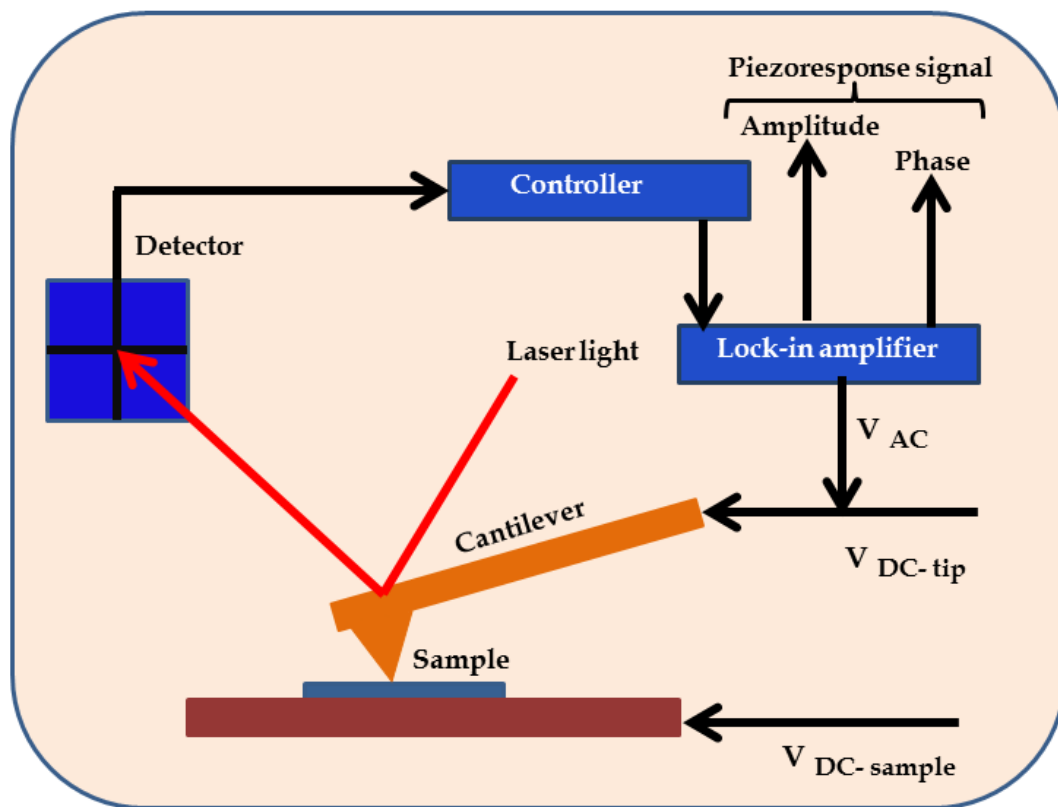


**Fig. 2.11:** Schematic diagram of piezoresponse force microscope where both ac and dc voltages are applied

## 2.4. Magnetic Characterization Techniques

### 2.4.1. Vibrating Sample Magnetometer (VSM)

Vibrating sample magnetometer (VSM) is a very profound and useful instrument which can measure incredibly small magnetic moment upto an order of $10^{-5}$ emu. In VSM the

sample is placed in a direct current (DC) magnetic field (H) and vibrated sinusoidally so that the resulting variation of magnetic flux (B) can induce a voltage in pickup coils. According to Faraday's law of induction an electromotive force (EMF), 'V' will be generated in a pickup coil of N identical loops and a cross-sectional area of A is given by

$$V = -NA \frac{dB}{dt} \qquad (2.3)$$

The direction of the EMF is given by Lenz's law. If the coil is placed in a constant magnetic field H, the flux B around it is given by,

$$B = \mu_0 H \qquad (2.4)$$

where, $\mu_0$ is the permittivity of vacuum. Now, if we place a magnetic sample having magnetization M around the pickup coil, then the total magnetic induction B can be written as

$$B = \mu_0 (H + M) \qquad (2.5)$$

Therefore the change in magnetic flux due to presence of magnetic material is given by

$$\Delta B = \mu_0 M \qquad (2.6)$$

Now the induced EMF in the pickup coil can be written as

$$V dt = -\mu_0 NAM \qquad (2.7)$$

Here the output signal is proportional to the magnetic moment of the material and independent of frequency of the sinusoidal motion. The schematic diagram of a VSM unit is shown in Fig. 2.12. The magnetic properties of our sample were studied by using a vibrating sample magnetometer (VSM, Lakeshore, model 7144). It generates a maximum of 1.6 T magnetic field. Here low temperature (80 to 400 K) measurement (moment versus temperature and isothermal hysteresis loops) can be measured using a cryogenic system (Liquid $N_2$) and RT to 1173 K for high temperature measurements can be measured with temperature stability of ± 0.2 K and temperature resolution of 0.001 K. Noise level of 1.25 µemu (RMS value) can be achieved using the system [Lake Shore Cryotronics, Inc., USA.].
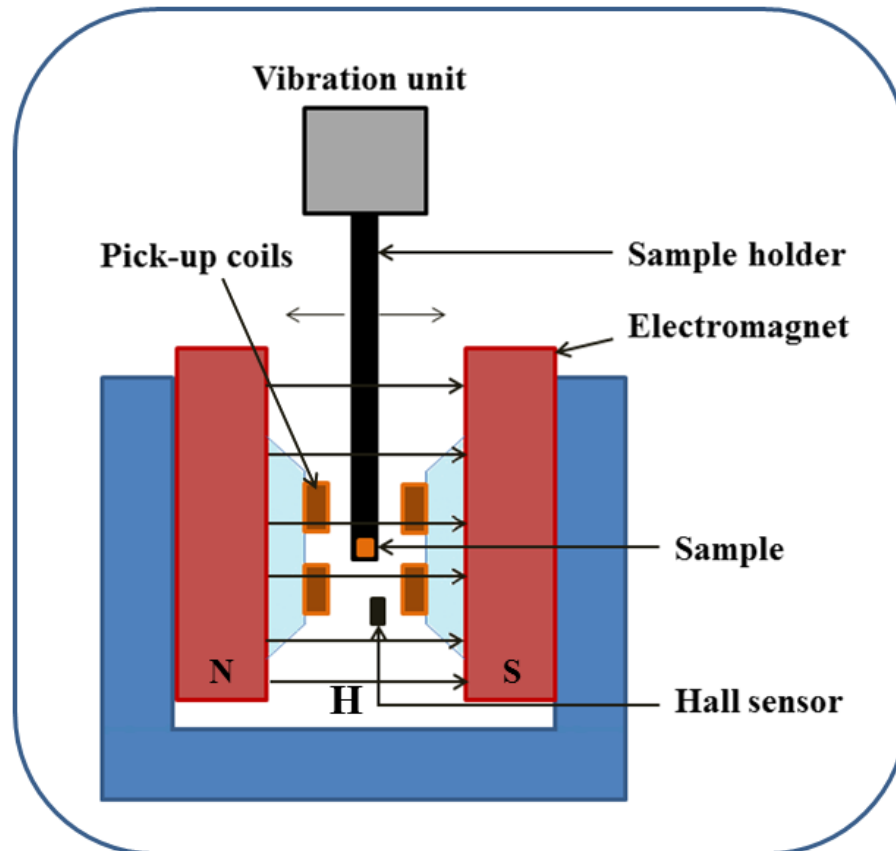
**Fig. 2.12:** Schematic diagram of a VSM unit.

## *2.4.2. Superconducting Quantum Interference Device (SQUID)*

SQUID is a most sensitive and valuable device for magnetic measurement, has been designed till now. It can measure very low magnetic moment having resolution of the order of $10^{-8}$ emu. The working principle of this device is based on the tunneling of cooper pairs across a very thin non conducting layer. It consist of two superconductor separated by an insulating layer to form two parallel Josephson junction [13]. The schematic diagram of a SQUID unit is shown in Fig. 2.13.
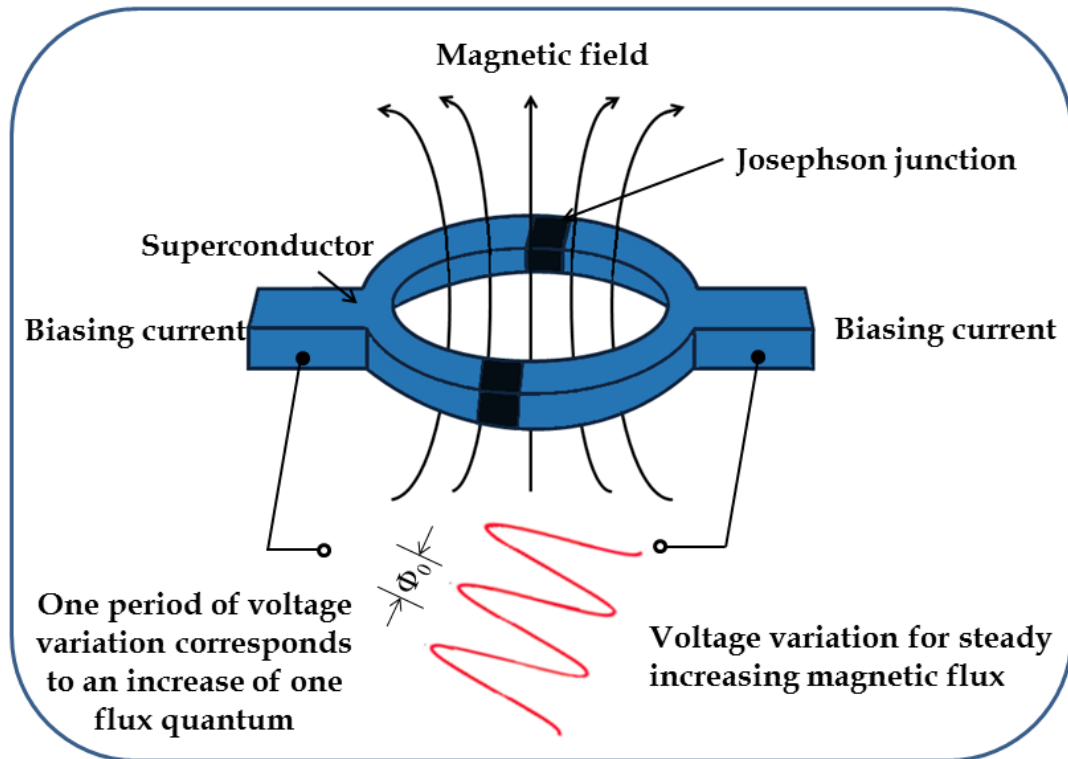
**Fig. 2.13:** Schematic diagram of a SQUID unit.

The insulating layer is thin enough such that the cooper pairs can easily tunnel through the insulating junction. The biasing current (I) splits into two parts equally and oppositely in two branches in absence of external magnetic field. According to Faraday's Law, when an external magnetic field is applied, a magnetic flux goes through the superconducting loop and induces a persistent current J. The induced current adds to the measuring current in one junction ($I_A = I/2 + J$), and subtracts in the other ($I_B = I/2 - J$). As soon as the current in either branch exceeds the critical current, $I_C$, of the Josephson junction, a voltage appears across the junction. Now if the external flux is further increased until it exceeds $\Phi_0/2$, half the magnetic flux quantum. Since the magnetic flux passing through a superconducting loop must be quantized. Hence there is interference between I after passing the junctions. When a magnetic material is placed in the loop containing a Josephson junction, an EMF is induced in the loop. This induced EMF generates a current with a frequency decided by the Josephson equations. The SQUID calculates the change in currents or frequency to measure the magnetic

moment of the sample. The magnetic properties of the nanostructure (nanowires, nanoparticles) were studied by using a superconducting quantum interference device (Quantum design, MPMS) magnetometer.

## 2.5. Optical Characterization Techniques

### *2.5.1. UV-Visible (UV-Vis) Absorption Spectroscopy*

In UV-Vis spectroscopy, light of visible and adjacent (near-UV and near- infrared (IR)) region of EM spectrum is absorbed by the molecule and undergo electronic transition from ground state to another excited state. Here a beam of light passing through the sample and measured the wavelength by a suitably placed detector. This measured wavelength gives valuable information about the solution. This technique is used to measure the concentration of absorbing kinds in solution using Beer-Lambert law. This law states that whenever a beam of monochromatic light is passed through a solution with an absorbing substance, the decreasing rate of the radiation intensity is proportional to the concentration of the solution and the incident radiation. The law as given bellow:

$$A = \log_{10}(I_0/I) = \varepsilon.C.l \tag{2.8}$$

where, A is the absorbance of sample, $I_0$ is the intensity of light, I is the intensity of departing light from the sample cell, C is the concentration of the absorbing kinds, *l* is the path length of the sample cell and ε is the molar absorptivity coefficient.
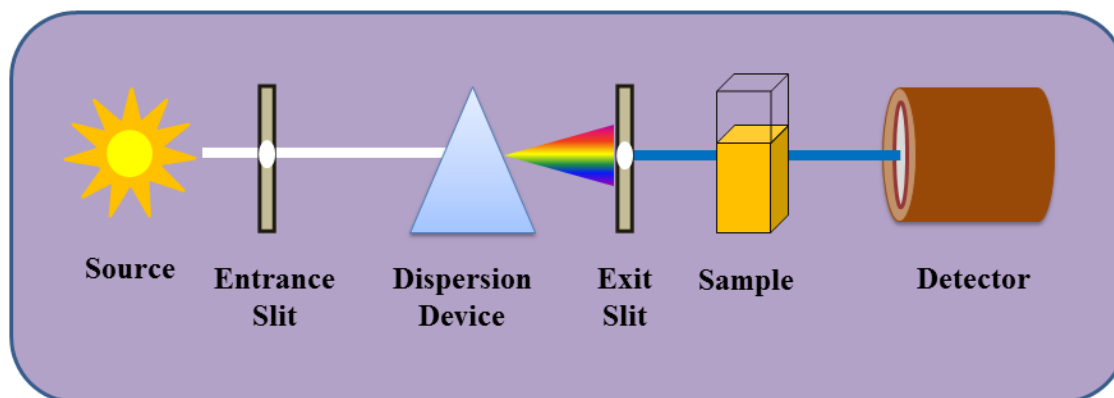


**Fig. 2.14:** Schematic diagram of a UV-Vis spectrometer.

The schematic diagram of the UV-Vis spectrometer is demonstrated in Fig. 2.14. In order to measure the UV−vis absorption of our sample and the degradation of MB with spectroscopic precision, the spectra are recorded with a Shimadzu model UV−2600 spectrophotometer using a quartz cuvette of 1 cm path length.

## *2.5.2. Fourier Transformed Infrared (FTIR) Spectroscopy*

FTIR is a unique instrument for the identification of functional groups and chemical bonds within a molecule. When an IR radiation is incident on a polar molecule it will vibrate and absorbed IR, after matching the frequency, FTIR signal is obtained. The absorption peaks get shifted or broadened according to interaction of functional groups with solvent molecules present. Fig. 2.15 shows schematic diagram of FTIR instrument.
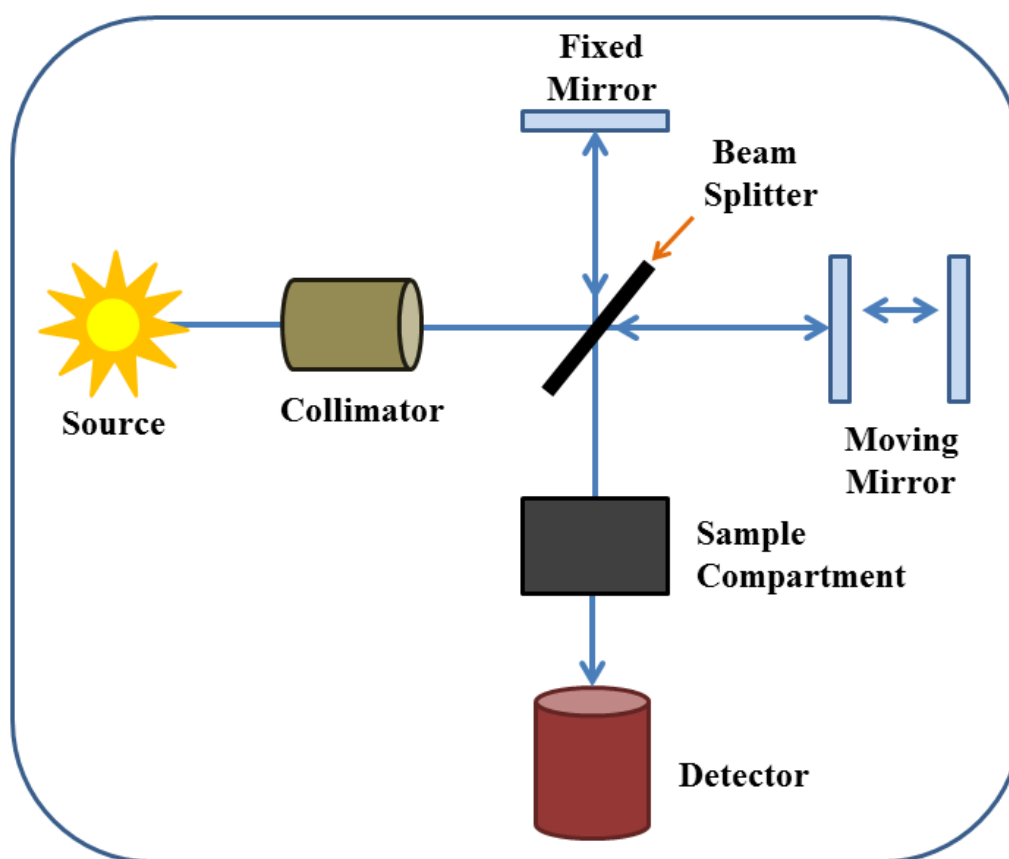


**Fig. 2.15:** Schematic diagram of FTIR spectrometer.

There are mainly two parts in IR spectroscopy, one is source and another is detector. The most common source of IR spectrometer is Nernst glower. It consists of Zirconium, Ytterbium, and Erbium mixture rod and heated up to 1773 K for IR radiation. Sodium chloride or other alkali metal halides are the best material to form cell container as they are transparent in IR region. The IR beam is passing through collimator and then reflected by and transmitted through the beam splitter (a half silvered mirror). The reflected and transmitted IR beam moves towards the fixed and moving mirrors, respectively. These two beam then interfere constructively or destructively at the backward side of the beam splitter mirror according to their wavelength and path difference introduced by the moving mirror. The resulting signal of these two beams is called interferogram. At last, Fourier transformation of this interferogram is performed to have a frequency spectrum (plot of intensity at each frequency). A JASCO Fourier transformed infrared (FTIR)−6300 spectrometer is used to confirm the attachment of tartrate ligand with our sample. For FTIR measurement, powdered sample is mixed with KBr powder and pelletized. The background correction is made by using a reference of KBr pellet.

## 2.5.3. Photoluminescence (PL) Spectroscopy

Photoluminescence (PL) spectroscopy is a powerful tool to identify various energy levels within the energy gap of materials. It is a non-contact and nondestructive method of probing the electronic structure of materials. Here a Xe lamp is used as a monochromatic light source. This monochromatic light is used to excite the electrons from valance band to conduction band if the incident photon energy ($E = hc/\lambda$) is greater than the band gap energy of the materials. The process is called photo excitation. During this excitation electrons get more energy and reaches higher energy conduction band. The electrons immediately loses their energy and coming to the lowest energy level of conduction band. At this situation electros also come down to the valance band and nearby acceptor states arises due to different defect levels. As the electrons fall down from higher energy level to lower energy level, the energy

associated with this imitation act as luminescent photons which are emitted from the material. The process of photon excitation followed by photon emission is called photoluminescence. The characteristic fluorescence excitation and emission spectra are measured of all our samples using a spectrofluorometer (Jobin Yvon Model Fluoromax−3 fluorometer) having Xe lamp source. The Schematic diagram of fluorescence spectrometer is shown in Fig. 2.16.
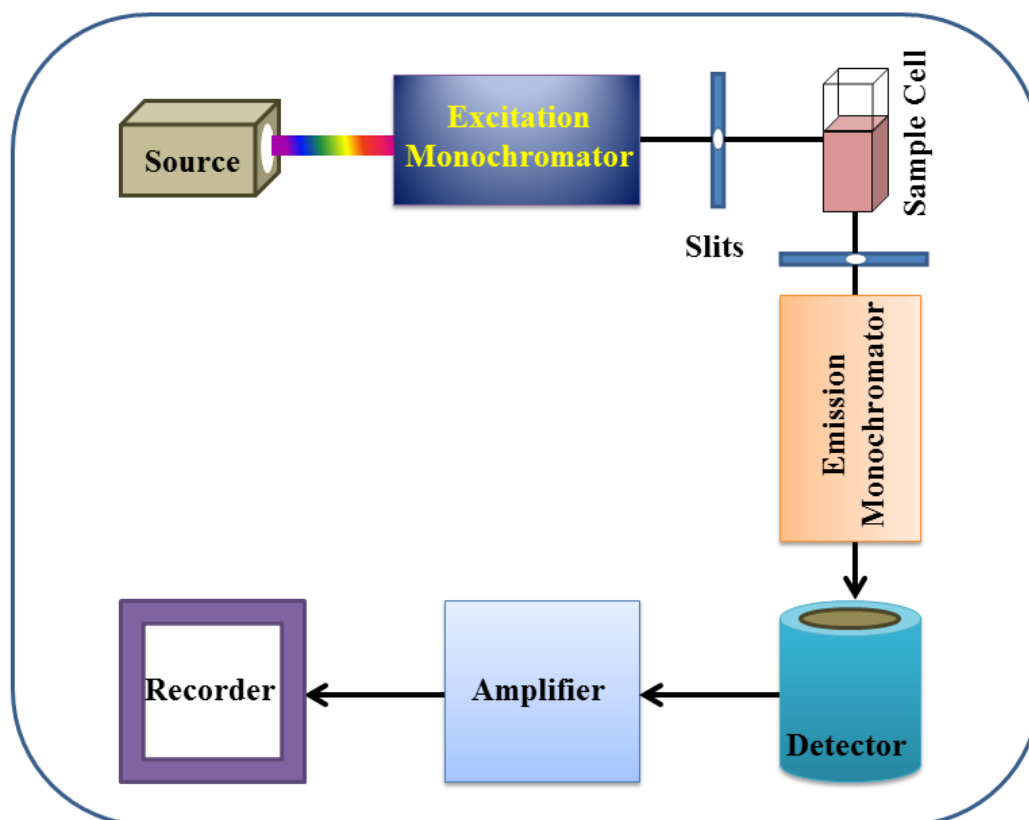


**Fig. 2.16:** Schematic diagram of fluorescence spectrometer.

## 2.6. Electrical Properties Measurement Techniques

### 2.6.1. Dielectric Properties Measurement Setup

Impedance analyzer or an LCR meter (Inductance (L), Capacitance (C), and Resistance (R)) is very important equipment used to measure the capacitance, inductance and resistance of a sample. Inductance or capacitance is not measured directly using this equipment. Here impedance is measured internally and then converted it into corresponding inductance or capacitance value.

An LCR meter measures impedance (capacitance, inductance and resistance) at spot frequencies or in a wide range of frequencies, and also measures the equivalent series resistance of capacitors and the Q factor of inductive sample. In this instrumental setup, the LCR meter is interface with a computer and the data (inductance, capacitance, AC conductance, and dissipation factor) is collected as a function of frequency with different temperature.

The dielectric constant ($\varepsilon$) of a sample is calculated using the formula,

$$\varepsilon = {Cd}/{A\varepsilon_0} \tag{2.9}$$

where C is the capacitance of the sample in Farad (F), d is the thickness of the sample in meter (M), A is the area of the active material in square meter (M$^2$), $\varepsilon_0$ is the free space permittivity (8.854 x 10$^{-12}$ F/m), $\varepsilon$ is the dielectric constant or relative permittivity of the sample.

Here the experimental sample is subjected to an AC voltage source [14, 15]. The analyser of the meter measures the voltage across and current through the sample. From the ratio of these two values meter can easily determine the accurate value of impedance. The phase angle of voltage and current is calculated from the equivalent inductance or capacitance and resistance of the sample. The analyser assumes parallel mode for LR measurement (as would be encountered in an inductor coil) and series for CR measurement (as would be encountered in measuring a capacitor with a leaky dielectric). Here we have also measured the impedance, inductance, capacitance, conductivity etc. in different temperature by using the LCR meter. In this case the sample is placed in an oven. The home-made experimental setup is shown in Fig. 2.17.

**Fig. 2.17:** Dielectric properties measurement setup.

## 2.6.2. *Ferroelectric Hysteresis Loop or PE Loop Tracer*

P-E hysteresis loop measurement is a very important measurement tools for the ferroelectric property of a multiferroic material. A P-E hysteresis loop is basically a plot of polarization manifested in a material on the engaging of applied electric field. In case of capacitor sample current leads the voltage by an angle 90 degree and we get a straight line P-E loop (Fig. 2.18(a)). For an ideal resistor the current and voltage are in phase condition, which gives a circular type of P-E loop with its centre at origin (Fig. 2.18(b)). Therefore a parallel combination of a resistor and a capacitor gives leaky type of P-E loop (Fig. 2.18(c)). The slope of the curve is proportional to the value of the capacitance and the area is proportional to the loss tangent of the device. Pure ferroelectric material gives P-E hysteresis loop (Fig. 2.18(d)).
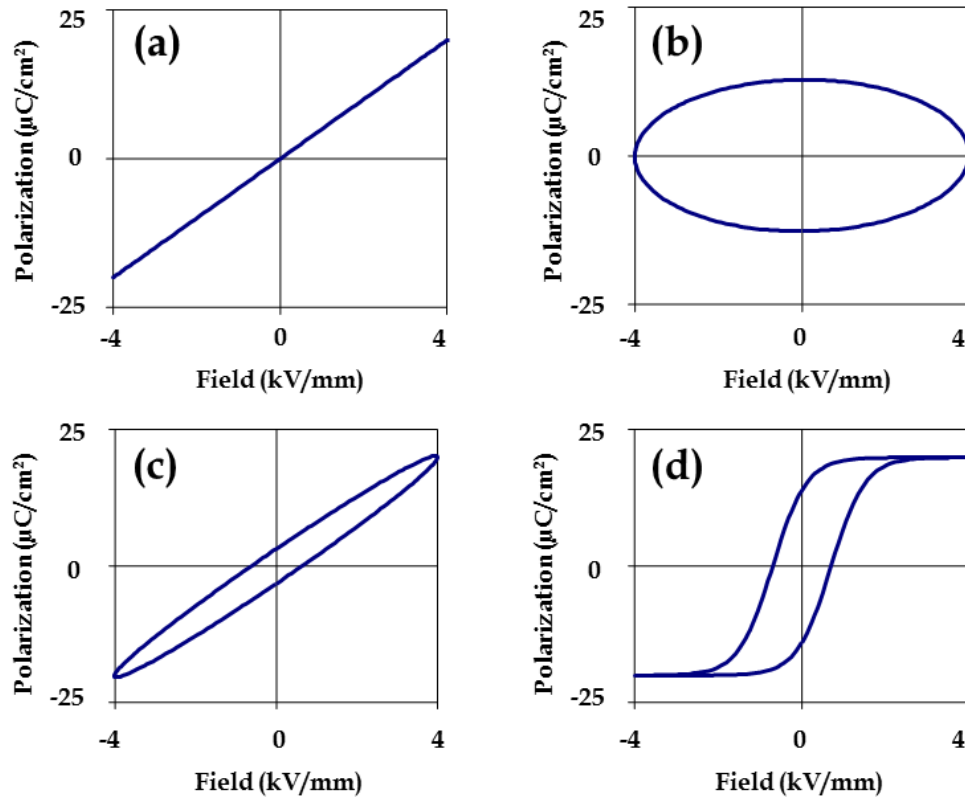
**Fig. 2.18:** (a) Ideal linear capacitor response, (b) Ideal resistor response, (c) Lossy capacitor response and (d) Non-linear ferroelectric response [16].
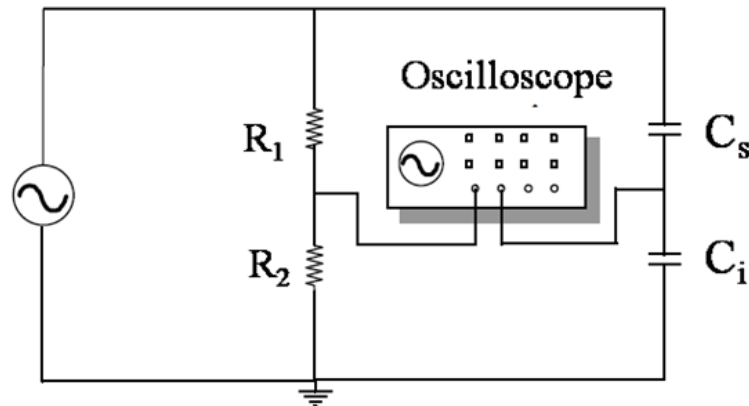


**Fig. 2.19:** Schematic of a Sawyer Tower circuit for P-E loop measurements [18].

The Polarization vs Electric Field hysteresis loop is measured based on Sawyer-Tower circuit [17]. Fig. 2.19 shows the schematic diagram of the circuit. It consists of two capacitors ($C_i$ and $C_s$ connected in series) and a load resistance (series combination of

two resistances). Here i stands for internal reference capacitor and s stands for sample. We can select an appropriate value for $C_i$ and load resistance. Since the two capacitors are connected in series so the same amount of charge (Q = CV) is developed in the capacitors.

$$Q_s = Q_i \tag{2.10}$$

$$C_s * V_s = C_i * V_i \tag{2.11}$$

$$V_T = V_i + V_s \tag{2.12}$$

where $V_T$ is the total applied voltage and $V_i$ is measured internally. Using equation we can calculate $C_s$. Multiplying $V_s$ with $C_s$ will give the $Q_s$ value. This $Q_s$ value gives the polarization value of the sample. Ferroelectric hysteresis loops of all the samples are studied by a PE loop tracer (Radiant Technologies, Model no 609B). The experimental setup is shown in Fig. 2.20.
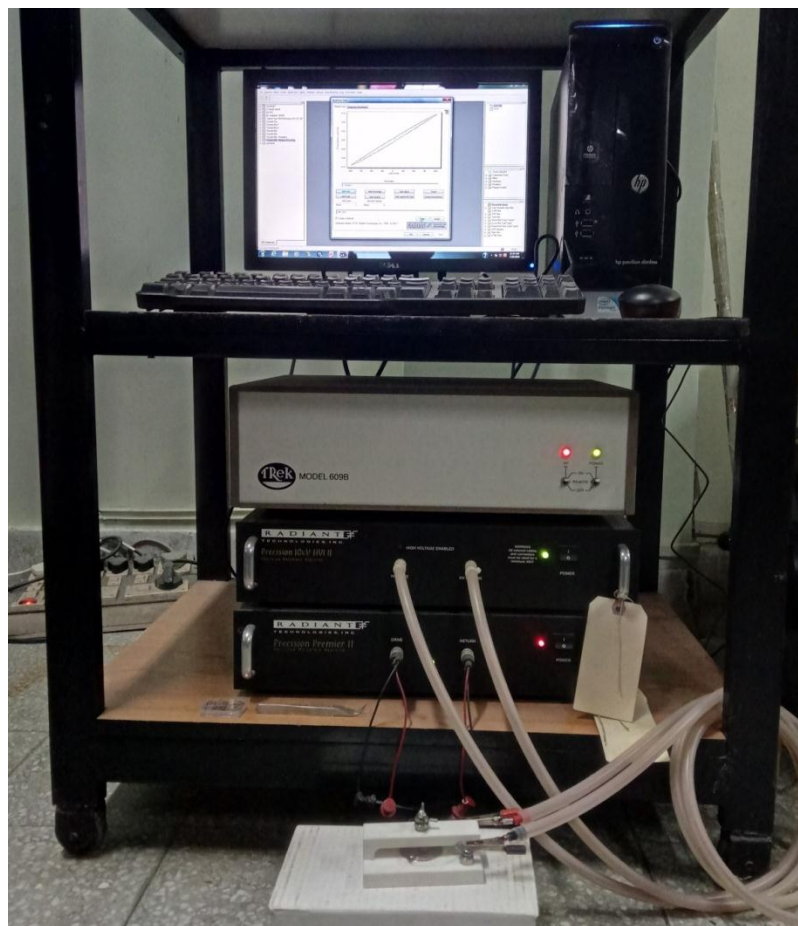


**Fig. 2.20:** The Polarization vs Electric Field hysteresis loop measurement setup.

## 2.6.3. *Magnetoelectric Co-efficient measurement*

The magnetoelectric coefficient is the measure of the strength in a magnetoelectric material about its coupling property. Magnetoelectric coupling is studied using a home-made set-up as shown in Fig. 2.21, with dynamic lock-in technique. The value of the magnetoelectric coefficient is determined using the formula

$$\alpha_{ME} = \frac{dE}{dH} = \frac{1}{d}\frac{V_{out}}{H_{ac}} \tag{2.13}$$

where d is the effective thickness of the sample (in the form of pellet). The sample is placed in between the two pole pieces of the electromagnet with its surface perpendicular to the field direction. A small ac magnetic field with a frequency 1 Hz to 10 kHz, produced by a Helmholtz coil ( turns with a diameter ), is superimposed on to the DC magnetic field. Here the AC magnetic field is driven by an AC current generated by a Lock in Amplifier (Stanford Research systems Model SR830 DSP) with input resistance and capacitance of 10M$\Omega$ and 25 pF, respectively. The voltage developed across the sample surfaces ($V_{out}$) duo to the ME effect is measured by a lock-in amplifier in presence of different DC magnetic field ranging from -5 KOe to +5 KOe. Here the time varying DC magnetic field is generated by using a constant current power supply electromagnet (model: DPS-175) with the current varying from 0 - 3A. To measure the DC magnetic field a Hall probe is used (Scientific Equipments Roorkee Model DGM-102). The output signal is measured by a lock-in-amplifier. This signal is actually the emf induced between the two surfaces of the sample because of the time varying ac field in the Helmholtz coil. This signal changes with the change in the dc field.
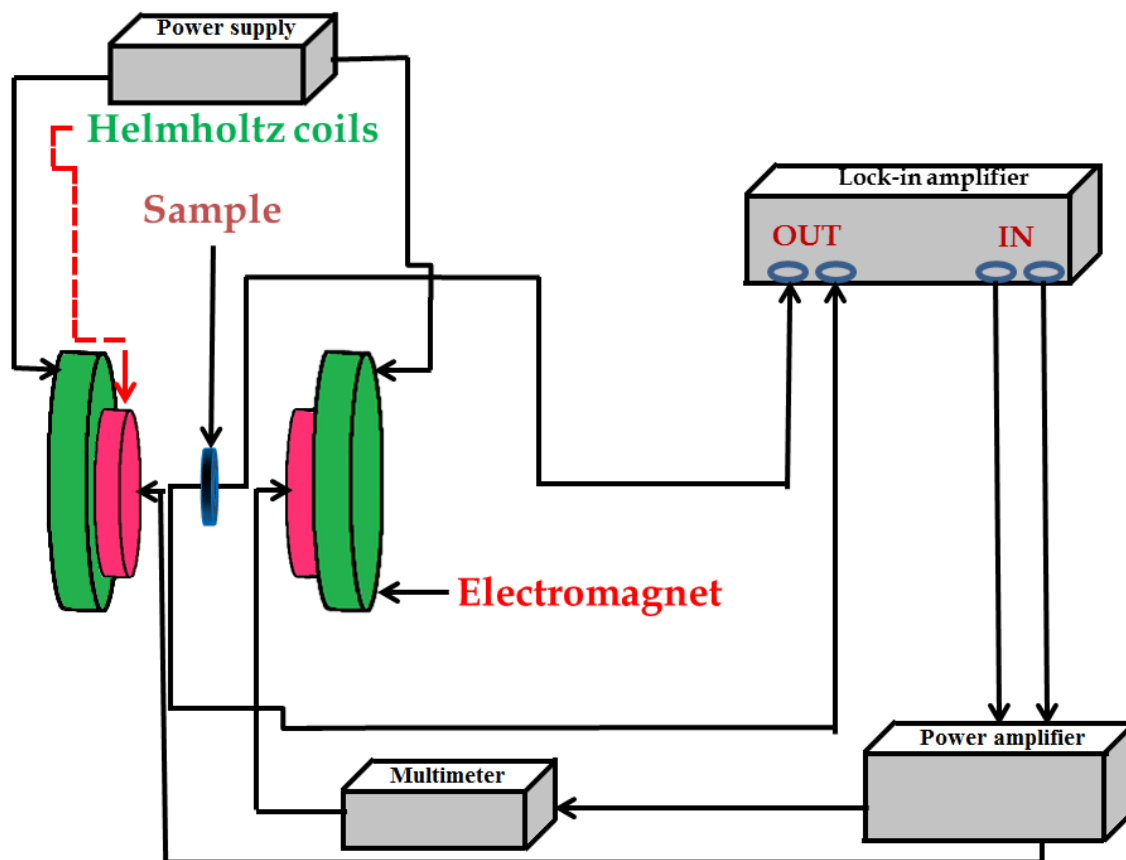
**Fig. 2.21:** Schematic diagram of magnetoelectric coefficient measurement set up.

## 2.7. Electrochemical Characterization Techniques

The electrochemical properties of the $Y_2NiMnO_6$ NWs and its bulk counterpart are investigated with cyclic voltammetry (CV) test by using a software controlled conventional three-electrode electrochemical cell (potentiostat Autolab-30) consisted of $Y_2NiMnO_6$ NWs over Ni foam as the working electrode, saturated Ag/AgCl as the reference electrode and a highly pure Pt wire as the counter electrode in a 0.5 M KOH electrolyte at room temperature.

### 2.7.1. Cyclic Voltammetry

Cyclic Voltammetry (CV) is an electrochemical technique which measures the current that develops in an electrochemical cell during the potential scans. To have a better agreement of the electrochemistry, oxidation and reduction are two main processes. Reduction occurs when a material gains electrons or in other words that material

becomes more negative. On the other, oxidation happens when a material loses electrons and gets positive. Fig. 2.22 shows a cyclic voltammogram resulting from a single electron reduction and oxidation according to following reversible reaction:

$$M^+ + e^- \leftrightarrow M \tag{2.14}$$
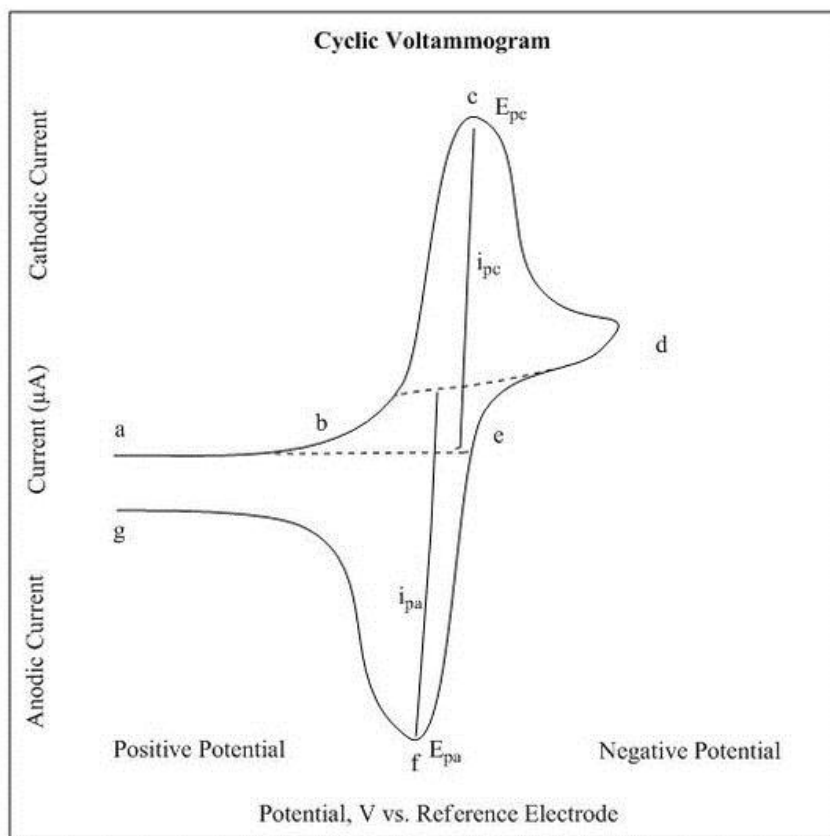


**Fig. 2.22:** Voltammogram of a Single electron oxidation-reduction [19].

In Fig. 2.22 the reduction process start from a to d, in which the potential is scanned negatively. In this region current is called cathode current ($i_{pc}$) and the corresponding peak potential is called cathodic peak potential ($E_{pc}$). After reaching d, the potential scans positively from d to g, in this region the corresponding current and peak potential is called anodic current ($i_{pa}$) and anodic peak potential ($E_{pa}$).

The specific capacitance ($C_{sp}$) is calculated from the current at the middle point of potential curve (*I*) and scan rate(*f*) using to the equation $C_{sp} = I/mf$ [20], where *m* is the active mass of the material. Usually the average specific capacitance is calculated from the CV curve according to following equation [21, 22],

$$C_{sp}\left(\frac{F}{g}\right) = \frac{Q}{2mV} = \frac{I}{2mVf}\int_{V_c}^{V_a} I\,(V)dV \tag{2.15}$$

where Q is the total charge obtained by the integration of positive and negative scans in a CV curve, *m* is the active mass of the material, *f* is the scan rate, $(V=V_a - V_c)$ represents the potential window.

## 2.7.2. Galvanostatic Charge-discharge

The specific capacitance ($C_{sp}$), energy density (*E*) and power density (*P*) are measured by using galvanostatic charging /discharging (GCD) experiments. The typical galvanostatic charge/discharge (GCD) curves are shown in Fig. 2.23. In this technique, the potential of a supercapacitor is linear, or almost linear with respect to the charge/discharge time (*dV/dt*= constant) during a constant current operation, so that the state-of-charge (SOC) can be exactly identified. The capacitances is calculated from the charging/discharging curves by using the following formula,

$$C_{sp} = \frac{I\Delta t_d}{m\Delta V} \tag{2.16}$$

where I is the discharge current, $\Delta t_d$ is the discharging time, $\Delta V$ is the potential window excluding IR drop region, and m is the active mass of the material. Furthermore, the energy and power densities of the electrodes are determined by the following formulae, respectively,

$$E = \frac{1}{2}\,C_{sp}\,(\Delta V)^2 \tag{2.17}$$

$$P = \frac{E}{\Delta t_d} \tag{2.18}$$

where E (Whkg$^{-1}$), P (kWkg$^{-1}$), $C_{sp}$ (Fg$^{-1}$), $\Delta V$ (V), and $\Delta t_d$ (s) are the energy density, power density, specific capacitance, potential window of discharge, and discharging time, respectively.
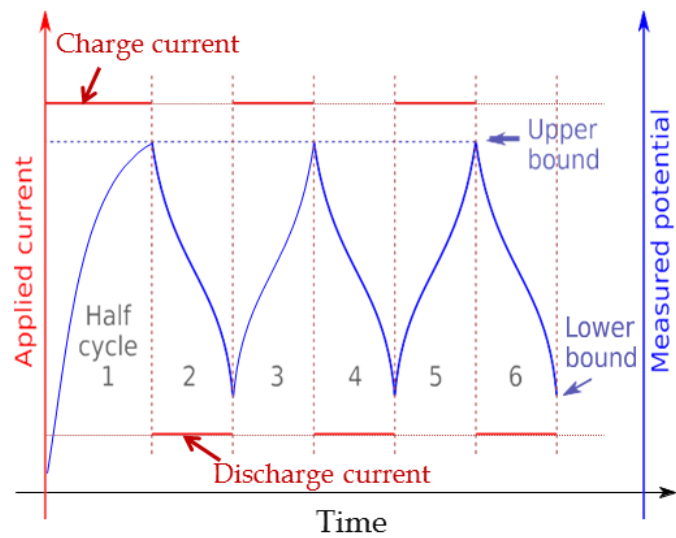
**Fig. 2.23:** Typical galvanostatic charge/discharge cycles [23].

## 2.8. Bibliography

[1]     R. I. Walton, *Chemical Society Reviews*  **31**, 230 (2002).

[2]     A. Chaudhuri, S. Mitra, M. Mandal, K. Mandal, *Journal of Alloys and Compounds* **491** 703 (2010).

[3]     A. Rabenau, *Angewandte Chemie International Edition in English*  **24**, 1026 (1985).

[4]     H. Bethe, *Ann. Physik* **3**, 133 (1929).

[5]     A. Chaudhuri, K. Mandal, *Materials Research Bulletin* **47**, 1057 (2012).

[6]     D. B. Chrisey and G. K. Hubler, *John Wiley & Sons*, 1994.

[7]     B. D. Cullity, S. R. Stock, *Elements of X-ray Diffraction, 3rd Edition, Prentice Hall* (2001).

[8]     J. F. Moulder, W. F. Stickle, P. E. Sobol and K. D. Bomben, *Physical Electronics Inc. Eden Prairie* (1995).

[9]     R. Erni, M. D. Rossell, C. Kisielowski, U. Dahmen, *Phys. Rev. Lett.* **102**, 096101 (2009).

[10]    T. R. Groves, H. C. Pfeiffer, T. H. Newman, and F. J. Hohn, *J. Vac. Sci. Technol. B* **6**, 2028 (1988).

[11]    C. R. Brundle, C. A. Jr. Evans, S. Wilson, *Butterworth-Heinemann publications*, (1992).

[12]    D. A. Bonnell, Scanning Probe Microscopy and Spectroscopy, 2nd edition, *Wiley-VCH* (2000).

[13]    L. Abelmann, S. Porthun, *J. Magn. Magn. Mater.* **190**, 135147 (1998).

[14]    A. G. Nanoscan AG, Quantum Leap in Hard Disk Technology.

[15]    B. D. Josephson, *Rev. Mod. Phys.* **46,** 251254 (1974).

[16]    Agilent 4294A Precision Impedance Analyzer, Operation Manual, Accessed in 2012.

[17]    J. Wu and J. Wang, *J. of App. Phys.* **105**, 124107 (2009).

[18]    Y. Xu, Ferroelectric Materials and Their Applications, North-Holland Elsevier Sci. Publ., Amsterdam 1991.

[19]   C. B. Sawyer and C. H. Tower, *Phys Rev.* **35**, 269 (1930).

[20]   M. Stewart & M. G. Cain, Ferroelectric Hysteresis Measurement & Analysis National Physical Laboratory, D. A. Hall, University of Manchester, May (1999).

[21]   P. T. Kissinger, W. R. Heineman, "Cyclic Voltammetry," *Journal of Chemical Education* **60**, 702 (1983).

[22]   P. Simon and Y. Gogotsi, *Nat. Mater.* **7**, 845 (2008).

[23]   A. Burke, *J. Power Sources,***91**, 37 (2000).

[24]   L. Piraux, S. Dubois, J. L. Duvail, K. Ounadjela and A. Fert, *J. Magn. Magn. Mater.*, **175**, 127 (1997).

[25]   T. Dobbelaere, P. M. Vereecken, C. Detavernier, *HardwareX* **2,** 34 (2017).

# Chapter 3

## Synthesis of CoFe$_2$O$_4$/ BiFeO$_3$ Bilayered Nano Hollow Spheres & Study Their Multiferroic Properties

In this chapter we have prepared CoFe$_2$O$_4$/BiFeO$_3$ bilayered nano hollow spheres through chemical co-precipitation route with different ionic ratios in order to study their magnetic, electric and magnetoelectric properties.

## 3.1. Background

Multiferroic materials are attractive because they have two ferroic properties and the interactions between the magnetic and electric polarization lead to additional functionalities. Because of their fundamental physical properties, multiferroic materials hold immense potential for multifunctional applications in data storage, random access memory, spintronics, filters, attenuators, sensors, and photovoltaic devices [1, 2, 3, 4, 5, 6]. The rare coexistence of ferromagnetic (FM) and ferroelectric (FE) ordering in a single-phase and their coupling interaction, known as magnetoelectric (ME) effect provides a wide opportunity for the mutual control and detection of magnetization and electrical polarization in these materials [7, 8]. However, having multiferroic materials with ferroelectricity and ferromagnetism in a single phase is difficult [7, 9]. The single phase magnetoelectric materials reported so far have either too weak coupling at room temperature or coupling occurs at very low temperature [3, 10, 11, 12]. Among the very limited members of the multiferroic family, rhombohedrally distorted perovskite $BiFeO_3$ (BFO) has become one of the most exciting functional materials because of its multiferroic properties at room temperature (RT), having a high ferroelectric Curie point ($T_C$ = 1103 K) and the G-type antiferromagnetic Neel temperature ($T_N$ = 647K) [4, 14]. However, many issues such as crystallinity, leakage property, and volatile nature of bismuth are needed to be addressed to improve the performance of $BiFeO_3$ for commercial use. To overcome the scarcity of the multiferroic materials, several strategies have been taken by the researcher to improve the multifunctionality of $BiFeO_3$ [15, 16, 17]. The composite type artificial multiferroic materials or thin films nanostructures have generated particular interest because of their stronger magnetoelectric response [19, 20, 21]. Despite this, the weak magnetic behavior of BFO limits its multifunctional applications [22]. To improve its magnetic properties, attempts have been made to develop composite nanostructures with spinel ferrites ($AB_2O_4$).

Spinel $CoFe_2O_4$ (CFO) is a well-known hard magnetic material, with moderate saturation magnetization and high coercivity as well as its chemical stability and

mechanical hardness [23]. However, for more stability CFO nano-hollow sphere (NHSs) is preferred to CFO nanoparticles [24], because NHSs have more coercivity compared to nanoparticles and have suitable value of saturation magnetization. A cracked NHS also has two active surfaces (inner and outer) for any interaction with other material. In our case, it plays a crucial role in magnetoelectric coupling. Recently, Soneet et al. reported an enhancement in the magnetic behavior of BFO by distributing CFO nanoparticles in its matrix [25]. Wan et al. developed a self-assembled composite thin film of CFO–PZT that exhibited good magnetic properties [26]. Bismuth ferrite ($BiFeO_3$), is considered as an attractive candidate for a composite partner in a magnetoelectric material, since it is ferroelectric and has a cycloidal spiral magnetic ordering [27].

Herein, we prepared ferromagnetic CFO nano-hollow spheres by solvothermal method with different diameter from 170-300 nm. Then we choose 250 nm diameter CFO NHSs and deposited a ferroelectric layer of BFO with different amount on the outer surface of CFO nano-hollow spheres by wet chemical method. Both CFO NHSs and CFO/BFO bilayered NHSs exhibit ferromagnetic behavior at room temperature. CFO/BFO bilayered NHSs also exhibit RT ferroelectric property. Since both the ferroic properties are present in the composite material, so we have measured the magnetoelectric coupling coefficient of CFO/BFO NHSs.

## 3.2. Experimental

The $CoFe_2O_4$ NHSs with different sizes (170, 200, 250 and 300 nm) are synthesized by template free solvothermal method (as described in *Chapter 2* in detail). Firstly metal ion salts, Iron (III) chloride hexahydrate (0.819 gm) and Cobalt (II) chloride hexahydrate (0.36 gm) and a base, urea (0.53 gm) are dissolved in a mixture of ethylene glycol (20 ml) and ethanol (10 ml) which are taken in a 2:1 ratio. Then the capping agent, oleylamine is added drop by drop to the solution. The resultant solution is stirred until a clear homogeneous solution is obtained and poured into a Teflon liner in a stainless steel autoclave. The autoclave is heated at 200 °C for 20 hours in an oven. Then the as-prepared $CoFe_2O_4$ NHSs are washed by ethanol and collected after centrifugation. The

removal of the mother solution is done by heating on a hot plate at a temperature of 80-90 °C for 30 min. Here we have prepared different size of CoFe$_2$O$_4$ NHSs by controlling the amount of capping agent and oleylamine. With an increase in capping agent amount the size of CoFe$_2$O$_4$ NHSs will decrease since capping agent prevents the growth of the nanocrystals. Here we have used 2.5, 2, 1, and 0.8 ml oleylamine for 170, 200, 250, and 300 nm CoFe$_2$O$_4$ NHSs respectively. The formation of CoFe$_2$O$_4$ NHSs is based on Ostwald ripening mechanism.

Basically at higher temperature urea transform into ammonia and it hydrolyse and produces hydroxyl groups. These hydroxyl groups interact with cobalt and iron ions and produce cobalt hydroxide and iron oxide hydroxide as a colloid. Then these two hydroxides interact with each other and produce cobalt ferrite. Now the formation of CoFe$_2$O$_4$ NHSs are followed a few steps. First of all $FeOOH$ and $Co(OH)_2$ nanocrystals are served as a nucleus and transformed into nano-leafs due to their monoclinic and rhombohedral crystal structure, respectively. Since the nano-leafs are extremely nano in size and thermodynamically unstable so they agglomerate with each other to form nanosphere and reduce their surface energy. This agglomeration is prevented by the oleylamine present in the solution mixture and act as a surface stabilizer due to repulsive force from its hydrophobic carbon chain. So the amount of oleylamine present in the solution determines the agglomeration of nano-leafs i.e. the size of the nanospheres. Now with the increase in time $FeOOH$ and $Co(OH)_2$ interact with each other and produce cobalt ferrite sphere with different shapes of small pores inside it. These pores are created inside the spheres because of the density of CoFe$_2$O$_4$ (5 gcm$^{-3}$) is higher than the FeOOH (3 gcm$^{-3}$) and Co(OH)$_2$ (3.59 gcm$^{-3}$). With an increase in time, these nanopores increase their size and merge with each other to produce a single large pore nano-hollow sphere. With further increase in time this outward migration resulted to form a cracked hollow sphere. The schematic illustration of the formation mechanism of CoFe$_2$O$_4$ nano-hollow spheres is shown in Fig. 3.1 and the possible chemical reactions are as follows:

$$CO(NH)_2 \rightarrow NH_3 + HCNO$$

$$NH_3 + H_2O \rightarrow NH_4^+ + OH^-$$

$$Co^{+2} + 2OH^- \rightarrow Co(OH)_2$$

$$Fe^{+3} + 3OH^- \leftrightarrow FeOOH + H_2O$$

$$Co(OH)_2 + 2FeOOH \rightarrow CoFe_2O_4 + 2H_2O + H^+$$
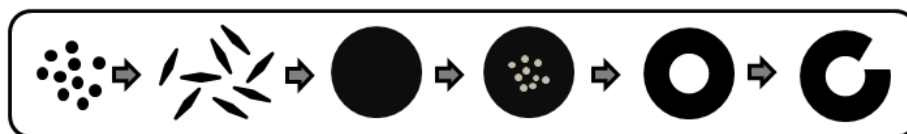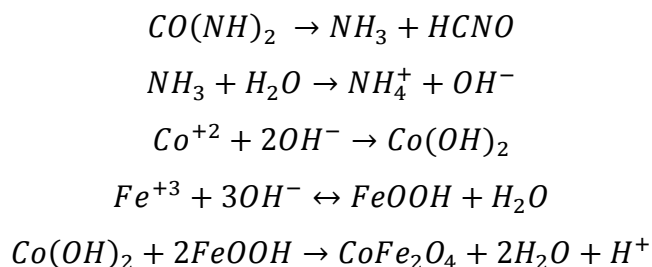


**Fig. 3.1:** The schematic illustration of the formation mechanism of $CoFe_2O_4$ nano-hollow sphere.

The $CoFe_2O_4/BiFeO_3$ bilayered NHSs are manufactured by a facile wet chemical method. In this process we have taken the 250 nm $CoFe_2O_4$ NHSs as a starting material and deposited a layer of $BiFeO_3$ with different amounts on the surface of it. The as prepared of $CoFe_2O_4$ NHSs are dipped into four different (0.05M, 0.1M, 0.2M and 0.3M) solution of bismuth(III) nitrate pentahydrate and iron(III) nitrate nonahydrate in 2-methoxyethanol at room temperature for 36 h. Afterward, the dip-coated sample is dried under IR lamp and annealed for 2 h in a tube furnace at 500 °C in air.

The crystal phases of the $CoFe_2O_4/BiFeO_3$ bilayered NHSs are studied by X- Ray Diffraction (XRD) using $CuK_\alpha$ line ($\lambda$ = 1.5418 Å). The morphology and crystal structure of the $CoFe_2O_4/BiFeO_3$ NHSs are investigated by Field Emission Scanning Electron Microscope (FESEM) operating at 5-10 kV. A FEG High-Resolution Transmission Electron Microscope (HRTEM) (80-200kV) is used to study the size, shape, morphology of NHS. The ferroelectric measurements are carried out using a high precession P-E system (Radiant Technologies). Magnetic properties are investigated at room temperature using a Vibrating Sample Magnetometer (VSM). A dynamic lock-in technique [28] is used to measure ME coupling coefficient. The experimental setup details are discussed in Chapter-2 (subsection 2.6.3) and the theory of measurement as disused in bellow.

When a multiferroic material is placed into a magnetic field of magnitude H, a voltage V developed across the sample surface. Assuming

$$V = f(H) = Constant + \alpha H + \beta H^2 + \gamma H^3 + \delta H^4 + \cdots \tag{3.1}$$

$$\Rightarrow \frac{dV}{dH} = \alpha + 2\beta H + 3\gamma H^2 + 4\delta H^3 + \cdots \tag{3.2}$$

When a small amount of AC magnetic field $h = h_0 sin\omega t$ is superimposed over the DC magnetic field H, then the total magnetic field: $H_{total} = H + h_0 sin\omega t$. So equation (3.1) becomes,

$$V = Constant + \alpha(H + h_0 sin\omega t) + \beta(H + h_0 sin\omega t)^2 + \gamma(H + h_0 sin\omega t)^3 + \delta(H + h_0 sin\omega t)^4 + \cdots$$

$$= \frac{1}{8}[(Constant + 4\beta h_0^2 + 3\delta h_0^4 + 8\alpha H + 12\gamma h_0^2 H + 8\beta H^2 + 24\delta h_0^2 H^2 + 8\gamma H^3 +$$

$$8\delta H^4) + (8\alpha h_0 + 6\gamma h_0^3 + 16\beta h_0 H + 24\delta h_0^3 H + 24\gamma h_0 H^2 + 32\delta h_0 H^3 sin\omega t) +$$

$$(-4\beta h_0^2 - 4\delta h_0^4 - 12\gamma h_0^2 H - 24\delta h_0^2 H^2)cos2\omega t + (-2\gamma h_0^3 - 8\delta h_0^3 H)sin3\omega t +$$

$$\delta h_0^4 cos4\omega t + \cdots]. \tag{3.3}$$

Now, the output voltage $V_{out}$ of the lock in amplifier is

$$V_{out} = \frac{1}{8}(8\alpha h_0 + 6\gamma h_0^3 + 16\beta h_0 H + 24\delta h_0^3 H + 24\gamma h_0 H^2 + 32\delta h_0 H^3)$$

$$= \frac{H^4}{8}\left[\frac{8\alpha}{H^3}\left(\frac{h_0}{H}\right) + \frac{6\gamma}{H}\left(\frac{h_0}{H}\right)^3 + \frac{16\beta}{H^2}\left(\frac{h_0}{H}\right) + 24\delta\left(\frac{h_0}{H}\right)^3 + \frac{24\gamma}{H}\left(\frac{h_0}{H}\right) + 32\delta\left(\frac{h_0}{H}\right)\right] \tag{3.4}$$

Now, neglecting the higher order terms in $\left(\frac{h_0}{H}\right)$ when $\left(\frac{h_0}{H}\right) \ll 1$

$$V_{out} = \frac{H^4}{8}\left(\frac{8\alpha}{H^3} + \frac{16\beta}{H^2} + \frac{24\gamma}{H} + 32\delta\right)\left(\frac{h_0}{H}\right)$$

$$= h_0(\alpha + 2\beta H + 3\gamma H^2 + 4\delta H^3)$$

$$= h_0\left(\frac{dV}{dH}\right), \tag{3.5}$$

So the magnetoelectric (ME) coefficient is

$$\alpha_{ME} = \frac{dE}{dH} = \frac{1}{d}\frac{dV}{dH} = \frac{V_{out}}{h_0 d} \tag{3.6}$$

where $d$ is the effective thickness of the sample.

## 3.3. Results and discussions

### *3.3.1. Morphology and structural analysis of CoFe₂O₄ nano-hollow spheres and CoFe₂O₄/BiFeO₃ bilayered nano-hollow spheres*

Fig. 3.2(a) shows all the XRD pattern of as-prepared $CoFe_2O_4$ NHSs confirming face-centre cubic inverse spinel structure of $CoFe_2O_4$ (JCPDS card no. 22-1086) [29]. From energy dispersive X-ray spectroscopic analysis (inset of Fig. 3.2(b)), it is confirmed that the absence of elemental composition of the capping agent, oleylamine, 2-methoxyethanol may disturb the other properties, and conducted to study their chemical composition clearly confirms only the presence of Co, Fe, and O in the hollow spheres. Figs. 3.2(b)-(e) show the FESEM images of all the nano-hollow spheres having a uniform distribution. Figs. 3.2 (f)-(i) reveal that the nano-hollow spheres having nearly homogeneous size distribution with an average size of 170, 200, 250 and 300 nm respectively.

Here we have taken 250 nm $CoFe_2O_4$ hollow spheres for further treatment because it has suitable value of coercivity as well as saturation magnetization compared to other NHSs and also it can retain the features of the nano-domain. Fig. 3.3(a) shows the TEM image of a single 250 nm $CoFe_2O_4$ nano-hollow sphere. The intensive contrast between the black margin and the bright centre of Fig. 3.3(a) confirms the synthesis of nano-hollow structure. To know the elemental distribution over the hollow sphere, energy-dispersive X-ray spectrometry (EDS) line scanning is performed across the hollow sphere diameter specified by an orange line in Fig. 3.3(b). Figs. 3.3(c-e) show EDS line scanning profile of Co, Fe, and O respectively. Where the Co, Fe, and O profile shows the higher intensity at the outer edge of the spectrum profile due to the formation of $CoFe_2O_4$ hollow sphere. Which confirm the successful synthesis of CFO NHSs. The HRTEM micrograph of the $CoFe_2O_4$ NHS, as shown in Fig. 3.3(g), clearly resolves their atomic lattice fringes. The lattice spacing between the (311) crystalline planes is found to be 0.24 nm. The selective area electron diffraction (SAED) pattern is

taken from the area covered under the HRTEM study also clarifies the single-crystalline nature of the NHSs as shown in Fig. 3.3(f).
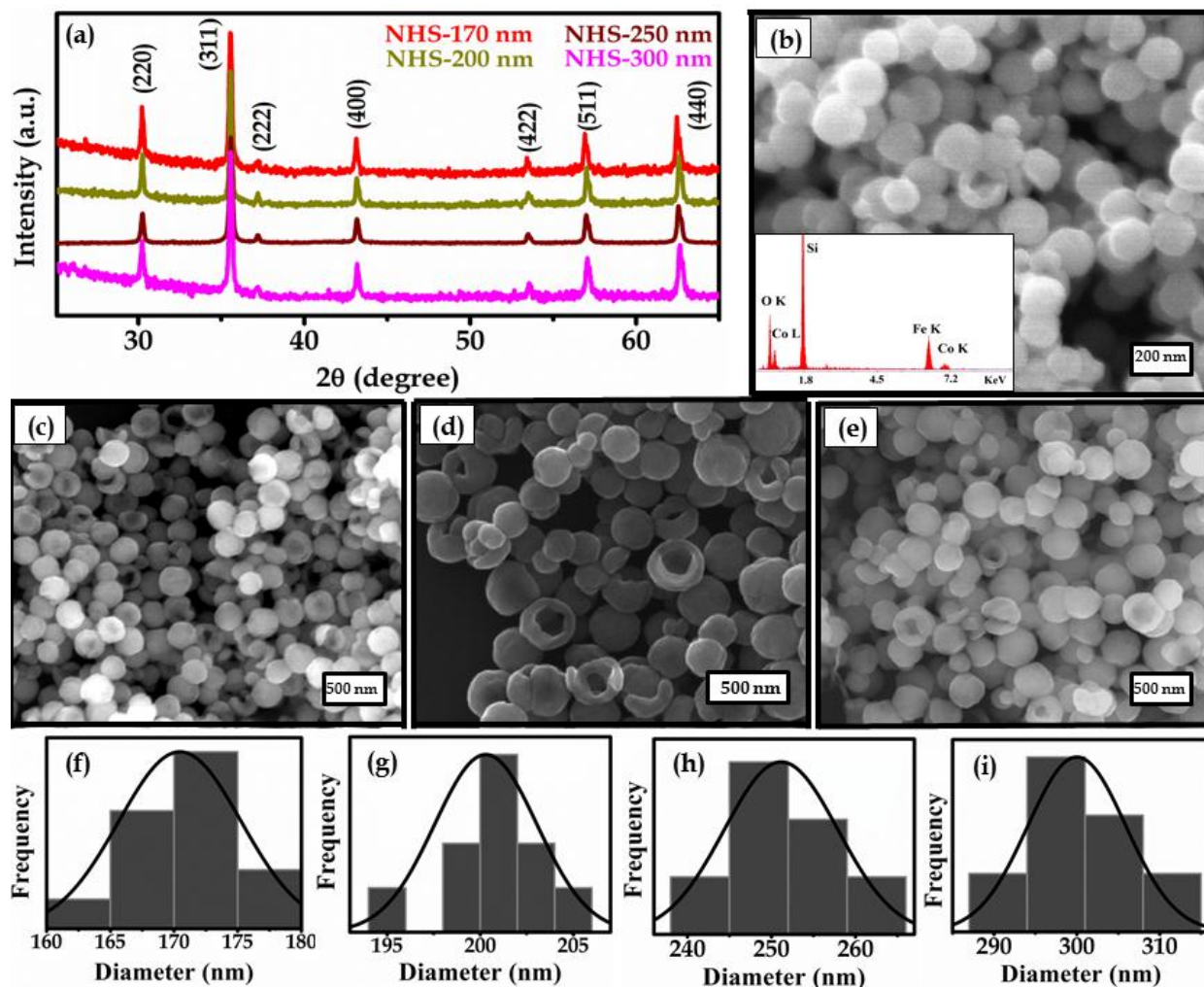


**Fig. 3.2:** (a) XRD pattern of all $CoFe_2O_4$ NHSs. SEM images of $CoFe_2O_4$ NHSs-(b) 170, (c) 200, (d) 250 and (e) 300 nm. Inset of (b) shows the EDX spectroscopic analysis. Size distribution of the $CoFe_2O_4$ nano-hollow spheres (f) 170, (g) 200, (h) 250, and (i) 300 nm.
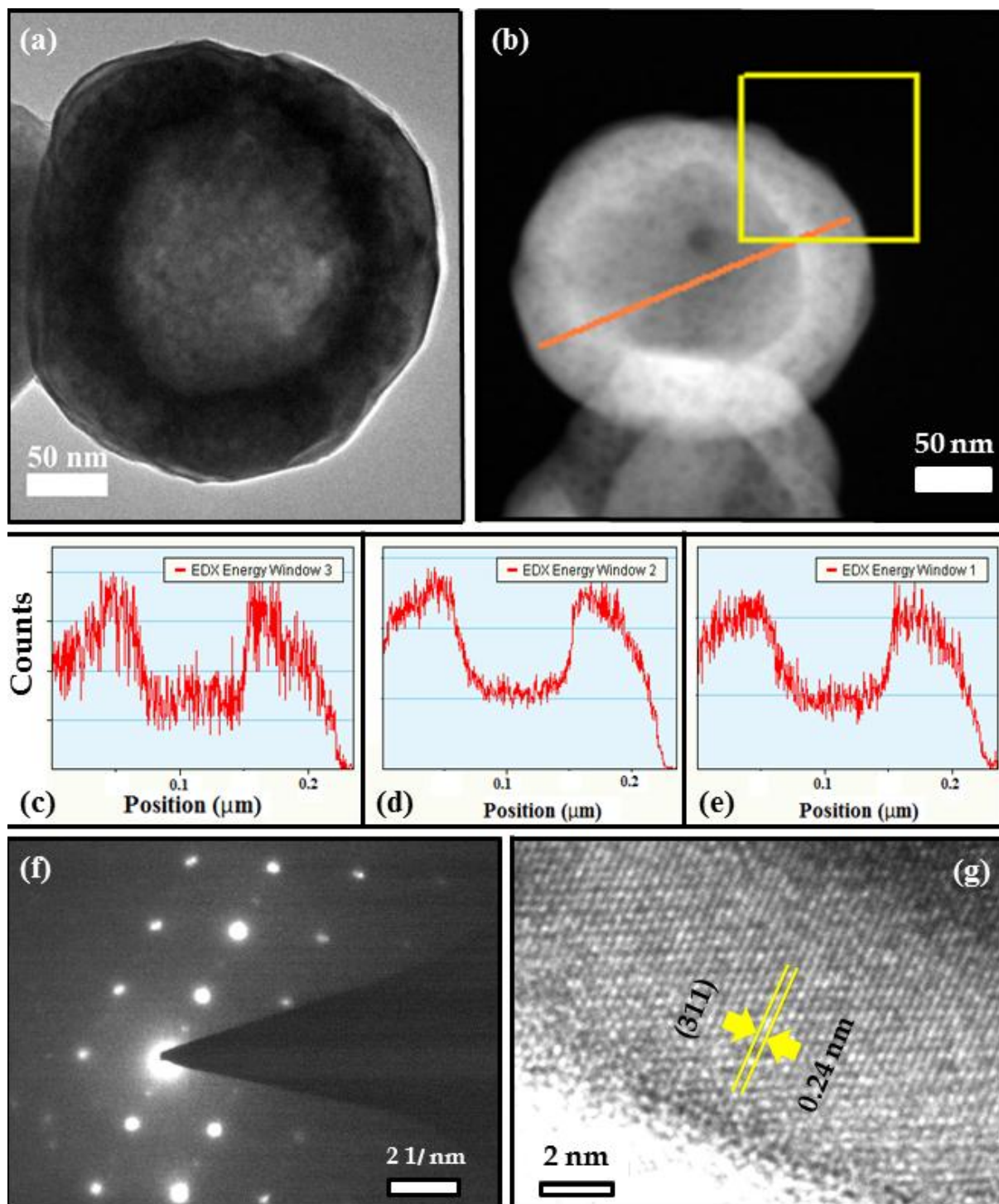
**Fig. 3.3:** (a) TEM image of CoFe₂O₄ NHSs. (b) STEM image of individual CoFe₂O₄ NHSs and (c-e) EDS line scanning of Co, Fe, and O respectively, across the CoFe₂O₄ NHSs indicated in (b). (f) SAED pattern and (g) HRTEM image of CoFe₂O₄ NHSs.

The XRD pattern of $CoFe_2O_4$ /$BiFeO_3$ bilayered NHSs is shown in Fig. 3.4 which corresponds well with the JCPDS Card no. 03-0864 and 22-1086, respectively [30, 31]. This suggests that the bilayered NHSs are largely consisted of two separate crystalline structures, spinel, and perovskite, without traces of any other impurity phase. The strong and broadened peaks around the $2\theta$ angles of $35.7^0$, $57.2^0$, and $62.9^0$, together with weak and broadened peaks around the $2\theta$ angles of $30.3^0$, $43.4^0$, and $54.3^0$ indicate the spinel cobalt ferrites with cubic structure. The peaks around the $2\theta$ angles of $22.4^0$, $31.8^0$, $32^0$, $39.5^0$, $45.8^0$, and $51.6^0$ suggest the perovskite bismuth ferrite with rhombohedral structure.
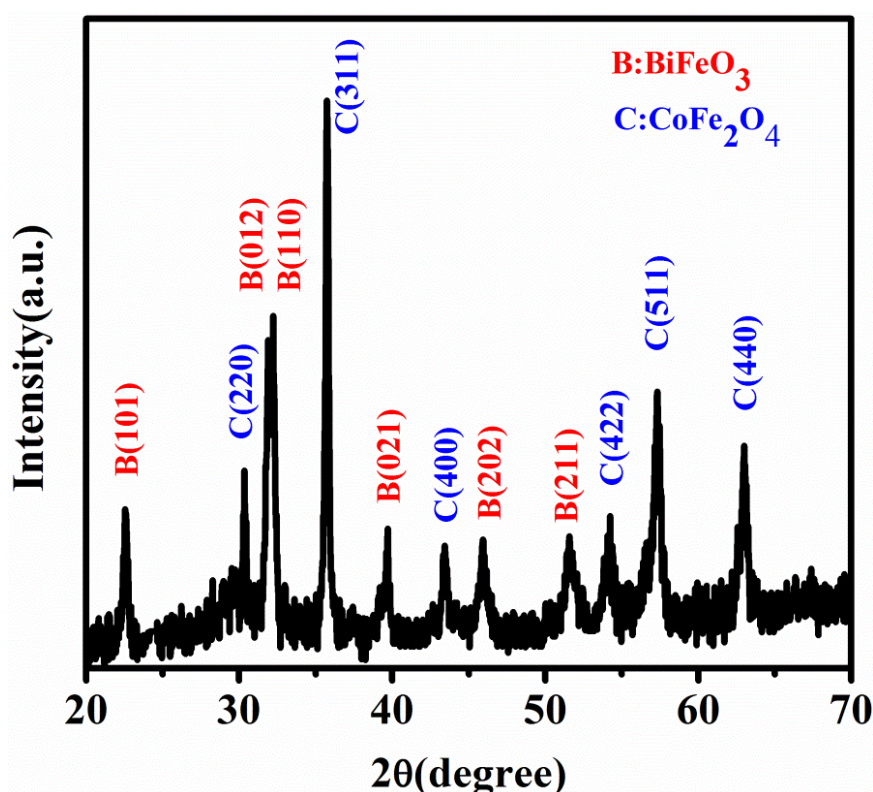


**Fig. 3.4:** XRD pattern of $CoFe_2O_4$ /$BiFeO_3$ bilayered NHSs.
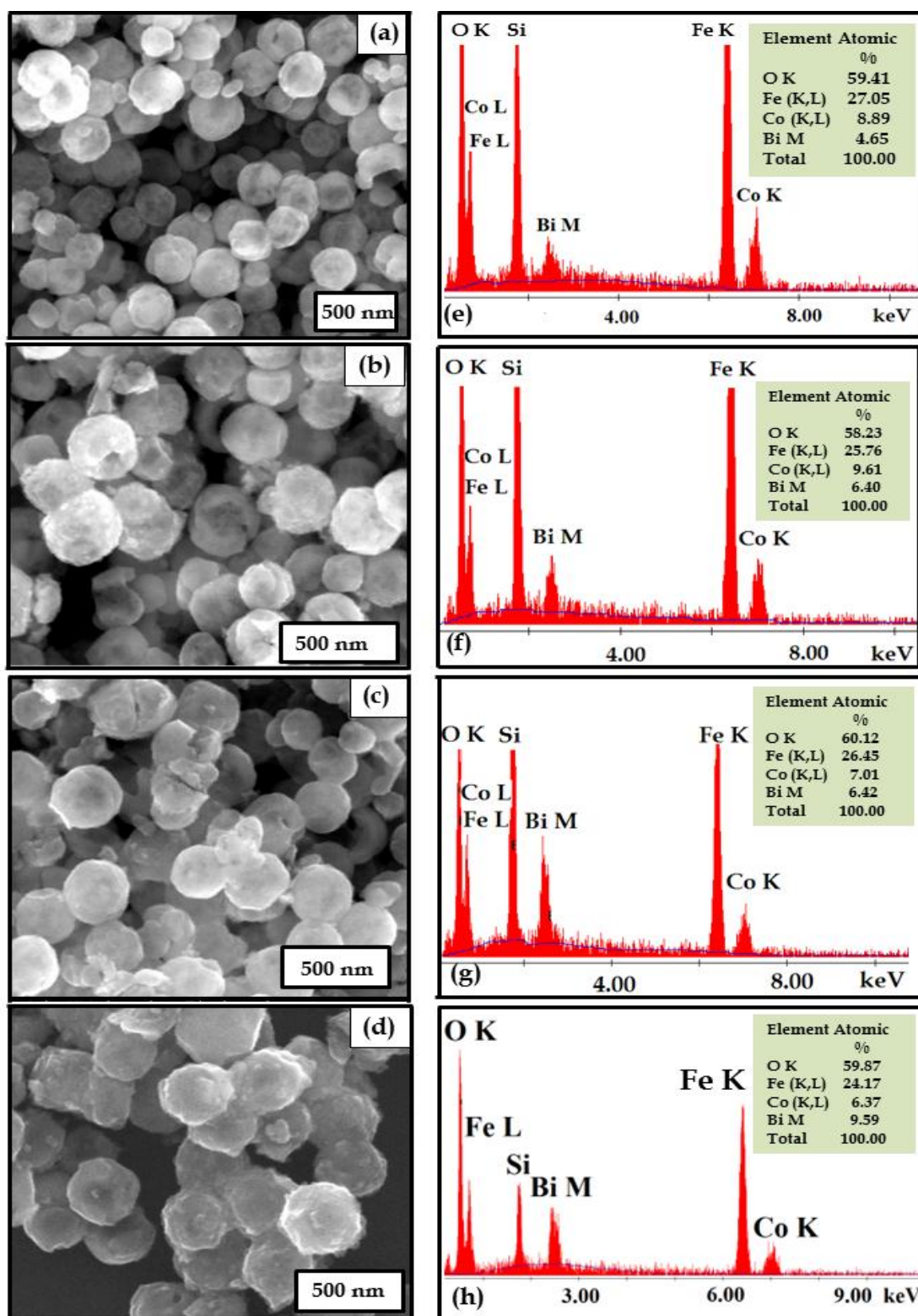
**Fig. 3.5:** SEM image of (a) 35BFO-65CFO, (b) 40BFO-60CFO, (c) 50BFO-50CFO, and (d) 60BFO-40CFO of $CoFe_2O_4/BiFeO_3$ bilayered NHSs. EDX spectroscopic analysis of (e) 35BFO-65CFO, (f) 40BFO-60CFO, (g) 50BFO-50CFO, and (h) 60BFO-40CFO of $CoFe_2O_4/BiFeO_3$ bilayered NHSs. Inset of (e, f, g, h) show the corresponding atomic ratio of their elements.

Structural analysis of CFO/BFO bilayered NHSs is carried out by using FESEM. Figs. 3.5(a, b, c, d) show the FESEM images of all the CFO /BFO composite samples. Here from Figs. 3.5(a, b, c, d) it is clear that the $BiFeO_3$ is deposited on the surface of $CoFe_2O_4$ NHSs and defined as 35BFO-65CFO (~270 nm), 40BFO-60CFO (~275 nm), 50BFO-50CFO (~280 nm), 60BFO-40CFO (~285 nm), respectively. Figs. 3.5(e, f, g, h) respectively show their EDAX spectra, which provides us to determine the qualitative and quantitative analysis of the distribution of all the elements are present in the composite samples. From EDAX spectra it is clear that all the elements originating from two components, BFO and CFO, are present in the bilayered composite samples. Here we have also observed Bi, Fe, Co, and O elements with their expected stoichiometry composition. Inset of Figs. 3.5(e, f, g, h) show their atomic ratio of all the elements present in the $CoFe_2O_4$ /$BiFeO_3$ bilayered composite samples. The single-particle TEM images of all the composite nano-hollow spheres are shown in Figs. 3.6(a, b, c, d). The HRTEM micrograph of the 60BFO-40CFO NHSs, as shown in Fig. 3.6(e), demonstrates the polycrystalline nature of the NHSs with dissimilar orientation of the different crystallographic planes having different lattice spacing. The calculated lattice spacing is found to be 0.24 nm which corresponds the (311) crystalline plane of $CoFe_2O_4$ and the 0.279 nm lattice spacing corresponds the (110) crystalline plane of $BiFeO_3$. The selective area electron diffraction (SAED) pattern taken from the area covered under the HRTEM study also clarifies the polycrystalline nature of the $CoFe_2O_4$ /$BiFeO_3$ NHSs (Fig. 3.6(f)). To know the elemental distribution over the $CoFe_2O_4$ /$BiFeO_3$ NHSs, energy-dispersive X-ray spectrometry (EDS) line scanning is performed over the hollow sphere diameter specified by orange lines in Figs. 3.7(a, f, k, p). Figs. 3.7(b-e, g-j, l-o, q-t) show EDS line scanning profile of Bi, Fe, Co, and O respectively, also confirm the synthesis of all $CoFe_2O_4$ /$BiFeO_3$ composite NHSs.
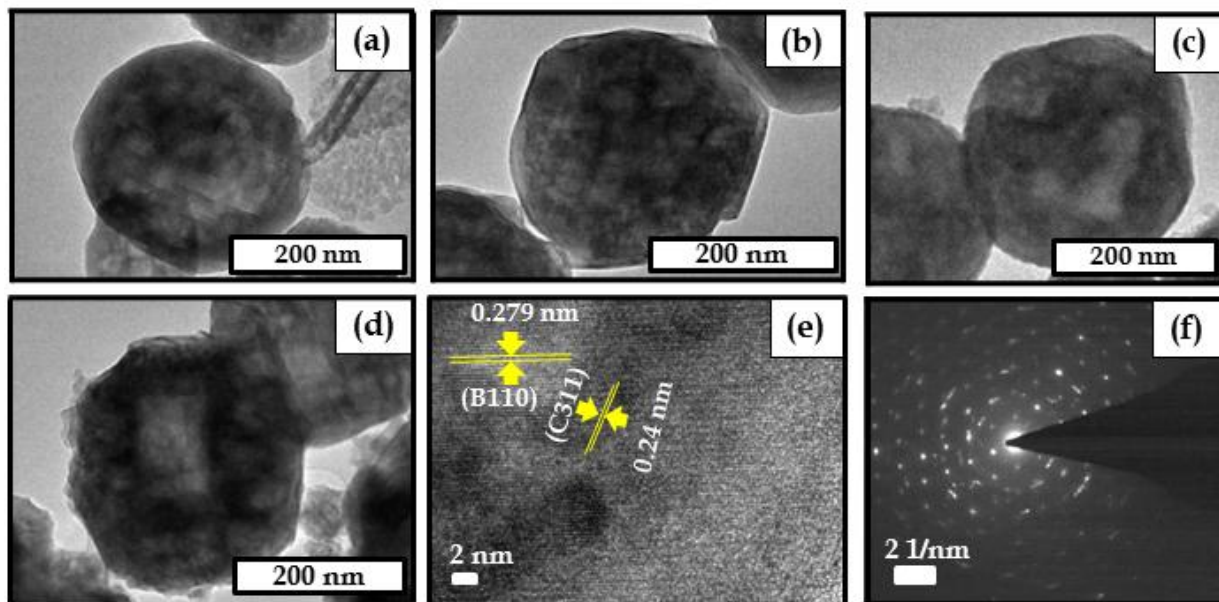
**Fig. 3.6:** Single particle TEM image of (a) 35BFO-65CFO, (b) 40BFO-60CFO, (c) 50BFO-50CFO, (d) 60BFO-40CFO $CoFe_2O_4/BiFeO_3$ bilayered NHS. (e) HRTEM image and (f) SAED pattern of 60BFO-40CFO $CoFe_2O_4/BiFeO_3$ bilayered NHS.
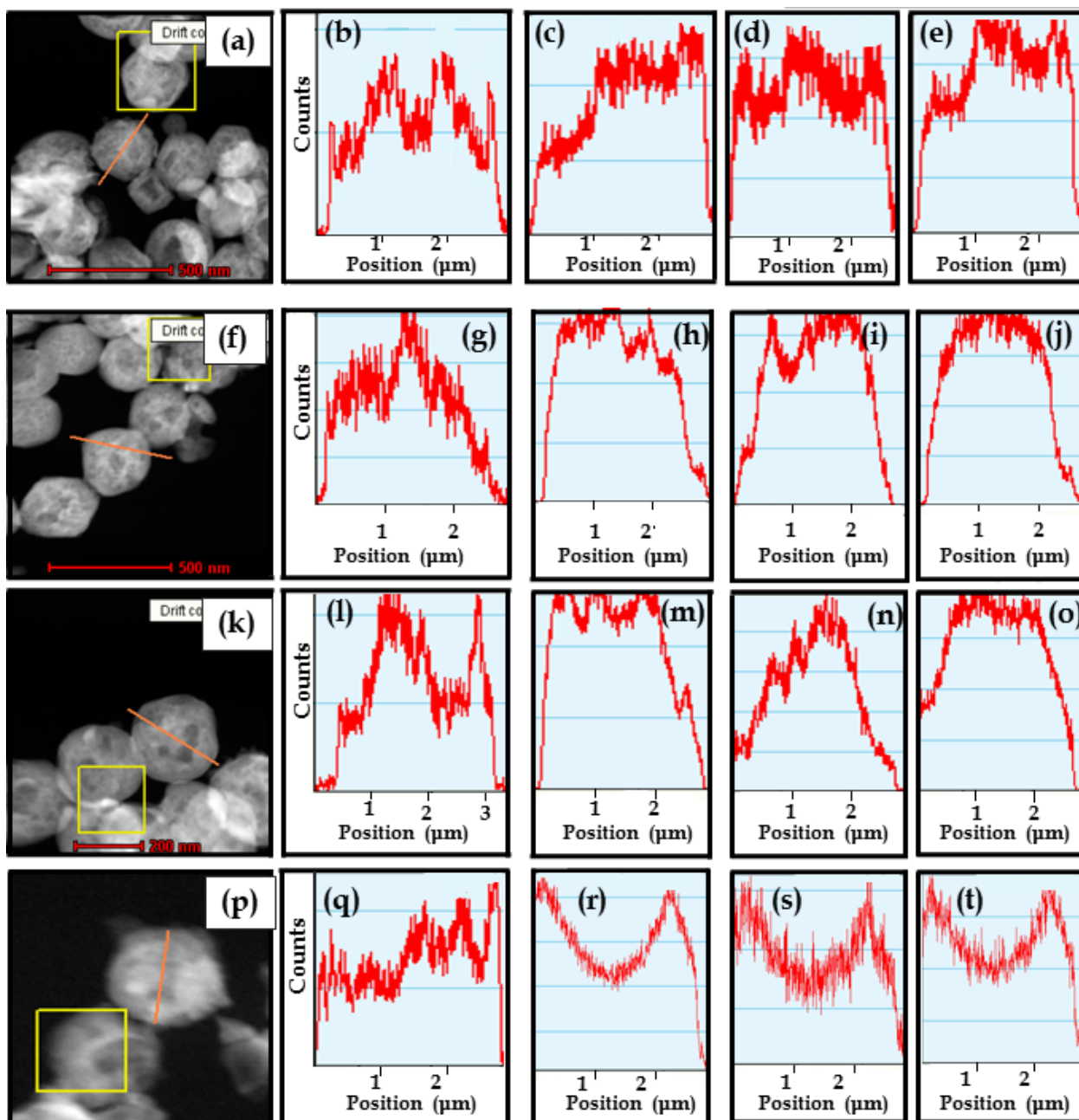
**Fig. 3.7:** (a) STEM image of individual 35BFO-65CFO bilayered NHS and (b-e) EDS line scanning of Bi, Fe, Co and O respectively. (f) STEM image of individual 40BFO-60CFO bilayered NHS and (g-j) EDS line scanning of Bi, Fe, Co and O respectively. (k) STEM image of individual 50BFO-50CFO bilayered NHS and (l-o) EDS line scanning of Bi, Fe, Co and O respectively. (p) STEM image of individual 60BFO-40CFO bilayered NHS and (q-t) EDS line scanning of Bi, Fe, Co and O respectively.

### 3.3.2. *Magnetic properties of CoFe₂O₄ nano-hollow spheres and CoFe₂O₄/ BiFeO₃ bilayered nano-hollow spheres*

Magnetic hysteresis loops of all $CoFe_2O_4$ NHSs at room temperature are shown in Fig. 3.8(a). All the *M-H* hysteresis loops indicate the presence of ferromagnetic ordering in the samples. The change in coercivity ($H_C$) and saturation magnetization ($M_S$) w.r.t. the diameter of all CFO NHSs is shown in Fig. 3.8(b) as well as in Table-3.1. The saturation magnetization increases with the diameter of the CFO NHSs but the coercivity decreases. Furthermore, with an increase in NHSs diameter from 170-300 nm the saturation magnetization increases from 44.47-64.65 emu/g, but the coercivity decreases from 713-524 Oe. Basically, increasing size of the NHS, the surface to volume ratio decreases and consequently decreases the surface spin disorder. As a result, the magnetocrystalline and surface anisotropy decreases. Inset of Fig. 3.8(c) shows RT (~300 K) magnetization curve indicate typically antiferromagnetic ordering of BFO. Magnetic properties of spinel-perovskite $CoFe_2O_4/BiFeO_3$ nano-composites are observed by using a VSM at RT with an applied magnetic field of -8 kOe ≤ H ≤ 8 kOe. Fig. 3.8(c) shows the room temperature magnetic hysteresis loop of all $CoFe_2O_4/BiFeO_3$ bilayered NHSs. All the $CoFe_2O_4/BiFeO_3$ NHSs composite samples are showed a wonderful ferromagnetic in nature, indicating the presence of magnetic order in composite nanostructures. Here the saturation magnetization of composite samples decreases compared to $CoFe_2O_4$ NHSs [24] because of the weight factor of low magnetic moment $BiFeO_3$ component. Here it is clear that with an increase in BFO component from 35BFO-65CFO to 60BFO-40CFO, the saturation magnetization decreases from 48.53 – 30.10 emu/g but coercivity increases from 970 - 1320 Oe. The values of saturation magnetization ($M_S$), and coercivity ($H_C$) of CFO NHSs having diameter 250 nm are ~ 59.52 emu/g, and 594 Oe, respectively, whereas those of CFO/BFO NHSs (285 nm) are ~30.1 emu/g, and 1320 Oe, respectively. The value of saturation magnetization and coercivity of all the composite samples are shown in Fig. 3.8(d) and listed in Table-3.2. The value of saturation magnetization and coercivity is comparable with the other reported articles [32, 33, 34]. Here the coercivity increases primarily arises because of

magnetoelastic coupling between two composite nanostructures. The coercivity ($H_C$) of CFO/BFO bilayered NHSs is found to be higher than that of CFO NHSs due to the presence of foreign atoms on the surface of CFO NHSs which develop steric hindrance on the movement of magnetization. In the CFO/BFO bilayered NHSs, applied magnetic field is used to change the magnetization of CFO and the ferroelectric polarization of BFO through its inherent magnetoelectric coupling as well as through the BFO/CFO magneto-elastic coupling [35, 36]. This may also be a reason for higher coercivity in CFO/BFO bilayered NHSs.
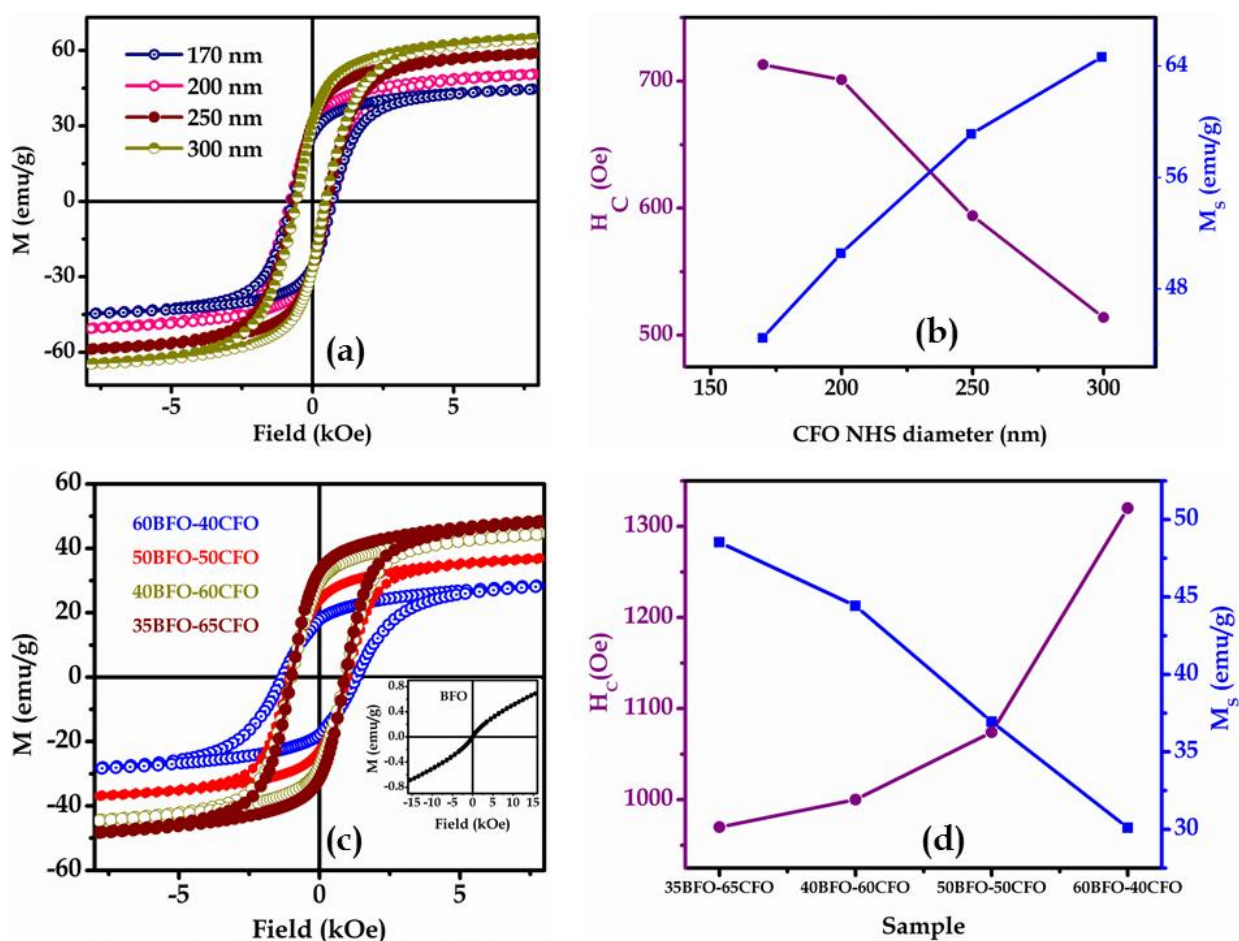


**Fig. 3.8:** (a) Variation of the room temperature M-H hysteresis loops, and (b) $H_C$ and $M_S$ values of all $CoFe_2O_4$ NHSs. (c) M-H hysteresis loops (inset shows M-H curve of $BiFeO_3$), and (d) $H_C$ and $M_S$ values of different composite of $CoFe_2O_4/BiFeO_3$ bilayered NHSs.

**Table 3.1:** List of $H_C$ and $M_S$ of all as-synthesized $CoFe_2O_4$ NHSs at room temperature.

| Sample | $H_C$ (Oe) | $M_S$ (emu/g) |
|---|---|---|
| $CoFe_2O_4$ NHSs -170 | 713 | 44.47 |
| $CoFe_2O_4$ NHSs -200 | 701 | 50.54 |
| $CoFe_2O_4$ NHSs -250 | 594 | 59.52 |
| $CoFe_2O_4$ NHSs -300 | 514 | 64.65 |

**Table 3.2:** List of $H_C$, $M_r$ and $M_S$ of all synthesized bilayered $CoFe_2O_4/BiFeO_3$ bilayered NHSs at room temperature.

| Sample | $H_C$ (Oe) | $M_r$ (emu/g) | $M_S$ (emu/g) |
|---|---|---|---|
| 35BFO-65CFO | 970 | 32.20 | 48.53 |
| 40BFO-60CFO | 1000 | 28.35 | 44.42 |
| 50BFO-50CFO | 1074 | 23.40 | 36.94 |
| 60BFO-40CFO | 1320 | 17.90 | 30.10 |

### 3.3.3. *Ferroelectric properties of CoFe₂O₄/BiFeO₃ bilayered nano-hollow spheres*

Fig. 3.9(a) shows the room temperature (RT) *P-E* hysteresis loops at a frequency 50 Hz of the BFO/CFO bilayered NHSs as a function of their ratios, and their BFO bulk counterpart. Inset of Fig. 3.9(b) shows the schematic of the experimental probe used for the ferroelectric hysteresis loop measurements where the silver paste acts as electrodes. Clear evidence of ferroelectric polarization is found due to the $BiFeO_3$ nanostructures. The variation of remnant polarization and saturation polarization with different BFO/CFO composition at a constant applied external electric field is shown in Fig. 3.9(b) and Table-3.3. With increase in BFO component from 35BFO-65CFO to 60BFO-40CFO the maximum polarization and remnant polarization increases from ~1.1 - 2.1 µC/cm², and 0.83 – 1 µC/cm², respectively. The main instability that drives the formation of the ferroelectric polarization is the ordering of Bi lone pairs or two valance electrons. These two electrons are capable to contribute in chemical bonding applying sp² hybridized state but they do not contribute in such bond. These two Bi electrons break the inversion symmetry and create charge

separation along the direction of the rhombohedral distortion (the [111] direction) below ~1100 K [36, 37, 38]. Here 60BFO-40CFO NHSs showed more stable ferroelectric behavior compare to other composite NHSs. For the 35BFO-65CFO and 40BFO-60CFO bilayered NHSs the ferroelectric behavior are slightly weak compared to other bilayered NHSs because of the high leakage current as shown in Fig. 3.10. The remnant polarization increases in the composite sample compared to pure BFO because of the coupling between BFO and CFO component present in the bilayered composite sample [4, 39, 40, 41].
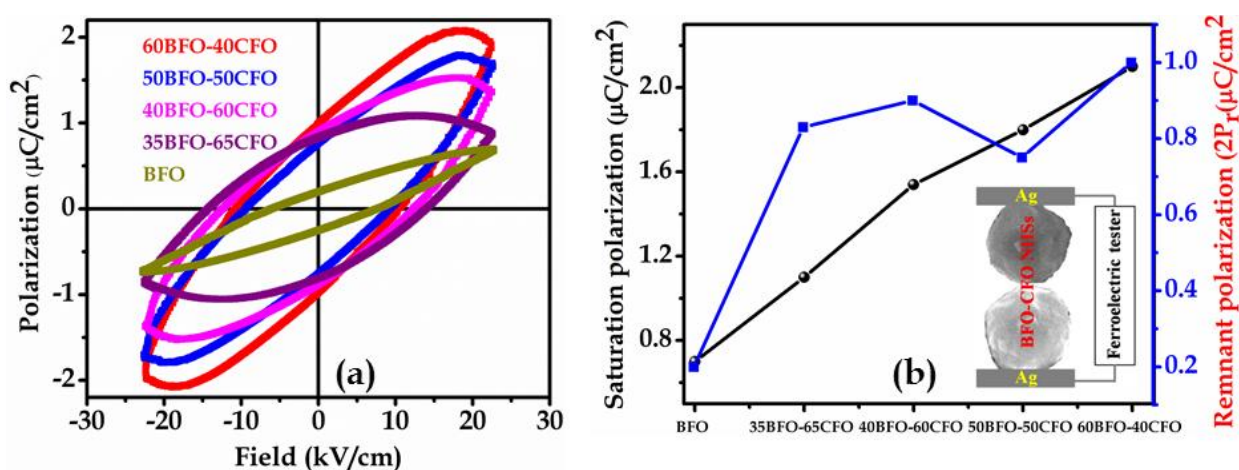


**Fig. 3.9:** Room temperature P-E hysteresis loops of all $CoFe_2O_4/BiFeO_3$ bilayered NHSs. (b) Saturation and remnant polarization of all BFO/CFO bilayered NHSs. Inset of (b) schematic of the experimental setup used for the P-E loop measurements.

**Table-3.3:** Comparison of maximum polarization, remnant polarization and coercive field of the $CoFe_2O_4/BiFeO_3$ NHSs.

| Sample | Maximum polarization ($\mu C/cm^2$) | Remnant Polarization ($2P_r$) ($\mu C/cm^2$) | Coercive field ($2E_c$) ($kV/cm^2$) |
|---|---|---|---|
| BFO | 0.7 | 0.2 | 6.8 |
| 35BFO-65CFO | 1.1 | 0.83 | 14.17 |
| 40BFO-60CFO | 1.54 | 0.90 | 12.3 |
| 50BFO-50CFO | 1.8 | 0.75 | 9.3 |
| 60BFO-40CFO | 2.1 | 1.00 | 10.5 |

Fig. 3.10 shows the leakage current behavior of the BFO/CFO bilayered NHSs as a function of their ratios. Here the leakage current increases with increasing CFO component because of its low electrical resistance property. The effect of this high leakage current also observed in the ferroelectric behavior, as shown in Fig. 3.9(a).
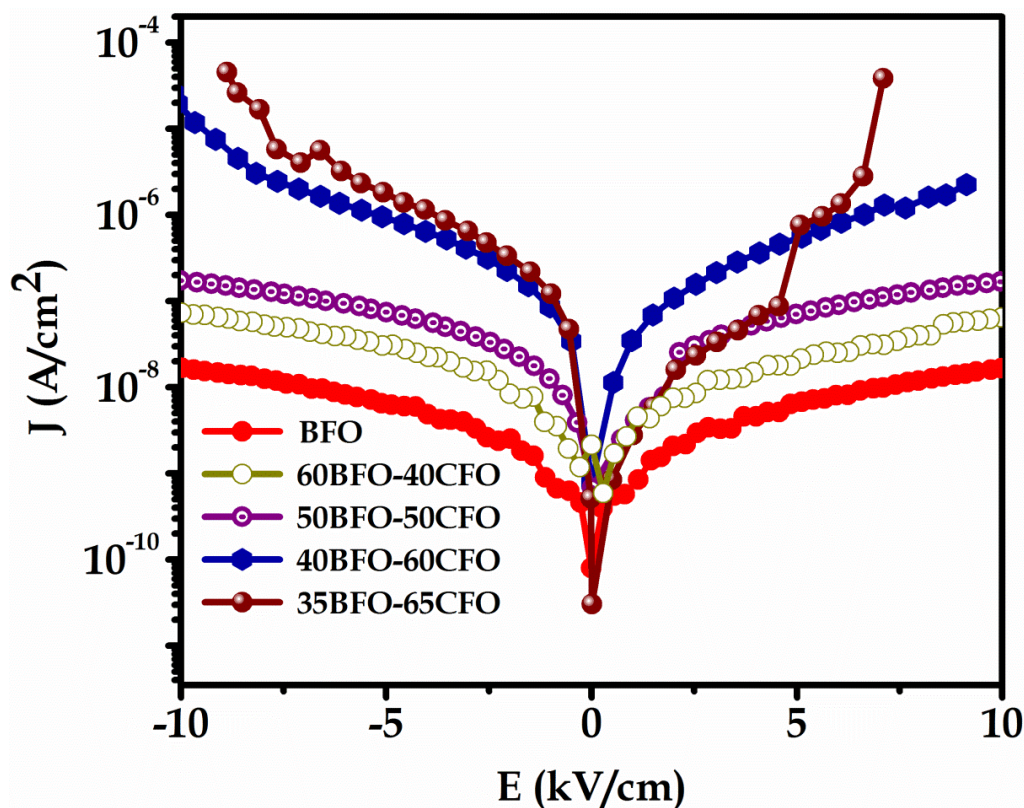


**Fig. 3.10:** Leakage current density of BFO and BFO/CFO bilayered NHSs as a function of applied electric field.

### 3.3.4. Magnetoelectric properties of CoFe₂O₄/BiFeO₃ bilayered nano-hollow spheres

The coexistence of the ferroelectric BiFeO$_3$ and ferromagnetic CoFe$_2$O$_4$ phases in the present composite gives rise to a ME effect. The magnetoelectric effect is characterized by the magnetoelectric voltage coefficient $\alpha_{ME} = \frac{dE}{dH}$. Fig. 3.11(a-d) show the variation of $\alpha_{ME}$ as a function of applied DC magnetic field, $H_{Bias}$ with an ac magnetic field of amplitude ~5 Oe and frequency 1 kHz, at room temperature of bilayered nano-composite materials. Inset of Fig. 3.11(a) also show the variation of $\alpha_{ME}$ for pure BFO.

The magnetoelectric coupling of different composite materials along with pure BFO is listed in Table-3.4. It is found that with an increase in BFO component in the nano-composite the magnetoelectric coupling coefficient increases. The maximum coupling coefficient is found in 60BFO-40CFO bilayered nano-composite. At $H_{Bias}$= 0, it exhibits an initial $\alpha_{ME}$ values of 8.5 mV/cm Oe. $\alpha_{ME}$ does not change significantly with $H_{Bias}$. $\alpha_{ME}$ also does not depend on the sweep rate of the DC bias field.

In presence of a small ac magnetic field, with increasing $H_{bias}$ from zero, the mobility of the magnetic domain wall in the $CoFe_2O_4$ is enhanced and magnetically favored domains grow. At $H_{bias}$~1.0 kOe, the motion of domains is the easiest which causes maximum magnetostriction in $CoFe_2O_4$ which in turn develops maximum ME coupling in the magnetostrictive ($CoFe_2O_4$)–ferroelectric ($BiFeO_3$) composite through stress-mediated magnetic–mechanical–electric transformation at the interface [26, 42].

**Table-3.4:** Comparison of magnetoelectric coefficient of the $CoFe_2O_4$ /$BiFeO_3$ NHSs.

| Sample | Magnetoelectric coefficient (mV/Oe cm) |
|---|---|
| BFO | 0.55 |
| 35BFO-65CFO | 3.35 |
| 40BFO-60CFO | 6.42 |
| 50BFO-50CFO | 7.47 |
| 60BFO-40CFO | 8.60 |
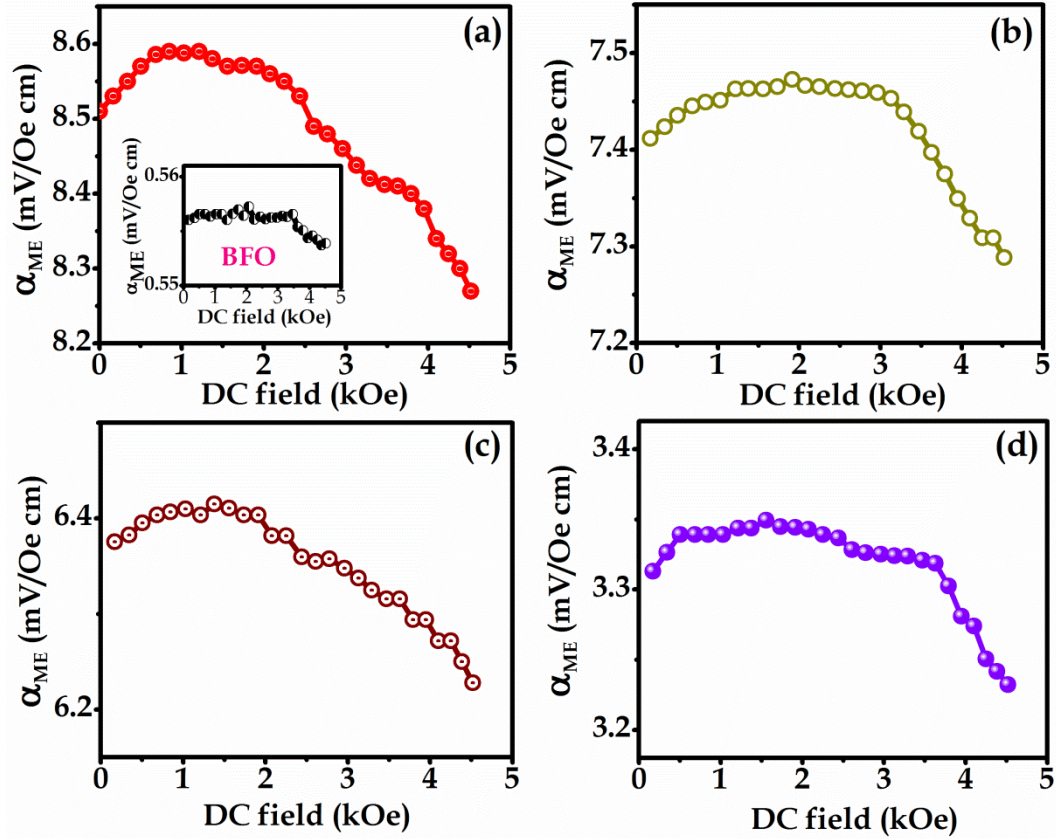
**Fig. 3.11:** DC bias magnetic field dependence of magnetoelectric coefficients ($\alpha_{ME}$) of (a) 60BFO-40CFO, (b) 50BFO-50CFO, (c) 40BFO-60CFO, and (d) 35BFO-65CFO for $CoFe_2O_4/BiFeO_3$ NHSs in ac magnetic field (5 Oe) of frequency $f$ = 1 kHz. Inset of (a) magnetoelectric coefficients for pure BFO.

## 3.4. Conclusions

In summary, we have successfully synthesized spinel phase of pure $CoFe_2O_4$ nano-hollow spheres using solvothermal method and spinel/perovskite of CFO/BFO bilayered nano-hollow spheres by a facile wet chemical method. The concentrations of BFO in the composite on the magnetic and electric properties of the bilayered system have been studied in details. The saturation magnetization, coercivity, saturation polarization and leakage current values have been changed with BFO concentration. The remnant polarization increases in the composite sample compared to pure BFO because of the coupling between BFO and CFO component present in the bilayered composite sample. The studies of electric and magnetic properties indicate excellent multiferroic behavior of CFO/BFO NHSs. The coexistence of the ferroelectric $BiFeO_3$ and ferromagnetic $CoFe_2O_4$ phases in the nano-composites give rise to a significant ME effect. The maximum magnetoelectric coefficient estimated to be ~ $\alpha_{ME}$ = 8.6 mV/cm Oe at a frequency of 1.0 kHz. These results might be useful to further understanding and designing new multiferroic nano-composites.

## 3.5. Bibliography

[1]     M. Fiebig, T. Lottermoser, D. Frohlich, A. V. Goltsev, and R. V. Pisarev, *Nature.* **419**, 818 (2002).

[2]     C. A. F. Vaz, J. Hoffman, C. H. Ahn, and R. Ramesh, *Adv. Mater.* **22**, 2900 (2010).

[3]     N. Hur, S. Park, P. A. Sharma, J. S. Ahn, S. Guha, and S. W. Cheong, *Nature.* **429**, 392 (2004).

[4]     J. Wang, J. B. Neaton, H. Zheng, V. Nagarajan, S. B. Ogale, B. Liu, D. Viehland, V. Vaithyanathan, D. G. Schlom, U. V. Waghmare, N. A. Spaldin, K. M. Rabe, M. Wuttig, and R. Ramesh, *Science* **299**, 1719 (2003).

[5]     T. Kimura, T. Goto, H. Shinatani, K. Ishizaka, T. Arima, and Y. Tokura, *Nature* **426**, 55 (2003).

[6]     M. Alam, K. Karmakar, M. Pal, and K. Mandal, *RSC Advances* **6**, 114722 (2016).

[7]     R. Ramesh and N. A. Spaldin, *Nature Mater.* **6**, 21 (2007).

[8]     M. Fiebig, *J. Phys. D: Appl. Phys.* **38**, 123 (2005).

[9]     N. A. Spaldin and M. Fiebig, *Science* **309**, 391 (2005).

[10]    R. Tackett, G. Lawes, B. C. Melot, M. Grossman, E. S. Toberer, and R. Seshadri, *Phys. Rev. B.* **76**, 024409 (2007).

[11]    Y. Yamasaki, S. Miyasaka, Y. Kaneko, J.-P. He, T. Arima, and Y. Tokura, *Phys. Rev. Lett.* **96**, 207204 (2006).

[12]    M. Alam, K. Mandal and G. G. Khan, *RSC Advances* **6**, 62545, (2016).

[13]    C. W. Beier, M. A. Cuevas, and R. L. Brutchey, *Small.* **4**, 2102 (2008).

[14]    Z. X. Cheng and X. L. Wang, *Phys. Rev. B* **75**, 172406 (2007).

[15]    Y. P. Wang, L. Zhou, M. F. Zhang, X. Y. Chen, J.-M. Liu, and Z. G. Liu, *Appl. Phys. Lett.* **84**, 1731 (2004).

[16]    K. Yin, M. Li, Y. Liu, C. He, F. Zhuge, B. Chen, W. Lu, X. Pan, and R.- W. Li, *Appl. Phys. Lett.* **97**, 042101 (2010).

[17]    H. Yang, Y. Q. Wang, H. Wang, and Q. X. Jia, *Appl. Phys. Lett.* **96**, 012909 (2010).

[18]    C. Wang, K. J. Jin, Z. T. Xu, L. Wang, C. Ge, H. B. Lu, H. Z. Guo, M. He, and G. Z. Yang, *Appl. Phys. Lett.* **98**, 192901 (2011).

[19]     J. Ma, J. Hu, Z. Li, C. Wen Nan, *Adv. Mater.* **23**, 1062 (2011).

[20]     Y. J. Chen, Y. H. Hsieh, S. C. Liao, Z. Hu, M. J. Huang, W. C. Kuo, Y. Y. Chin, T. M. Uen, J. Y. Juang, C. H. Lai, H. J. Lin, C. T. Chen, Y. H. Chu, *Nanoscale* **5**, 4449 (2013).

[21]     Y. H. Hsieh, H. H. Kuo, S. C. Liao, H. J. Liu, Y. J. Chen, H. J. Lin, C. T. Chen, C. H. Lai, Q. Zhan, Y. L. Chueh, Y. H. Chu, *Nanoscale* **5**, 6219 (2013).

[22]     H. Naganuma, Y. Inoue, S. Okamura, *IEEE Trans. Ultrason. Ferroelectr. Freq. Control.* **55**, 1046 (2008).

[23]     T. Kodama, Y. Kitayama, M. Tsuji, Y. Tamaura, *J. Appl. Phys.* **71**, 5926 (1992).

[24]     R. Rakshit, K. Serita, M. Tonouchi, and K. Mandal, *Journal of Applied Physics* **120**, 203901 (2016).

[25]     K. Sone, S. Sekiguchi, H. Naganuma, T. Miyazaki, T. Nakajima, *J. Appl. Phys.* **111**, 124101 (2012).

[26]     J. G. Wan, X. W. Wang, Y. J. Wu, M. Zeng, Y. Wang, H. Jiang, W. Q. Zhou, G. H. Wang, J. M. Liu, *Appl. Phys. Lett.* **86**, 122501 (2005).

[27]     I. Sosnowska, W. Schaffer, W. Kockelmann, K. H. Anderson, I. O. Troyanchuk, *Appl. Phys. A* **74**, 1040 (2002).

[28]     G. S. Lotey, N. K. Verma, *Chemical Physics Letters*. **579,** 78 (2013).

[29]     P. Vlazana, M. Stoia, *Ceramics International*. 44, 530 (2018).

[30]     S. Dabas, P. Chaudhary, M. Kumar, S. Shankar, O. P. Thakur, *Journal of Materials Science: Materials in Electronics.* **30**, 2837 (2019).

[31]     R. Das, K. Mandal, *Journal of Magnetism and Magnetic Materials*. **324**, 1913 (2012).

[32]     G. Allaedini, S. M. Tasirin, P. Aminayi, *Int. Nano Lett.* **5**, 183 (2015).

[33]     K. Maaz, A. Mumtaz, S. K. Hasanain, A. Ceylan, *J. Magn. Magn Mater.* **308**, 289 (2007).

[34]     K. S. Rao, G. S. V. R. K. Choudary, K.H. Rao, C. Sujatha, Procedia Mater. Sci. **10**, 19 (2015).

[35]     H. Zheng, J. Wang, S. E. Lofland, Z. Ma, L. M. Ardabili, T. Zhao, L. S. Riba, S. R. Shinde, S. B. Ogale, F. Bai, D. Viehland, Y. Jia, D. G. Schlom, M. Wuttig, A. Roytburd, R. Ramesh, *Science* **303**, 661 (2004).

[36]    J. R. Teague, R. Gerson, and W. J. James, *Solid State Commun.* **8**, 1073 (1970).

[37]    R. Seshadri and N. A. Hill, *Chem. Mater.* **13**, 2892 (2001).

[38]    D. Khomskii, *J. Magn. Magn. Mater.* **306**, 1 (2006).

[39]    J. G. Wu, J. L. Zhu, D. Q. Xiao, and J. G. Zhu, *Appl. Phys. Lett.* **91**, 212905 (2007)

[40]    J. G. Wu, D. Q. Xiao, J. G. Zhu, J. L. Zhu, J. Z. Tan, and Q. L. Zhang, *Appl. Phys. Lett.* **90**, 082902 (2007).

[41]    H. W. Jang, S. H. Baek, D. Ortiz, C. M. Folkman, R. R. Das, Y. H. Chu, P. Shafer, J. X. Zhang, S. Choudhury, V. Vaithyanathan, Y. B. Chen, D. A. Felker, M. D. Biegalski, M. S. Rzchowski, X. Q. Pan, D. G. Schlom, L. Q. Chen, R. Ramesh, and C. B. Eom, *Phys. Rev. Lett.* **101**, 107602 (2008).

[42]    G. Srinivasan, E. T. Rasmussen, J. Gallegos, R. Srinivasan, Y. I. Bokhan, V. M. Laletin, *Phys. Rev. B* **64**, 214408 (2001).

# Chapter 4

## Multiferroic and Fluorescence Properties of ErFeO$_3$ Nanoparticles

In this chapter we have demonstrated the synthesis of ErFeO$_3$ nanoparticles through microwave method and studied their magnetic, electric, dielectric and fluorescence properties.

## 4.1. Background

Current-induced magnetization (M) reversal is one of the key techniques in spintronics which were explored widely for metallic or semiconducting materials [1, 2, 3, 4, 5, 6, 7]. In insulating multiferroics, magnetization can be controlled by an electric field (E) without any major current flow and it would be more interesting and highly desirable because the current flow in metal or semiconductor materials essentially accompanies higher energy dissipation. Multiferroics are promising candidates for such an action by fully utilizing their magnetoelectric (ME) coupling properties.

Orthoferrites have been studied for decades, because of their centrosymmetric Pnma/Pbnm structure there is no report of ferroelectricity. However, recent reports suggest not only low-temperature ferroelectricity in Gd(Dy)FeO$_3$ but also room-temperature ferroelectricity in SmFeO$_3$ [8, 9, 10]. Antiferromagnetically (AFM) aligned magnetic moments of Fe$^{3+}$ in RFeO$_3$ follow a magnetic transition to a canted antiferromagnetic state at a temperature ranging from 620 K to 750 K. Because of high Neel temperature (>600 K) and large magnetic moment in the Fe$^{3+}$ side, RFeO$_3$ compounds show a very good multiferroic behavior at room temperature (RT) [9, 10, 11, 12]. The same-origin of polarization and magnetism is desirable to achieve large ME coupling [13]. It is reported that the spiral magnets like orthorhombic RMnO$_3$ (R-Dy, Tb, etc.) [11, 12], MnWO$_4$ [13], CoCr$_2$O$_4$ [14] shows a large ME coupling. However, these materials show polarization (P) below spiral spin transition and the value of P is very small (~ 10$^{-2}$ μC/cm$^2$). In DyFeO$_3$, because of its gigantic ME coupling, a small magnetic field could induce a large polarization. At room temperature, induced polarization of ~ 93 μC/m$^2$ is observed along the a-axis in SmFeO$_3$ due to magnetic-ordering. Hexagonal ErFeO$_3$ thin film also shows polarization at RT [15].

In general transition metal oxide materials such as Fe$_3$O$_4$ [16], MnFe$_2$O$_4$ [17], Mn$_3$O$_4$ [18], and MFe$_2$O$_4$ [19], etc, demonstrate excellent photocatalytic property and fluorescence imaging. Multiferroic materials play a crucial role in digital electronics, such as spintronics devices, sensors, magnetic data storage devices, transducers,

actuators, energy storage devices, memory, and logic devices etc [20, 21, 22, 23, 24, 25]. The remarkable photocatalytic and fluorescence properties of Er, Fe based oxides have driven our interest to study their optical property. In recent years, the multifunctional material development, we are surprised by the recent findings about multiferroics, such as $BiFeO_3$ nanoparticles [26], $BiFeO_3$ microspheres, microcubes, submicrocubes [27], $BiFeO_3$ nanowires [28], cation-doped $BiFeO_3$ materials [29], Ca, Mn Co-doped $BiFeO_3$ Nanofibres [30], $Bi_7Fe_3Ti_3O_{21}$ Material [31], nanoparticulate $ErFeO_3$ [32], nanosized $Ni^{+2}$ doped $ErFeO_3$ [33] as potential candidates for photocatalysis. $BiFeO_3$ nanoparticles [26] take more than 8 hours to degrade 100% of methyl orange. In case of $BiFeO_3$ microspheres, the degradation of congo red is negligible; $BiFeO_3$ microcubes degrade congo red 15% after 3h, whereas it is 40% for $BiFeO_3$ submicrocubes [27]. Ca, Mn, Co-doped $BiFeO_3$ Nanofibres [30] degrade congo red about 60% in 2h in presence of visible light. Nanoparticulate $ErFeO_3$ [32] degrade methyl orange 100% within 180 minutes while nanosized $Ni^{+2}$ doped $ErFeO_3$ [33] takes about 150 minutes to degrade 100% methyl orange. But there are no reported multiferroic materials which show photocatalytic property along with fluorescence behaviour.

In the present work, we prepared $ErFeO_3$ (EFO) nanoparticles (NPs) (~200 nm) by cost-effective and much less time-consuming microwave method anticipating that size reduction may improve magnetization due to incomplete antiferromagnetic arrangement and studied their multiferroic properties and magnetoelectric coefficient ($\alpha_{ME}$). We did not attempt to prepare $ErFeO_3$ NPs below 100 nm as in that case, thermal energy could play a significant role in disturbing magnetic and ferroelectric polarization. From our study, $ErFeO_3$ NPs showed ferroelectricity as well as antiferromagnetism at RT. Antiferro to canted antiferromagnetic transition appeared at 620 K and after 923 K, $ErFeO_3$ is completely transformed to paramagnetic state. Due to the presence of ferroelectric and magnetic property, $ErFeO_3$ NPs also show a significant value of magnetoelectric coefficient at room temperature. Detailed investigation on the dielectric properties of $ErFeO_3$ NPs is also performed over a temperature range of 30-300 $^0$C and in the frequency range of $10^{-1} – 10^6$ Hz.

We have also reported the development of ErFeO$_3$ NPs as a multifunctional nanoprobe having intrinsic multicolor photoluminescence and excellent photocatalytic activity, simultaneously. To study the effect of ligand on the properties of ErFeO$_3$, we solubilized the as-prepared ErFeO$_3$ NPs into water by functionalization with disodium tartrate ligand. For further surface modification approach, we have observed the emergence of multicolour fluorescence (starting from blue, cyan, green to red) from the water-soluble tartrate-functionalized ErFeO$_3$ NPs and tried to investigate the mechanical origin of different fluorescence properties by using different spectroscopic techniques. It has been found that the origin of multicolor fluorescence is due to the ligand-to-metal charge-transfer (LMCT) transition from the highest occupied molecular orbital (HOMO) of tartrate ligand to the lowest unoccupied molecular orbital (LUMO) of Fe$^{3+}$ or Er$^{3+}$ metal ions in the NPs and f-f transitions (Er$^{3+}$). Also, ErFeO$_3$ NPs exhibit excellent photocatalytic property in the degradation of methylene blue (MB) which is commonly used organic dye in textile industries and a model water-contaminant.

## 4.2. Experimental

Erbium nitrate [Er(NO$_3$)$_3$, 5H$_2$O], Iron nitrate [Fe(NO$_3$)$_3$, 9H$_2$O] and Sodium hydroxide [NaOH] are the chemical reagents used in the present work. All the reagents are of analytical grade (99.99%) purchased from Sigma Aldrich and used in the preparation without further purification. Crystalline perovskite ErFeO$_3$ nanoparticles are prepared by successive microwave processing and further high-temperature calcination. In a typical process, [Er(NO$_3$)$_3$, 5H$_2$O] and [Fe(NO$_3$)$_3$, 9H$_2$O] are respectively dissolved in double distilled water according to their stoichiometric ratios at room temperature. A 5M solution of NaOH is added drop by drop to the above solution until the pH of the solution reaches 12. Due to the addition of NaOH, Er(OH)$_3$, and Fe(OH)$_3$ are precipitated and it is stirred for another 30 min. Then the reaction solution is placed into a microwave oven and processed for 3 min until the combustion is completed under 800 W power. It is then cooled naturally to room temperature. The product thus obtained is washed successively by double distilled water followed by acetone, ethanol and dried

at 60 $^0$C for 12 h. The resultant product is heated for 1 h at 1000 $^0$C to get single-phase ErFeO$_3$ NPs.

For fluorescence, the as-prepared ErFeO$_3$ NPs are cyclomixed with 0.5M Na-tartrate solution for 12 h at room temperature. The resultant yellow-radish colored solution containing tartrate modified ErFeO$_3$ NPs is called as fl. Modified T-ErFeO$_3$. The larger size of functionalized nano particles are filtered out with a syringe filter of 0.22 μm diameter. To get a free anionic form of all tartrate ligands for better fluorescence property, T-ErFeO3 NPs further modified by heat treatment at ~ 70 °C for 15 h after maintaining the pH ~ 12 of the solution through drop wise addition of NaOH solution.

The phase and structure of the samples are investigated by X-ray diffraction (XRD) using CuK$_α$ radiation (Panalytical, X'part Pro, λ = 1.5418 Å). Field Emission Scanning Electron Microscope (FESEM) (FEI QUANTA FEG-250) and High-Resolution Transmission Electron Microscope (HRTEM) are used to study the morphology and particle size of ErFeO$_3$ NPs. Elemental analysis is performed from energy dispersive X-ray (EDX) spectrum. Superconducting Quantum Interference Device (SQUID) is used for magnetic measurements while ferroelectric measurements (inherent electric polarization) are carried out using a high precession P-E measurement system (Radiant Technologies). For the measurement of electrical properties, pellets with a diameter of 5 mm and thickness of 0.5 mm are prepared with both sides pasted with silver paste to connect electric wires. An LCR meter (NF Corporation) is used to measure dielectric properties of ErFeO$_3$ NPs over the frequency range $10^{-1}$-$10^6$ Hz. Magnetoelectric coupling is studied using a home-made set-up as discussed earlier (Chapter-2 (subsection 2.6.3)) [34] with dynamic lock-in technique.

In order to measure the UV−vis absorption of ErFeO$_3$ NPs and the degradation of MB with spectroscopic precision, the spectra are recorded with a Shimadzu model UV−2600 spectrophotometer using a quartz cuvette of 1 cm path length. The characteristic fluorescence excitation and emission spectra are recorded on a Jobin Yvon Model Fluoromax−3 fluorometer. UV-vis absorption spectra are measured on a UV-vis

spectrometer (we used an 8 W UV lamp as the UV light source and a 100 W incandescent bulb, its optical spectra exactly mimic sunlight having a continuum throughout the visible region, as the visible light source, from Philips). The initial concentration of MB is 0.1 mmol with a catalyst ($ErFeO_3$ NPs) loading of 6 mmol $L^{-1}$ are homogeneously mixed for 1 h in a quartz cuvette in the dark, maintaining the pH of the solution at ~3. Then the cuvette is placed ~2 cm apart from the light source and the absorbance of MB in the reaction mixture is measured time to time by the UV−vis spectrophotometer and the absorption peak at 663 nm is monitored to obtain the photocatalytic degradation efficiency. We added the same amount of MB to the solution after every cycle without further addition of catalyst for the recyclability test.

A JASCO Fourier transformed infrared (FTIR)−6300 spectrometer is used to confirm the attachment of tartrate ligand with $ErFeO_3$ NPs. For FTIR measurement, a powdered sample is mixed with KBr powder and pelletized. The background correction is made by using a reference of KBr pellet.

## 4.3. Results and discussions

### 4.3.1. *Morphology and structural analysis of ErFeO₃ nanoparticles*

The peaks in the XRD pattern of $ErFeO_3$ NPs, shown in Fig. 4.1(a), can be indexed as orthorhombic space group Pbnm (JCPDS file No. 72-1281) with the unit cell dimensions of a = 5.2670 Å, b = 5.5810 Å, c = 7.5930 Å, and $\alpha = \beta = \gamma = 90^0$ [35]. The typical SEM micrograph of the $ErFeO_3$ NPs is shown in Fig. 4.1(b), where the inset shows a representative energy dispersive X-ray (EDX) pattern. Fig. 4.1(c) shows the HRTEM image of EFO nanoparticles. The selected area electron diffraction pattern (SAED) is shown in the inset of Fig. 4.1(c). Fig. 4.1(d) shows the single-particle TEM micrograph of a single $ErFeO_3$ NPs. The size of the NPs is found to be quite uniform (~200 nm) in nature. The calculated inter-planar distance (Fig. 4.1(c)) between the lattice fringe is about 0.27 nm, which corresponds to the distance between (112) planes of $ErFeO_3$ NPs.
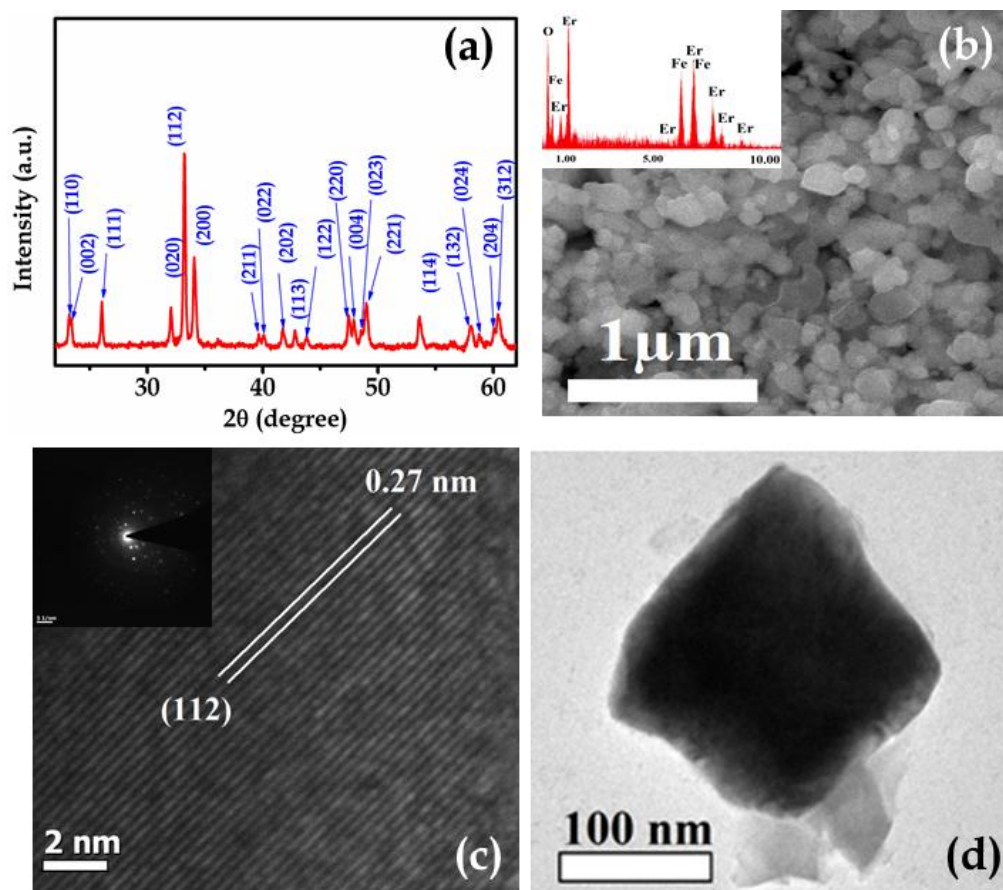
**Fig. 4.1:** (a) XRD pattern, (b) FESEM micrograph and EDAX spectrum (inset), (c) HRTEM micrograph, SEAD pattern (inset) and (d) single particle TEM micrograph of ErFeO₃ NPs.

The chemical composition of the ErFeO₃ NPs is studied by X-ray photoelectron spectroscopy (XPS). Fig. 4.2(a) shows the XPS spectrum for Er, where the peak of Er $4d_{5/2}$ situated at 170 eV represent the +3 oxidation state of Er in ErFeO₃ [36]. The Fe $2p_{3/2}$ and $2p_{1/2}$ peaks (Fig. 4.2(b)) located at 710.9 and 724.7 eV, respectively corresponds to the $Fe^{3+}$ oxidation state of iron [37, 38]. Here, no peak at 708.2 eV for $Fe^{2+}$ is observed which indicates that the ErFeO₃ NPs have a single phase with a $Fe^{3+}$ valence state of iron [39]. The O *1S* core level peak appears at 531 eV (Fig. 4.2(c)) and can be assigned to the −2 oxidation state of oxygen in the ErFeO₃ NPs.
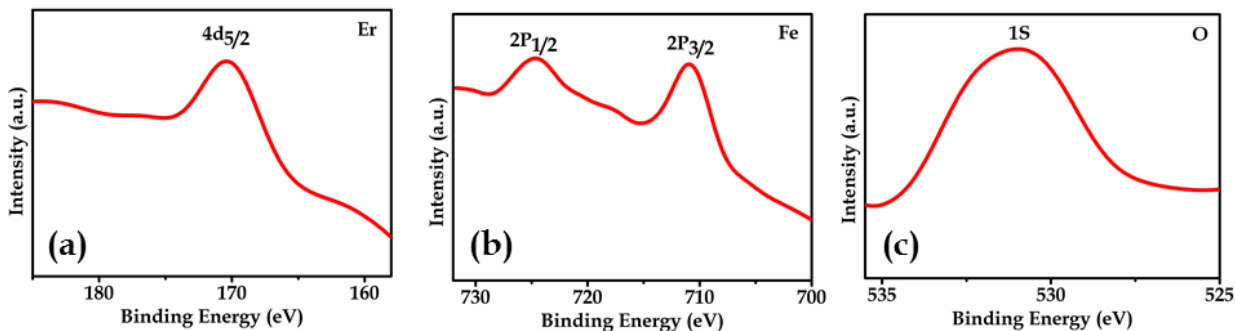
**Fig. 4.2:** (a-c) The high resolution XPS spectrum of the Er 4d, Fe 2p, O 1s respectively, of ErFeO$_3$ NPs.

## 4.3.2. Dielectric properties of ErFeO$_3$ nanoparticles

Figs. 4.3 and Fig. 4.4 show temperature-dependent real ($Z'$) and imaginary parts ($Z''$) of the impedance of ErFeO$_3$ NPs respectively. Above 100 $^0$C all the curves (Fig. 4.3) show dispersion followed by a plateau region at low frequency. With the increase in temperature, the dispersion region spreads to a higher frequency regime. The value of $Z'$ drops off sharply with increasing frequency due to the dielectric relaxation. After 5 kHz all the curves taken at different temperatures merge with each other. $Z''$ *vs f* curves (Fig. 4.4(a)) show the appearance of peaks at a characteristic frequency $f_{max}$ above 100 $^0$C. Fig. 4.4(b) shows the $f_{max}$ *vs T* curve and with increasing temperature $f_{max}$ is shifted toward higher frequency region, indicating a decrease of relaxation time ($\tau = 1/2\pi f_{max}$). The peak value of $Z''$ decreases with increase in temperature indicating loss in resistive property of the sample. The type of relaxation response in this material can be found in calculating the activation energy ($E_r$) for dielectric relaxation of the ErFeO$_3$ NPs. Fig. 4.4(c) shows $ln\tau$ *vs* $1/k_BT$ curve, where the activation energy, $E_r$ is estimated to be 0.92 eV using the Arrhenius equation:

$$\tau = \tau_0 \exp\left(\frac{E_r}{K_BT}\right) \tag{4.1}$$

where $\tau_0$ is the prefactor, $E_r$, the activation energy for dielectric relaxation, $T$, the absolute temperature and $k_B$, the Boltzmann constant.
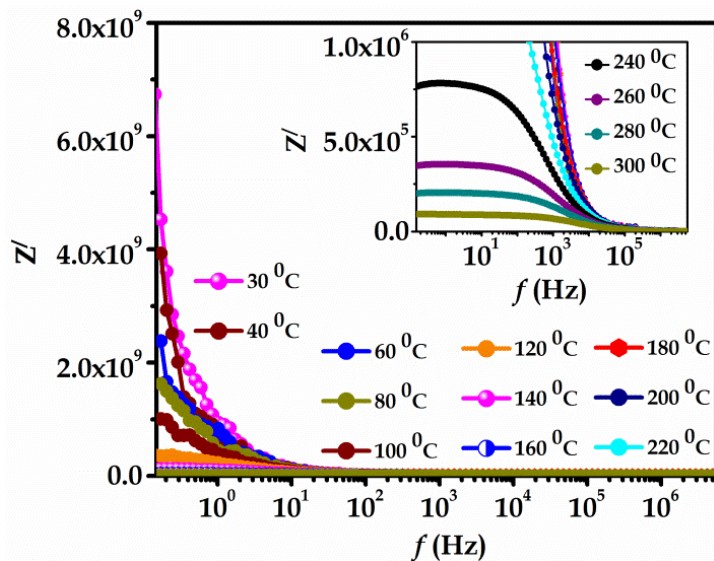
**Fig. 4.3:** Real part of impedance for ErFeO$_3$ NPs as a function of frequency measured at different temperatures, inset also shows impedance at higher temperatures.
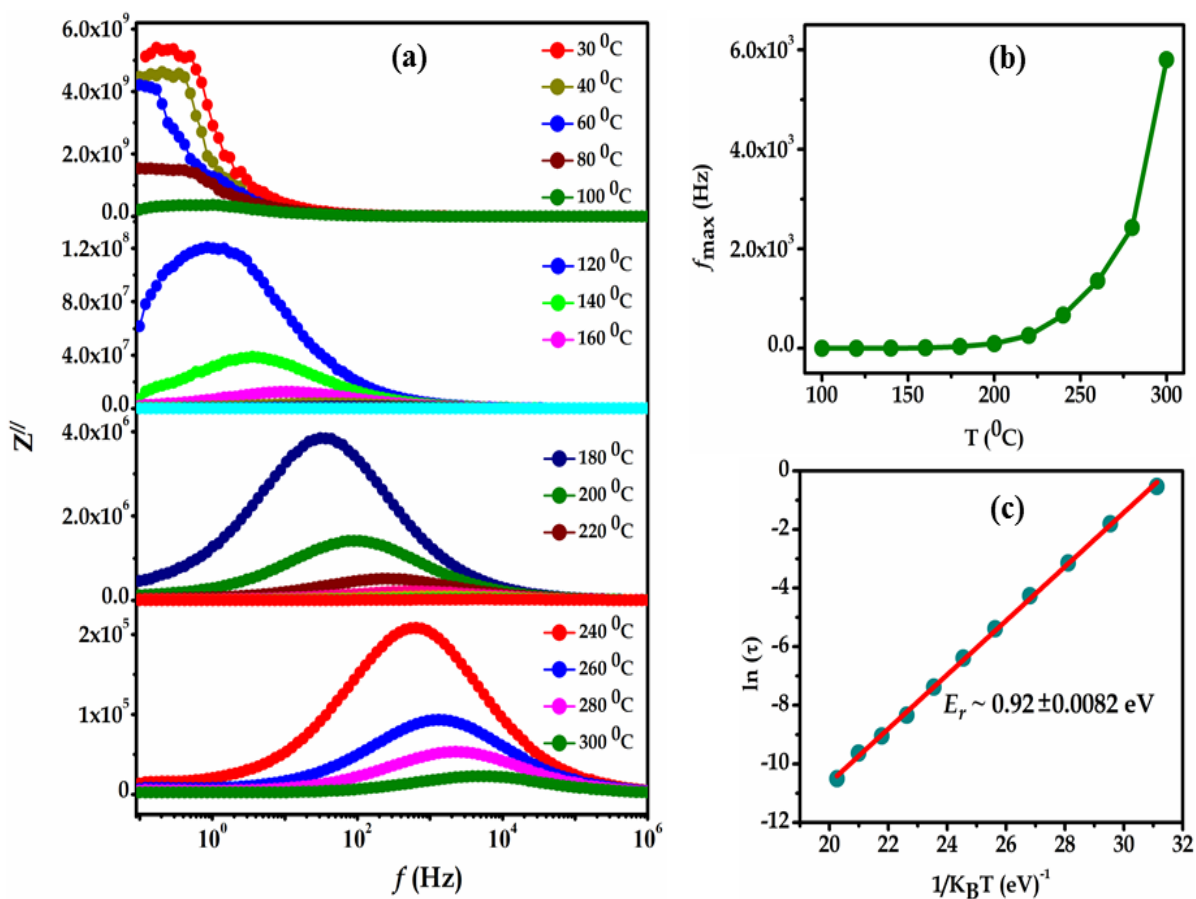


**Fig. 4.4:** (a) Temperature dependent imaginary part (Z″) of impedance as a function of frequency of ErFeO$_3$ NPs. (b) $f_{max}$ of ErFeO$_3$ NPs as a function of temperature. (c) Arrhenius plot ($f_{max}$ *vs T*) for the relaxation time in the temperature range of 100–300 °C of ErFeO$_3$ NPs.

Complex impedance spectroscopy [40] is a very well-known technique to get an idea about the electrical properties of a material using an equivalent circuit model (inset of Fig. 4.5). In the impedance spectra, a circular/semi-circular arc in the Nyquist plot arises because of grain and grain-boundary effects. In the Nyquist plot, bulk property corresponds to the higher frequency region and arises due to the parallel combination of bulk resistance ($R_g$) and bulk capacitance ($C_g$), of the materials. Similarly, the low-frequency one arises due to the parallel combination of grain boundary resistance ($R_{gb}$) and grain boundary capacitance ($C_{gb}$) of the materials.

Fig. 4.5 shows the complex impedance spectra (Nyquist plot) of $ErFeO_3$ NPs at different temperatures. With the increase in temperature, the diameter of impedance spectra decreases because of an increase in the conductivity of the sample. Since the impedance spectra are not perfectly semicircle, they are not modeled with a simple parallel RC circuit [41, 42]. The depressing nature of the impedance spectra confirms the relaxation process to be non-Debye type. To measure the deviation from Debye relaxation, it is needed to introduce a constant phase element (CPE) to the capacitor in the RC circuit. The impedance of CPE is in the form of $Z_Q = (j\omega)^{-\phi}/Q$, where $Q$ is a constant and $\phi$ is the exponent where $0<\phi<1$ describe the deviation from the ideal Debye relaxation process. Here the impedance data is well fitted with the modeled one. The value of $R_g$, $R_{gb}$, $C_g$, and $C_{gb}$, are listed in Table-4.1, show that grain boundary resistance and capacitance are greater than the grain one.
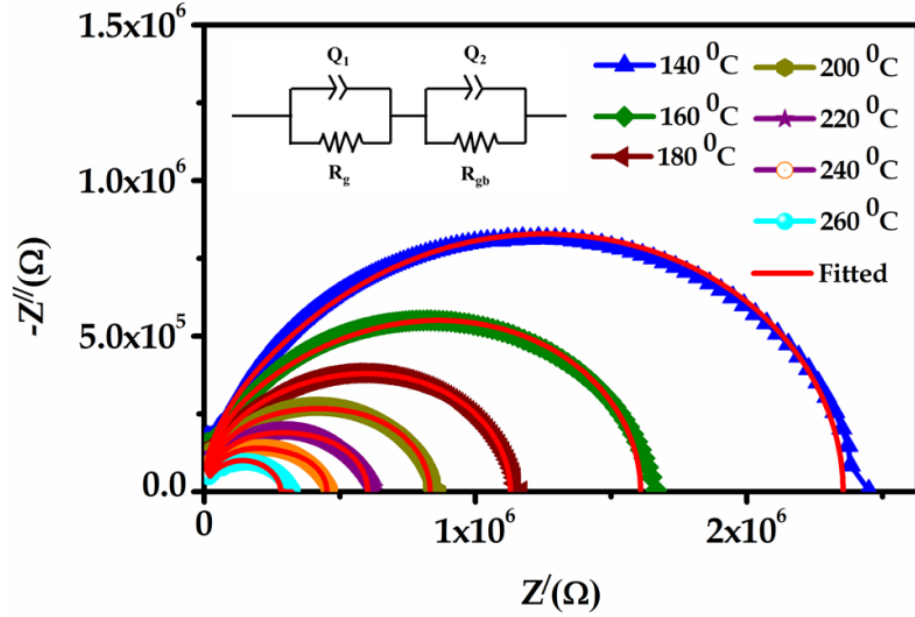
**Fig. 4.5:** Nyquist plot of EFO NPs at different temperatures and inset shows equivalent circuit diagrame.

**Table-4.1:** The value of $R_g$, $R_{gb}$, $C_g$, and $C_{gb}$ after fitting using RQ circuits.

| Temperature ($^0$C) | $R_g$ (kΩ) | $C_g$ (pF) | $R_{gb}$ (MΩ) | $C_{gb}$ (nF) |
|---|---|---|---|---|
| 140 | 44.20 | 60 | 2.3439 | 0.092 |
| 160 | 32.99 | 61 | 1.5764 | 0.174 |
| 180 | 23.75 | 62 | 1.0921 | 0.211 |
| 200 | 19.11 | 61.7 | 0.7829 | 0.296 |
| 220 | 13.25 | 63 | 0.5446 | 0.372 |
| 240 | 10.74 | 64 | 0.3895 | 0.423 |
| 260 | 7.242 | 78 | 0.2546 | 0.436 |

Figs. 4.6(a) and (b) respectively represent the real and imaginary part of dielectric constant at different temperatures. Fig. 4.6(c) represents the dielectric loss $(\tan \delta = \frac{\varepsilon''}{\varepsilon'})$ value with the variation of frequency at different temperatures. The dielectric constant $(\varepsilon^*)$ is calculated by using Mott theory [43],

$$\varepsilon^* = \varepsilon'(\omega) + j\varepsilon''(\omega), \tag{4.2}$$

$$\text{where, } \varepsilon' = \frac{Z''}{\omega C_0 \left( Z'^2 + Z''^2 \right)}, \text{ and } \varepsilon'' = \frac{Z'}{\omega C_0 \left( Z'^2 + Z''^2 \right)}$$

here, $C_0 = \frac{\varepsilon_0 A}{d}$, $C_0$ is the measured value of capacitance of a sample, d, the thickness, and A, the surface area and , $\varepsilon_0$ the dielectric permittivity of air. Here the real part $(\varepsilon'(\omega))$

represents the stored energy i.e. the dielectric polarization and the imaginary part of dielectric constant ($\varepsilon''(\omega)$) is associated with dissipation energy of the system. With increase in temperature the dielectric constant and dielectric loss increase very rapidly specially at low frequency region. At higher temperature the movement of charge carriers increase and comparable with the frequency of applied electric field. So they easily hop out at the low energy side leading to increase in net polarization and higher dielectric constant. But, at high frequency, the charge carriers lag behind the applied electric field. This leads to a decrease in dielectric constant. Again from Table-4.1, we can say that the capacitance of grain boundary (nF) is greater than the grain (pF) interior one, so the charge carriers are easily accumulated at the lower frequency grain boundary region.
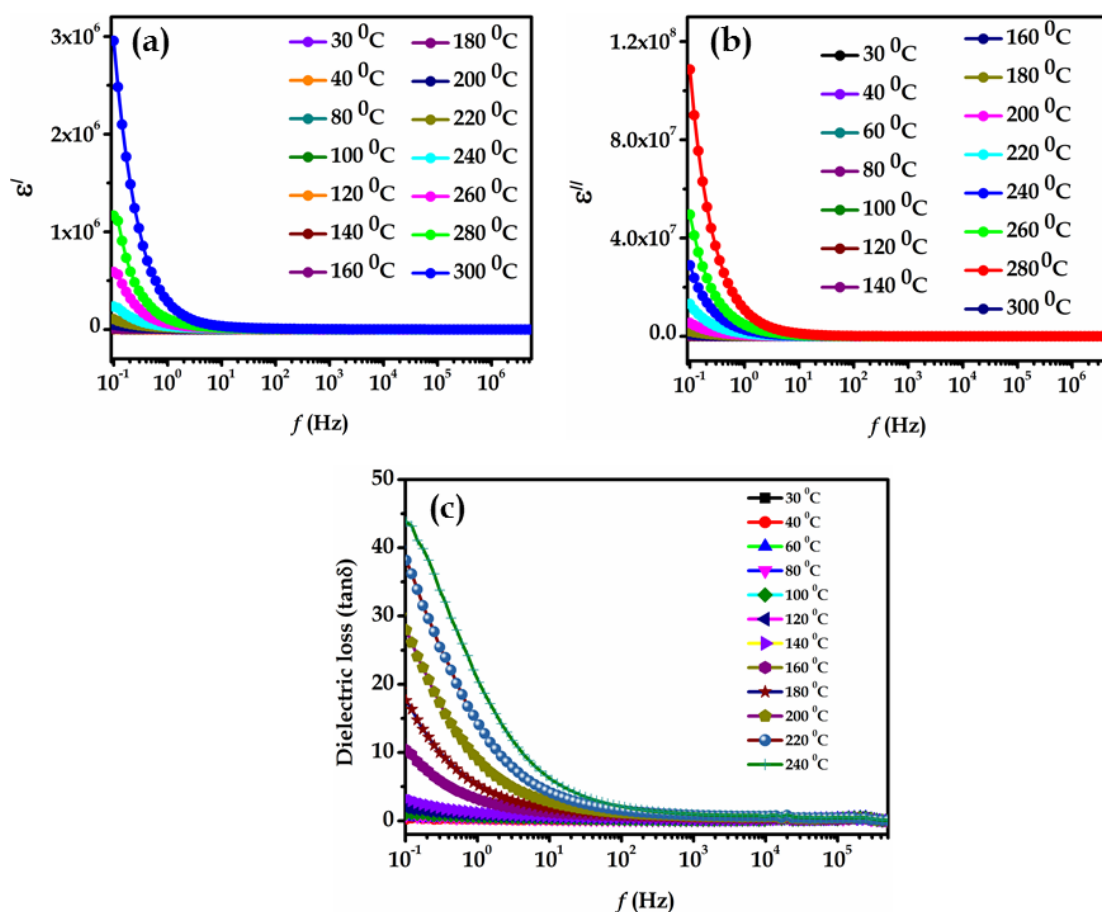


**Fig. 4.6:** Frequency dependence of (a) $\varepsilon'$ and (b) $\varepsilon''$ and (c) dielectric loss (tan δ) of ErFeO$_3$ NPs with different temperatures.

Electric modulus, defined as the inverse of relative permittivity, can be an important tool for analyzing dielectric behaviour of insulating materials especially at high temperatures. In terms of the complex dielectric constant ($\varepsilon^*$), the complex electric modulus $(M)^*$ is calculated as [44]

$$M^* = M' + jM'' = \frac{1}{\varepsilon^*} = j\omega CZ \tag{4.3}$$

$$\text{where, } M' = \frac{\varepsilon'}{((\varepsilon')^2 + (\varepsilon'')^2)}, \quad M'' = \frac{\varepsilon''}{((\varepsilon')^2 + (\varepsilon'')^2)}$$

The frequency-dependent complex electric modulus ($M''$) with different temperatures is shown in Fig. 4.7(a) which exhibits broad and asymmetric peaks an indication of non-Debye type relaxation process. With the increase in temperature, the relaxation peaks are shifted towards the higher frequency because of the thermally activated relaxation process.

The electric modulus ($M^*$) can be represented in terms of Fourier transform of a relaxation function $\phi(t)$ [44]

$$M^* = M_\infty[1 - \int_0^\infty \exp(-\omega t)(-\frac{d\phi}{dt})dt] \tag{4.4}$$

Here the stretched exponential function $\phi(t)$ is taken as Kohlrausch–Williams–Watts (KWW) function [45, 46]

$$\phi(t) = \exp\left[-\left(\frac{t}{\tau_m}\right)^\beta\right] \tag{4.5}$$

where $\tau_m$ is the conductivity relaxation time and the exponent $\beta$ indicates the deviation from the ideal Debye-type relaxation. For experimental data fitting, we apply Bergman [47] suggestion about KWW function defined as,

$$M'' = \frac{M''_{max}}{\left((1-\beta) + \frac{\beta}{1+\beta}\left[\beta\left(\frac{\omega_{max}}{\omega}\right) + \left(\frac{\omega}{\omega_{max}}\right)^\beta\right]\right)} \tag{4.6}$$

here $M''_{max}$ represents the peak value of the $M''$ and $\omega_{max}$ is the corresponding frequency. The experimental data are fitted well using the above equation (4.6) (solid lines) as shown in Fig. 4.7(a). The values of $\beta$ obtained from the fitting at different temperatures are shown in Fig. 4.7(b) and it is found to be less than 1, which also suggests that the relaxation process in our material is non-Debye type.
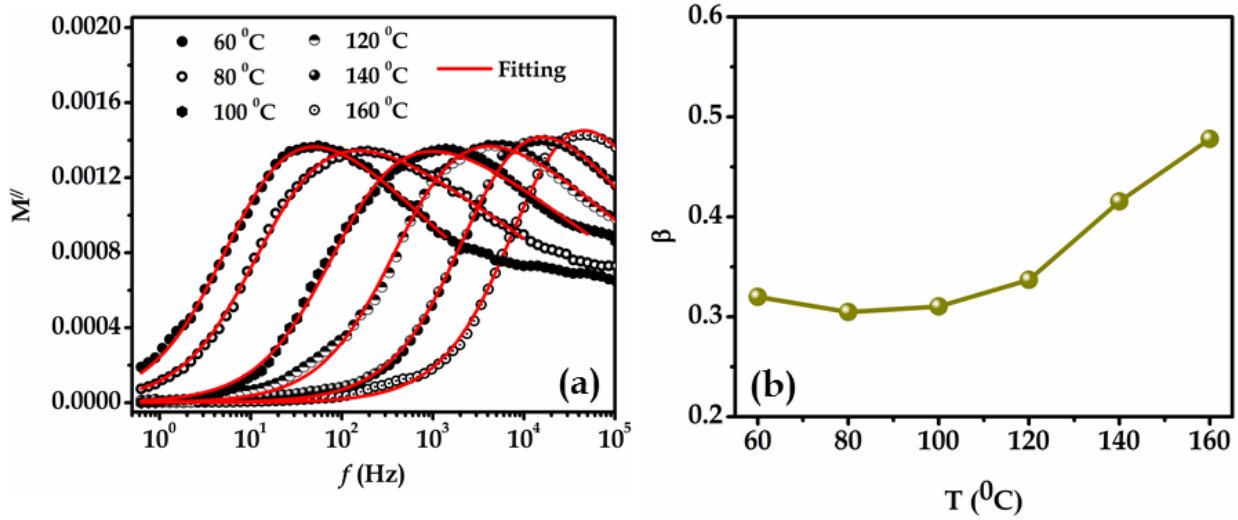
**Fig. 4.7:** (a) Complex modulus (*M″*) plot at different temperatures; the solid lines are the theoretical fits and (b) temperature dependent of β of EFO NPs.

To get an idea about the conduction mechanism of ErFeO₃ NPs, we have measured the frequency-dependent conductivity at various temperatures (30 - 300 °C) and are shown in Fig. 4.8(a). The whole graph can be divided into two regions, the low-frequency dc flat region and high-frequency ac exponential component. The conductivity in the high-frequency region is just the fingerprint of hopping conductivity, but in the low frequency region the electric field cannot disturb the hopping conduction mechanism because of jumping relaxation.

The phenomenon of conductivity dispersion is analyzed using Jonscher's law: [48]

$$\sigma_{ac}(\omega, T) = \sigma_{dc}(T) + A\omega^n(T) \qquad (4.7)$$

here, $\sigma_{dc}$ is the dc conductivity of the material, A is material dependent and *n* is a temperature-dependent parameter, where *0 < n < 1* depending on the mechanism of conduction. From the curves of *log $\sigma_{ac}$ vs. f*, according to Jonscher's power law, *n* values for different temperatures are shown in Fig. 4.8(b). Here exponent *n* decreases with increasing temperature and follow correlated barrier hopping (CBH) conduction model [49, 50]. According to CBH model, charges are transported between two localized states due to hopping over the potential barriers. Here in perovskite material the oxygen vacancy is an unspoken defect because the sample is prepared by high temperature

calcination. This oxygen vacancy serves as a donors conduction electron through $Fe^{+2}$ =$Fe^{+3}$+e transformation. Inset of Fig. 4.8(a) shows the dc conductivity (low frequency) region at different temperature which can be expressed by Arrhenius equation:

$$\sigma_{dc} = \sigma_0 exp\left( {-E_{dc}}/{k_B T} \right) \tag{4.8}$$

where $\sigma_0$, $E_{dc}$ respectively represent the pre-exponential constant and activation energy of conduction. The calculated value of activation energy is ~ 0.85 eV, which is comparable with that calculated from impedance data.
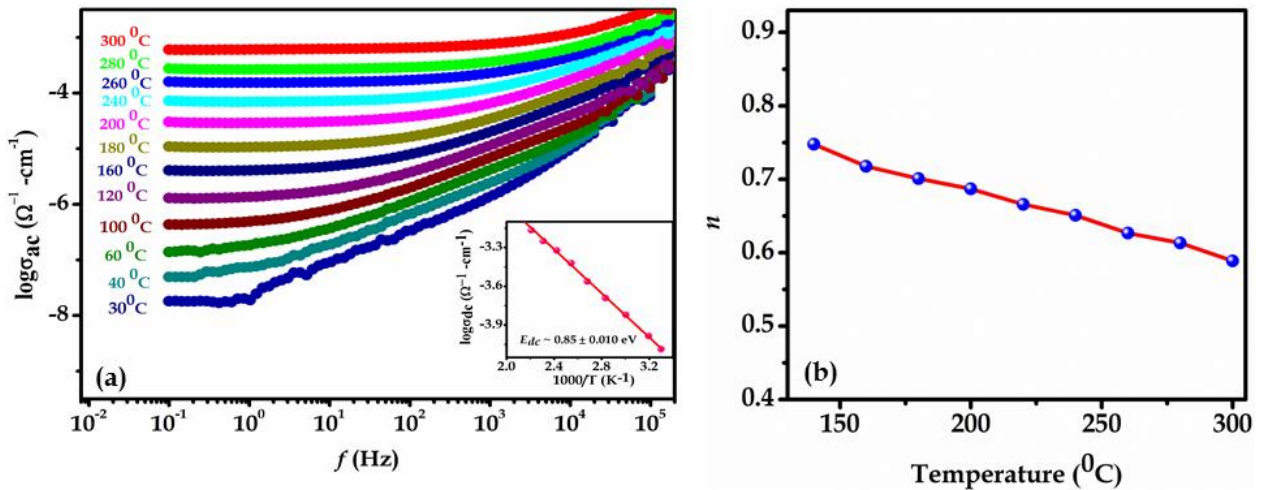


**Fig. 4.8:** (a) The ac conductivity ($\sigma_{ac}$); Inset shows the dc conductivity vs 1000/T and (b) Temperature dependence of *n* of EFO NPs.

### 4.3.3. *Magnetic properties of ErFeO₃ nanoparticles*

For strong evidence of multiferroic property, we performed *M-H*, *P-E* and magnetoelectric coupling measurements on the EFO nanoparticles at room temperature (RT). The field cooled (*FC*) and zero field cooled (*ZFC*) *M-T* curves with 100 Oe applied field are shown in the inset of Fig. 4.9(a). With the decrease in temperature from RT, there is a spin reorientation takes place on the $Fe^{+3}$ sites because of anisotropy produced by the $Er^{+3}$ cations [51]. The moments of the rare-earth ions and the Fe ions become equal and opposite at a particular temperature, called compensation point, where net magnetization is zero. On further decrease in temperature, magnetization increases due

to higher magnetic moment of $Er^{+3}$ with respect to $Fe^{+3}$. Fig. 4.9(a) shows *M-H* hysteresis loops at RT, 120, 80, 10 and 5 K. At RT, magnetization changes linearly with the magnetic field, a typical behavior for the antiferromagnetic arrangement of the $Fe^{3+}$ magnetic moments [52, 53]. However, at 5 K, s-shaped magnetization curve confirms the weak ferromagnetic (FM) nature, as discussed earlier, because of higher difference of antiparallel magnetic moment of $Er^{+3}$ (9.59$\mu_B$) and $Fe^{+3}$ (5.9$\mu_B$), which is gradually enhanced with decreasing temperature. Similar properties are also exhibited by other oxide samples [54, 55].

Inset of Fig. 4.9(b) shows the (high) temperature dependence of magnetization of $ErFeO_3$ NPs in the presence of a magnetic field, $H$ = 1 kOe. A canted antiferromagnetic nature is observed within the temperature range of 620 K ($T_{m1}$) and 894 K ($T_{m2}$). Anti-ferromagnetic and paramagnetic behavior is observed below and above this range respectively. Fig. 4.9(b) shows the *M-H* curves at 300, 761 and 953 K which corresponds to different region of high-temperature *M-T* curve.
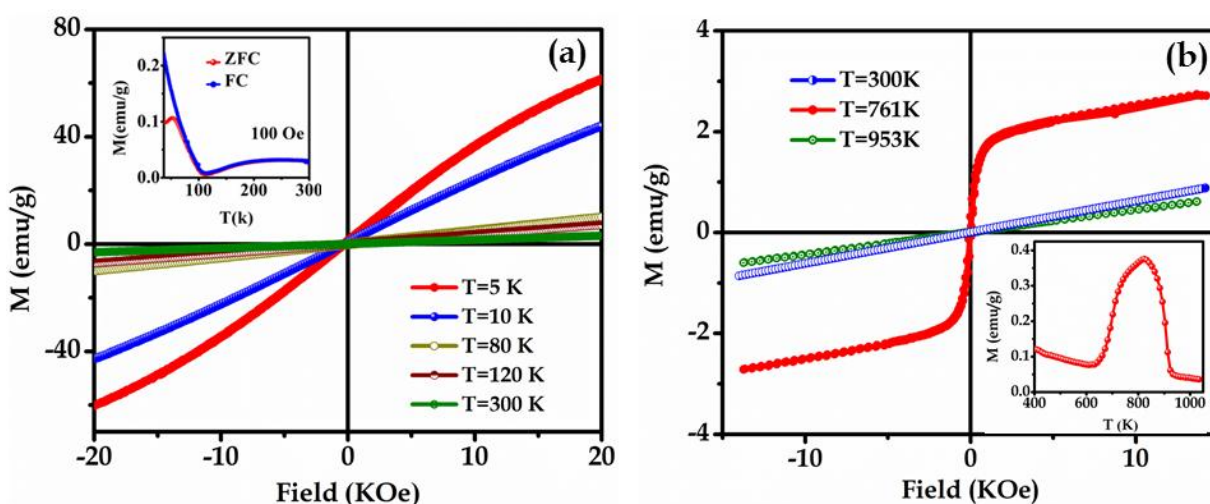


**Fig. 4.9:** (a) (Low) Temperature dependence magnetization measured in external field of H =100 Oe and family of hysteresis loop. (b) High temperature magnetic hysteresis loop measured in three different region, of the $ErFeO_3$ NPs, (High) temperature dependence magnetization measured in external field of H=1 KOe.

### 4.3.4. Ferroelectric properties of ErFeO₃ nanoparticles

The room temperature *P-E* hysteresis loop of $ErFeO_3$ NPs is shown in Fig. 4.10(a) with $P_{max}$ = 4.5 µC/cm² at a frequency of 50 Hz. Fig. 4.10(a) and (b) show stable and

repeatable P-E hysteresis loop at room temperature with remnant polarization and coercive field, larger than that of $ErFeO_3$ thin film [34]. From Fig. 4.10(a) it is clear that the polarization value increases gradually with increasing applied electric field. But after attaining the maximum value of polarization it decreases gradually because of the time delay between the polarization and the electric field. This type of unsaturated *P-E* hysteresis loop is reported earlier [56]. Here $ErFeO_3$ NPs show improper saturation polarization and concave curve, thereby indicating the presence of intrinsic ferroelectricity in this sample [57].

In the case of rare-earth orthoferrites, three exchange interaction ($Re^{3+}$- $Re^{3+}$, $Re^{3+}$-$Fe^{3+}$ and $Fe^{3+}$-$Fe^{3+}$) play a crucial role in magnetic ordering. Out of three, $Re^{3+}$-$Re^{3+}$ exchange interaction happens at very low temperatures [58]. $Fe^{3+}$-$Fe^{3+}$ interaction basically happens at high temperature and determines the antiferromagnetic ordering [59]. The $Fe^{3+}$-$Fe^{3+}$ exchange interaction is more important. Here the $Fe^{3+}$-O-$Fe^{3+}$ bond angle is close to $144^0$ [60]. This $Fe^{3+}$-O-$Fe^{3+}$ super-exchange interaction contributes an AFM ordering with a weak FM component. An antisymmetric Dzyaloshinskii-Moriya (DM) exchange interaction ($D_i . S_i \times S_j$) (where $D_i$ is the exchange interaction intensity, $S_i$ and $S_j$ are two nearest spins) is attributed to the weak FM component between adjacent spins and introduced spin-orbit interaction. As a result an electric polarization $P \sim e_{ij} \times (S_i \times S_j)$ is produced due to local crystal anisotropy [61, 62, 63, 64].
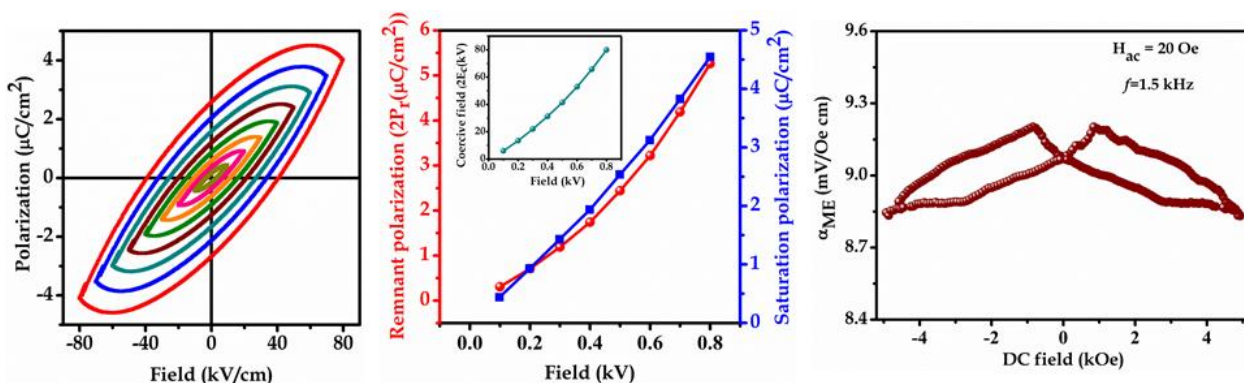


**Fig. 4.10:** (a) P-E hysteresis loop, (b) saturation polarization and remnant polarization and (inset) coercive field with applied voltage. (c) Variation of magnetoelectric coefficient of $ErFeO_3$ NPs with applied DC magnetic field at a constant frequency, *f* = 1500 Hz of $H_{ac}$ (20 Oe).

## 4.3.5. *Magnetoelectric properties of ErFeO₃ nanoparticles*

In addition to the coexistence of ferroelectric and magnetic order in this multiferroic, their coupling, expressed by $\alpha_{ME}$, is also required for device applications. The value of the magnetoelectric coefficient is determined using the formula,

$$\alpha_{ME} = \frac{dE}{dH} = \frac{1}{d}\frac{V_{out}}{H_{ac}} \tag{4.9}$$

where d is the effective thickness of the sample (in the form of the pellet). A small ac magnetic field, $H_{ac}$ produced by a Helmholtz coil is superimposed to a DC magnetic field, $H_{dc}$. The voltage developed across the sample surfaces ($V_{out}$) duo to the ME effect is measured by a lock-in amplifier in the presence of different DC magnetic field within ±5 kOe. The $\alpha_{ME}$ is measured with $H_{ac}$ ~20 Oe at a frequency of $f$ ~ 1.5 kHz in presence of $H_{dc}$ varying within ±5 kOe and is shown in Fig. 4.10(c). The maximum $\alpha_{ME}$ ~ 9.2 mV/Oe cm is obtained near $H_{dc}$ ~ 1.0 kOe. The behavior of the ME coefficient with applied DC magnetic field is similar to the other reported results [65, 66]. The maximum ME coefficient is higher than those reported earlier for $CoFe_2O_4$–$BaTiO_3$ composite (3.0081 to 5.5886 mV/cm Oe) [67], $(BiFeO_3)_{1-x}$–$(BaTiO_3)_x$(2.17 to 2.53 mV/cm Oe) [68], $Bi_{1-x}Nd_xFeO_3$ solid solutions  (0.7 to 2.75 mV/cm Oe) [66], $CoFe_2O_4$–$BaTiO_3$ core–shell structure (3.4mV/cm Oe) [66] and smaller than those reported in ref [65, 69].

## 4.3.6. *Photocatalytic property of ErFeO₃ nanoparticles*

ErFeO₃ NPs have been showed wonderful photo-catalytic properties towards the degradation of methylene blue (shown in Fig. 4.11(a)), a commonly used dye in textile industries and a model water-contaminant, upon UV irradiation at $pH$ ~ 3. As a typical organic contaminant, MB is stable under UV irradiation since after 90 min without ErFeO₃ NPs, the degradation of MB is less than 3% (Inset of Fig. 4.11(b)). However, with ErFeO₃ NPs as a photocatalyst, 100% of MB is decolorizing after 90 min (shown inset of Fig. 4.11(a)) under UV irradiation. Here, we have also found that the photodegradation of MB in the presence of ErFeO₃ NPs takes place almost exponentially with time following first-order rate equation with a kinetic rate constant ($k$) 8.7 x $10^{-3}$ min$^{-1}$. We have also verified the reusability of the catalyst, in the degradation of MB by adding the

same amount of MB into the reaction mixture every 90 min for up to 5 does, keeping the catalyst concentration fixed (without any addition of extra catalyst after the 1st cycle), and measured the MB decomposition rate of the different cycles by tuning the decrease of MB absorbance at 663 nm using UV-visible spectroscopy. Fig. 4.11(b) shows the relative concentration of MB versus time, up to 5 consecutive cycles, which ensure the reusability of ErFeO₃ NPs catalyst with an almost compatible degradation rate.

On the basis of the above experimental results, a possible mechanism for the enhanced photocatalytic degradation of MB by the EFO NPs photocatalyst is proposed as follows: The electron and the hole are generated in the conduction and valance band of EFO under UV light irradiation, respectively (equation 4.10). The photo induced conduction electron ($e_{CB}^-$) transfers from EFO NPs to the surface of the photocatalyst could capture the adsorbed $O_2$ and reduced it to $O_2^{\cdot-}$ superoxide radical (equation 4.11). Now, the superoxide radical reacts with the MB and forms a colorless solution which signifies the complete degradation of MB which is shown in equation 4.12. On the other hand, the formation of the hole in the valance band also takes part in the reaction to degrade MB. The photo-generated holes ($h_{VB}^+$) can transfer to the photo-catalyst surface and also react with the $H_2O$ which is present in the reaction medium to form hydroxyl free radical ($HO^{\cdot}$). Formation of hydroxyl free radical leads the degradation of MB by reacting with this blue coloured dye and forms the colourless solution, shown in equation 4.14. The proposed photocatalytic mechanism of EFO NPs for MB degradation could be described as follows:

$$ErFeO_3 + h\nu \;\rightarrow\; e_{CB}^- + h_{VB}^+ \tag{4.10}$$

$$e_{CB}^- + O_2 \;\rightarrow\; O_2^{\cdot-} \tag{4.11}$$

$$O_2^{\cdot-} + MB \rightarrow Product\;(colour\;less) \tag{4.12}$$

$$h_{VB}^+ + H_2O \;\rightarrow HO^{\cdot} + H_{aq}^+ \tag{4.13}$$

$$HO^{\cdot} + MB \rightarrow Product\;(colour\;less) \tag{4.14}$$
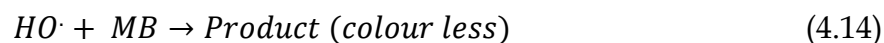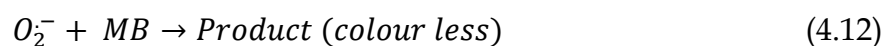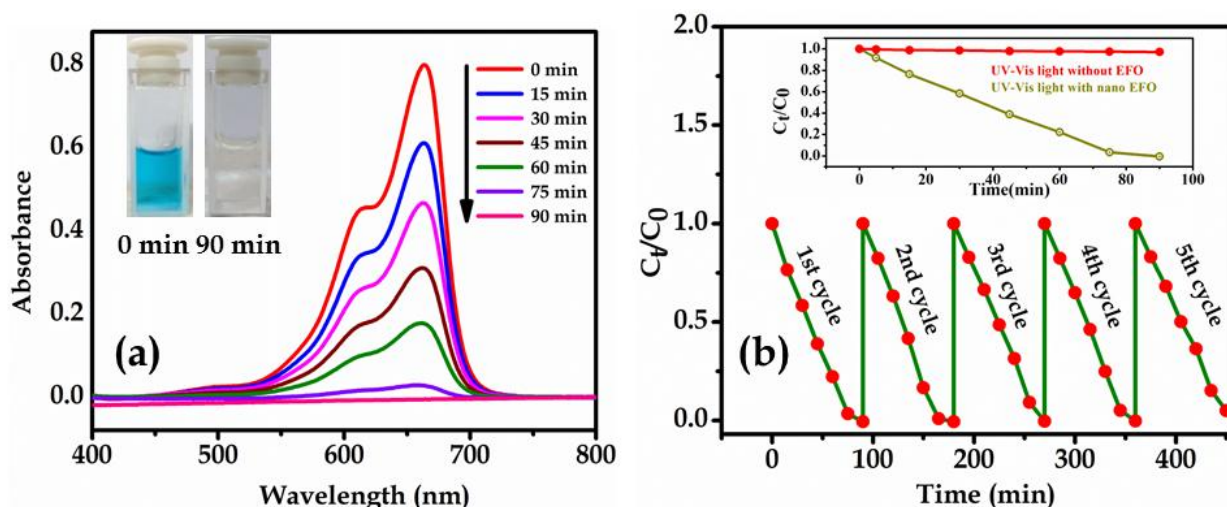
**Fig. 4.11:** (a) UV−vis spectral changes of aqueous solution of methylene blue (MB) in the presence of ErFeO$_3$ NPs with time, under UV irradiation. (Inset shows after 0 min and 90 min irradiation), (b) Reusability of ErFeO$_3$ NPs in the degradation of MB under UV light irradiation of wavelength 253 nm over five cycles (Inset shows comparative rate of degradation of MB alone and in the presence of ErFeO$_3$ NPs under UV irradiation ) in UV-vis spectroscopy.

To confirm the attachment of tartrate ligand to the surface of the nanoparticles, we used a FTIR spectroscopy. The FTIR spectra of bare ErFeO$_3$ NPs and T-ErFeO$_3$ NPs along with Na tartrate alone are shown in Fig. 4.12. The specific region shows the characteristic vibration of *Fe-O* stretching bond and *Er-O* at 571 cm$^{-1}$ and 481 cm$^{-1}$ respectively [31, 32]. These two Metal–Oxygen peaks are not arising separately after surface modification, which proves that the effective surface modification of ErFeO$_3$ NPs has taken place upon interaction with tartrate ligands.  In case of tartrate, two sharp peaks arising at 1066 and 1112 cm$^{-1}$ are due to the *C–OH* stretching modes [33], and peaks at 1411 and 1622 cm$^{-1}$ are attributed to symmetric and asymmetric stretching modes of the carboxylate groups (*COO*$^-$) of tartrate, respectively [70]. In the case of functionalized ErFeO$_3$ NPs, all the characteristic bands are perturbed significantly in the functionalization process.
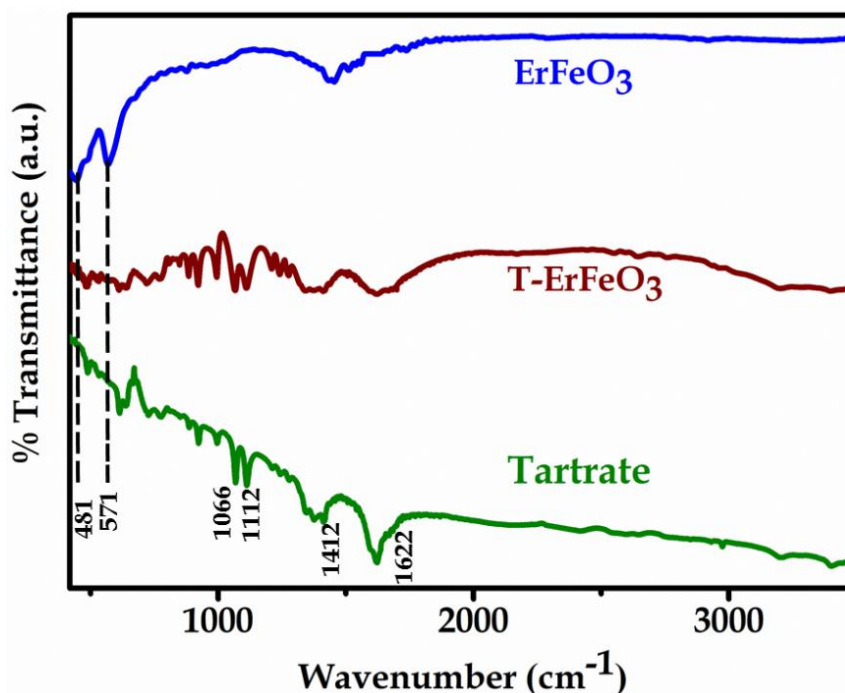
**Fig. 4.12:** FTIR spectra of as-prepared $ErFeO_3$ and T- $ErFeO_3$ NPs along with Na-tartrate alone.

## 4.3.7. Fluorescence property of $ErFeO_3$ nanoparticles

To study the effect of ligand on the properties of $ErFeO_3$, we solubilized the as-prepared $ErFeO_3$ NPs into the water by functionalization with disodium tartrate ligand. Up on functionalization with tartrate ligand, $ErFeO_3$ NPs exhibit a distinct broad absorption band ranging from 290-430 nm in UV-vis spectroscopy which is shown in Fig. 4.13. Since the tartrate does not show any absorption peak in UV-vis spectroscopy, the broadband at *pH* ~ 7 is clearly due to the ligand-to-metal charge transfer (LMCT) transition from the tartrate to the metal surface of $Er^{3+}$ and $Fe^{3+}$ ions [71]. At *pH* ~ 7, all the tartrate ligands do not exhibit in its anionic form. To get a free anionic form of all tartrate ligands for better LMCT transition, T-$ErFeO_3$ NPs further modified by heat treatment at ~70 °C for 15 hours after maintaining the pH~12 of the solution through dropwise addition of NaOH solution. At this pH, the broad absorption peak splits into distinguishable peaks in case of fl. modified T-$ErFeO_3$ NPs, probably due to the enhancement of LMCT and f-f transition. The fl. modified T-$ErFeO_3$ NPs is found to exhibit absorption peaks at 312, 364 and 431 nm, indicating the significant changes in

the surface of the NPs after functionalization with tartrate ligand. After getting the absorption peaks of fl. modified T-ErFeO$_3$ NPs, we carried out their excitation and emission study in fluorescence spectroscopy.
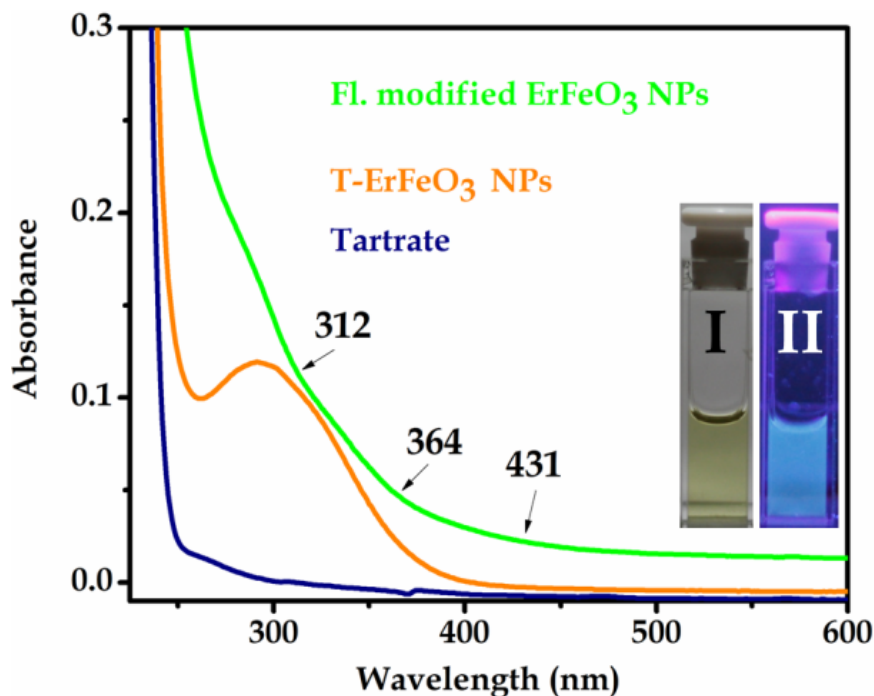


**Fig. 4.13:** UV−vis absorption spectra of tartrate, ErFeO$_3$ NPs, T−ErFeO$_3$ NPs and fl. Modified T−ErFeO$_3$ NPs. Inset exhibits the photographs of aqueous T− ErFeO$_3$ NPs solution under visible (image I) and UV light (image II) respectively.

Fig. 4.14(a) shows the normalized emission spectra of fl. modified T-ErFeO$_3$ NPs at 403, 491 and 556 nm upon exciting at 312, 364 and 431 nm respectively. The fluorescence peak at $\lambda_{em}$= 403 nm upon exciting the sample at $\lambda_{ex}$ = 312 nm, is probably due to the charge-transfer transition from the highest occupied energy level of the tartrate ligand to the lowest unoccupied energy level of Er$^{3+}$ and Fe$^{3+}$ ions. The origin of another two emission peaks at 491 and 556 nm is due to the f-f transitions involving $^4I_{15/2} \rightarrow {}^4I_{13/2}$ and $^4I_{15/2} \rightarrow {}^4I_{11/2}$ transitions respectively [72]. However, these transitions are purely for Er$^{3+}$ (f$^{11}$). There is no possibility of d-d transition for Fe$^{3+}$ (d$^5$) due to spin and laporte forbidden according to the selection rules for electronic spectra but the fundamental selection rules are not so longer valid for rare earth elements since the high atomic number of Er$^{3+}$ induces a decrease in electrostatic interactions [73, 74, 75].

Corresponding normalized different excitation spectra at 312, 364 and 433 nm is shown in Fig. 4.14(b). Different excitations of T-ErFeO$_3$ NPs arises multicolor fluorescence like blue, green and red upon excitations in the range of 340-380, 450-490, and 515-560 nm using different filters is evident from Fig. 4.14 ((c)-(e)).
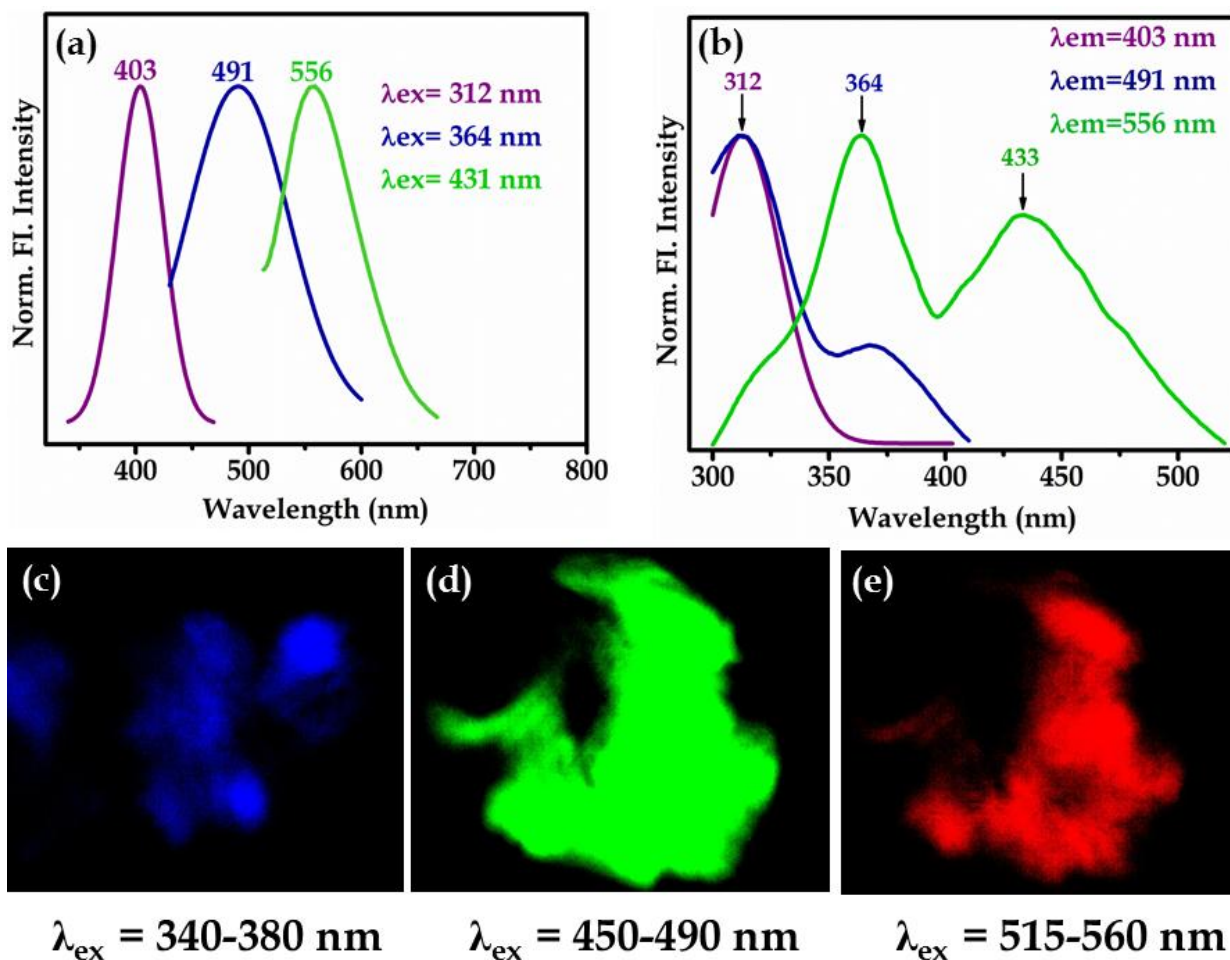


**Fig. 4.14:** (a) Normalized steady−state fluorescence emission spectra at three different excitation wavelengths of 312, 364, and 431, (b) Normalized steady−state fluorescence excitation spectra at different emission wavelengths of 403, 491, and 556 nm of fl. Modified T− ErFeO$_3$ NPs. Fluorescence microscopic images of the same NPs powder under (c) UV, (d) blue and (e) green light irradiations. The scale bars in all the images are 500 $\mu$m.

## 4.4. Conclusion

We have prepared ErFeO$_3$ NPs by microwave method and studied their multiferroic properties and magnetoelectric coefficient at room temperature (RT). ErFeO$_3$ NPs also shows weak ferromagnetic at low temperature and room temperature ferroelectricity. Dzyaloshinskii-Moriya exchange interaction between Fe ions induced by the spin-orbit interaction, which reflects the local crystal anisotropy are the origin of ferroelectric polarization. ErFeO$_3$ shows a high Magnetoelectric coefficient. After successfully analyzed complex impedance, modulus spectra and fitted with the equivalent circuit diagram it is clear about the contribution of grain and grain boundary to the electrical response of the material. The imaginary part of electric modulus is fitted by using Kohlrausch–Williams–Watts (KWW) function and find out the stretched exponent (0.3< β<0.48) which confirms the relaxation method is non-Debye type. The conduction mechanism of ErFeO$_3$ NPs is analyzed by using Jonscher's power law and get the power component (0.6<n<0.75), which follow the correlated barrier hopping (CBH) model. More importantly, we show that ErFeO$_3$ NPs are a new class of multiferroics.

We have also modified the surface of ErFeO$_3$ NPs with disodium tartrate dihydrate ligand gives the opportunity for studying their surface electronic structures of 4f metals. Using the spectroscopic technique, we have tried to investigate the optical property of our modified NPs. We have also explored the origin of multicolor fluorescence of 4f metals through LMCT transition from the tartrate ligand to the lowest unoccupied energy level of Er$^{3+}$ ions and f-f transitions over Er present in the NPs. We have also demonstrated the excellent catalytic activity of ErFeO$_3$ NPs for degradation of MB, a model water contaminant under UV light. We hope that the explore of multifunctional T-ErFeO$_3$ NPs will open up a new door for bio-imaging, drug delivery, and wastewater treatment.

## 4.5. Bibliography

[1]     M. Fiebig, J. Phys. D: Applied Physics **38,** 123 (2005).

[2]     S.-W. Cheong and M. Mostvoy, *Nature Mater.* **6**, 13 (2007).

[3]     R. Ramesh and N. A. Spaldin, *Nature Mater.* **6**, 21 (2007).

[4]     Y. Tokura, *J. Magn. Magn. Mater.* **310**, 1145(2007).

[5]     M. Alam, K. Karmakar, M. Pal, and K. Mandal, *RSC Advances* **6**, 114722 (2016).

[6]     J. A. Katine, F. J. Albert, R. A. Buhrman, E. B. Myers, & D. C. Ralph, *Phys. Rev. Lett.* **84**, 3149 (2000).

[7]     C. Chappert, A. Fert, & F. N. V. Dau, *Nat. Matter.* **6**, 813 (2007).

[8]     Y. Tokunaga, N. Furukawa, H. Sakai, Y. Taguchi, T. Arima, and Y. Tokura, *Nature Mater.* **8**, 558 (2009).

[9]     Y. Tokunaga, S. Iguchi, T. Arima, and Y. Tokura, Phys. Rev. Lett. **101**, 097205 (2008).

[10]    J. H. Lee, Y. K. Jeong, J. H. Park, M. A. Oak, H. M. Jang, J. Y. Son, and J. F. Scott, *Phys. Rev. Lett.* **107**, 117201 (2011).

[11]    T. Kimura, T. Goto, H. Shintani, K. Ishizaka, T. Arima & Y. Tokura, *Nature (London)* **426**, 55 (2003).

[12]    T. Goto, T. Kimura, G. Lawes, A. P. Ramirez, and Y. Tokura, *Phys. Rev. Lett.* **92**, 257201 (2004).

[13]    K. Taniguchi, N. Abe, T. Takenobu, Y. Iwasa, and T. Arima, *Phys. Rev. Lett.* **97,** 097203 (2006).

[14]    Y. Yamasaki, S. Miyasaka, Y. Kaneko, J.-P. He, T. Arima, and Y. Tokura, *Phys. Rev. Lett.* **96**, 207204 (2006).

[15]    H. Yokota, T. Nozue, S. Nakamura, M. Fukunaga, and A. Fuwa, *Jpn. J. Appl. Phys.* **54,** 10NA10 (2015).

[16]    M. B. Gawande, P. S. Branco, R. S. Varma, *Chem. Soc. Rev.* **42,** 3371 (2013).

[17]    P. Guo, G. Zhang, J. Yu, H. Li, X. S. Zhao, *Colloids and Surfaces A: Physicochemical and Engineering Aspects* **395**, 168 (2012).

[18]    P. Zhang, Y. Zhan, B. Cai, C.Hao, J. Wang, C. Liu, Z. Meng, Z. Yin, Chen, *Q. Nano Res.* **3**, 235 (2010).

[19]    S. Sun, H. Zeng, D. B. Robinson, S.Raoux, P. M. Rice, S. X. Wang, G. Li, *J. Am. Chem. Soc.* **126**, 273 (2003).

[20]    J. Wang, J. B. Neaton, H. Zheng, V. Nagarajan, S. B. Ogale, B. Liu, D. Viehland, V. Vaithyanathan, D. G. Schlom, U. V. Waghmare, N. A. Spaldin, K. M. Rabe, M. Wuttig and R. Ramesh, *Science* **299**, 1719 (2003).

[21]    M. Alam, K. Mandal and G. G. Khan, *RSC Advances* **6**, 62545 (2016).

[22]    F. D. Martini, V. Buzek, F. Sciarrino and C. Sias, *Nature* **419**, 815 (2002).

[23]    W. Eerenstein, N. D. Mathur and J. F. Scott, *Nature* **442**, 759 (2006).

[24]    M. Alam, K. Karmakar, M. Pal and K. Mandal, *RSC Advances* **6**, 114722 (2016).

[25]    S. Li, Y.-H. Lin, B.-P.Zhang, Y. Wang, and C.-W. Nan, *J. Phys. Chem. C* **114**, 2903 (2010).

[26]    F. Gao, X. Y. Chen, K. B. Yin, S. Dong, Z. F. Ren, F. Yuan, T. Yu, Z. G.Zou, J. M. Liu, *AdV. Mater.* **19**, 2889 (2007).

[27]    C. Madhu, Manjunath B Bellakki& V. Manivannan, *Indian Journal of Engineering & Materials Sciences* **17**, 131 (2010).

[28]    F. Gao, Y. Yuan, K. F. Wang, X. Y. Chen, F. Chen, J. M. Liu, Z. F. Ren, *Appl. Phys. Lett.* **89**, 102506 (2006).

[29]    Y. Feng, H. Wang, Y. Shen, Y. Lin, C. Nan, *Modern Research in Catalysis* **2**, 1 (2013).

[30]    X. Li, Z. Zhu, F. Li, Y. Huang, X. Hu, H. Huang, R. Peng, X. F. Zhai, Z. Fu & Y. Lu, *Scientific report* **5**, 15511 (2015).

[31]    I. J. Bruce, J. Taylor, M. Todd, M. J. Davies, E. Borioni, C. Sangregorio and T. Sen, *J. Magn. Magn.Mater.* **284**, 145 (2004).

[32]    F. Azad,A. Maqsood, *Electron. Mater.Lett.* **10**, 557 (2014).

[33]    N. Kaneko, M. Kaneko, and H. Takahashi, *Spectrochim. Acta* **40**, 33 (1984).

[34]    G. S. Lotey, N. K. Verma, *Chemical Physics Letters* **579**, 78 (2013).

[35]    J. L. Ye, C.C. Wang, W. Ni, X. H. Sun, *Journal of Alloys and Compounds.* **617**, 850 (2014).

[36]    T. –M. Pan, F. –H. Chen and Y. –H. Shao, *RSC Advances* **5**, 51286 (2015).

[37]    S.-W. Chen, C.-C. Lee, M.-T. Chen, J.-M. Wu, *Nanotechnology* **22**, 115605 (2011).

[38]   F. Yan, M.-O Lai, L. Lu, T.-J. Zhu, *J. Phys. Chem. C* **114**, 6994 (2010).

[39]   W. B. Luo, J. Zhu, Y. R. Li, X. P. Wang, D. Zhao, J. Xiong, Y. Zhang, *Appl. Phys. Lett.* **91**, 082501 (2007).

[40]   J.R. Macdonald and W. B. Johnson, E, Barsoukov and J. R. Macdonald, Hoboken, *NJ: Wiley*, (2005).

[41]   C-H. Chang, K-C. Tien, S-H.Liu, T-H.Ke and C-C. Wu, *Org. Electron.* **11,** 1901 (2010).

[42]   M. Meier, S. Karg and W. Riess, *J. Appl. Phys.* 82, 1961 (1997).

[43]   N. F. Mott, E. A. Davis, Clarendon Press, Oxford, (1979).

[44]   P.B. Macedo, C.T. Moynihan, and R. Bose, *Phys. Chem. Glasses* **12**, 171 (1972).

[45]   R.Kohlrausch, *Prog. Ann. Phys.* **91,** 179 (1854).

[46]   G. Williams and D. C. Watts, *Trans Faraday Soc.* **6,** 80 (1970).

[47]   R. Bergman, *J. Appl. Phys.* **88**, 1356 (2000).

[48]   A.K. Jonscher, *J. Mater. Sci.* **34**, 3071 (1999).

[49]   S.R. Elliott, *Adv. Phys.* **36,** 135 (1987).

[50]   A. Ghosh, *Phys. Rev. B* **42**, 1388 (1990).

[51]   R. L. White, *J. Appl. Phys.* **40**, 1061 (1969).

[52]   S. T. Zhang, M. H. Lu, D. Wu, Y. F.Chen, N. B. Ming, *Appl. Phys. Lett* **87**, 262907 (2005).

[53]   D. Lebeugle, D. Colson, A. Forget, M. Viret, P. Bonville, J. F. Marucco, S. Fusil, *Phys. Rev. B* **76**, 024116 (2007).

[54]   B. Raneesh, A. Saha, D. Das, N. Kalarikkal, *Journal of Alloys and Compounds* **551**, 654 (2013).

[55]   S. Li, Y. –H. Lin, B. –P. Zhang, Y. Wang, and C.-W. Nan, *J. Phys. Chem C* **114**, 2903 (2010).

[56]   P. Manimuthu and C. Venkateswaran, *J. Phys. D: Appl. Phys*. **45**, 015303 (2012).

[57]   J. F. Scott, *J. Phys.: Condens. Matter* **20,** 021001 (2008).

[58]   Z. Y. Zhao, X. M. Wang, W. Tao, X. G. Liu, W. P. Ke, F. B. Zhang, X. Zhao, and X. F. Sun, *Phys. Rev. B* **83**, 014414 (2011).

[59]     G. Deng, P. Guo, W. Ren, S. Cao, H-E- M Casely, M. Avdeev and G-J Mclntyre, *Journal of Applied Physics* **117**, 164105 (2015).

[60]     S.-J. Kim, G. Demazeau, I. Presniakov, and J.-H. Choy, *J. Solid State Chem.* **161**, 197 (2001).

[61]     J.-H. Lee, Y. K. Jeong, J. H. Park, M.-A. Oak, H. M. Jang, J. Y. Son, and J. F. Scott, *Phys. Rev. Lett.* **107**, 117201 (2011).

[62]     B. Berini, A. Fouchet, E. Popova, J. Scola, Y. Dumont, N. Franco, R. M. C. da Silva, and N. Keller, *J. Appl. Phys.* **111**, 053923 (2012).

[63]     H. Katsura, N. Nagaosa, and A. V. Balatsky, *Phys. Rev. Lett.* **95**, 057205 (2005).

[64]     H. Shen, Z. Cheng, F. Hong, J. Xu, S. Yuan, S. Cao, and X. Wang, *Appl. Phys. Lett.* **103**, 192404 (2013).

[65]     N. Ortega, A. Kumar, J. F. Scott and R. S. Katiyar, *Journal of Physics: Condens. Matter* **27**, 5040002 (2015).

[66]     G. V. Duong, R. Groessinger, M. Schoenhart, D. Bueno-Basques, *J. Magn. Magn. Mater.* **316**, 390 (2007).

[67]     S. Mazumder, G.S. Bhattacharyya, *Ceram. Int.* **30**, 389 (2004).

[68]     E. Jartych, T. Pikula, K. Kowal, J. Dzik, P. Guzdek and D. Czekaj, *Nanoscale Research letter* **11**, 234 (2016).

[69]     M. Alam, S. Talukdar, K. Mandal, *Materials Letters* **210,** 80 (2018).

[70]     V. Ramakrishnan and J. M. T. Maroor, *Infrared Phys.* **28**, 201 (1988).

[71]     M. E. Bodini, L. A. Willis, T. L. Riechel, D. T. Sawyer, *Inorg. Chem.* **15**, 1538 (1976).

[72]     X. Zhou, Peter A. Tanner, and Miche`le D. Faucher, *J. Phys. Chem. C* **111**, 683 (2007).

[73]     J. E. Huheey, E. A.Keiter, R. L.Keiter, Inorganic Chemistry 4th ed.; Pearson Education: Singapore, (2006).

[74]     P. C. de S. F. Juliana, F. Lima, andO. A. Serra, *J. Braz. Chem. Soc.* **26**, 2471 (2015).

[75]     J. Vuojola, T. Soukka, *Methods Appl. Fluoresc* **2**, 012001 (2014).

# Chapter 5

## Study of Multiferroic and Supercapacitive Properties of Double Perovskite $Y_2NiMnO_6$ Nanowires

In this chapter we have demonstrated the synthesis of double perovskite $Y_2NiMnO_6$ nanowires through hydrothermal method and studied their multiferroic and Supercapacitive properties.

## 5.1. Background

The coexistence of ferroelectric and magnetic dipoles in multiferroic and magnetoelectric materials holds immense promise for potential applications in sensors, data storage, and novel spintronics devices [1, 2, 3]. However, there are few multiferroic materials having coexistence of ferromagnetic and ferroelectric properties in the same phase. Therefore, the pursuit of the novel multiferroics, where these two phenomena are mutually coupled, is of significant scientific and technological concern [4, 5]. In Type-II multiferroic materials, the coupling between the electrical and magnetic ordering coexists and they have the same origin, where ferroelectricity is caused by an unusual magnetic order. However, the compounds or semiconductors having perovskite structure have been found to exhibit spontaneous magnetic and electrical ordering in the same phase, where both the polarization and magnetization can be switched by an applied electric and magnetic field, respectively [5, 6, 7]. Generally, multiferroicity has been found to exist in perovskites at low temperature, where the polarization values are low [6, 7]. Hence, the quest for high-temperature multiferroics is still very challenging. Among various approaches adopted, doping of metal ions and fabrication of various nanostructures help to improve the coexistence of the magnetic and electrical properties of the perovskites at room temperature [8,9]. Recently, the multiferroic properties of the different double perovskites have attracted considerable attention [10, 11]. Among them bulk $Y_2NiMnO_6$ (YNMO) have been found having low Curie temperature and *E*-type antiferromagnetic (AFM) ordering [12].

In general, redox active transition-metal oxide (TMOs) such as $RuO_2$, $Fe_2O_3$, ZnO, $TiO_2$, NiO, $MnO_2$, $SnO_2$, CuO, $Co_3O_4$, $WO_4$, $V_2O_5$ etc. [13, 14, 15, 16, 17, 18, 19, 20, 21, 22, 23, 24, 25] have demonstrated high specific capacitance, fast and excellent reversible faradic reaction. Multiferroic oxide materials play a crucial role in digital electronic materials industries such as memory devices, actuators, transducers, spintronics devices, magnetic data storage media, sensors, logic devices and so on [26, 27, 28, 29]. The remarkable supercapacitance property of Mn, Ni and Y based oxides have driven our interest to study their complex oxide, double perovskite $Y_2NiMnO_6$, a newly

emerged multiferroic material [29]. In the present era of developing multifunctional materials, we are inspired by the recent findings of multiferroics such as $BiFeO_3$ thin film, nanorod, and nanoflake, $BiMn_2O_5$ nanoparticles to be potential candidates for Supercapacitors (SCs) electrodes [30, 31, 32, 33, 34]. The specific capacitance of $BiFeO_3$ nanoflake is 72.2 $Fg^{-1}$ at a current density of 1 $Ag^{-1}$ and sharply falls to 36.3 F $g^{-1}$ at a current density of 5 $Ag^{-1}$. This indicates that only 50% of capacitance was retained as the current density increased from 1 $Ag^{-1}$ to 5 $Ag^{-1}$ [31]. Electrodeposited $BiFeO_3$ thin film showed a comparable specific capacitance of 81 $Fg^{-1}$ [30]. However, till date, there is no report in the literature about the electrochemical properties of $Y_2NiMnO_6$.

In this work, we have fabricated and studied the multiferroic and supercapacitive property of the $Y_2NiMnO_6$ nanowires (NWs), prepared by the solvothermal route. The unique one dimensional (1D) morphology and high aspect ratio of the NWs provide ample opportunity to tune the multiferroic property of the $Y_2NiMnO_6$ compound. Although the Curie temperature of the $Y_2NiMnO_6$ NWs is ~ 50 K, the NWs are found to exhibit unexpected weak ferromagnetism and ferroelectric ordering at room temperature. Here, we have explored the fundamental physics behind the mutual coexistence of ferromagnetism and ferroelectricity at room temperature. Comparing the results of the bulk $Y_2NiMnO_6$ with that of the $Y_2NiMnO_6$ NWs we demonstrate that the surface spin and the surface charge polarization is responsible for the unusually high temperature multiferroic property of the NWs. It is found that the spontaneous ferromagnetism and ferroelectricity are mutually coupled and they have the same origin.

Here, we have also reported the electrochemical properties of $Y_2NiMnO_6$ bulk and nanowires. $Y_2NiMnO_6$ bulk exhibiting specific capacitance of 17.4 $Fg^{-1}$, the energy density of 0.197 $Whkg^{-1}$, the power density of 7.81 $Wkg^{-1}$ and 85% retention efficiency after 1800 cycles. Moreover to improve the supercapacitance property, due to enhanced surface area and better charge transportation at nano-scale, the NWs show superior electrochemical properties having a specific capacitance of 77.76 $Fg^{-1}$, the energy density of 0.98 $Whkg^{-1}$, the power density of 19.27 $Wkg^{-1}$ and retention of 70.17% efficiency after

1800 cycles. We hope that our newly developed synthesis strategy and supercapacitance of $Y_2NiMnO_6$ NWs will open up the applicability of this material in the area of energy storage devices.

## 5.2. Experimental

Single-phase polycrystalline $Y_2NiMnO_6$ NWs are fabricated by the solvothermal route. $Y(NO_3)_3.6H_2O$, $Ni(NO_3)_3.6H_2O$ and $C_4H_6MnO_4.4H_2O$ are dissolved in equal weights in 40 ml DI water. A 5M 10 ml solution of NaOH is added drop by drop to the above solution to adjust the *pH* of the solution to 12. After the addition of NaOH the precipitation of mixed $Y(OH)_3$, $Ni(OH)_2$ and $Mn(OH)_2$ took place. The mixture is stirred for 30 minutes and then transferred it into a Teflon-lined stainless steel autoclave. The autoclave is tightly sealed and then heated at 200 $^0$C for 24 hours. The product thus obtained is washed successively in DI water, acetone and ethanol and dried at 70 $^0$C for another 24 hours.

The bulk powder of polycrystalline $Y_2NiMnO_6$ is prepared by the sol-gel method. High purity $Y(NO_3)_3. 6H_2O$, $Ni(NO_3)_3.6H_2O$ and $C_4H_6MnO_4. 4H_2O$ are dissolved in DI water in equal weights according to their stoichiometric ratios, followed by constant stirring of the mixture for about 30 minutes at room temperature. The citric acid is added to the solution with a 2:1 molar ratio with respect to metal ions under constant stirring. Afterwards, the solution is heated at 150 $^0$C until a thick solution is formed and then the thick mixture is calcined at 1000 $^0$C for 12 h to prepare the powder sample.

The phase and structure of the samples are investigated by X-ray diffraction (XRD) using CuK$_\alpha$ radiation (Panalytical, X'part Pro, $\lambda$ = 1.5418 Å). Field Emission Scanning Electron Microscope (FESEM) (FEI QUANTA FEG-250) and High-Resolution Transmission Electron Microscope (HRTEM) are used to study the morphology and particle size of $Y_2NiMnO_6$ NWs. Elemental analysis is performed from energy dispersive X-ray (EDX) spectrum. Superconducting Quantum Interference Device (SQUID) is used for magnetic measurements while ferroelectric measurements (inherent electric polarization) are carried out using a high precession *P-E* measurement

system (Radiant Technologies). An LCR meter (NF Corporation) is used to measure dielectric properties of $Y_2NiMnO_6$ NWs over the frequency range $10^{-1}$-$10^6$ Hz. Magnetoelectric coupling is studied using a home-made set-up as discussed earlier in Chapter-2 (subsection 2.6.3) [35] with dynamic lock-in technique.

For electrochemical measurements, the working electrodes are constructed by mixing the active material, acetylene black (AB), polyvinylidene fluoride (PVDF) binder in a weight ratio of 8:1:1, which are mixed in N-methyl-2-pyrrolidinone (NMP) solvent and dropped uniformly into the Ni foam. Then it is dried under IR lamp for 10 minutes and immersed into vacuum. The mass of the deposited product is calculated by carefully weighing the piece of Ni foam before and after having grown $Y_2NiMnO_6$ bulk and nanowires.

The electrochemical properties of the $Y_2NiMnO_6$ NWs and its bulk counterpart are investigated with cyclic voltammetry (*CV*) tests by using a software-controlled conventional three-electrode electrochemical cell (potentiostat Autolab-30) consisted of $Y_2NiMnO_6$ NWs over Ni foam as the working electrode, saturated *Ag/AgCl* as the reference electrode and a highly pure *Pt* wire as the counter electrode in a 0.5 M KOH electrolyte at room temperature. The *CV* measurement is carried out at different scan rates of 2, 5, 10, 25, 50 and 100 mV/s within a potential range of 0.2 to 0.5 V at room temperature. The specific capacitance ($C_{sp}$), the energy density (*E*) and power density (*P*) are measured by using galvanostatic charging /discharging (*GCD*) experiments at different current densities such as 30, 45, 60, 90, 120 and 150 mA/g. The specific capacitances are determined from the charging/discharging curves by using the following formula,

$$C_{\text{sp}} = \frac{I\Delta t_d}{m\Delta V} \tag{5.1}$$

where *I* is the discharge current, $\Delta t_d$ is the discharging time, $\Delta V$ is the potential window excluding IR drop region, *m* is the active mass of the material, i.e. the mass of NWs and powder (for bulk) over Ni foam substrate.

Furthermore, the energy and power densities of the electrodes are determined by the following formulae, respectively,

$$E = \frac{1}{2}C_{\text{sp}}(\Delta V)^2 \tag{5.2}$$

$$P = \frac{E}{\Delta t_d} \tag{5.3}$$

where $E$ (Whkg$^{-1}$), $P$ (kWkg$^{-1}$), $C_{sp}$ (Fg$^{-1}$), $\Delta V$ (V), and $\Delta t_d$ (s) are the energy density, power density, specific capacitance, potential window of discharge, and discharging time, respectively. The alternating current ($AC$) complex impedance is measured in the frequency range from 10 mHz to 10 kHz at the amplitude of the $AC$ signal of 5 mV. The average mass loadings densities of $Y_2NiMnO_6$ bulk and NWs on Ni foam are 3 and 2.5 mg cm$^{-2}$, respectively.

## 5.3. Results and discussions

### 5.3.1. Morphology and structural analysis of $Y_2NiMnO_6$ nanowires

The XRD pattern (Fig. 5.1(a)) indicates the single-phase polycrystalline monoclinic structure of the $Y_2NiMnO_6$ NWs with $P2_1/n$ space group [6, 36]. Fig. 5.1(b) shows the FESEM image of the as-prepared $Y_2NiMnO_6$ NWs. The diameter of the NWs is found to be quite uniform (~200 nm) in nature. Fig. 5.1(c) shows the energy dispersive X-ray (EDX) spectra of YNMO NWs, which confirm all the elements are present in the NWs. Transmission electron microscope (TEM) image of a single $Y_2NiMnO_6$ NW, shown in Fig. 5.2(a), again clarify the uniformity in the diameter of the NW. The representative high-resolution TEM (HRTEM) micrograph of the NW, as shown in Fig. 5.2(b), demonstrates the polycrystalline nature of the NW with a dissimilar orientation of the different crystallographic planes having different lattice spacing. The lattice spacing between the (012) and (112) crystalline planes has been measured as 0.31 and 0.26 nm, respectively. The selective area electron diffraction ($SAED$) pattern taken from the area covered under the HRTEM study also clarifies the polycrystalline nature of the NWs (Fig. 5.2(c)). Fig. 5.2(d)-(g) represent the energy filtered TEM ($EFTEM$) micrographs of a single $Y_2NiMnO_6$ NW, where the colour mapping of different elements present in $Y_2NiMnO_6$ shows a uniform distribution in the body of the NW, which again confirms the successful synthesis of the NWs.
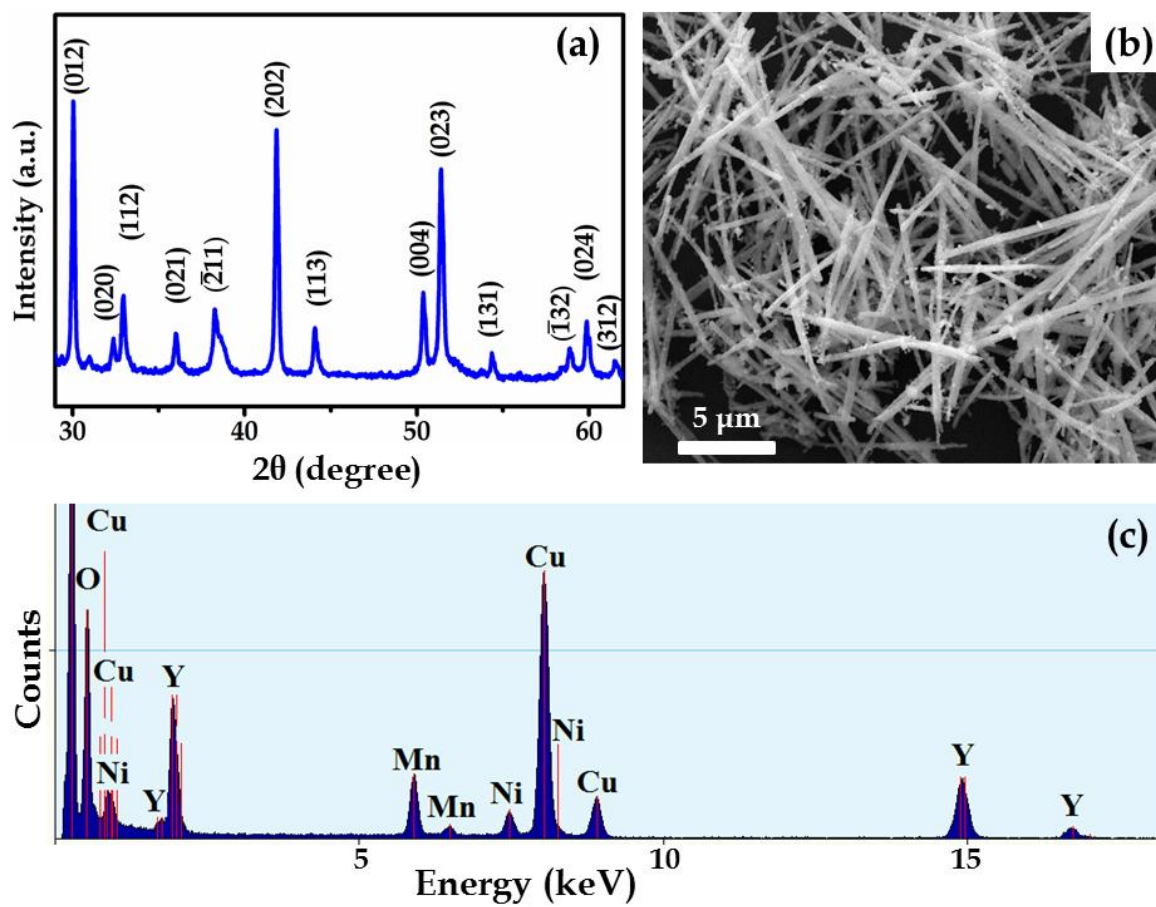
**Fig. 5.1:** (a) XRD pattern, (b) SEM image and (c) EDX spectroscopic analysis of $Y_2NiMnO_6$ NWs.
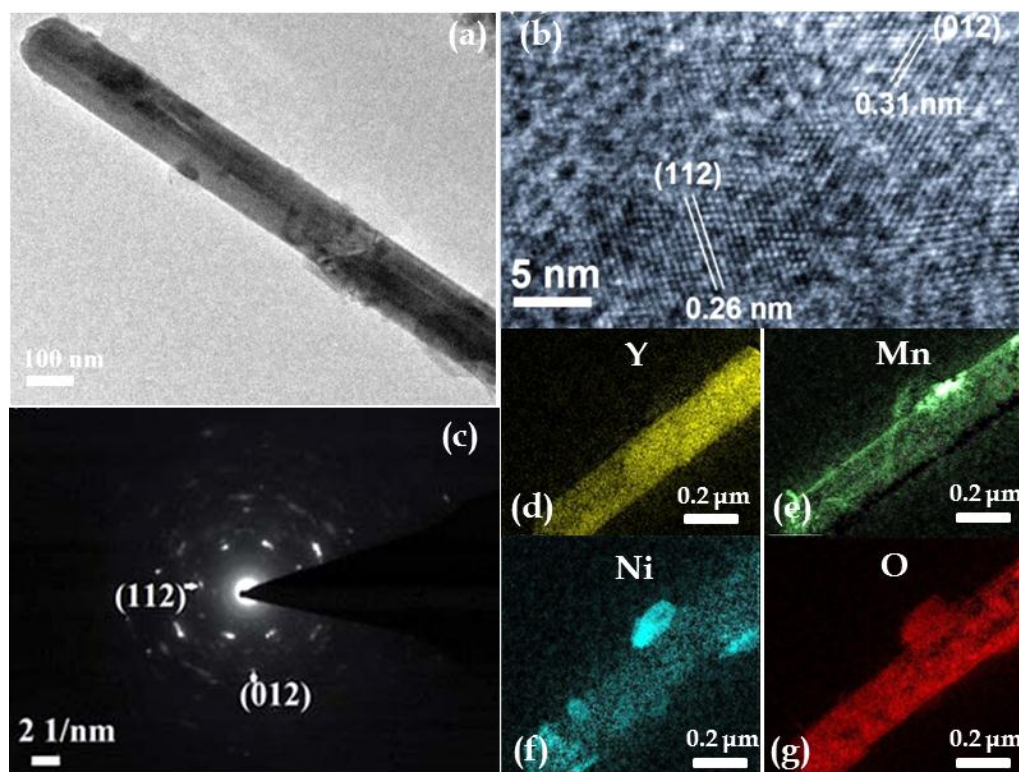
**Fig. 5.2:** (a) TEM, (b) HRTEM micrographs and (c) SAED pattern of the as prepared $Y_2NiMnO_6$ NWs. (d–g) EFTEM micrographs of the $Y_2NiMnO_6$ NWs.

The chemical composition of the as-prepared $Y_2NiMnO_6$ NWs has also been studied by x-ray photoelectron spectroscopy (*XPS*). In the as-prepared NWs the $Y3d_{5/2}$ and $Y3d_{3/2}$ doublet peaks appear at 156.5 and 158.5 eV, respectively, which indicate the +3 oxidation state of Y in $Y_2NiMnO_6$ [37] as shown in Fig. 5.3(a). Fig. 5.3(b) shows the *XPS* spectrum for the Ni, where the peaks of Ni $2P_{3/2}$ and Ni $2P_{1/2}$ situated at 855.5 and 873.4 eV, respectively, represent the divalent (+2) state for Ni in $Y_2NiMnO_6$ [6, 7]. The broad peak around 862 eV is a satellite peak related to Ni $2P_{3/2}$, again indicating +2 oxidation state of Ni in the compound [37]. In the *XPS* spectrum of Mn (Fig. 5.3(c)) the positions of the characteristics peaks of Mn $2P_{3/2}$ and Mn$2P_{1/2}$ have been found at 642.2 and 653.4eV, respectively, correspond to the tetravalent (+4), the oxidation state of Mn in the NWs. The XPS spectrum of O 1s core level, as shown in Fig. 5.3(d), shows a sharp Gaussian peak centred on 529.7 eV can be assigned to the −2 oxidation state of oxygen in the $Y_2NiMnO_6$ NWs [38].
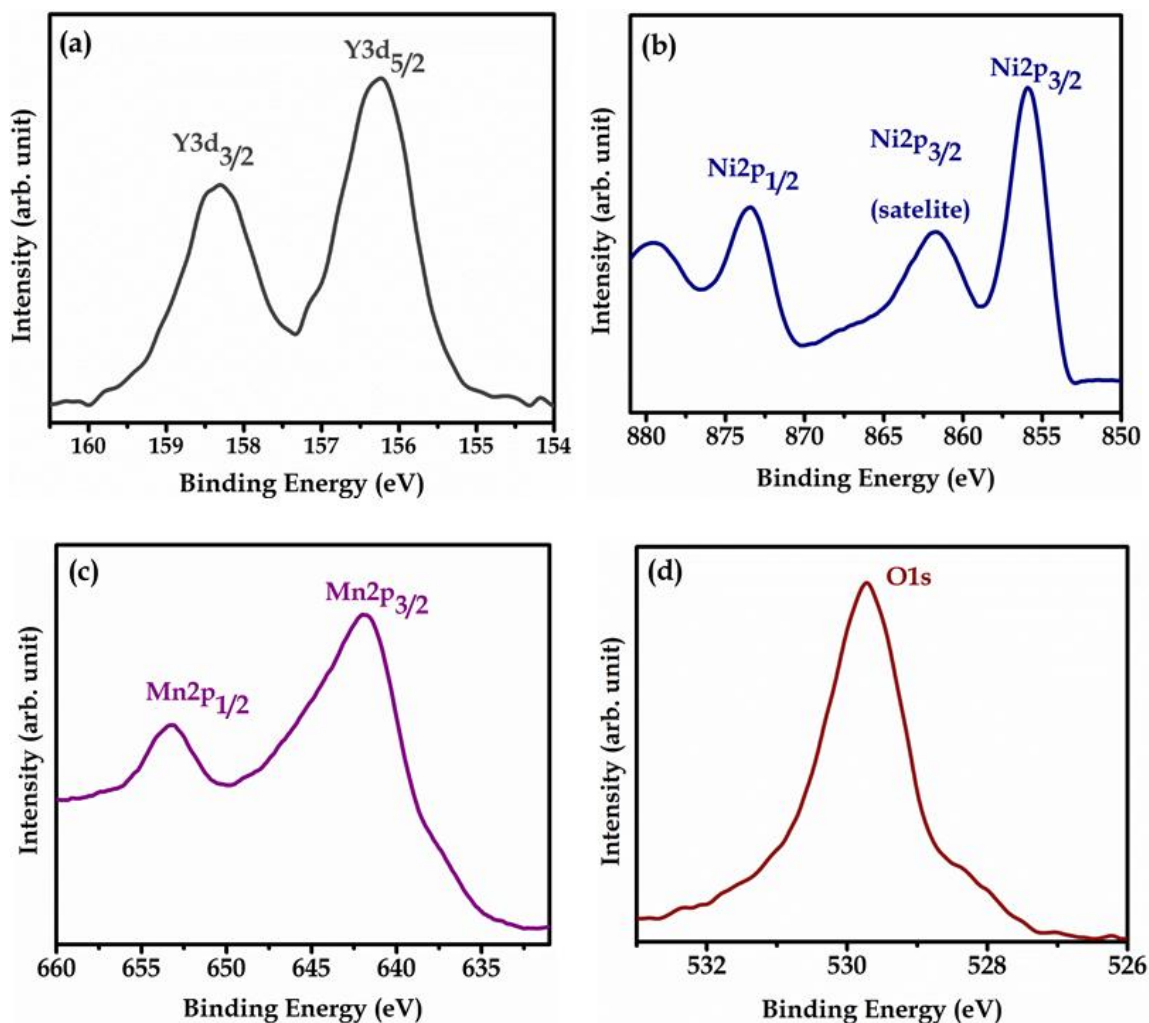
**Fig. 5.3:** XPS spectra of (a) Y3d, (b) Ni2p, (c) Mn 2p and (d) O 1s core levels of the $Y_2NiMnO_6$ NWs.

### 5.3.2. *Magnetic properties of $Y_2NiMnO_6$ nanowires*

$Y_2NiMnO_6$ NWs have been found to exhibit interesting magnetic properties. The variation of magnetization as a function of temperature under both zero field cooled (*ZFC*) and field cooled (*FC*) condition, measured at 1 kOe of the applied field are shown in Fig. 5.4(a) for the NWs and bulk $Y_2NiMnO_6$. The sharp change of the *FC* and *ZFC* curves at a particular temperature indicates the ferromagnetic transition. The ferromagnetic Curie temperature ($T_C$) calculated for bulk and NWs of $Y_2NiMnO_6$ are 91 and 50 K, respectively. The $T_C$ for the NWs has been found to be considerably lower than that of the bulk $Y_2NiMnO_6$. However, both the NWs and bulk $Y_2NiMnO_6$ exhibit

ferromagnetism (FM) at 4 K, as shown in Fig. 5.4(b). The ferromagnetism in the $Y_2NiMnO_6$ bulk and NWs samples indicates strong coupling among the dipoles at temperature below $T_C$. Fig. 5.4(c) shows the magnetization versus magnetic field (*M-H*) hysteresis curves for the $Y_2NiMnO_6$ NWs at different temperatures, below and well above $T_C$. It is evident that $Y_2NiMnO_6$ NWs exhibit weak FM above $T_C$. The saturation magnetism is found to decrease with increase in temperature as expected. Fig. 5.4(d) compares the *M-H* curve of the bulk and NWs of $Y_2NiMnO_6$ at 300 K. It is evident that at 300K, the bulk sample exhibits strong paramagnetic behavior whereas the NWs still show weak ferromagnetic signature.

$Y_2NiMnO_6$ is demonstrated as an *E*-type antiferromagnetic (AFM) material with ↑↑↓↓ spin structure because of the superexchange interaction between $Ni^{2+}$ and $Mn^{4+}$ [6, 12]. From the *XPS* experiment, we also have evidenced the presence of $Ni^{2+}$ and $Mn^{4+}$ in $Y_2NiMnO_6$. However, very interestingly the magnetic measurements indicate definite ferromagnetic characteristics of the $Y_2NiMnO_6$ NWs and bulk with specific $T_C$. It is reported that the ↑↑↓↓ spin structure in $Y_2NiMnO_6$ only exists at zero magnetic field and this AFM spin order can be destroyed with the applied magnetic fields [6]. Therefore, we propose that, below $T_C$, the AFM (↑↑↓↓) spin arrangement of $Y_2NiMnO_6$ have been transformed into ferromagnetic ordering under the applied magnetic field and this is the reason behind the FM of NWs and bulk structure of $Y_2NiMnO_6$ below $T_C$. However, most surprisingly, $Y_2NiMnO_6$ NWs shows weak FM above $T_C$, whereas the bulk $Y_2NiMnO_6$ structure is found to exhibit purely paramagnetic ordering beyond $T_C$. This type of unexpected room temperature (RT) FM is reported for nanostructures of different antiferromagnetic oxides [8, 9, 39]. The RTFM for such oxides could have different origins as demonstrated in different reports. However, in the present study, the unusual RTFM in $Y_2NiMnO_6$ NWs is attributed to the surface spins, which are expected to dominate because of their lower coordination and uncompensated exchange couplings in nanostructures [40, 41, 42, 43]. Moreover, in 1D nanostructures like NWs the concentration of surface electron is significantly higher because of the large surface area and high aspect ratio of the NWs. Now, an applied magnetic field can

orient the surface spins and the interaction among the uncompensated surface spins lead to the ferromagnetic ordering in the NWs [42]. Therefore, the surface electron spins or spins of the space charge are responsible for the high-temperature FM in $Y_2NiMnO_6$ NWs whereas such spin coupling is weak for the bulk sample because of its low surface area and hence the bulk $Y_2NiMnO_6$ shows paramagnetism at high temperature (above $T_C$).
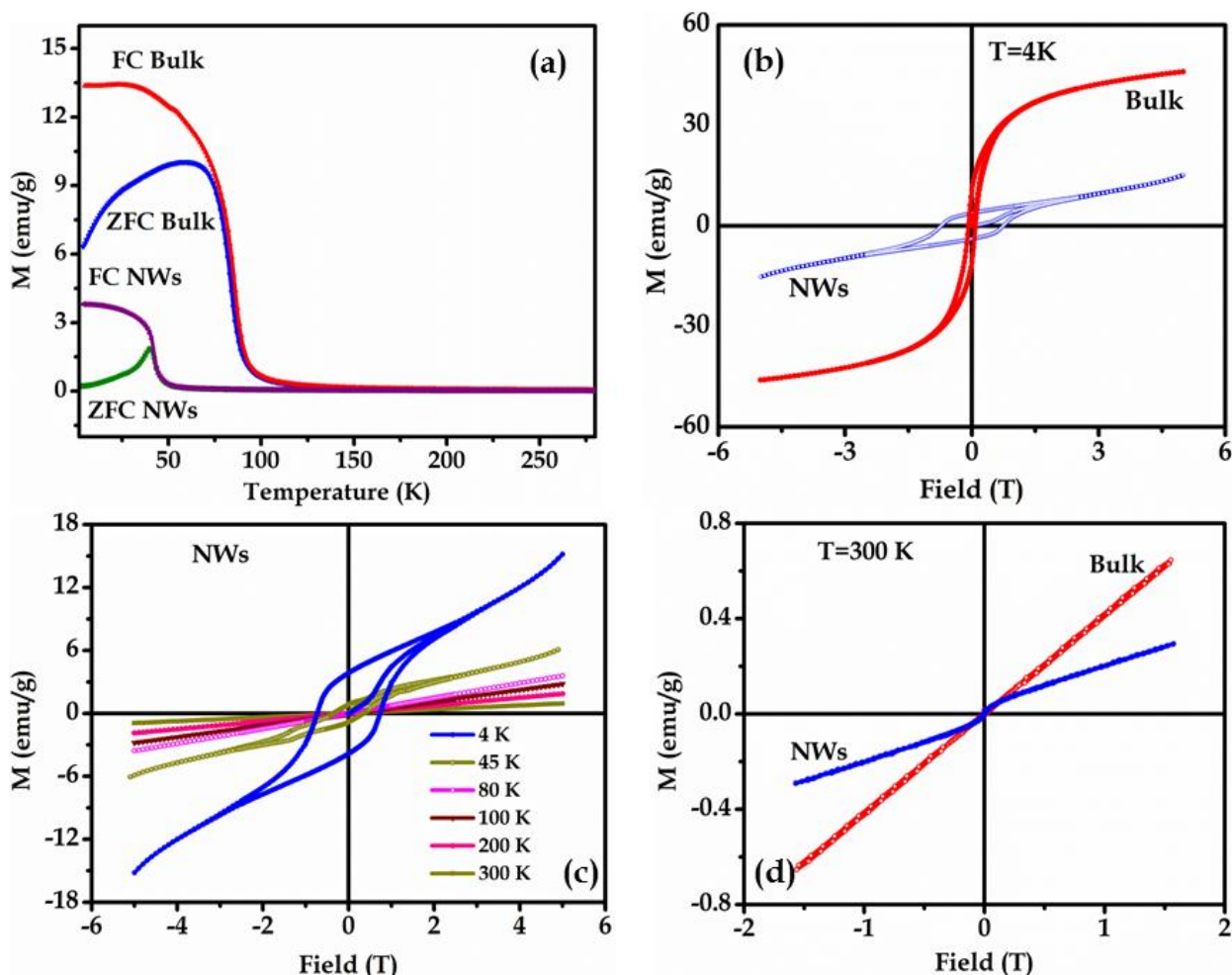


**Fig. 5.4:** (a) Variation of magnetization as a function of temperature under ZFC and FC condition for the $Y_2NiMnO_6$ NWs and bulk samples measured in magnetic field of 1KOe. Magnetization versus magnetic field hysteresis loops for the (b) $Y_2NiMnO_6$ NWs and bulk at 4 K, (c) $Y_2NiMnO_6$ NWs at 4, 45, 80, 100, 200 and 300 K and (d) $Y_2NiMnO_6$ NWs and bulk at 300 K.

### 5.3.3. *Ferroelectric properties of $Y_2NiMnO_6$ nanowires*

More clear understanding of the origin of unusually high temperature ferromagnetic behaviour of $Y_2NiMnO_6$ NWs can be obtained from the study of the ferroelectric

property of the sample. Recently, it is reported that the magnetic order can build up weak ferroelectricity and vice versa [4, 44]. The above studies indicate that the magnetic order and electric polarization likely to be mutually coupled and seem to have a similar origin [3]. Hence, study on the ferroelectric property of the $Y_2NiMnO_6$ NWs could be meaningful in order to understand the unusual RTFM of the NWs. The ferroelectric *P-E* loop of the $Y_2NiMnO_6$ NWs has been measured by dispersing the NWs assembly on FTO glass substrate and by connecting with the wire through conducting Ag paste as shown in Fig. 5.5(a). The same measurement has been performed on the bulk $Y_2NiMnO_6$ sample by preparing a pellet using the powder $Y_2NiMnO_6$. Fig. 5.5(b) and (c) display the *P-E* loops of the $Y_2NiMnO_6$ NWs and bulk samples recorded at 80 and 300 K. It is evident from Fig. 5.5(b) that at 80 K both the $Y_2NiMnO_6$ NWs and bulk samples exhibit stable ferroelectric property (measured at a applied bias of 1 V), where the bulk sample shows strong ferroelectric signature compared to the NWs. On the other hand, very interestingly, at 300 K, the $Y_2NiMnO_6$ NWs exhibit strong and stable ferroelectric polarization compared with the bulk sample, which shows a loosy type feeble ferroelectric characteristics (Fig. 5.5(c)). The RT (~300 K) *P-E* hysteresis loops of the $Y_2NiMnO_6$ NWs measured at different applied voltages also found to be stable and repeatable as shown in Fig. 5.5(d).

This study reveals that at the temperature of 80 K (which is below the $T_C$ for $Y_2NiMnO_6$ bulk samples ~ 91 K but above the $T_C$ for $Y_2NiMnO_6$ NWs ~ 50 K) both the $Y_2NiMnO_6$ bulk and NWs sample exhibit stable ferromagnetism and ferroelectricity, whereas, only the $Y_2NiMnO_6$ NWs possess a net electric polarization and ferromagnetism above $T_C$ (also at 300 K). The bulk $Y_2NiMnO_6$ sample exhibits stable paramagnetism and feeble ferroelectricity at a temperature of 300 K. Based on these results, it is evident that the electric polarization is intimately coupled to the ferromagnetic ordering. It is found that whenever ferromagnetism exists the dielectric polarization exists and if there is no ferromagnetism there is no ferroelectric polarization too. Hence, this coexistence of ferromagnetism and ferroelectricity is most expectedly having the similar origin [6, 45]. Here, we expect that the space charges

associated with the large surface area of the $Y_2NiMnO_6$ NWs, which are responsible for the ferromagnetic order in the NWs under applied magnetic field at 300 K (room temperature), can also induce electric polarization and tune the *P-E* hysteresis loops and field distributions in NWs [46, 47]. However, for bulk $Y_2NiMnO_6$ sample the coexistence of the ferromagnetism and ferroelectricity at a temperature below its $T_C$ has already been reported in details based on the braking of the spatial inversion symmetry [6, 7].

However, the coexistence of ferromagnetism and ferroelectricity in the same phase of different compound materials are known, where the spontaneous magnetization can be switched by an applied external magnetic field and the electrical polarization can be triggered by an applied electric field too [5, 48]. In most of the magnetic ferroelectric materials the coexistence of the ferromagnetism and ferroelectricity below Curie temperature are demonstrated based on the braking of the spatial inversion symmetry [5, 12]. However, in our work the unusually high-temperature FM and ferroelectricity in $Y_2NiMnO_6$ NWs must have different origin and that could be ascribed to the effects of space charge. The steady variation of the remnant polarization, saturation polarization and coercive field with applied external bias clearly demonstrate the stable ferroelectric characteristics of the $Y_2NiMnO_6$ NWs at room temperature, 300 K (Fig. 5.5(e)-(f)).
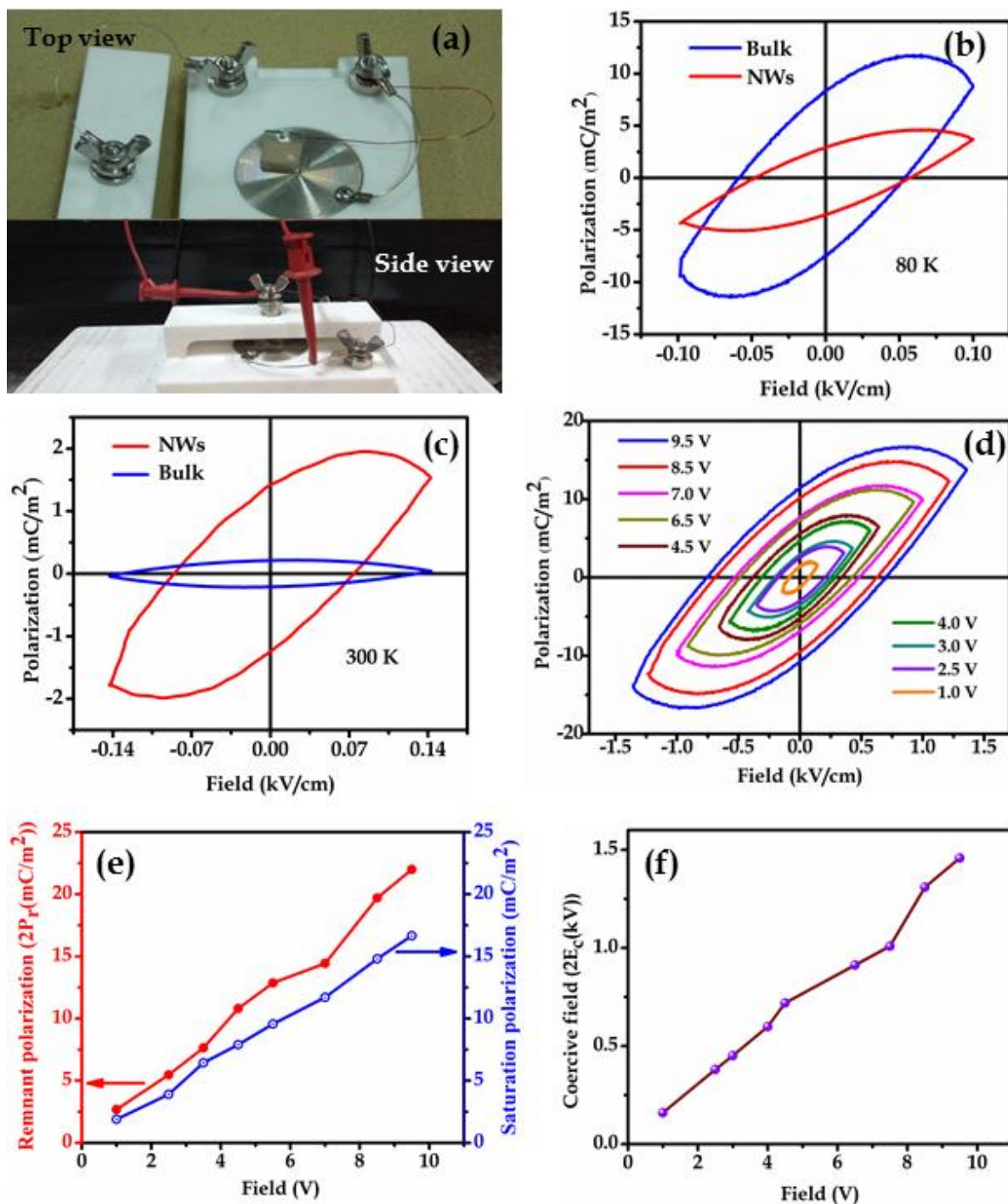
**Fig. 5.5:** (a) The photographs for the *P–E* measurement set up for the Y$_2$NiMnO$_6$ NWs. (b) Variation of the *P–E* hysteresis loops for the Y$_2$NiMnO$_6$ NWs and bulk at (b) 80 K and (c) 300 K (room temperature). (d) Variation of the room temperature (300 K) *P–E* hysteresis loops with applied voltage for the Y$_2$NiMnO$_6$ NWs. Variation of the (e) saturation polarization and remnant polarization and (f) coercive field with applied voltage in Y$_2$NiMnO$_6$ NWs.

## 5.3.4. Dielectric properties of Y₂NiMnO₆ nanowires

The frequency-dependent dielectric constant of $Y_2NiMnO_6$ NWs with different temperature is shown in Fig. 5.6(a), (b). Here from figures, we see that the dielectric constant of $Y_2NiMnO_6$ NWs is very high ~ (at 1 kHz). The dielectric constant increases significantly with increasing temperature especially at low frequency as shown in Fig. 5.6. The dielectric loss (Fig. 5.6(b)) increases because of the contribution of DC conductivity in $Y_2NiMnO_6$ NWs, probably due to the hopping conduction between $Mn^{+3}$ to $Mn^{+4}$. The frequency-dependent dielectric constant and dielectric loss at different temperature are fitted with a modified Debye equation,

$$\varepsilon^* = \varepsilon' + j\varepsilon'' = \varepsilon_\infty + \frac{\varepsilon_s - \varepsilon_\infty}{[1 + (i\omega\tau)^\alpha]} \tag{5.4}$$

where $\varepsilon_\infty$, $\varepsilon_s$ are the high and low frequency dielectric constants, $\omega$ is the angular frequency, and $\tau$ is the mean relaxation time. $\alpha$ is the measure of the distribution of relaxation ($\alpha$ = 1 corresponds to the standard Debye relaxation). The calculated value of $\alpha$ is close to 0.85 [49]. The fitted results are presented as solid lines in Fig 5.6.
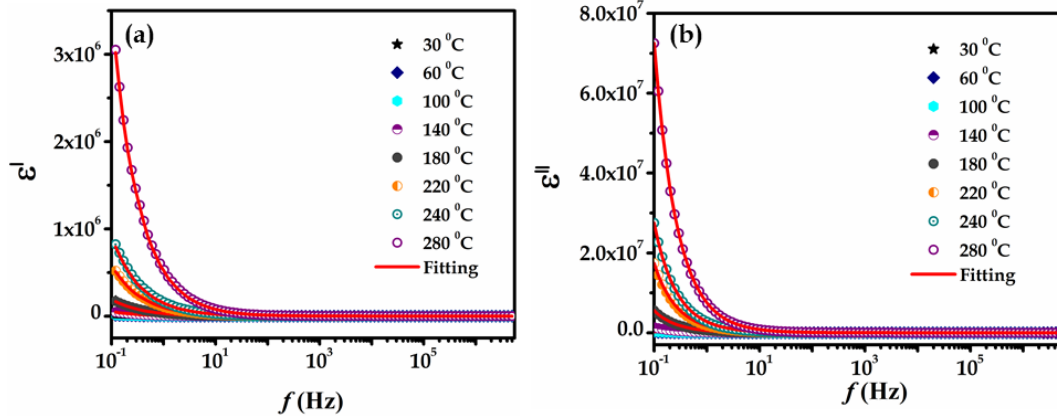


**Fig. 5.6:** Frequency dependence of (a) $\varepsilon'$ and (b) $\varepsilon''$ of $Y_2NiMnO_6$ NWs with different temperatures, the solid lines are the theoretical fits.

Using this relaxation time, the activation energy of $Y_2NiMnO_6$ NWs are calculated from Arrhenius equation

$$\tau = \tau_0 exp\left(\frac{E_r}{K_B T}\right) \tag{5.5}$$

where $\tau_0$ is the prefactor, $E_r$, the activation energy for dielectric relaxation, $T$, the absolute temperature and $K_B$, the Boltzmann constant. From Fig. 5.7 the calculated value

of activation energy is about ~ 0.16 eV, which is close to the energy required to transfer an electron from $Ni^{+2}$ to $Mn^{+4}$.
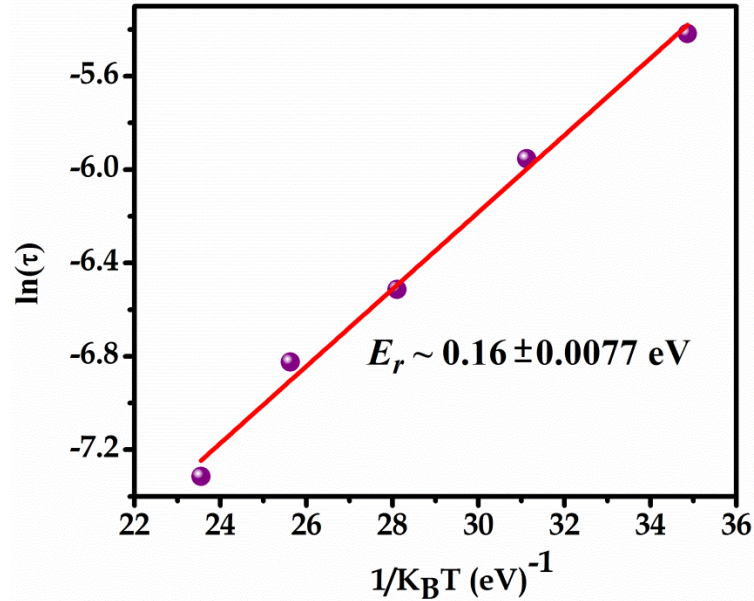


**Fig. 5.7:** Arrhenius plot of the relaxation time for the $Y_2NiMnO_6$ NWs.

## 5.3.5. *Magneto-dielectric and magnetoelectric coupling properties of* $Y_2NiMnO_6$ *nanowires*

The magnetic field dependence of dielectric constant, which is called magnetodielectric (MD) effect, is measured to confirm the ME coupling of the YNMO NWs sample. Fig. 5.8(a) shows that magnetic field dependent of MD effect, using the expression $[\varepsilon_r(H)-\varepsilon_r(0)]/\varepsilon_r(0)$ at different frequencies of the YNMO sample.

It is more clear understanding of the origin of unusual room temperature ferromagnetism and ferroelectricity of $Y_2NiMnO_6$ NWs can be obtained by using the magnetoelectric coupling coefficient measurement of the sample. The value of the magnetoelectric coefficient is determined using the formula

$$\alpha_{ME} = \frac{dE}{dH} = \frac{1}{d}\frac{V_{out}}{H_{ac}}\tag{5.6}$$

where $d$ is the effective thickness of the sample (in the form of pellet). A small ac magnetic field, $H_{ac}$ produced by a Helmholtz coil, is superimposed to a DC magnetic field, $H_{dc}$. The longitudinal magnetoelectric coefficient versus DC magnetic field

exposes hysteresis curve as shown in Fig. 5.8(b). Here the magnetoelectric coefficient increases with increasing DC magnetic field and attains a maximum value about ~ 25 mV/Oe cm when the maximum magnetostriction appears, as claimed by Sosnowska et al [50]. The obtained value of the magnetoelectric coefficient is quite high compared to the other reported sample [51, 52, 53] and is smaller than some other thin films [54, 55].
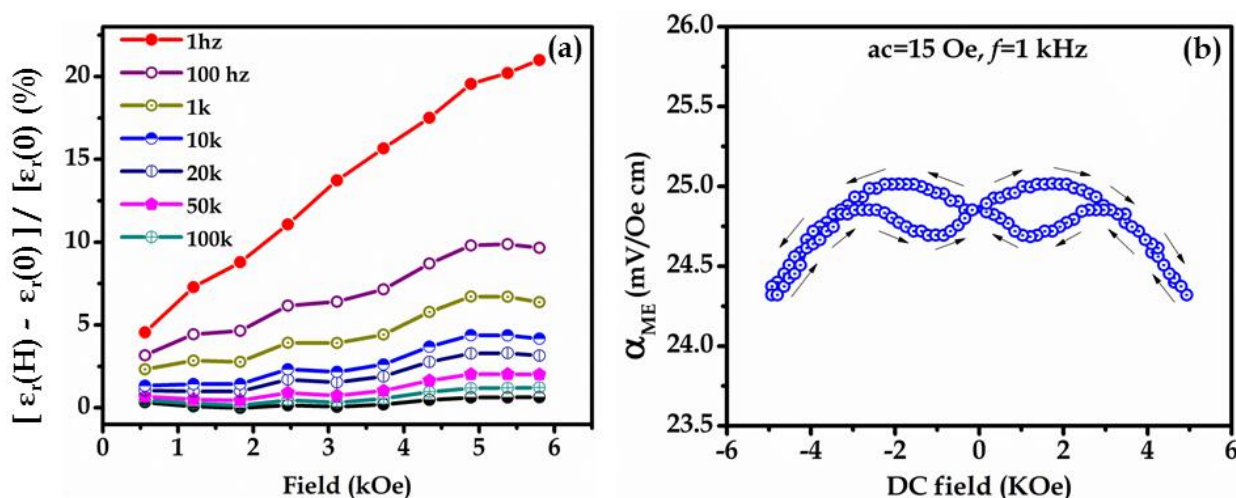


**Fig. 5.8:** (a) MD vs applied field plot of $Y_2NiMnO_6$ NWs at different frequencies. (b) Variation of magnetoelectric coefficient of $Y_2NiMnO_6$ NWs with applied DC magnetic field at a constant frequency, $f$=1 kHz of $H_{ac}$.

### 5.3.6. Supercapacitive property of $Y_2NiMnO_6$ nanowires

Fig. 5.9(a) and (b) respectively show the cyclic voltammetry (*CV*) curves of the $Y_2NiMnO_6$ bulk/Ni foam and $Y_2NiMnO_6$ NWs/Ni foam electrodes measured at different scan rates of 2, 5, 10, 25, 50 and 100 mV/s within the same voltage window of 0.2-0.5 V in 0.5 M aqueous KOH electrolyte. Distinct oxidation and reduction peaks in each of the curves demonstrate the pseudocapacitive behavior of the $Y_2NiMnO_6$ bulk as well as $Y_2NiMnO_6$ NWs, which is quite different from the nearly rectangular *CV* loops for conventional electric double-layer capacitors (EDLC). It is evident that with increasing scan rates the current response of the electrode increases and the shape of the *CV* curves remains the same through-out the whole range of scan rates (2 to 100 mV s-1). At low scan rates, a thick diffusion layer grows over the electrode which limits electrolyte flux towards the electrode resulting lower current. However, at higher scan

rates, the diffusion layer cannot grow wide over the electrolyte surface, which enhances electrolyte flux towards the electrode leading to increment of current. Again, from both bulk and NWs *CV* curves it is found that with increasing scan rates the upper and lower redox peaks shift towards positive and negative side respectively because of the development of over-potential which limits the faradic reactions. Our comparative investigation with only Ni foam and $Y_2NiMnO_6$ NWs grown over Ni foam at a scan rate of 100 mV/s, as demonstrated in Fig. 5.10, reveals that only Ni foam has a negligible contribution to the total capacitance. To further investigate electrochemical performances of the $Y_2NiMnO_6$ bulk and NWs grown over Ni foam as the electrodes for supercapacitors, we performed galvanostatic charging/discharging (*GCD*) experiments at various current densities in the potential window of 0.2 - 0.5 V as shown in Fig. 5.9(c) and (d). The specific capacitance values of the two electrodes at various current densities are determined based on their corresponding *GCD* curves (Fig. 5.11(a), and (b)). Table-I shows the basic comparison of specific capacitance ($C_{sp}$) of two electrodes ($Y_2NiMnO_6$ bulk/Ni and NWs/Ni foam), it clearly shows that the specific capacitance significantly increases in the case of $Y_2NiMnO_6$ NWs/Ni foam due to the increase in active surface area. Moreover, the $C_{sp}$ of the NWs remains 63.6 $Fg^{-1}$ even if the current density is increased to as high as 150 $mAg^{-1}$, implying 81.8% retention of its initial value as the current density is increased by 5 times. But in case of bulk only 56.33% capacitance is retained with 7.27 times increment of current density. This high specific capacitance with impressive rate capability of the NWs can be attributed to the higher surface area of the electrode with nano architectural design.
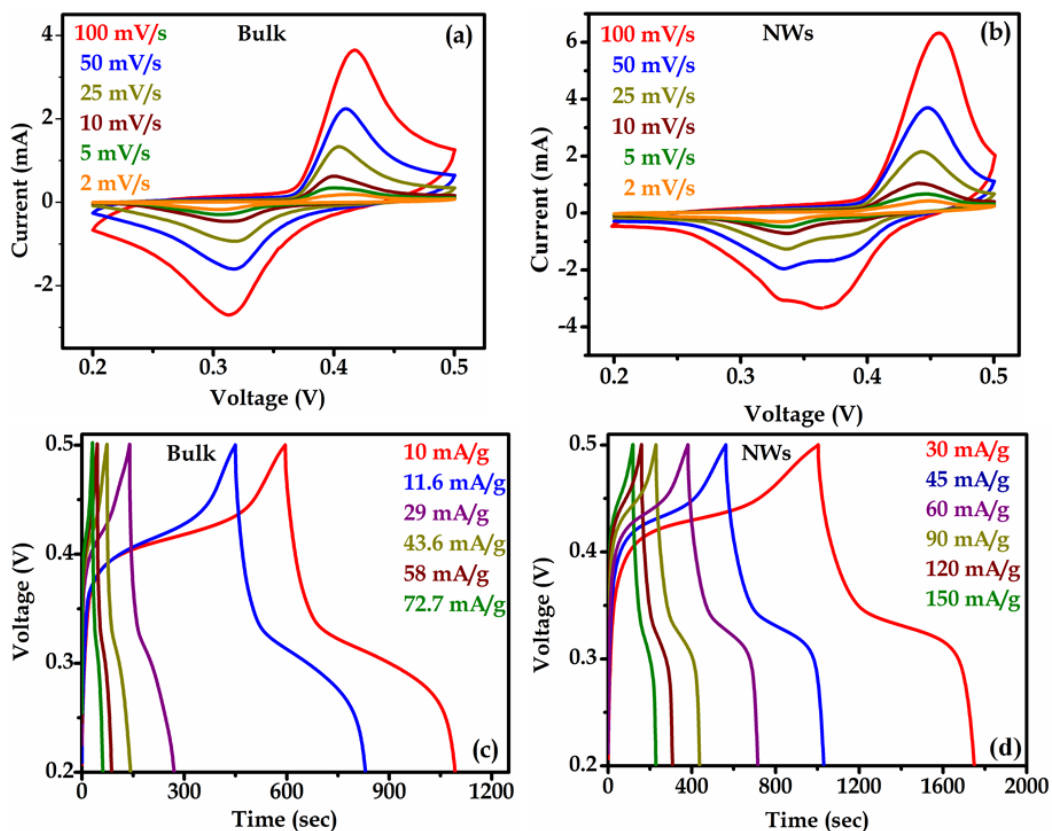
**Fig. 5.9:** Cyclic voltammetry curves of the $Y_2NiMnO_6$ bulk (a), and NWs (b) electrodes recorded at different scan rates in 0.5 M aqueous KOH electrolyte. Galvanostatic charge/discharge curves of the $Y_2NiMnO_6$ bulk (c) and NWs (d) electrodes recorded at different constant current densities.
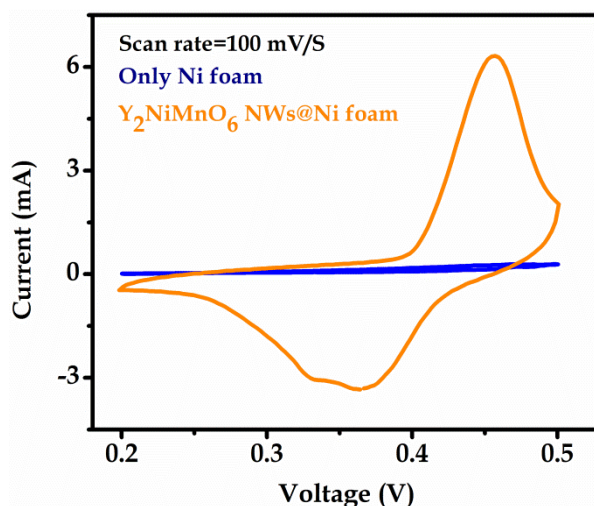


**Fig. 5.10:** Comparison between the CV curves of only Ni foam and $Y_2NiMnO_6$ NWs over Ni foam at scan rate of 100 mV s$^{-1}$.
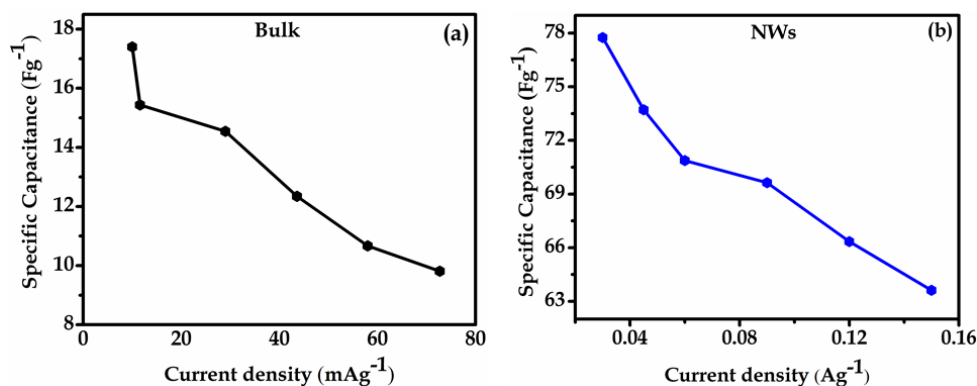
**Fig. 5.11:** Variation of Specific capacitance as a function of current densities of the $Y_2NiMnO_6$ bulk (a) and NWs (b), respectively, calculated from the charge/discharge curves.

**Table-5.1:** Comparison of the specific capacitance of $Y_2NiMnO_6$ bulk/Ni foam and $Y_2NiMnO_6$ NWs/Ni foam electrodes.

| | $Y_2NiMnO_6$ bulk/Ni foam electrodes | | | | | $Y_2NiMnO_6$ NWs/Ni foam electrodes | | | | |
|---|---|---|---|---|---|---|---|---|---|---|
| Current density (mAg$^{-1}$) | 10 | 29 | 43.6 | 58 | 72.7 | 30 | 60 | 90 | 120 | 150 |
| Specific capacitance(Fg$^{-1}$) | 17.4 | 14.4 | 12.3 | 10.6 | 9.8 | 77.7 | 70.8 | 69.6 | 66.3 | 63.6 |

Fig. 5.12(a) shows the energy density of the $Y_2NiMnO_6$ bulk electrode decreases from 0.197 to 0.0629 Whkg$^{-1}$ and the power density increases from 1.43 to 7.81 Wkg$^{-1}$ with the increment of current density from 10 to 72.7 mAg$^{-1}$. For NWs electrode, shown in Fig. 5.12(b), the energy density decreases from 0.98 to 0.58 Whkg$^{-1}$ and the power density increases from 4.32 to 19.27 Wkg$^{-1}$, as the current density increases from 30 to 150 mAg$^{-1}$. The $Y_2NiMnO_6$ NWs have superior supercapacitance as compared to its bulk counterpart exhibiting higher power density as well as energy density. Fig. 5.12(c) and (d) show the cyclic stability of the $Y_2NiMnO_6$ bulk and NWs electrodes, where charge/discharge tests have been conducted at a current density of 43.6 mAg$^{-1}$ and 30 mAg$^{-1}$, respectively, for 1800 cycles. The specific capacitance of $Y_2NiMnO_6$ bulk and NWs electrodes reduce 85% and 70.17%, respectively, after 1800 cycles, which confirms good stability of the electrodes. The inset of Fig. 5.12(c) and (d) respectively show the last 10 charge/discharge cycles of bulk and NWs electrodes and it can be seen that the symmetric triangular shape of the charging/discharging profile remains the same during the long cycle test, which implies that electrodes exhibit stable

electrochemical performance and facile charge transfer during the reaction without any significant structural change.
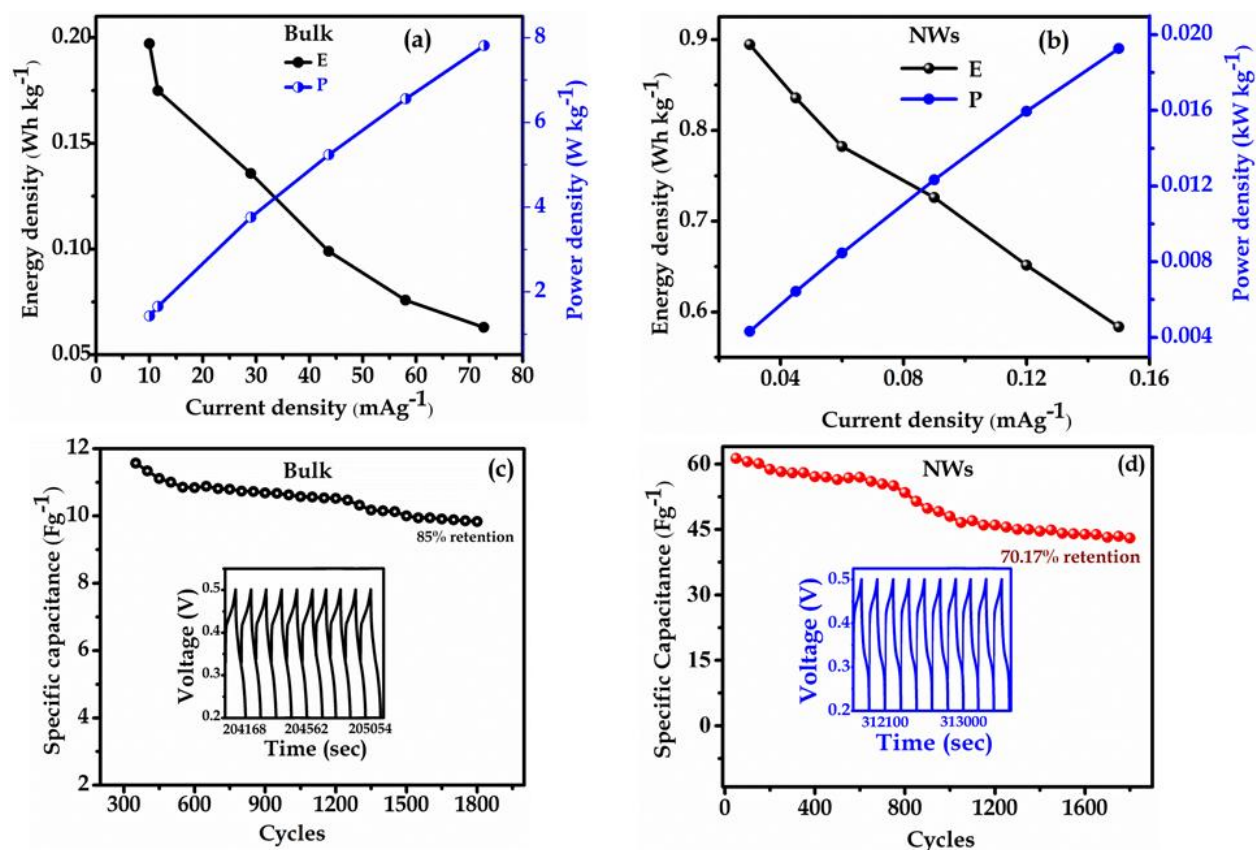


**Fig. 5.12:** Variation of power density, energy density of Y₂NiMnO₆ bulk (a) and NWs (b) electrodes as a function of different current density. Cyclic performance of Y₂NiMnO₆ bulk (1800 charge/discharge cycles at a constant current density of 43.6 mA/g) (c) and NWs (1800 charge/discharge cycles at a constant current density of 150 mA/g) (d) electrodes. Insets of (c) and (d) show last 10 cycles of the charging/discharging curves for bulk and NWs, respectively.

The electrochemical impedance spectroscopy (EIS) measurement of Y₂NiMnO₆ bulk and NWs are carried out at open circuit potential within a frequency range of 10 mHz to $10^4$ Hz with a voltage amplitude of 5 mV, as shown in Fig. 5.13(a) and (b). The frequency response of capacitance reflects the amount of the surface area accessible to the electrolyte. Capacitance at the high-frequency region shows the outer surface, which may depend on grain boundaries and other inter-particle phenomena. The plot clearly shows that at the high-frequency region, the imaginary part of the impedance is parallel to the X-axis whereas at the low frequency range, it is inclined to the X-axis, suggesting

that the charge transfer resistance rates at the high-frequency side are faster than that of the low-frequency region [31]. The intercept of the curve in the high-frequency region on the X-axis represents the equivalent series resistance ($R_S$), whereas the semicircle at the high-frequency region signifies the charge transfer resistance ($R_{ct}$) of the electrode. Using equivalent circuit [56, 57] (inset of Fig. 5.13(a-b)) the calculated value of $R_S$ (=2.44 Ω) and $R_{ct}$ (=56.65 Ω) are found to be low in case of $Y_2NiMnO_6$ NWs electrode compared to the $Y_2NiMnO_6$ bulk electrode ($R_S$=3.2 Ω, $R_{ct}$=210.86 Ω), which indicate the higher electrical conductivity of $Y_2NiMnO_6$ NWs electrode and quick ion-charge transfer at the contact of electrode-electrolyte during redox reaction. The straight line in the low-frequency range represent the Warburg resistance ($R_W$), which shows a steep slope due to the high diffusion rate of ions during redox reactions [21, 58].
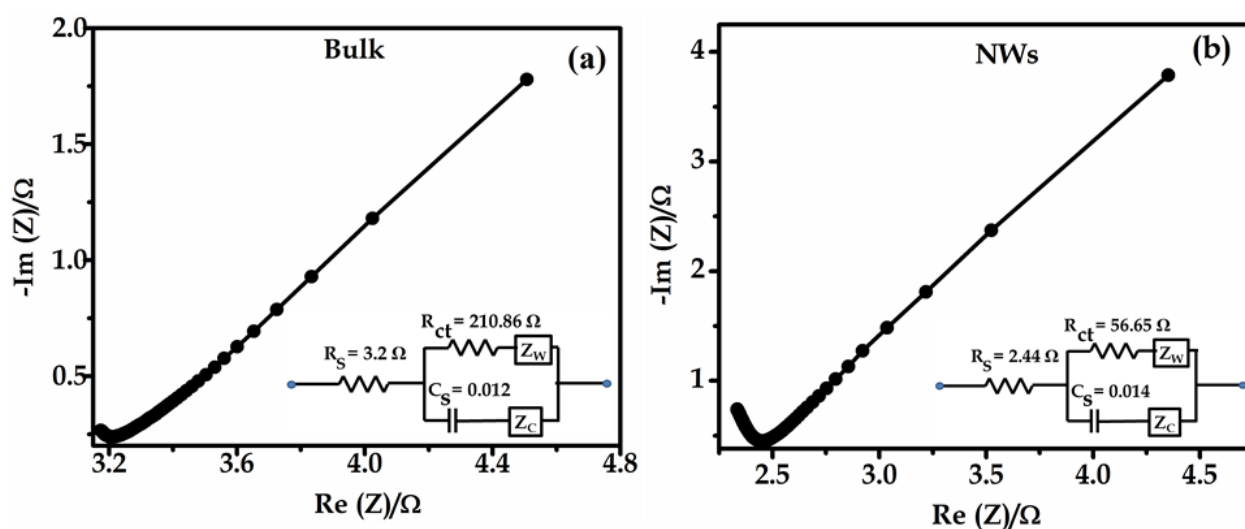


**Fig. 5.13:** Nyquist plot of the $Y_2NiMnO_6$ bulk (a) and NWs (b) electrodes over the frequency range from 10 mHz to 10 kHz. Inset of (a) and (b) show the respective equivalent circuit.

## 5.4. Conclusion

In summary, single-phase, high crystalline double perovskite $Y_2NiMnO_6$ NWs have been successfully fabricated by the solvothermal route. $Y_2NiMnO_6$ NWs exhibit unexpected weak ferromagnetism and ferroelectricity at room temperature though the Curie temperature of the NWs is 50 K, which is much lower than that of the bulk $Y_2NiMnO_6$ ($\sim$ 91 K). The coexistence of the ferromagnetic and ferroelectric ordering in $Y_2NiMnO_6$ NWs at high temperature is ascribed to the large concentration of surface spin and surface polarization of the electron, respectively, associated with the large surface area of the one-dimensional NWs. The study indicates that for $Y_2NiMnO_6$ NWs, at room temperature, ferroelectricity and ferromagnetism are mutually coupled with each other and have similar origin too.

The comparative study demonstrates that $Y_2NiMnO_6$ NWs as a new material for pseudocapacitors exhibit higher specific capacitance, power density, and energy density in contrast to their bulk counterpart. The remarkable electrochemical performance develops due to the large surface area of $Y_2NiMnO_6$ NWs which leads to better interaction of electrolyte with the nano structure, resulting in shorter ion transfer pathway. It is evident that along with multiferroic behavior, $Y_2NiMnO_6$ NWs will be a promising candidate in the field of electrochemical supercapacitor.

## 5.5. Bibliography

[1]     J. F. Scott, *Nat. Mater.* **6**, 256 (2007).

[2]     R. Ramesh, & N. A. Spaldin, *Nature Mater.* **6**, 21 (2007).

[3]     S. W. Cheong, & M. Mostovoy, *Nature Mater.* **6**, 13 (2007).

[4]     W. Eerenstein1, N. D. Mathur & J. F. Scott, *Nature* 442, 759 (2006).

[5]     M. Fiebig, T. Lottermoser, D. Frohlich, A. V. Goltsev& R. V. Pisarev, *Nature* **419,** 818 (2002).

[6]     J. Su, Z. Z. Yang, X. M. Lu, J. T. Zhang, L. Gu, C. J. Lu, Q. C. Li, J.-M. Liu, and J. S. Zhu, *ACS Appl. Mater. Interfaces* **7**, 13260 (2015).

[7]     C. Zhang, T. Zhang, L. Ge, S. Wang, H. Yuan and S. Feng, *RSC Adv.* **4**, 50969 (2014).

[8]     R. Das, G.G. Khan and K. Mandal, *Journal of Applied Physics* **111**, 104115 (2012).

[9]     D. P. Dutta, O. D. Jayakumar, A. K. Tyagi, K. G. Girija, C. G. S. Pillaia, and G. Sharma, *Nanoscale* **2**, 1149 (2010).

[10]    Y. J.Jo, S.Lee, E. S.Choi, H. T.Yi, W.Ratcliff, Y. J.Choi, V.Kiryukhin, S. W.Cheone, L.Balicas, *Phys. Rev. B* **79**, 012407 (2009).

[11]    N. S. Rogado, J. Li, A. W. Sleight and M. A. Subramanian, *Advanced materials* **17**, 2225 (2005).

[12]    S.Kumar, G.Giovannetti,J. V. D.Brink, S.Picozai, *Phys. Rev. B* **82**, 134429 (2010).

[13]    X. Lang, A. Hirata, T. Fujita and M. W. Chen, *Nature Nanotechnology* **6**, 232 (2011).

[14]    J. Kang, A. Hirata, L. Kang, X. Zhang, Y. Hou, L. Chen, C. Li, T. Fujita, K. Akagi and M. Chen, *Advanced Materials* **52**, 1664 (2013).

[15]    L. Wang, H. Ji, S. Wang, L. Kong, X. Jiang and G. Yang, *Nanoscale* **5**, 3793 (2013).

[16]    T. Brezesinski, J. Wang, J. Polleux, B. Dunn and S. H. Tolbert, *Journal of American Chemical Society* **131**, 1802 (2009).

[17]    A. David, C. Tompsett, S. C. Parker and M. S. Islam, *Journal of American Chemical Society* **136**, 1418 (2014).

[18]    M. Liu, L. Gan, W. Xiong, Z. Xu, D. Zhu and L. Chen, *Journal of Materials Chemistry A* **2,** 2555 (2014).

[19]  J. Yan, E. Khoo, A. Sumboja and R. S. Lee, *ACS Nano*  **4**, 4247 (2010).

[20]  L. Athoue, F. Moser, R. Dugas, O. Crosnier, D. Belanger and T. Brousse, *Journal of Physics Chemical C*  **112**, 7270 (2008).

[21]  A. K. Singh, D. Sarkar, G. G. Khan and K. Mandal, *American Chemical Society Applied Materials & Interfaces* **6**, 4684 (2014).

[22]  Y. Luo, D. Kong, J. Luo, Y. Wang, D. Zhang, K. Qiu, C. Cheng, C. M. Li  and T. Yu, *Royal Society of Chemistry Advances* **4**, 13241 (2014).

[23]  Z. Chen, V. Augustyn, X. Jia, Q. Xiao, B. Dunn and Y. Lu, *American Chemical Society Nano* **6**, 4319 (2012).

[24]  M. Sathiya, A. S. Prakash, K. Ramesha, J. M. Tarascon and A. K. Shukla, *Journal of American Chemical Society* **133**, 16291 (2011).

[25]  M. Pal, R. Rakshit, A. K. Singh, and K. Mandal, *Energy* **103**, 481 (2016).

[26]  J. Wang, J. B. Neaton, H. Zheng, V. Nagarajan, S. B. Ogale, B. Liu, D. Viehland, V. Vaithyanathan, D. G. Schlom, U. V. Waghmare, N. A. Spaldin, K. M. Rabe, M. Wuttig and R. Ramesh, *Science* **299,** 1719 (2003).

[27]  F. D. Martini, V. Buzek, F. Sciarrino and C. Sias, *Nature* **419**, 815 (2002).

[28]  W. Eerenstein, N. D. Mathur and J. F. Scott, *Nature* **442**, 759 (2006).

[29]  M. Alam, K. Mandal and G. G. Khan, *RSC Advances* **6**, 62545 (2016).

[30]  C. D. Lokhande, T. P. Gujar, V. R. Shinde, R. S. Mane and S. H. Han, *Electrochemistry Communication* **9**, 1805 (200).

[31]  V. V. Jadhav, M. K. Zate, S. Liu, Mu. Naushad, R.S. Mane, K. N. Hui, S. -H. Han, *Applied nanoscience* **6**, 511 (2015).

[32]  N.  Dutta, S. K. Bandyopadhyay, S. Rana, P. Sen and A. K. Himanshu, *Cornell University Library* **1309**, 5690 (2013).

[33]  Y. Liu, I. Zhitomirsky, *Journal of Power Sources* **284,** 377 (2015).

[34]  A. Sarkar, A. K. Singh, D. Sarkar, G. G. Khan and K. Mandal, *ACS Sustainable Chemistry & Engineering* **3**, 2254 (2015).

[35]  G. S. Lotey, N. K. Verma, *Chemical Physics Letters* **579,** 78 (2013).

[36]  B. H. Toby, EXPGUI, *J. Appl. Crystallogr*. **34**, 210 (2001).

[37]  J. R. Manders, S. W. Tsang, M. J. Hartel, T. H. Lai, S. Chen, C. M. Amb and J. R. Reynolds, *Adv. Funct. Mater.* **23**, 2993 (2013).

[38]  P. D. Rouffignac, J.-S. Park, and R. G. Gordon, *Chem. Mater.* **17**, 4808 (2005).

[39]  N. F. Troitiño, S. L. Viñas, B. R. González, Z.-A. Li, M. Spasova, M. Farle, and V. Salgueiriño, *Nano Lett.* **14**, 640 (2014).

[40]  M. Sparks, *Phys. Rev. Lett.* **22,** 1111 (1969).

[41]  S. Mørup, D. E. Madsen, C. Frandsen, C. R. H. Bahl and M. F. Hansen, *J. Phys.: Condens. Matter* **19**, 213202 (2007).

[42]  B. Song, J. C. Lin, P. Tong, M. Wang, C. Yang, X. G. Guo, S. Lin and Y. P. Sun, *RSC Adv.* **5**, 106213 (2015).

[43]  S. Mørup and C. Frandsen, *Phys. Rev. Lett.* **92**, 217201 (2004).

[44]  T. Kimura, T. Goto, H. Shintane, K. Ishizaka, T. Arima, Y. Tokura, *Nature* **426**, 55 (2003).

[45]  S. Y.-Vilar, E. D. Mun, V. S. Zapf, B. G. Ueland, J. S. Gardner, J. D. Thompson, J. Singleton, M. S-And´ujar, J. Mira, N. Biskup, M. A. S-Rodr´ıguez, and C. D. Batista, *Phys. Rev. B* **84**, 134427 (2011).

[46]  P. Zubko, D. J. Jung, and J. F. Scott, *Journal of Applied Physics* **100**, 114112 (2006).

[47]  S. Bu, D. Chun and G. Park, *Journal of the Korean Physical Society* 31, 223 (1997).

[48]  N. A. Hill, *J. Phys. Chem. B* **104**, 6694 (2000).

[49]  Y.Q. Lin, X.M. Chen, X.Q. Liu, *Solid Sate Commun*. **149**, 784 (2009).

[50]  I. Sosnowska, T.P. Neumaier, E. Streichele, *J. Phys. C* **15,** 4835 (1982).

[51]  G. V. Duong, R. Groessinger, M. Schoenhart, D. Bueno-Basques, *J. Magn. Magn. Mater.* **316**, 390 (2007).

[52]  S. Mazumder, G.S. Bhattacharyya, *Ceram. Int.* **30**, 389 (2004).

[53]  E. Jartych, T. Pikula, K. Kowal, J. Dzik, P. Guzdek and D. Czekaj, *Nanoscale Research letter.* **11**, 234 (2016).

[54]  N. Ortega, A. Kumar, J. F. Scott and R. S. Katiyar, *Journal of Physics: Condens. Matter* **27**, 5040002 (2015).

[55]  M. Alam, S. Talukdar, K. Mandal, *Materials Letters* **210,** 80 (2018).

[56] X. L. Guo, X. Y. Liu, X. D. Hao, S. J. Zhu, F. Dong, Z. Q. Wen, Y. X. Zhang, *Electrochimica Acta* **194**, 179 (2016).

[57] X. Li, J. Rong, B. Wei, *ACS Nano* **4**, 6039 (2010).

[58] J. Liu, J. Jiang, C. Cheng, H. Li, J. Zhang, H. Gong, H. J. Fan, *Advanced Materials* **23**, 2076 (2011).

# Chapter 6

**Room Temperature Multiferroic Properties in Double Perovskite Y$_2$NiMnO$_6$ Nanostructure Thin Film**

In this chapter, we have demonstrated the synthesis of double perovskite Y$_2$NiMnO$_6$ nanostructured thin film using a pulse laser deposition technique and studied their multiferroic properties.

## 6.1. Background

Multiferroic magnetoelectric (ME) materials, which simultaneously exhibit ferroelectric and ferromagnetic properties in a single phase along with the effective coupling between the dual order parameters, have shown remarkable potential for multifunctional device applications in magnetic data storage, fast writing, sensors, transducers, spintronics, and high-power applications [1, 2, 3, 4, 5, 6]. However, there are only few single-phase multiferroic materials exhibiting the coexistence of electric and magnetic orders simultaneously. Multiferroic materials, where the significant coupling between electric and magnetic ordering coexists, are the ideal candidate for suitable applications because of the opportunity to tune electric dipoles by applied magnetic fields and the magnetic spins by applied voltages [4]. The type-II multiferroic materials exhibit significant coupling between electric and magnetic ordering, where ferroelectricity originates because of the magnetic ordering. Still, the low polarization and low critical temperature are the main limitations of the type-II multiferroic materials for device applications. Therefore, room-temperature (RT) multiferroic materials are still very challenging to achieve. The perovskite materials have shown significant potential as multiferroics with coexistence of electric and magnetic orders. The strong room-temperature magnetoelectric (RTME) coupling in the single-phase double perovskite materials makes them interesting over the single perovskite materials, which exhibit comparatively weak RTME coupling. Recently, the double perovskite $Y_2NiMnO_6$ has drawn attention considering its multiferroic properties in single-phase [7, 8, 9, 10, 11]. Although $Y_2NiMnO_6$ is not a well-studied material considering its multiferroic properties, especially in the nano-scale dimension.

In this backdrop, the present work demonstrates the fabrication of multiferroic double perovskite $Y_2NiMnO_6$ (YNMO) nanostructured (NS) thin films on gold-sputtered Si(100) substrate by pulsed laser deposition (PLD) technique. The as-prepared YNMO NS thin films are found to exhibit unexpected ferromagnetism (FM) and ferroelectricity (FE) above room temperature (300 K). Studies show that both RTFM and the spontaneous RTFE are mutually coupled with each other and they have a similar

origin. The unusual RTFM and the RTFE are believed to be originated because of the unsaturated surface spins and surface charge polarization, respectively, associated with the large surface area of the NS thin films. The surface area and the associated surface spins/charges are found to be largely dependent upon the size of the nanostructures and the surface roughness of the YNMO NS thin films.

## 6.2. Experimental

YNMO NS thin films are deposited on gold-sputtered Si(100) wafer substrates at 600 °C, using pulsed laser deposition (PLD) technique in oxygen and argon atmospheres using the KrF excimer laser having a wavelength of 248 nm. The thin films are deposited at a repetition rate of 5 Hz in two different (0.1 and 0.3 mbar) oxygen and argon atmospheric pressures and a fluence of 3.5 J.cm$^{-2}$. The YNMO thin films synthesized at oxygen pressures of 0.1 and 0.3 mbar are defined as YNMO(O1), YNMO(O2), respectively, whereas the thin films deposited at argon pressures of 0.1 and 0.3 mbar are defined as YNMO(Ar1), YNMO(Ar2), respectively. After the deposition, the PLD chamber is cooled to room temperature under the same oxygen and argon pressures. Before PLD a thin gold layer is grown on one surface of the Si(100) wafer substrates by Planar Magnetron RF/DC sputtering (Model-12 MSPT). A well-characterized gold sample is used for the gold sputtering. The base pressure of the sputtering chamber was 10$^{-5}$ mbar and the sputtering is carried out for 4 minutes until a uniform and homogeneous film is created. The PLD target is prepared by using polycrystalline $Y_2NiMnO_6$ powder, which is fabricated by the sol−gel method. Briefly, $Y(NO_3)_3.6H_2O$ (2.0084 gm), $Ni(NO_3)_3.6H_2O$ (1.855 gm), and $C_4H_6MnO_4.6H_2O$ (1.136 gm) are the starting reagents, which are successively dissolved in double distilled water with their stoichiometric rations. A suitable amount of citric acid is added to the solution during stirring and the molar ratio of citric acid with the metal elements present in the solution is 2:1. Afterwards, the solution is stirred for 30 minutes until a homogenous mixture is formed. The solution is then heated at 150 °C until a thick solution is formed. After the formation of a thick solution, the mixture is calcined at 1000 °C for 12 hours to prepare

the powder sample of $Y_2NiMnO_6$. The powder sample of $Y_2NiMnO_6$ is converted to a pellet to use it for the PLD target.

The surface morphology of all the as-prepared YNMO NS thin films are studied by field emission scanning electron microscopy (FESEM, FEI Quanta 200 FEG) and the atomic force microscopy (AFM, Innova, Bruker). The elemental analysis of the films is performed by recording energy dispersive X-ray (EDX) spectrum. The grazing incidence X-ray diffraction (GIXRD) patterns of the YNMO thin films are recorded using Cu$K_\alpha$ radiation (λ= 1.5418 Å, Panalytical, X'part Pro diffractometer) to study the crystal structure of the material. The transmission electron microscopy (TEM, FEI TECNAI G2 TF20ST) and high-resolution TEM (HRTEM) studies of the mechanically broken films are conducted to further study the crystal structures of the films. X-ray photoelectron spectroscopy (XPS, VGMicrotech VGX 900-W, beamline: Mg$K_\alpha$) are employed to determine the chemical composition of the as-prepared thin films. The magnetic properties of the thin films are studied by using a vibrating sample magnetometer (VSM, Lakeshore, model 7144) and magnetic force microscopy (MFM). The ferroelectric properties of the thin films are studied using the high precession *P-E* system (Radiant Technologies) and the piezoelectric force microscopy (PFM).

In this backdrop, the present work demonstrates the fabrication of multiferroic double perovskite $Y_2NiMnO_6$ (YNMO) nanostructured (NS) thin films on gold sputtered Si(100) substrate by pulse laser deposition (PLD) technique. The as prepared YNMO NS thin films are found to exhibit unexpected ferromagnetism (FM) and ferroelectricity (FE) above room temperature (300 K). Studies show that both RTFM and the spontaneous RTFE are mutually coupled with each other and they have similar origin. The unusual RTFM and the RTFE are believed to be originated because of the unsaturated surface spins and surface charge polarization, respectively, associated with the large surface area of the NS thin films. The surface area and the associated surface spins/charges are found to be largely dependent upon the size of the nanostructures and the surface roughness of the YNMO NS thin films.

## 6.3. Results and discussions

### *6.3.1. Morphology and structural analysis of Y$_2$NiMnO$_6$ thin films*

The GIXRD patterns (Fig. 6.1(a)) of the as-prepared YNMO thin films indicate the polycrystalline nature of the films. The GIXRD pattern signifies the formation of single-phase YNMO having a monoclinic crystal structure with $P2_1/n$ space group (JCPDS No. 01-076-7889) [12, 13, 14]. The broad nature of the XRD pattern indicates the formation of nanostructured (NS) YNMO thin films, which is later confirmed by the AFM studies. The XRD pattern of the Y$_2$NiMnO$_6$ structure has also been simulated (Fig. 6.1(e)) based on the information obtained from the XRD experiment employing the PowderCell program [15]. It has been found that the simulated XRD pattern matches well with the experimental results. The representative FESEM micrograph of the top surface of YNMO film (Fig. 6.1(b)) shows a uniform and well spread growth of the as-prepared NS thin films on the substrate. The thickness of all the YNMO NS thin films is found to be in 'µm' length scale from the cross-sectional FESEM study. The thickness of the YNMO(Ar2) NS thin film is found to be ~1 µm, which is the lowest among the thin films (inset of Fig. 6.1(b)). Fig. 6.1(c) shows the TEM image of the mechanically broken part of YNMO NS thin film grown on gold deposited Si (100) substrate. The corresponding HRTEM micrograph (Fig. 6.1(d)) of the YNMO NS thin film with different orientation of the crystallographic planes and different lattice spacing again confirms the polycrystalline nature of the NS thin film. The estimated inter-planar distances of 0.26, 0.27 and 0.225 nm, are corresponding to the distance between the (112), (020) and (211) lattice planes of the YNMO NS thin films, respectively. The single area electron diffraction (SAED) pattern of the YNMO NS film (inset of Fig. 6.1(d)) obtained from the area covered under the HRTEM also confirms the polycrystalline nature of the as-prepared YNMO NS thin film. The EDX spectroscopy analysis (inset of Fig. 6.1(e)) of the YNMO film also confirms the presence of Y, Ni, Mn and O elements, where the atomic ratio of the elements is found to be close to 2:1:1:6.
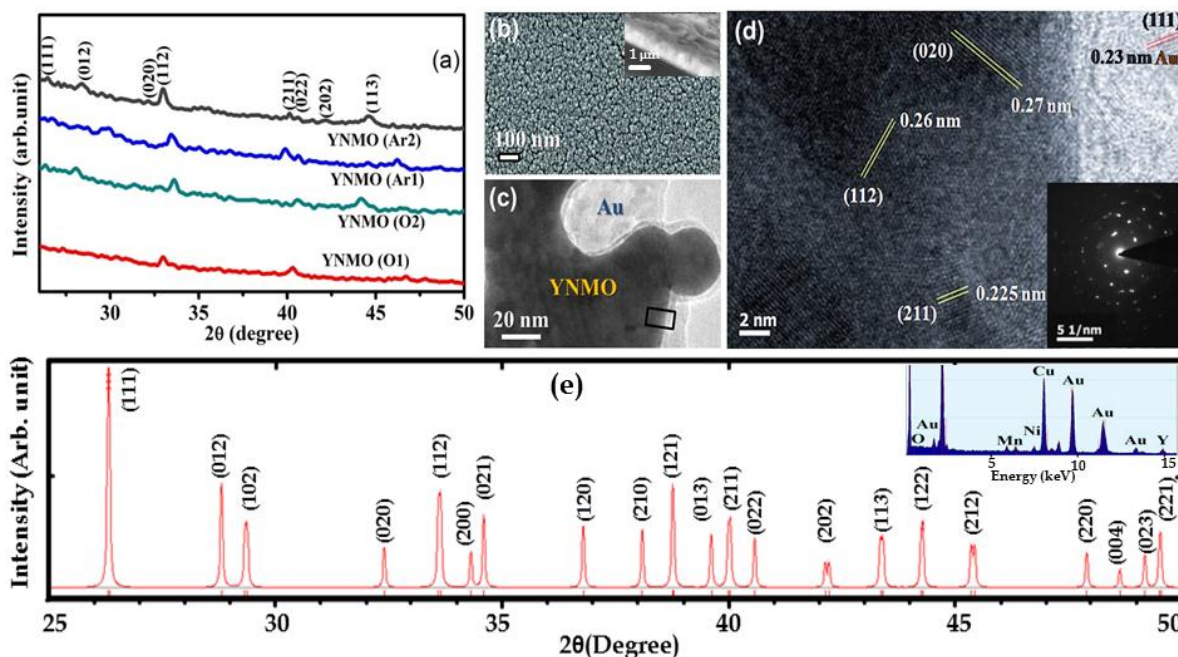
**Fig. 6.1:** (a) GIXRD pattern of the as prepared YNMO NS thin films. (b) FESEM, (c) TEM and (d) HRTEM micrographs of the YNMO NS thin film. Inset of (d) SAED pattern of the YNMO NS thin film. (e) Simulated XRD pattern using Powder Cell program of the YNMO NS thin film. Inset of (e) EDAX spectra of YNMO NS thin film.

The XPS studies have been performed for further information of the chemical state of the elements present in the YNMO NS thin films. Fig. 6.2(a) shows the XPS spectrum for Y, where the doublet peaks for Y$3d_{5/2}$ and Y$3d_{3/2}$ are located at 156.4 and 158.2 eV, respectively, correspond to the trivalent (+3) oxidation state of Y in the YNMO NS thin films [8, 16]. For all the films, Ni$2p_{3/2}$ and Ni$2p_{1/2}$ doublet peaks are found to appear at 854.8 and 872.5 eV, respectively, with two broad satellite peaks for Ni $2p_{3/2}$ and Ni $2p_{1/2}$ centered at 860.9 and 878.8 eV, respectively, represents the +2 oxidation state of Ni in the YNMO thin film (Fig. 6.2(b)) [9, 17, 18]. Fig. 6.2(c) shows the XPS spectrum of Mn $2p$, where the characteristic peaks for Mn $2p_{3/2}$ and Mn $2p_{1/2}$ appears at 642.4 and 653.6 eV, respectively. This result indicates the presence of Mn$^{4+}$, signifying the +4 oxidation state of Mn in the YNMO NS thin films [8, 10]. The XPS spectrum of O $1s$ core level (Fig. 6.2(d)) shows a sharp peak at 529.4 eV, which can be attributed to the O$^{2-}$ species in the lattice oxygen in the YNMO NS thin films [9].
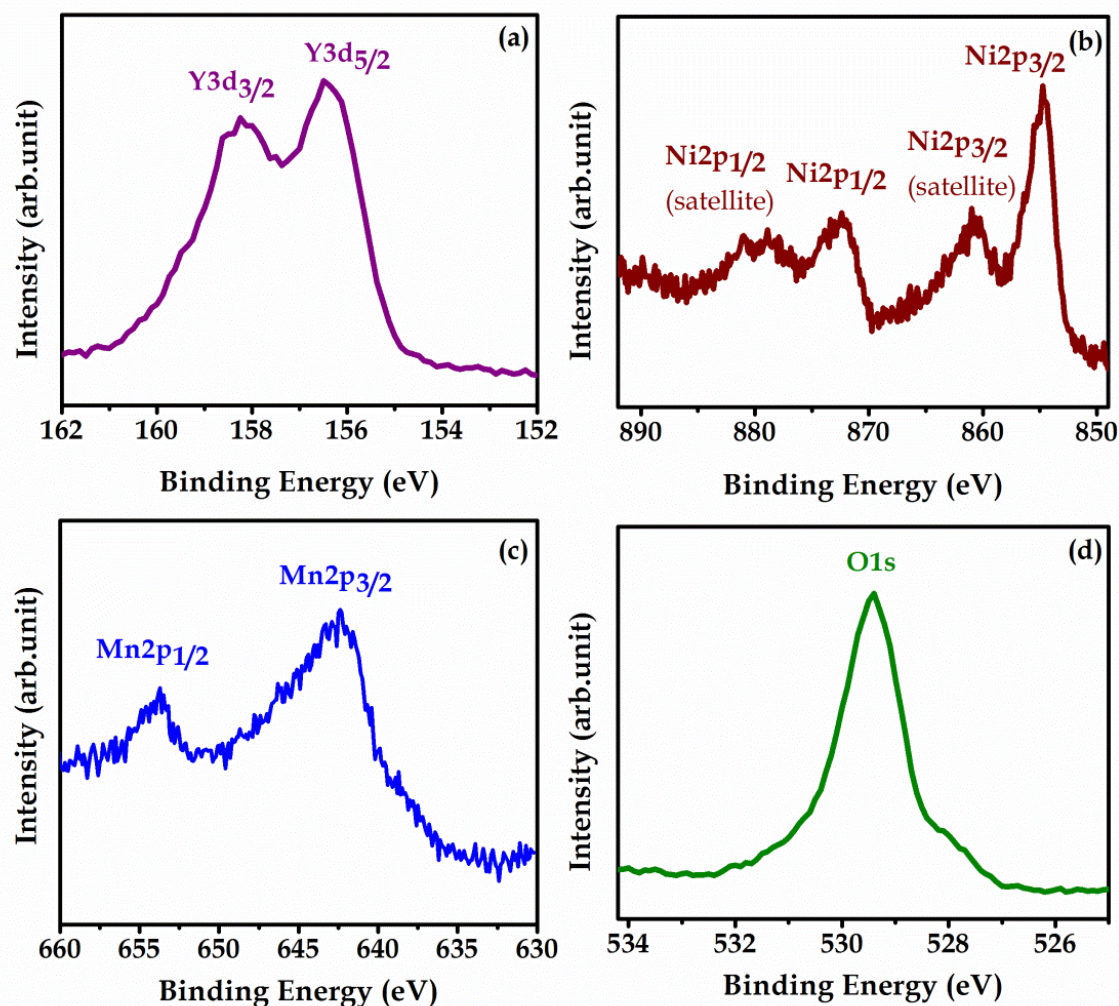
**Fig. 6.2:** XPS spectra of (a) Y 3d, (b) Ni 2p, (c) Mn 2P and (d) O 1s core levels of the YNMO NS thin film.

### 6.3.2. *Magnetic properties of Y₂NiMnO₆ thin films*

Bulk $Y_2NiMnO_6$ has been reported to exhibit *E*-type antiferromagnetic behavior with ↑↑↓↓ spin structure resulting from the super-exchange interaction between $Ni^{2+}$ and $Mn^{4+}$ [9, 11]. Hence, to study the magnetic ordering of YNMO NS thin films, the *M-H* hysteresis loops of the films are recorded at room temperature (~300 K) (Fig. 6.3(a)). Surprisingly, from Fig. 6.3(a), it is evident that all the YNMO NS thin films show weak ferromagnetism at RT. However, in our previous work (*Chapter 5*) [8] we also have evidenced that the bulk YNMO exhibits weak ferromagnetism below the Curie temperature and it is believed to be originated because of the reorientation of the ↑↑↓↓

spin structure to ferromagnetic order due to the applied external magnetic field [8, 9, 11]. In this work, the bulk YNMO exhibits clear paramagnetic signature at RT (above the Curie temperature ~ 91 K) as shown in the inset of Fig. 6.3(a). The temperature dependence of magnetization M(T) recorded for the representative YNMO thin film under a constant applied magnetic field of 1 kOe (Fig. 6.3(b)), indicates that the ferromagnetic transition occurs around 89 K. From the plot (inset of Fig. 6.3(b)) of the saturation magnetization ($M_S$) of different YNMO NS thin films, it is clear that the YNMO(Ar2) and YNMO(Ar1) exhibits highest and lowest saturation magnetization ($M_S$), respectively.
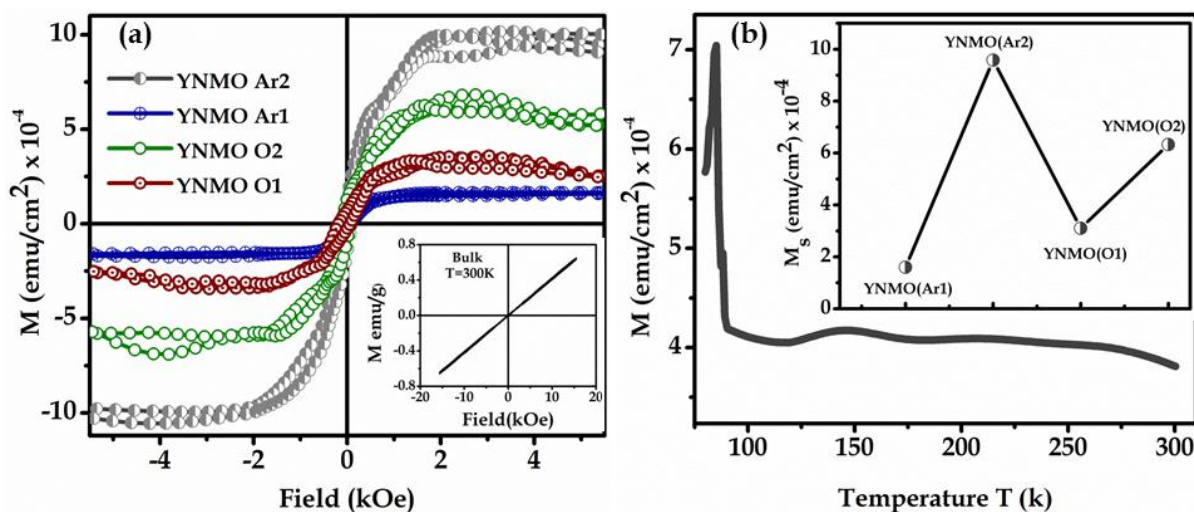


**Fig. 6.3:** (a) Room temperature (300 K) ferromagnetic hysteresis curves of the as prepared YNMO NS thin films. Inset of (a) room temperature (300 K) paramagnetic hysteresis curve of bulk YNMO. (b) Variation of magnetization as a function of temperature under applied magnetic field of 1 kOe for the representative YNMO(Ar2) NS thin film. Inset of (b) variation of saturation magnetization of the as prepared YNMO NS thin films.

However, the existence of the RT ferromagnetism in the YNMO nanostructured thin films also coincides with our previous work (*Chapter 5*) [8], where the $Y_2NiMnO_6$ nanowires exhibited RT ferromagnetic behavior. The existence of this type unexpected RT ferromagnetism in YNMO NS thin films is believed to be because of the presence of a large concentration of uncompensated surface spins due to the surface electrons associated with large surface areas of the nanostructured thin films [19, 20]. The orientation of the uncompensated surface spins can even exist at high temperatures

above RT resulting RT ferromagnetism. However, to probe the reason behind the different ferromagnetic response of the as-prepared YNMO NS thin films, here, all the films have been studied extensively by AFM and MFM. Fig. 6.4 represents the two dimensional (2D) AFM and the corresponding MFM micrographs of the top surface of different YNMO NS thin films. The three dimensional (3D) AFM images of the as-prepared thin films are shown in Fig. 6.5. The AFM images clearly confirm the formation of the homogeneous and compact YNMO nanostructured thin films on Si(100) substrate. It is evident from the AFM images that the YNMO(Ar2) thin film (Fig. 6.4(g)) contains the tiniest granular nanostructures, whereas the YNMO(O1) thin film (Fig. 6.4(a)) is made of largest size nanostructures among all the thin films. It is also evident from the AFM images that the surface roughness of the as-prepared thin films depends upon the fabrication parameters. Fig. 6.6 shows the AFM and its corresponding surface roughness study of YNMO thin films. Table-6.1 shows the detail calculation of RMS and average roughness study of thin films. The surface roughness of YNMO(O1) thin film is maximum from the AFM and its corresponding surface roughness study. On the other hand, the YNMO(Ar2) thin film has minimum surface roughness among all the NS thin films. However, it is obvious that the increase of the surface roughness will eventually enhance the effective surface area of the nanostructured thin films. The increase of the surface roughness/surface area will result in more surface spin leading to enhanced RTFM [21]. Hence, it is quite expected that though the YNMO(O1) thin-film contains course nanostructures compared with the YNMO(Ar1), the large effective large surface area for YNMO(O1) results in higher $M_S$ for the same. On the other hand, the surface roughness for YNMO(Ar2) is comparable with that of YNMO(Ar1), but the extremely tiny nanostructures of the YNMO(Ar2) NS thin film lead to the large effective surface area and large surface spins resulting highest RTFM signature in this thin film.
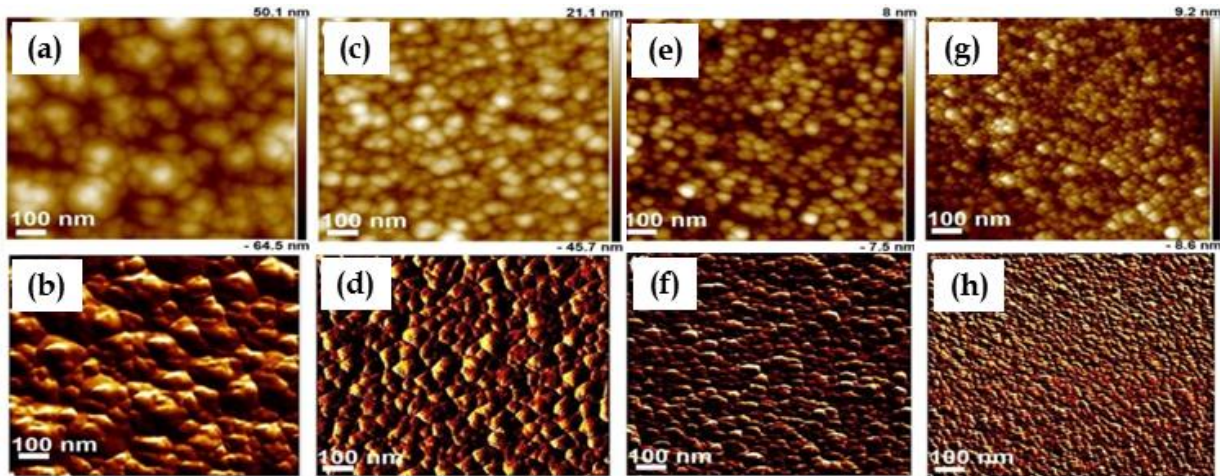
**Fig. 6.4:** AFM micrographs of (a) YNMO(O1), (c) YNMO(O2), (e) YNMO(Ar1) and (g) YNMO(Ar2) thin films. The corresponding MFM phase images of (b) YNMO(O1), (d) YNMO(O2), (f) YNMO(Ar1) and (h) YNMO(Ar2) thin films.
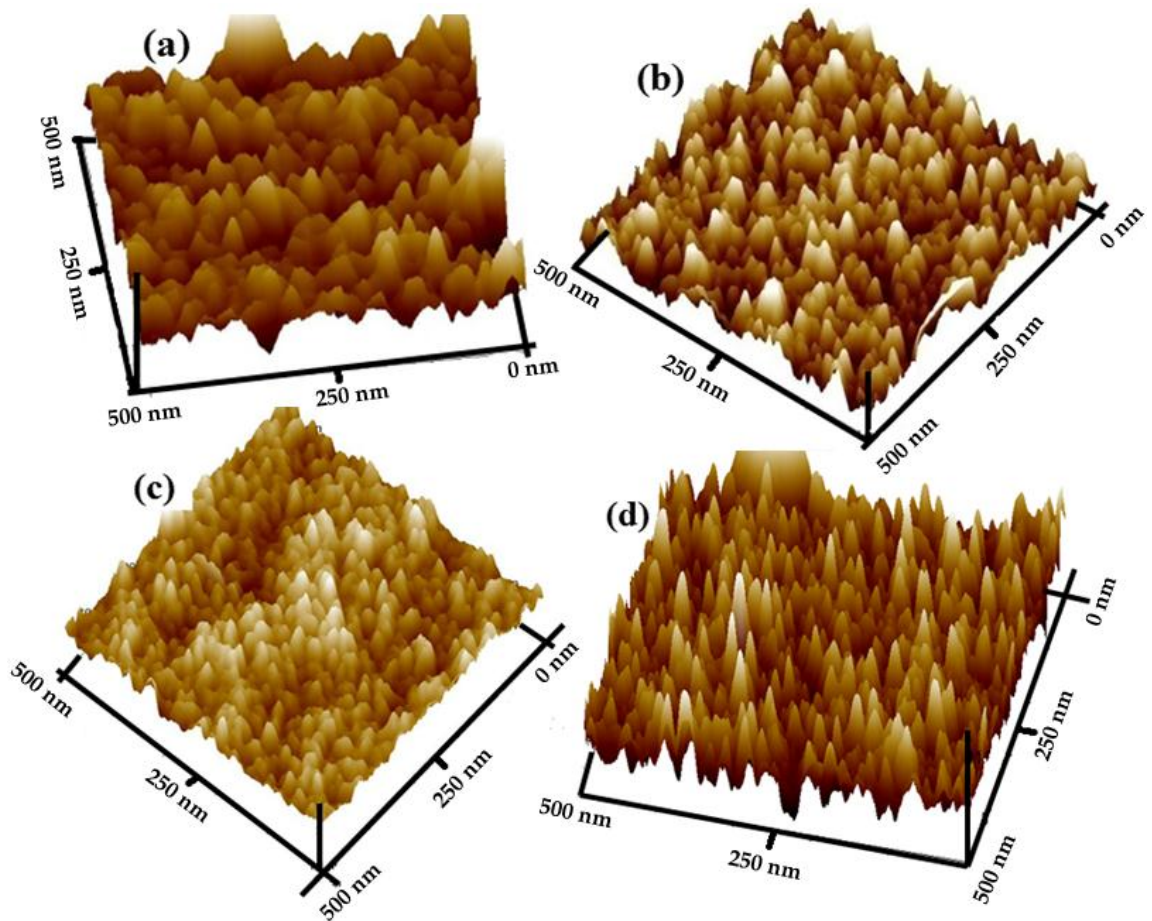


**Fig. 6.5** Three dimensional AFM images of the as grown (a) YNMO(O1), (b) YNMO(O2), (c) YNMO(Ar1) and (d) YNMO(Ar2) thin films.

The RT magnetic signature of the YNMO NS thin films has been further investigated by MFM, where MFM is employed to identify the magnetic fields associated with the magnetic domains of the thin films. MFM phase micrographs (Fig. 6.4(b), (d), (f) and (h)) show the image of the magnetic domains and domain boundary structures of the as-prepared YNMO NS thin films. The bright and dark contrast of the MFM micrographs represents the magnetic spin domains with high concentrations of positive and negative spins, respectively [22, 23, 24]. It is evident from MFM images that the domain size and domain configuration for different YNMO NS thin films are also different. Hence, it is quite obvious that the magnetic signature of the thin films will also be different, as the domain size and domain configuration are responsible for the magnetic property of the materials. However, it is evident that for YNMO(Ar1) NS thin film (Fig. 6.4(f)), the magnetic domains are most randomly distributed and because of this YNMO(Ar1) NS thin film exhibits weakest RTFM. For YNMO(O1) (Fig. 6.4(b)), the domain size is found to be larger with improved homogeneity compare to YNMO(Ar1) film and because of that the RTFM signature for YNMO(O1) is better than YNMO(Ar1). Furthermore, it is evident from Fig. 6.4(h), that the YNMO(Ar2) NS thin film contains tiniest domains, which are homogeneity distributed resulting in the long-range magnetic ordering across the film surface leading to highest RTFM in the same [24, 25]. Hence, the MFM and AFM investigation of the YNMO NS thin films also completely support the quantitative value of magnetization of the film obtained by *M-H* hysteresis studies.
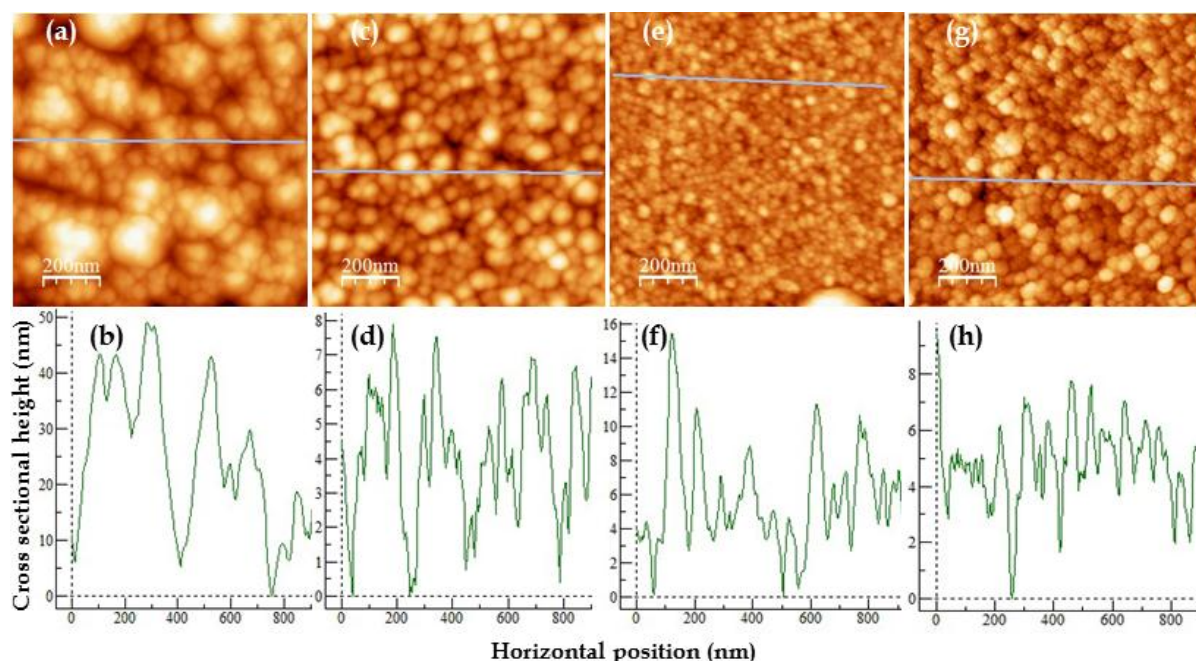
**Fig. 6.6:** AFM micrographs of (a) YNMO(O1), (c) YNMO(O2), (e) YNMO(Ar1) and (g) YNMO(Ar2) thin films. The corresponding roughness images of (b) YNMO(O1), (d) YNMO(O2), (f) YNMO(Ar1) and (h) YNMO(Ar2) thin films.

**Table-6.1:** The value of RMS and average roughness of YNMO thin films.

| Sample | RMS roughness (nm) | Average roughness (nm) |
|---|---|---|
| YNMO(O1) | 13.9 | 10.9 |
| YNMO(O2) | 4.32 | 3.83 |
| YNMO(Ar1) | 7.5 | 5.71 |
| YNMO(Ar2) | 1.89 | 1.49 |

## 6.3.3. Ferroelectric properties of $Y_2NiMnO_6$ thin films

The nature of the inherent ferroelectric response (electric polarization) of the Ag/YNMO/Au capacitor thin films grown on Si(100) substrates has been investigated by the *P-E* hysteresis loop measurements. The room temperature (300 K) *P-E* hysteresis loops of the Ag/YNMO/Au capacitor thin films are shown in Fig. 6.7(a). Inset of Fig. 6.7(a) shows the schematic of the experimental setup used for the ferroelectric hysteresis loop measurement, where silver and gold act as electrodes. Clear evidence of ferroelectric polarization at RT is found for all the as-prepared YNMO NS thin films. The estimated values of the saturation polarization, remnant polarization and coercive

field of the YNMO NS thin films are presented in Table-6.2. It is found that the YNMO(Ar2) NS thin film exhibits the maximum saturation polarization, $P_{max}$ = 0.38 µC/cm². It is to mention that the YNMO(Ar2) NS thin film also shows the maximum saturation magnetization. Here, both the YNMO(O1) and YNMO(Ar1) NS thin films also exhibit nearly identical values of $P_{max}$ similar to their values of magnetic saturation. A little higher value of $P_{max}$ for YNMO(O1) compare to YNMO(Ar1) may be because of the leakage property of the as-prepared films as it is expected that the films grown in the oxygen-rich atmosphere should contain a low concentration of oxygen vacancy defects, responsible for the dielectric leakage. Now, to confirm the inherent ferroelectric polarization of the thin films the leakage current density ($J$) as a function of the external electric field ($E$) is recorded at room temperature (Fig. 6.8). It is obvious that at the high external electric field of ± 90 kV cm$^{-1}$, the YNMO(O1) NS film exhibits the maximum leakage current density of ~10$^{-5}$ Acm$^{-2}$, which is even found to be significantly lower than the reported values of leakage current density of the well-known ferroelectric doped bismuth ferrite [26, 27, 28, 29, 30, 31]. Hence, the extremely low leakage current density of the as-prepared YNMO NS thin films strongly signifies the existence of the inherent ferroelectric polarization of the films [27]. However, the maximum value of leakage current density of YNMO(O1) NS film is believed to be due the presence of large grains with inhomogeneous morphology and enhanced surface roughness [26, 31]. On the other hand, the significantly low value of leakage current density of YNMO(Ar2) NS film can be attributed to the uniformly distributed tiny grains with reduced surface roughness as evident from the AFM study also. Hence, the low leakage current density of YNMO(Ar2) NS film helps to achieve significantly improved ferroelectric behaviour of the film [26]. It is evident from Fig. 6.8 that at the low external electric field the YNMO films exhibit high resistance state (HRS) whereas the films gradually turn into low resistance state (LRS) when the external electric field is increased. The change of the electrical state of the films from HRS to LRS is most expectedly because of the release of the donor type oxygen vacancy defects from the pinning sites leading to high leakage current density [30].

Further evidence of spontaneous polarization and polarization switching of the YNMO NS thin films samples have been obtained from 'Positive Up and Negative Down' (PUND) measurements. PUND measurement conducted for the representative YNMO(Ar2) NS thin film at 300 kV/cm², with a pulse width of 0.8 ms and a delay time of 100 ms, is shown in Fig. 6.7(b). The net switchable polarization can be obtained as: dP = (±P*)−(±P^), where, P* is the summation of switchable and non-switchable polarization and P^ is the non-switchable polarization. Similarly, the net switchable remnant polarization can be calculated as: $dP_r$ or $2P_r$= (±$P_r$*)−(±$P_r$^), where, $P_r$* is the summation of switchable and non-switchable remnant polarization and $P_r$^ is the non-switchable remnant polarization. The as calculated value of the remnant polarization (dP$_r$ or 2P$_r$) for the YNMO(Ar2) NS thin film is ~ 0.275 μC/cm².
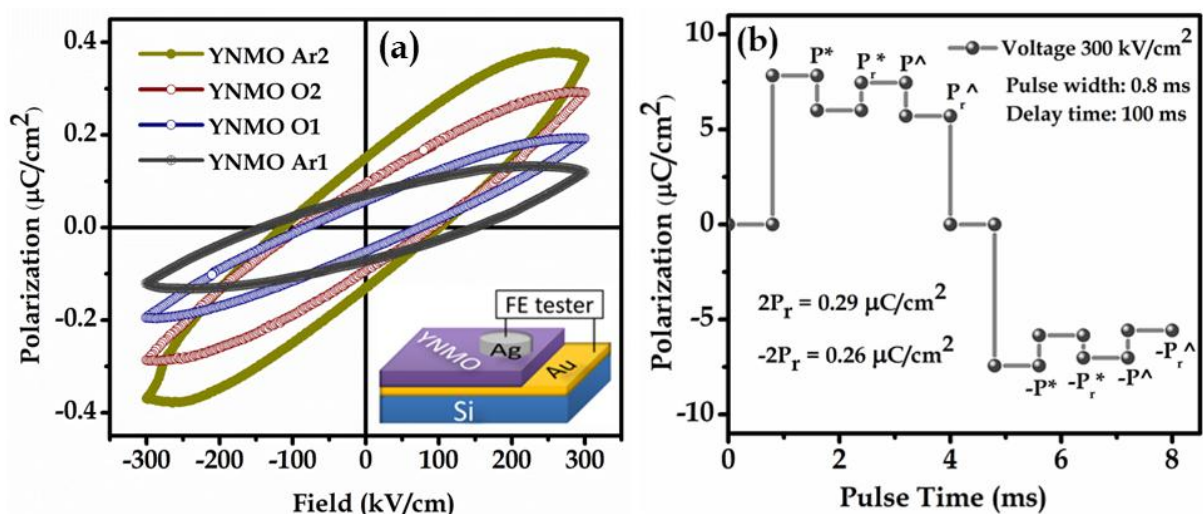


**Fig. 6.7: (**a) Room temperature *P-E* hysteresis loops of the YNMO NS thin films. Inset of (a): schematic of *P-E* hysteresis loop measurement set up for YNMO NS thin films. (b) Study of ferroelectric polarization for the YNMO (Ar2) NS thin film using PUND measurement.

**Table-6.2:** Comparison of maximum polarization, remnant polarization and coercive field of the as prepared YNMO NS thin films.

| YNMO Sample | Maximum polarization ($\mu C/cm^2$) | Remnant Polarization ($2P_r$) ($\mu C/cm^2$) | Coercive field ($2E_c$) ($V/cm^2$) |
|---|---|---|---|
| YNMO(O1) | 0.19 | 0.10 | 156 |
| YNMO(O2) | 0.29 | 0.18 | 189 |
| YNMO(Ar1) | 0.13 | 0.14 | 292 |
| YNMO(Ar2) | 0.38 | 0.28 | 215 |

However, correlating the results of the magnetic and ferroelectric studies of the YNMO NS thin films, it is evident that both the ferromagnetism and dielectric polarization are correlated and they have the similar origin [4]. In fact, the studies show that the magnetic ordering can help to develop weak spontaneous electric polarization in material and vice versa [4, 5, 6]. It is found that when ferromagnetism exists in the material, the dielectric polarization also exists and whenever there is no ferromagnetic ordering, there is no ferroelectric polarization also [6, 8]. So the coexistence of ferromagnetism and ferroelectricity is most expectedly having the similar origin and they appear to be mutually coupled with each other [4]. Therefore, here, it is believed that the uncompensated surface spins are not only responsible for RTFM in YNMO NS thin films but also for the spontaneous RT ferroelectricity in the same due to the surface charge associated with the surface electrons and they are mutually coupled with each other too.
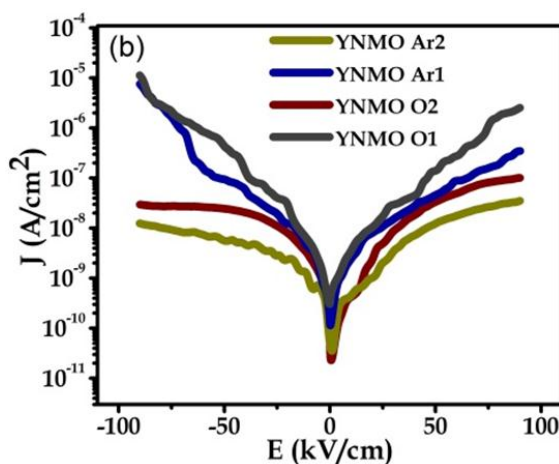


**Fig. 6.8:** Leakage current density-electric field (*J-E*) plots of the films recorded at room temperature.

The spontaneous RT (300 K) ferroelectric behavior of the YNMO thin films has also been studied by PFM. Fig. 6.9(a), (b) and (c) show the topography, phase image and corresponding amplitude image of the representative YNMO(Ar2) NS thin film, respectively, obtained over an area of 500 nm$^2$ on the film surface. Domains with out-of-plane and in-plane polarizations have been observed in the PFM amplitude image and phase image, respectively. Fig. 6.9(b) clearly demonstrates the contrast of the ferroelectric phases (180° phase change) on the film surface, which can be ascribed to the presence of ferroelectric domains having in-plane antiparallel polarization [32, 33, 34, 35]. The intermediate contrast in the amplitude image (Fig. 6.9(c)) are due to the weak vertical component of the piezoresponse signal, as the vertical PFM technique is only sensitive for the grains with in-plane polarization (out-of-plane polarization component becomes nearly zero). However, the distinct dark and bright phase images of the representative YNMO(Ar2) NS thin-film clearly demonstrate the presence of spontaneous intrinsic RT ferroelectricity in the as prepared thin films.
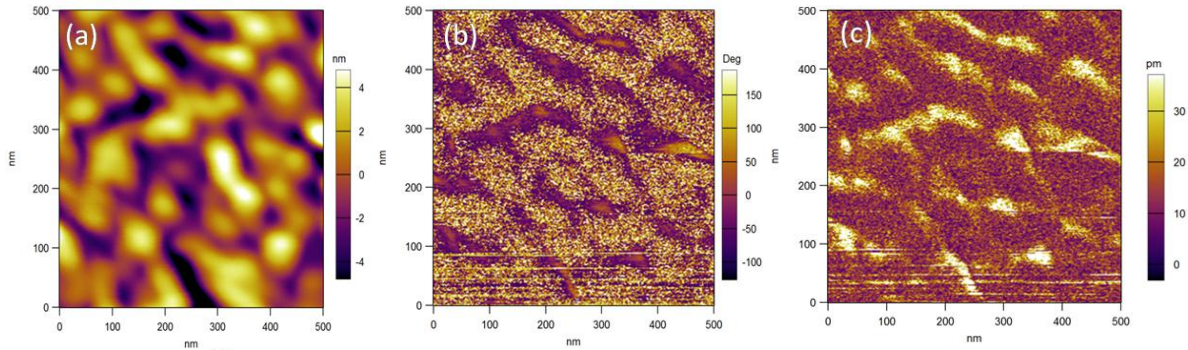


**Fig. 6.9:** PFM images of the YNMO(Ar2) NS thin films at room temperature (300 K) (a) Topography image, (b) phase image and (c) corresponding amplitude image.

## 6.4. Conclusions

In summary, single phase, highly crystalline double perovskite $Y_2NiMnO_6$ nanostructured thin films have been successfully deposited on gold sputtered Si(100) substrates by using pulse laser deposition technique under oxygen and argon atmospheres. All the films are found to exhibit unexpected room temperature ferromagnetism and spontaneous ferroelectricity. It is found that the size of the nanostructures and the surface roughness of the YNMO thin films define and control their inherent ferromagnetic and ferroelectric properties. YNMO nanostructured thin films with large surface area exhibits enhanced room temperature ferromagnetism and ferroelectricity. Studies on the magnetic and ferroelectric properties of YNMO nanostructured thin films indicate that the uncompensated surface spins and the surface charges associated with the large surface areas of the films are responsible for the room temperature ferromagnetism and ferroelectricity, respectively, and they are also mutually coupled with each other. Evidence of room temperature ferromagnetism in the YNMO nanostructured thin films has also been confirmed from MFM studies, which clearly shows the presence of ferromagnetic spin domains on the film surface. The MFM studies also completely support the results of the magnetic studies on the YNMO nanostructured thin films. Existence of ferroelectric domains with antiparallel polarizations in the thin films surface has also been established by PFM studies. This study demonstrates that there is ample opportunity to tailor the inherent electric and magnetic orders at room temperature in perovskite materials down in nanoscale dimension.

## 6.5. Bibliography

[1]     J. F. Scott, *Nat. Mater.* **6**, 256 (2007).

[2]     M. Fiebig, *J. Phys. D,* **38**, 123 (2005).

[3]     R. Ramesh, and N. A. Spaldin, *Nat. Mater.* **6**, 21 (2007).

[4]     S. W. Cheong, and M. Mostovoy, *Nat. Mater.* **6**, 13 (2007).

[5]     W. Eerenstein, N. D. Mathur, J. F. Scott, *Nature* **442**, 759 (2006).

[6]     T. Kimura, T. Goto, H. Shintani, K. Ishizaka, T. Arima, Y. Tokura, *Nature* **426**, 55 (2003).

[7]     C. Xie, L. Shi, *Applied Surface Science* **384**, 459 (2016).

[8]     M. Alam, K. Mandal, and G. G. Khan, *RSC Advances* **6,** 62545 (2016).

[9]     J. Su, Z. Z. Yang, X. M. Lu, J. T. Zhang, L. Gu, C. J. Lu, Q. C. Li, J. –M. Liu, and J. S. Zhu, *ACS Appl. Mater. Interfaces* **7**, 13260 (2015).

[10]    C. Zhang, T. Zhang, L. Ge, S. Wang, H. Yuan, and S. Feng, *RSC Adv.* **4**, 50969 (2014).

[11]    S. Kumar, G. Giovannetti, J. V. D Brink, and S. Picozai, *Phys. Rev. B* **82**, 134429 (2010).

[12]    M. Mouallem-Bahout, T. Roisnel, G. Andre, D. Gutierrez, C. Moure, O. Pena, *Solid State Commun.* **129**, 255 (2004).

[13]    T. Siritanon, N. Chathirat, C. Masingboon, T. Yamwong, S. Maensiri, *J Mater Sci: Mater Electron* **25**, 1361 (2014).

[14]    M. H. Tang, Y. G. Xiao, B. Jiang, J. W. Hou, J. C. Li, J. He, *Appl Phys A* 105, 679 (2011).

[15]    W. Kraus,  G. Nolze, *Journal of Applied Crystallography* **29**, 301 (1996).

[16]    M. Alam, K. Karmakar, M. Pal, and K. Mandal, *RSC Advances* **6**, 114722 (2016).

[17]    A. N. Mansour, *Surface Science Spectra* **3**, 231 (1994).

[18]    J. R. Manders, S. W. Tsang, M. J. Hartel, T. H. Lai, S. Chen, C. M. Amb, and J. R. Reynolds, *Adv. Funct. Mater.* **23**, 2993 (2013).

[19]    S. Mørup, and C. Frandsen, *Phys. Rev. Lett.* **92**, 217201 (2004).

[20] S. Mørup, D. E. Madsen, C. Frandsen, C. R. H. Bahl, and M. F. Hansen, *J. Phys.: Condens. Matter* **19**, 213202 (2007).

[21] M. Charilaou, and F. Hellman, *Journal of Applied Physics* **117**, 083907 (2015).

[22] H. C. Jeon, Y. S. Jeong, T. W. Kang, T. W. Kim, K. J. Chung, W. Jhe, S. A. Song, *Adv. Mater.* **14**, 1725 (2002).

[23] L. Yue, Z. Li, R. Kirby, D. Sellmyer, *Ultramicroscopy* **109,** 1040 (2009).

[24] S. Ghosh, G. G. Khan, and K. Mandal, *ACS Appl. Mater. Interfaces* 4, 2048 (2012).

[25] T. S. Herng, M. F. Wong, D. Qi, J. Yi, A. Kumar, A. F. Huang, C. Kartawidjaja, S. Smadici, P. Abbamonte, C. Sánchez-Hanke, S. Shannigrahi, J. M. Xue, J. Wang, Y. P. Feng, A. Rusydi, K. Zeng, J. Ding, *Adv. Mater.* **23**, 1635 (2011).

[26] Y. Wang, C. W. Nana, *Appl. Phys. Lett.* **89**, 052903 (2006).

[27] Y. Li, T. Sritharan, S. Zhang, X. He, Y. Liu, T. Chen, *Appl. Phys. Lett.* **92**, 132908 (2008).

[28] G. W. Pabst, L. W. Martin, Y. H. Chu, R. Ramesh, Appl. Phys. Lett. **90**, 072902 (2007).

[29] X. Qi, J. Dho, R. Tomov, M. G. Blamire, J. L. MacManus-Driscoll, *Appl. Phys. Lett.* **86**, 062903 (2005).

[30] I. Bretos, R. Jiménez, C. Gutiérréz-Lázaro, I. Montero, M. L. Calzada, *Appl. Phys. Lett.* **104**, 092905 (2014).

[31] H. W. Chang, F. T. Yuan, K. T. Tu, Y. C. Lo, S. Y. Tu, C. R. Wang, A. B. Yang, C. S. Tu, S. U. Jen, Y. C. Chang, *J. Appl. Phys.* **117**, 17C734 (2015).

[32] A. L. Kholkin, V. V. Shvartsman, A. Y. Emelyanov, *Appl. Phys. Lett.* 82, 2127 (2003).

[33] S. Song, H. M. Jang, N.-S. Lee, J. Y. Son, R. Gupta, A. Garg, J. Ratanapreechachai, and J. F. Scott, *NPG Asia Materials* **8**, 242 (2016).

[34] Y. Zhao, B. Luo, H. Xing, C. Chen, J. Wang, and K. Jin, *ACS Appl. Mater. Interfaces* **9**, 6609 (2017).

[35] W-Q. Liao, Y.-Y. Tang, P. -F. Li, Y. -M. You, and R.-G. Xiong, *Journal of American Chemical Society* 139, 18071 (2017).

# Chapter 7 | Conclusion and Scope for Future Work

This chapter gives an overall conclusion of the work described
so far and the scopes for further work in this specific field.

## 7.1. Epilogue

In this thesis, we have investigated multiferroic properties of nanostructured $BiFeO_3$ (bilayered nano-hollow spheres) compounds, $ErFeO_3$ (nanoparticles) and $Y_2NiMnO_6$ (thin film, and nanowires). We have found that two separate crystalline structures, spinel, and perovskite structure of CFO/BFO bilayered nano-hollow remains unchanged after heating. With the addition of CFO, the magnetic property increases dramatically and the magnetoelectric coupling properties also increases. Here the coercivity increases primarily because of magnetoelastic coupling between two composite nanostructures. The coercivity ($H_c$) of CFO/BFO NHSs are found to be higher than that of CFO NHSs due to the presence of foreign atoms on the surface of CFO NHSs which develop steric hindrance on the movement of magnetization. An applied magnetic field is used to change the magnetization of CFO and the ferroelectric polarization of BFO through its inherent magnetoelectric coupling as well as through the BFO/CFO magneto-elastic coupling. This may also be a reason for higher coercivity in CFO/BFO NHSs. The coexistence of the ferroelectric $BiFeO_3$ and ferromagnetic $CoFe_2O_4$ phases in the nano-composites gives rise to a significant ME effect through stress-mediated magnetic-mechanical-electric transformation at the interface.

In case of type-II multiferroic materials significant coupling between FE and FM occurs, as the origin of ferroelectricity is triggered by an exotic magnetic ordering. Magnetoelectric properties also shows significant increment in single perovskite type-II $ErFeO_3$ orthoferrite. Dzyaloshinskii-Moriya exchange interaction between Fe ions induced by the spin-orbit interaction, which reflect the local crystal anisotropy are the origin of ferroelectric polarization. The dielectric relaxation is non-Debye type and the conduction mechanism follows the correlated barrier hopping (CBH) model. Here, it is also explored the origin of multicolor fluorescence of 4f metals is twofold: one is LMCT transition from the tartrate ligand to the lowest unoccupied energy level of $Er^{3+}$ ions, another one is f-f transitions over Er present in the $ErFeO_3$. More importantly, $ErFeO_3$ is a new class of multiferroics and magnetoelectric coupling property is easier compared to type-I multiferroics.

In an attempt to solve the problem of weak magnetoelectric coupling in single perovskite type-I multiferroic material, we demonstrated another double perovskite type-II mulferroic material $Y_2NiMnO_6$. This work demonstrates the unusual room temperature ferromagnetism and ferroelectricity of the double perovskite multiferroic $Y_2NiMnO_6$ nanowires and thin films. The physics behind the co-existence and coupling of ferroelectricity and ferromagnetism in $Y_2NiMnO_6$ nanostructures (nanowires and thin films) at high temperature is the key focus of this article. The coexistence of the ferromagnetic and ferroelectric ordering in $Y_2NiMnO_6$ nanostructures (NWs and thin films) at high temperature is ascribed to the large concentration of surface spin and surface polarization of the electron, respectively, associated with the large surface area of the one-dimensional nanostructures (NWs and thin films). The studies indicate that for Y2NiMnO6 nanostructures (NWs and thin films), at room temperature, ferroelectricity and ferromagnetism are mutually coupled with each other and have similar origins too. Evidence of room temperature magnetoelectric coupling in the YNMO NWs has been confirmed from ME coupling coefficient studies. Confirmation of room temperature ferromagnetism in the YNMO nanostructured thin films has also been confirmed from MFM studies, which clearly shows the presence of ferromagnetic spin domains on the film surface. The MFM studies confirm the results of the magnetic studies on the YNMO nanostructured thin films. Existence of ferroelectric domains with antiparallel polarizations in the thin films surface has also been established by PFM studies. This study demonstrates that there is ample opportunity to tailor the inherent electric and magnetic orders at room temperature in perovskite materials down in nano-scale dimension. It is evident that along with multiferroic behavior, $Y_2NiMnO_6$ NWs will be a promising candidate in the field of electrochemical supercapacitor. Our study yields a proper comparison of the multiferroic properties in single (type-I and type-II) and double perovskite (type-II) nanostructures (nanoparticles, nanowires, nano-hollow spheres and thin films) together with their various applications.

## 7.2. Scope for future study:

In this thesis we have studied the effect of $CoFe_2O_4$ on $BiFeO_3$ and seen that enhances all the multiferroic properties. It would be more interesting to study the effect of magnetic material on ferroelectric material using their magneto-elastic property. Here $BiFeO_3$ supplies the ferroelectric polarization of the bilayered nano-hollow spheres. So it is possible the CFO fixed and vary BFO site with different ferroelectric materials and vice-versa for optimum condition. From the present studies it is clear that bilayered nano-hollow spheres shows better multiferroic properties. To get a observable value of multiferroic property one can easily prepare multilayer composite system (such as BFO/CFO/BFO or CFO/BFO/CFO etc.) as a thin film and study their magnetoelectric properties.

We have also studied the multiferroic properties of $ErFeO_3$ a new type of multiferroic material. This material also gives an opportunity to study its thin film, nano wire and other nanostructures for its multiferroic properties. We have also studied the multiferroic properties of $Y_2NiMnO_6$ bulk, NWs and thin films. Here NWs and thin film showed unusual room temperature ferromagnetism and ferroelectricity. To get higher value of multiferroic property one can easily prepare $Y_2NiMnO_6$ nanotubes or composite thin films.

Therefore, high magnetoelectric properties of BFO/CFO bilayered nano-hollow spheres, $ErFeO_3$ NPs and $Y_2NiMnO_6$ NWs and thin films scope to use in technology, magnetoelectric based electronic devices such as MERAM, FeRAM, MRAM, sensors, and so on. $ErFeO_3$ NPs having excellent photocatalytic activity in degradation of methylene blue and multi-colour fluorescence property also open up a new door for bio-imaging, drug delivery and wastewater treatment. $Y_2NiMnO_6$ NWs may establish as a promising material for supercapacitor and as a part of storage devices.